TESE DE DOUTORAMENTO

CALIBRATING JET IMAGING OF QCD COLLECTIVITY

João Lourenço Henriques Barata

ESCOLA DE DOUTORAMENTO INTERNACIONAL DA UNIVERSIDADE DE SANTIAGO DE COMPOSTELA

PROGRAMA DE DOUTORAMENTO EN FÍSICA NUCLEAR E DE PARTÍCULAS

SANTIAGO DE COMPOSTELA

2021

USC
UNIVERSIDADE
DE SANTIAGO
DE COMPOSTELA

DECLARACIÓN DEL AUTOR/A DE LA TESIS

D. João Lourenço Henriques Barata

Título da tese: Calibrating Jet Imaging of QCD Collectivity

Presento mi tesis, siguiendo el procedimiento adecuado al Reglamento y declaro que:

1) La tesis abarca los resultados de la elaboración de mi trabajo.
2) De ser el caso, en la tesis se hace referencia a las colaboraciones que tuvo este trabajo.
3) Confirmo que la tesis no incurre en ningún tipo de plagio de otros autores ni de trabajos presentados por mí para la obtención de otros títulos.

Y me comprometo a presentar el Compromiso Documental de Supervisión en el caso que el original no esté depositado en la Escuela.

En Santiago de Compostela, a 30 de Marzo de 2021.

Firma electrónica

USC
UNIVERSIDADE
DE SANTIAGO
DE COMPOSTELA

AUTORIZACIÓN DEL DIRECTOR/TUTOR DE LA TESIS

D. Carlos Alberto Salgado López

En condición de: Diretor de la Tesis

Título de la tesis: Calibrating Jet Imaging of QCD Collectivity

INFORMA:

Que la presente tesis, se corresponde con el trabajo realizado por D. João Lourenço Henriques Barata, bajo mi dirección/tutorización, y autorizo su presentación, considerando que reúne los requisitos exigidos en el Reglamento de Estudios de Doctorado de la USC, y que como director/tutor de esta no incurre en las causas de abstención establecidas en la Ley 40/2015.

En Santiago de Compostela, a 30 de Marzo de 2021

Firma electrónica

USC
UNIVERSIDADE
DE SANTIAGO
DE COMPOSTELA

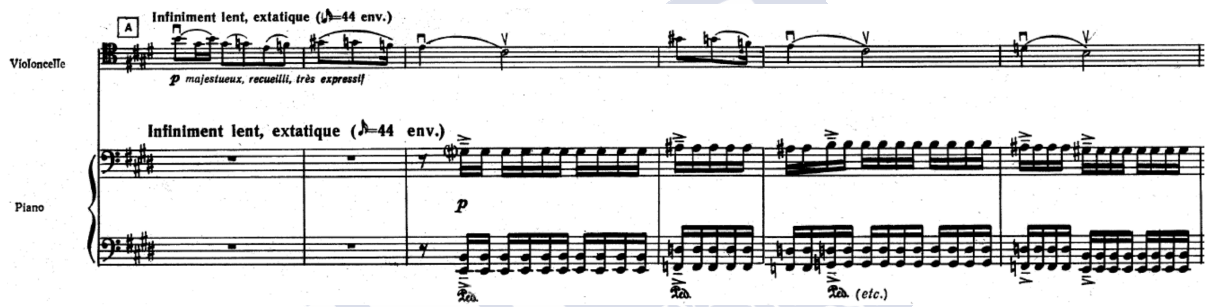

"[...] *Une grande phrase, infiniment lente, du violoncelle, magnifie avec amour et révérence l'éternité de ce Verbe puissant et doux, "dont les années ne s'épuiseront point". Majestueusement, la mélodie s'étale, en une sorte de lointain tendre et souverain* [...]".

V. *Louange à l'Eternité de Jésus*, from *Quatuor pour la fin du temps*,
Olivier Messiaen (1941)

USC
UNIVERSIDADE
DE SANTIAGO
DE COMPOSTELA

João Lourenço Henriques Barata

Acknowledgments

First of all, I am very grateful to Carlos Salgado for having agreed to supervise my thesis. Carlos, despite being a very busy person, always found time to discuss with me and to share his quite unique way of thinking, which has greatly influenced me. I am also lucky that Carlos gave me a lot of freedom to pursue different interests. Most of the times such deviations lead to no concrete result, but besides the learning experience, I think this freedom to pursue different goals is well reflected in this thesis. Perhaps more importantly, Carlos was also always a very supportive adviser, which I found particularly helpful in the great year of 2020.

Besides Carlos, I was also lucky to have met many smart and sometimes unique people while in Santiago. I am particular in debt: to Nestor Armesto for always being available to answer my questions, to the many post-docs (Riccardo, Miguel, Max, Tan, Daniele, and the many more I apologize to have forgotten to mention) which made working at IGFAE more fun, to Ricardo Rodríguez for guiding me through the wonderful world of Spanish bureaucracy and to Marcos Seco for helping me with my deficiency in working with computers.

I am also in debt to Yacine Mehtar-Tani and Raju Venugopalan for having hosted me at BNL, even if only for two (very productive) months. As it is evident in the following pages, I have benefited greatly from this visit and I learned a lot from the group at BNL.

This thesis would also not have been possible without the many fantastic collaborators I had the pleasure to work with: Liliana Apolinário, Guilherme Milhano, Victor Vila, Carlos Salgado, Fabio Dominguez, Yacine Mehtar-Tani, Konrad Tywoniuk, Alba Soto-Ontoso, Raju Venugopalan, Niklas Mueller and Andrey Tarasov (in no particular order). I am particularly grateful to Alba and Niklas, who always had time to answer my questions and without their work the results presented here would not exist.

I also would like to thank Xabier Feal for giving me a helping hand while visiting BNL and for the many insightful discussions we had. I would also not have been able to complete this thesis without the help of Victor, who has always been there to help me when I needed. I am also grateful to Guilherme for helping me start on this field many years ago when I was still an undergraduate.

Finalmente, quero agradecer todo o apoio dos meus pais e do meu irmão ao longo destes anos, sem o qual nunca teria sido possível escrever esta tese. À Laura agradeço o amor e o carinho, que me fazem uma pessoa feliz todos os dias.

The project that gave rise to this thesis received the support of a fellowship from "la Caixa" Foundation (ID 100010434). The fellowship code is LCF/BQ/ DI18/11660057. This project has received funding from the European Union's Horizon 2020 research and innovation program under the Marie Sklodowska-Curie grant agreement No. 713673. JB is supported by Ministerio de Ciencia e Innovacion of Spain under project FPA2017-83814-P; Unidad de Excelencia Maria de Maetzu under project MDM-2016-0692; European research Council project ERC-2018-ADG-835105 YoctoLHC; and Xunta de Galicia (Conselleria de Educacion) and FEDER. I also the acknowledge the support from the Fulbright Commission and Brookhaven National Lab.

USC
UNIVERSIDADE
DE SANTIAGO
DE COMPOSTELA

João Lourenço Henriques Barata

Abstract

Over the last decades, heavy ions collisions experiments at CERN and BNL have offered an unique window to study QCD under hot and dense conditions. In such high energy events a new state of matter, the Quark Gluon Plasma, is formed and a big effort has been made towards exploring its properties, which are intimately related to the origins of the Universe and the fundamental nature of ordinary matter.

This thesis is embedded in the effort towards a higher precision and improved physical description of high energy QCD processes relevant for heavy ion physics. In a first section, we explore a novel analytic treatment of in-medium single parton evolution, the key theoretical tool of jet quenching. In a second chapter, we propose a novel strategy to simulate high energy scattering processes using a digital quantum computer. Finally, we lay the first stones for the simulation of a full medium induced parton cascade using quantum simulation techniques.

Keywords: Jet Quenching, High Energy QCD, Quantum Simulation.

USC
UNIVERSIDADE
DE SANTIAGO
DE COMPOSTELA

Resumen

Durante las últimas décadas, los experimentos de colisiones de iones pesados en el CERN y BNL han ofrecido una ventana única para estudiar QCD en condiciones cálidas y densas. En eventos de tan alta energía se forma un nuevo estado de la materia, el plasma de quarks y gluones, y se ha realizado un gran esfuerzo para explorar sus propiedades, que están íntimamente relacionadas con los orígenes del Universo y la naturaleza fundamental de la materia ordinaria.

Esta tesis está integrada en el esfuerzo hacia una mayor precisión y una descripción física mejorada de los procesos QCD de alta energía relevantes para la física de iones pesados. En una primera sección, exploramos un tratamiento analítico novedoso de la evolución de partón único en medio, la herramienta teórica clave de jet quenching. En un segundo capítulo, proponemos una estrategia novedosa para simular procesos de dispersión de alta energía utilizando una computadora cuántica digital. Finalmente, colocamos las primeras piedras para la simulación de una cascada de partones inducida por lo medio, utilizando técnicas de simulación cuántica.

Palabras clave: Jet Quenching, QCD de alta energía, simulación cuántica

USC
UNIVERSIDADE
DE SANTIAGO
DE COMPOSTELA

João Lourenço Henriques Barata

Resumo

Durante as últimas décadas, experimentos de colisión de ións pesados no CERN e BNL ofreceron unha xanela única para estudar a QCD en condicións de alta temperatura e densidade. Netes eventos de tan alta enerxía, fórmase un novo estado da materia, o plasma de quarks e gluóns, e un gran esforzo está a ser realizado para explorar as súas propiedades, que están intimamente relacionadas coas orixes do Universo e coa natureza fundamental da materia ordinaria.

Esta tese está integrada no esforzo cara a unha maior precisión e unha mellor descrición dos procesos de QCD de alta enerxía relevantes para a física dos ións pesados. Na primeira parte da tese exploramos un novidoso tratamento analítico da evolución no medio dun único partón, a ferramenta teórica clave do jet quenching. Na segunda parte, propomos unha nova estratexia para simular procesos de dispersión de alta enerxía mediante un ordenador cuántico dixital. Por último, colocamos as primeiras pedras para a simulación dunha fervenza de partóns inducida polo medio, empregando técnicas de simulación cuántica.

Palabras chave: Jet Quenching, QCD de alta enerxía, simulación cuántica

USC
UNIVERSIDADE
DE SANTIAGO
DE COMPOSTELA

Contents

List of Figures

USC
UNIVERSIDADE
DE SANTIAGO
DE COMPOSTELA

Extended Abstract

Since its formulation in the second half of the last century, QCD has been one of the most successful physical theories ever devised. In the most recent decades, the study of QCD has been pushed towards exploring extreme density and temperature conditions, where new states of matter can be found. Indeed, the formation of the Quark Gluon Plasma (QGP), a hot and dense state of matter composed by free quarks and gluons interacting strongly, has been observed both at LHC and RHIC, and is one of the greatest scientific findings of the last one hundred years.

Besides offering a way to probe the nature of the confinement/deconfinement phase transition and other fundamental properties of QCD, the study of the QGP is also expected to shed a new light on the first microseconds of our Universe and thus it is a promising avenue to find new fundamental physics. Nonetheless, the QGP formed in experiments is so short lived that not even light is fast enough to probe its dynamics. As such, probes generated in the same events from which the QGP emerges have to be used in order to indirectly extract the characteristics of the medium.

In this thesis, we study the dynamics of hard parton probes that have to transverse the QGP, giving rise to particle jets. The modifications of the jets' properties with respect to the vacuum benchmark due to the presence of the QGP medium is referred to as *jet quenching*. The first section of this thesis is dedicated to improving the theoretical and phenomenological description of jet quenching.

- **Jet quenching beyond the multiple soft and single hard divide**: We study the physics of multiple scattering of a hard parton in a background field. In the last two decades, the studies of this problem, which form the basis of jet quenching phenomenology, have been either divided into the regime of multiple soft interactions with the medium, a single hard interaction or relied on numerical routines. In this thesis, we review a recent proposal to merge the single hard and multiple soft approaches into a single theoretical framework. In particular, we will show that the theoretically formulation of this approach is well formulated to all orders in perturbation theory and that it can be used either to study medium induced radiation or momentum broadening effects.

Although having access to probes of the QGP is useful, first principle simulations of high energy QCD processes also provide a way to study the QGP and many other aspects of QCD. Unfortunately, it is well known that the simulation of QCD, and quantum field theories (QFTs) in general, is not feasible in classical computers. However, over the last years a great interest and rapid development has been witnessed in using quantum computers to simulate the dynamics of complex theories like QFTs. Although current approaches are still highly constrained by the current hardware capabilities, it is hoped that in the coming decades quantum computing might lead to the exploration of physics currently inaccessible to classical methods. In a second section of this thesis, we introduce a novel strategy to simulate QFTs in a digital quantum computer.

- **High energy scattering in a digital quantum computer**: We study high energy scattering in scalar ϕ^4 theory in a digital quantum computer, using a digitization in part motivated by the parton model picture of high energy QCD. Although such an approach is still far from allowing a meaningful simulation to be done in current hardware, it provides a formulation of the problem much closer to the one typically used in high energy physics.

Finally, quantum interference effects, so critical to have a complete picture of jet quenching, are mostly absent from classical Monte Carlo jet quenching simulations, in favor of a probabilistic and factorizable picture which allows for an easier treatment of multiple radiation sources. Although such approaches have been very successful and constitute the backbone of jet quenching phenomenology, being able to explore the full quantum nature of medium induced parton showers would be of invaluable importance. This is the final topic explored in this thesis.

- **Towards the quantum simulation of jet quenching**: We present a simple quantum simulation strategy to study the dynamics of a single particle propagating inside a QCD medium, while ignoring the formation of induced radiation. This constitutes the first step towards the simulation of medium induced parton showers, capturing their full quantum nature, which can in principle be efficiently explored using a quantum computer, but well beyond the capabilities of any classical method.

1

Introduction

In this brief chapter, we provide a broad introduction to the two topics to be further explored in this thesis. The first subject is Quantum Chromodynamics (QCD), the Quantum Field Theory (QFT) that describes the strong interaction. The second topic is Quantum Computing (QC), which relates to the interest of exploring the quantum world to perform computations.

1.1 The Basics of QCD

The origins and the QCD Lagrangian

QCD is perhaps the most remarkable Quantum Field Theory which can be experimentally tested [14].

The pre-QFT origins of QCD[1] can be traced back to the works of Gell-Mann, Zweig and others on particle spectroscopy [16–18]. In the so called Gell-Mann's *Eightfold Way* [17] one could understand the every increasing zoo of particles produced in particle physics experiments of the time in terms of the irreducible representations of the $SU(3)_{\text{flavor}}$ group. This assumed that hadronic matter was formed by more elementary particles, corresponding to the QCD quarks, which had 1/2-spin and could have three different flavors. At the time, there were two big issues with this proposal i) some states, like the Δ^{++} and Ω^{-} baryons [19,20], seemed to violate the Spin-Statistics theorem ii) the

[1] See [15] for an historical review of QCD by one of its major contributors.

introduced new fundamental particles seemed illusive and had never been experimentally observed.

The first of these two problems was solved by introducing yet another quantum number: color [21]. On top of the spin and flavor content, these elementary particles also carried a $SU(3)_{\text{color}}$ charge and could combine such that observable states were white, i.e. had no net color charge. The second problem was solved by realizing that there must be some strong attractive interaction between fundamental particles, which ensures that at low energies fundamental particles can not exist alone. Such an interaction suggests the existence of a gauge boson, latter corresponding to the QCD gluon.

In the modern QFT formulation, QCD corresponds to a $SU(3)_{\text{color}}$ Yang-Mills theory [22] coupled to matter composed of 1/2-spin particles transforming in the fundamental representation of $SU(3)_{\text{color}}$. The massive fermions correspond to *quarks*, while the massless gauge bosons are referred to as *gluons*. The QCD Lagrangian can be written as [23–27]

$$\mathcal{L}_{\text{QCD}} = \mathcal{L}_{\text{Dirac}} + \mathcal{L}_{\text{gauge}} \,. \tag{1.1}$$

The matter content is described by a Dirac Lagrangian

$$\mathcal{L}_{\text{Dirac}} = \sum_f \bar{q}_i^f(x) \left[i\gamma^u D_\mu(x) - m_f \right]_{ij} q_j^f(x) \,, \tag{1.2}$$

where $q_i^f(x)$ stands for the quark fermion field, with color index $i \in \{1,2,3\}$ (in the fundamental color representation), flavor $f \in \{\text{u},\text{d},\text{s},\text{c},\text{b},\text{t}\}$ and mass m_f. Also, γ^μ are the Dirac gamma matrices and, as usual, $\bar{q} = q^\dagger \gamma^0$. The covariant derivative D_μ ensures that the full Lagrangian is invariant under local gauge transformations and reads

$$D_\mu(x) = \partial_\mu - igA_\mu^a(x)t^a \,, \tag{1.3}$$

where g is the strong coupling constant, A_μ^a the (gluon) gauge field with adjoint color index $a \in \{1,2,\cdots,8\}$ and t^a are the $SU(3)_{\text{color}}$ in the fundamental representation.

The pure gauge field content of the QCD Lagrangian can be compactly written in terms of the gauge field tensor $F_{\mu\nu}^a$

$$\mathcal{L}_{\text{gauge}} = -\frac{1}{4} F_{\mu\nu}^a F^{a\mu\nu} \,, \tag{1.4}$$

which is itself given by

$$F_{\mu\nu}^a = \partial_\mu A_\nu^a - \partial_\nu A_\mu^a + g f^{abc} A_\mu^b A_\nu^c \,. \tag{1.5}$$

Here $f^{abc}t^c = -i[t^a, t^b]$ are the color group structure constants. We choose generators of the fundamental representation of the color group to be given by $2t^a = \lambda^a$, where λ^a are the eight Gell-Mann matrices [23, 24].

Finally, to construct the Feynman QCD rules one needs to make the gauge dependence explicit, so that the propagator for the gluon field can be defined. This can be done by applying the Fadeev-Popov identity trick [28], leading to two additional terms in Lagrangian: one containing the gauge condition, thus breaking gauge symmetry, and a term containing the Fadeev-Popov ghost field that cancels non-physical degrees of freedom. In this thesis, we will always work in the light cone gauge, where $A^+ = (A^0 + A^3)/\sqrt{2} = 0$, and thus the ghost field can be integrated out. The Feynman rules can then be easily obtained from the resulting generating function using standard methods [23, 24].

The running of the coupling, factorization and DIS

Perhaps one of the most remarkable features of QCD is the running in energy of its coupling, which evolves in exactly the opposite way compared to gravity or electrodynamics. At small distances (large energies), quarks and gluons behave almost as free particles. This feature, usually referred too as *asymptotic freedom* [27,29], implies that the coupling in this regime must be small and standard perturbation theory techniques must be applicable. On the other hand, as the relevant energy scale decreases, the coupling grows up to the point where interactions are so strong that quarks and gluons can not break free from each other. In this regime of *confinement*, hadrons are the physical QCD degrees of freedom.

The origin of this striking behavior of QCD can be traced back to the fact the color gauge group is non-Abelian. Expanding out Eq. (1.1), and comparing to Quantum Electrodynamics (QED), which has a $U(1)_{\rm Y}$ Abelian gauge symmetry, one finds extra three and four gluon vertices, due to the last term in Eq. (1.5) which is absent in QED. At the level of the running of the coupling $\alpha_s(Q^2) = g^2(Q^2)/(4\pi)$, this results that at one loop order the coupling evolves as [27, 30]

$$\alpha_s(Q^2) = \frac{1}{\beta \log \frac{Q^2}{\Lambda^2_{\rm QCD}}}\,, \tag{1.6}$$

where $\Lambda_{\rm QCD} \approx 200\,{\rm MeV}$ is the scale separating the strong and weakly coupled regimes, of the order of the (inverse) typical size of a hadron, $\beta = (11N_c - 2n_f)/(12\pi)$, with $N_c = 3$ the number of colors and n_f the number active light flavors. We thus see that for large values of the relevant energy scale in the problem, Q^2, the coupling vanishes and the theory is that of free QCD, where the physical degrees of freedom are quarks and gluons, while when $Q^2 \to \Lambda^2_{\rm QCD}$ the coupling diverges and the theory is not amenable to perturbative treatment. This behavior has not only been theoretically predicted, but it has also been experimentally verified to a very high degree of accuracy (see Fig. 1.1), constituting one of the major successes of QCD.

The above scaling of the coupling with the energy scale is crucial to understand high energy scattering of hadrons. At very short distances, where $Q^2 \gg \Lambda^2_{\rm QCD}$, the coupling is small and perturbation theory is applicable. At such scales, scattering must occur at spatial scales $\sim 1/Q \ll 1/\Lambda_{\rm QCD}$ where this last scale is roughly the typical size of a hadron.

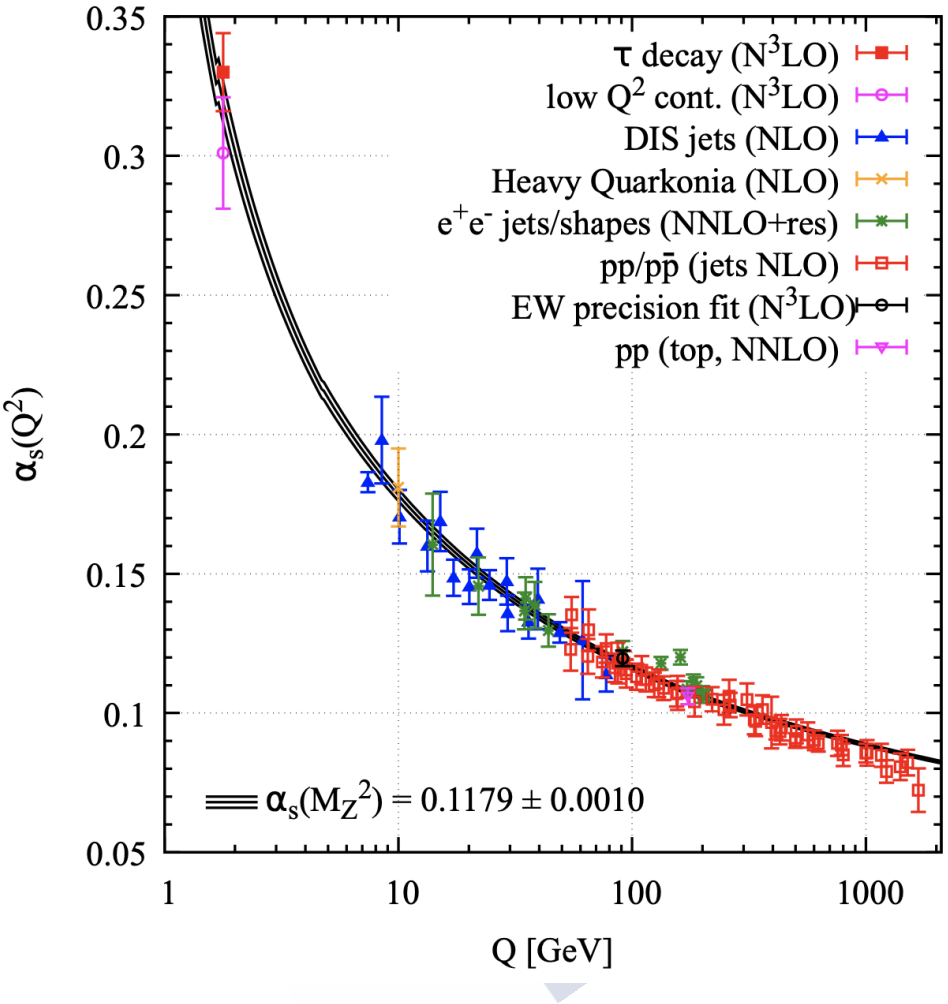

Figure 1.1: The running of α_s, with a comparison between the result obtained from the renormalization group evolution and experimental results obtained from different physical processes. Figure taken from [1] under a Creative Commons license.

Thus, hard scattering must be amenable to a description based on the quark and gluon degrees of freedom deep inside different hadrons. Additionally, when scattering hadrons, their structure, which can not be described perturbatively, should be independent of the particular details of the collision (i.e. hadrons' structure is universal). One is then lead to conclude that a full scattering event can be written as a convolution of *soft* universal terms associated to the non-perturbative structure of the hadrons and *hard* pieces which detail the microscopic local interactions between quarks and gluons. This property is called *factorization* and, although it has only been proven theoretically to hold for a small class of events [31,32], it provides a good description of data. In particular, if one is interested to know the cross-section for obtaining, for example, the hadronic final state C (and some other state X) from the collision of two other hadrons A and B, assuming the process is

factorizable amounts to writing (schematically)

$$\sigma^{A+B\to C+X} = f_a^A(x_a, Q^2) \otimes f_b^B(x_b, Q^2) \otimes \hat{\sigma}^{a+b\to c}(x_a, x_b, Q^2, \alpha_s(Q^2)) \otimes D_c^C(x_c, Q^2)\,. \quad (1.7)$$

Here, f_a^A is a parton distribution function (PDF), corresponding (at leading order) to the probability of finding parton a, i.e. a quark or a gluon, inside hadron A with energy fraction fraction x_a, while D_c^C is a fragmentation function (FF) encapsulating the hadronization of parton c to the hadron C. Both these objects can only be described non-pertubatively, unlike the partonic cross-section $\hat{\sigma}$. The scale Q^2, connecting the hard and soft contributions is arbitrary, meaning that different choices for this scale must lead to the same cross-section. Therefore, one can devise a renormalization group equation describing the evolution of the PDFs and FFs with Q^2. Thus, first extracting them from data that at some energy scale allows one to access the distributions at any other scale. This evolution in energy is governed by the Dokshitzer-Gribov-Lipatov-Altarelli-Parisi (DGLAP) equations [33–35]. They are applied to extract PDFs and FFs at different energy ranges in so called global analyses, which are only possible due to the universality property mentioned above.

The QCD factorization theorems are crucial to study the high energy processes experimentally explored at the Large Hadron Collider (LHC) at CERN, the Relativistic Heavy Ion Collider (RHIC) and future Electron Ion Collider (EIC) at Brookhaven National Laboratory (BNL). The paradigmatic example of a QCD high energy scattering experiment is Deep Inelastic Scattering (DIS), consisting on scattering a highly energetic electron off a hadron, producing new hadronic final states. As pointed out by Bjorken and Feynman [36, 37], at high energies DIS can be understood as the scattering of an off-shell photon probe, with momentum q, emitted by the incoming electron on the pointlike partons forming the hadron, which has momentum P. This partonic picture portrays the hadron as a collection of loosely bound partons (quarks and gluons), whose motion is aligned with that of the parent hadron, and each parton carries an energy fraction x_i of the total energy of the hadron. Then, the kinematical variable

$$x_{\rm BJ} \equiv \frac{Q^2}{2P_\mu q^\mu}\,, \quad (1.8)$$

with $Q^2 = -q^2 \gg \Lambda^2_{\rm QCD}$ the photon's virtuality, can be identified with the energy fraction carried by the struck parton, i.e. $x = x_{\rm BJ} = k^0/P^0$, with k the parton's momentum.

An important consequence of the emergent parton description of high energy QCD scattering is the formation of a clear spacetime picture for the scattering process. Indeed, in the rest frame of the hadron, it is easily realized that there is a clear separation of scales, between the photon-hadron interaction time and the time over which the probe remains in a coherent partonic state. In this frame, one can parametrize $q^\mu = (q^0, 0, 0, q^3)$ and $P^\mu = (M_h, 0, 0, 0)$ (with M_h the hadron mass), such that one obtains

$$q^0 = \frac{Q^2}{2M_h x} \gg Q\,, \quad (1.9)$$

with the relevant longitudinal scale being [23, 38]

$$\tau_0 \sim \frac{q^0}{Q^2} \sim \frac{2}{M_h x} \equiv \tau_{\text{Ioffe}}\,, \tag{1.10}$$

where τ_{Ioffe} is the so called Ioffe time [39, 40]. This (large) coherence scale over which the photon state is frozen should be compared to the typical interaction time $\tau_I \sim 1/Q$, which comes from the fact Q is the relevant hard scale in the problem. Thus, DIS (and high energy scattering in general) can be viewed, in this parton picture, as the photon instantly probing a region of transverse size $\sim 1/Q$ of the hadrons wavefunction, which for a fixed x is given by the direct product of single particle Fock states. This construction goes beyond the formal S–matrix formulation of scattering, where at high energies one would expect that the probe could explore arbitrarily high occupation number states of the hadron wavefunction, since the energy gap between states with different particle number vanishes at high energy. This is however not the case in QCD due to the appearance of extra physical scales such as τ_I and τ_{Ioffe}. In chapter 5 we present a strategy for (quantum) simulating high energy scattering processes, partially motivated by the emergent partonic picture of QCD at high energies.

QCD hard probes in a medium

One of the ultimate goals of the QCD physics program is to understand the QCD phase diagram. As pointed out many decades ago [41, 42], collisions evolving heavy nucleus allow the exploration of phase diagram regions where matter exists in a deconfined and dense state, the so called Quark Gluon Plasma (QGP). Thus, such experiments offer an unique opportunity to explore aspects such as the confined/deconfined phase transition, properties of the early universe and more generally extract the QCD equation of state. Experimentally, it is however not possible to directly extract the physical properties of the QGP since it is very short lived; rather one makes use of self-generated indirect probes which are sensitive to the underlying medium.

One of the most successful and interesting probes of the QGP are jets, particularly due to their capability of resolving the time evolution of the medium [43, 44] and to the excellent benchmarking possible with respect to in-vacuum jets [45, 46].

As in vacuum, in-medium processes are still assumed to be factorizable [47, 48], and thus the study of jet evolution in a background medium is still modular. The major differences to the case of jets being produced in *cleaner* hadron collisions lies in the fact that PDFs must be updated to nuclear PDFs (nPDFs), which now describe the non-perturbative structure of the colliding nucleus. The hard scattering partonic cross-sections are assumed to be unchanged, since such processes take place on scales $\sim 1/Q$, where medium effects are negligible. Finally, the modification of the jet structure will show up in a new fragmentation pattern, due to the final state interaction between the jets produced in the hard scattering event and the underlying medium produced in the same event. The modification of jets due to final state interactions with a background

medium is referred to as *jet quenching*, first proposed by Bjorken as a way to study the properties of the QGP [49] and first experimentally observed at RHIC [50].

The ultimate goal of the jet quenching physics program, which has been active for the last decades, is to successfully connect the underlying local probe-medium physics to the observed fragmentation pattern of jets. From a phenomenological/theoretical point of view, medium induced jet modifications are built up from studying the medium modifications to a single hard propagating parton, which can either result in the modification of its four-momenta or the production of medium induced radiation. Thus, the main theoretical effort has been in computing the differential probabilities associated with these two types of processes. In chapter 2, we review some of the key aspects of jet quenching theory, and discuss the elastic and radiative effects which dominate jet quenching phenomenology. This sets the stage for chapter 3, where such effects are studied beyond commonly used analytic *single hard vs. multiple soft* approximations. In chapter 6, we give the first steps towards quantum simulating jet quenching, which, if possible, could in principle allow for a complete treatment of quantum effects absent from traditional classical simulation routines [51–57].

1.2 The Basics of Digital Quantum Computing

The necessity to have quantum computers to simulate some physical systems was first recognized by Feynman [58] in the 1980's. This observation was immortalized by the now famous quote

> *I'm not happy with all the analyses that go with just the classical theory, because nature isn't classical, dammit, and if you want to make a simulation of nature, you'd better make it quantum mechanical.*

The successful application of quantum computation techniques requires three ingredients: efficient quantum algorithms, reliable quantum devices and the identification of physical problems where the quantum advantage is critical. The first point relates to designing algorithms that do not violate the laws of quantum mechanics and can outperform their classical counterparts while the second point relates to the necessity to have controllable quantum devices one can use to perform computations. We proceed to briefly discuss some aspects of these two points in the following sections.

Regarding the last point, quantum computing has shown to be an essential tool in areas as distinct as physics, chemistry, finance, machine learning and many others [59–63]. In this thesis our interest is in the application of quantum computing techniques to i) explore the dynamics of high energy scattering in QFT ii) take the first steps towards the full quantum simulation of jet quenching. While i) has been a topic of interest in the high energy physics community for already some time, first initiated by [64, 65], ii) has not been explored so far. We further discuss these topics in detail in chapters 5 and 6, respectively.

Quantum algorithms

Quantum computing aims at exploring the possibility of controlling quantum systems in order to perform computations more efficiently than their classical counterpart. Naively, the so called *quantum advantage* quantum algorithms enjoy over classical ones is fundamentally related to the possibility to represent information in terms of highly entangled quantum states, e.g.

$$|\psi\rangle \propto c_{10010}\,|10010\rangle + c_{10011}\,|10011\rangle + \cdots\,, \tag{1.11}$$

where each c is a numerical coefficient, and due to the fact that quantum mechanics is linear, which leads to efficient ways of implementing logical gate operations, e.g.

$$U\,|\psi\rangle \propto c_{10010}U\,|10010\rangle + c_{10011}U\,|10011\rangle + \cdots\,, \tag{1.12}$$

where U is an operator. If one were to mimic such a state representation in a classical device, the number of bits (or some other basic form of representing information) would be exponentially larger than the number of quantum basic information units. On top of this, implementing a gate operation would also entail the application of an exponential number of basic operators, leading to less trivial implementations.

On the other hand, quantum algorithms are constrained by the laws of quantum mechanics, and thus not all operations possible in the classical setting find a quantum analog. Combined with the fact that classical algorithms have been developed for a long time, these perhaps justifies why so few quantum algorithms which can outperform classical ones are known. Fundamentally, algorithmic design for quantum devices requires using a *quantum way of thinking*, in order to take advantage of the properties of Quantum Mechanics. This is of course estranged to the usual (classical) intuition, and thus the design of quantum strategies requires a great deal of ingenuity.

To the present day, three big classes of quantum algorithms (which can outperform their classical counterparts) are known.

- **Quantum factoring**: The most famous factoring algorithm is Shor's algorithm [66], which is exponentially faster than its classical counterpart. Essentially, quantum factoring aims at determining with high accuracy (and probability) the eigenvalues of a target operator. In short, the factoring problem can be stated as: given an unitary U and a state $|\phi\rangle$ such that

  $$U\,|\phi\rangle = e^{i\lambda}\,|\phi\rangle\,, \tag{1.13}$$

  find λ. For applications of QC, it is easily realized that factoring algorithms are critical in order to, for example, extract the expectation value of observables. Indeed, in chapter 5, we will make use of the quantum Phase Estimation Algorithm [67] (PEA), which is a factoring algorithm, in order to extract the momentum and energy of states being produced in high energy scattering experiments.

- **Quantum search**: Search algorithms are based on the work by Grover [68] and have a quadratic speed up over classical algorithms. The search problem can formulated as: given $x \in \{0, 1, 2, \cdots, N\}$, and U such that

$$U|x\rangle = \begin{cases} -|x\rangle & , \text{ if } x = x_0; \\ |x\rangle & , \text{ else,} \end{cases} \tag{1.14}$$

  find x_0. A generalization of Grover's algorithm is the Amplitude Amplification (AA) algorithm [69], which given a state $|\phi\rangle = \cos(\alpha)|\psi\rangle + \sin(\alpha)|\psi_\perp\rangle$, where $\langle\psi|\psi_\perp\rangle = 0$, the AA algorithm gives a way to prepare the state $\cos((2n+1)\alpha)|\psi\rangle + \sin((2n+1)\alpha)|\psi_\perp\rangle$, for some positive integer n. Thus, this algorithm allows one boost the probability of preparing the state $|\psi\rangle$; as we will show in chapter 5, the partition of the Hilbert into orthogonal sub-spaces is natural when discussing kinematical cuts of the phase space associated to the states produced in a scattering experiment. Thus, generalizations of the AA algorithm are useful for amplifying the probability of producing states in the desired region of phase space.

- **Quantum simulation**: The possibility to simulate Nature using controllable quantum devices was first pointed out by Feynman and Manin [58, 70] and then further developed by Lloyd [71]. The quantum simulation algorithm is essentially a map between a hermitian but not necessarily unitary operator H (a Hamiltonian) and the associated unitary $U = \exp(-iHt)$ (the time evolution operator). For physical Hamiltonians, one can always write $H = \sum_k H_k$, where each H_k only acts on a local sub-space of the full Hilbert, and thus quantum simulation boils down to finding an efficient and accurate way of implementing U using this decomposition. This algorithm is the main focus of chapter 4, where we give a more detailed discussion. The quantum simulation algorithm is applied in chapters 5 and 6, to simulate high energy scattering and the evolution of a energetic parton in a dense QCD medium.

- **One to unite them all**: Recently, it was realized that in fact all these quite different algorithms can be viewed as particular cases of a more general framework [72]. Although we will not further discuss this topic in this thesis, it is too much of a remarkable result not to be mentioned.

Physical realizations of a quantum computer

In the previous section, the treatment of the states storing information neglected their physical origin, e.g. when (loosely) writing $|1\rangle$ or $|0\rangle$ we missed to detail the Hilbert space where these states live. Typically, when discussing quantum algorithms manipulating quantum bits, they can be theoretically treated as if they were the spin state along the z direction of a 1/2-spin particle. Nonetheless, these *logical* states do not have to correspond to the spin state of a physical fermionic particle, rather they are usually engineered from other more complex quantum systems. Typically the choice of the system must obey Di

Vincenzo's criteria [73][2], which essentially state that the system chosen should be scalable, have a long enough coherence times and quantum bits and quantum operations can be implemented[3]. In addition, preparing the system in a fiducial state and the capability of measuring it in a specific basis must also be required, so that one can perform controllable computations.

Selecting the correct quantum system to provide a physical realization of a quantum computer is a difficult task. For example, an array of 1/2-spin particles could in principle be used to represent an array of quantum bits, with an external magnetic field being used to control the state of each spin. However, in reality the spin-field coupling is weak and thus it would be hard to control such a system. On top of that, spins will also have couplings between themselves which can not be ignored and they can also couple to the environment. As such, more elaborate constructions are necessary. Indeed, many realizations of a digital quantum computer exist[4] each with its merits and disadvantages.

We consider here, for illustration, a simplified picture of two popular physical realizations of a quantum computer: cavity QED [75] and circuit QED [76, 77]. In the simplest possible terms, in these approaches there is a cavity which stores a spatially well localized monochromatic electromagnetic mode. In addition to the cavity, there is an atom (transmon) which can be modeled as a two level system, with a coupling to the mode in the cavity. The system evolves accordingly to the Jaynes–Cummings Hamiltonian [78, 79], which treats the cavity modes as a quantum harmonic oscillator, the atom (transmon) as a 1/2-spin and includes a atom-cavity interaction term. Thus, one can picture the system as is depicted in Fig. 1.2.

In the first scenario, **a**), one considers several atoms interacting with the cavity, each storing a quantum bit of information. In this case, adding more atoms increases the amount of information being stored, with the atom-cavity coupling allowing the implementation of different quantum gates. On the other hand, one can instead use the cavity to solely store the information of the system and the atom to implement transformations on the system state. In this case, multiple quantum bits can be constructed by tensoring together several cavities.

A simple realization of a quantum logical bit of information is immediate to formulate in this latter case. If $\{|0\rangle, |1\rangle, |2\rangle, |3\rangle, |4\rangle\}$ is the set of the lowest occupation eigenstates of the cavity mode, then one can define the logical states $|0\rangle_{\mathrm{L}}$ and $|1\rangle_{\mathrm{L}}$ as [80]

$$|0\rangle_{\mathrm{L}} = \frac{1}{\sqrt{2}}(|0\rangle + |4\rangle), \quad |1\rangle_{\mathrm{L}} = |2\rangle \ , \tag{1.15}$$

which is a particularly interesting encoding, since in case the photon number drops, the parity of the state changes and thus the logical qubit is protected against such types of quantum errors.

[2] We review some of the criteria in chapter 4.

[3] In this thesis we are only considering digital quantum computers, although many analog strategies have also been considered.

[4] A further discussion on the currently available realizations, although interesting, and their properties goes well beyond the aims of this section, we refer the reader to [74].

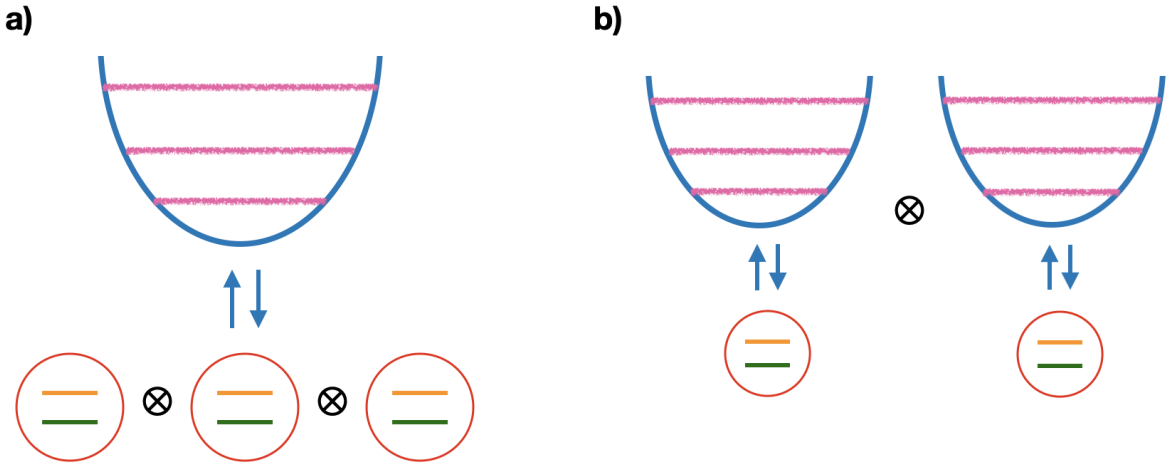

Figure 1.2: Here the band represents the different electromagnetic modes of the cavity (which are analogous to the energy modes of a harmonic oscillator) while the two level system denotes the atom (transmon) coupled to the cavity. In **a**) one couples many atoms together, each being a two level system working effectively as a quantum bit. In this case, the cavity allows to implement different quantum gate operations. In the opposite case, **b**), the cavity modes store the digital information, while the two-level system allows one to perform operations on them.

In the next chapters of this thesis, we will use quantum computing as a tool to explore high energy QFT/QCD physics. As such, we keep the discussion on the details related to QC up to the level necessary for the applications considered. As a consequence, some QC aspects, such as the physical realization of qubits or the detailed implementation of common quantum algorithms, are not further discussed.

In chapter 4 we give a more detailed review of the quantum circuit model, typically used to represent the implementation of quantum algorithms. In addition, we provide a brief introduction to the quantum simulation algorithm. The results from that chapter are then used in QCD/QFT applications in chapters 5 and 6.

1.3 Objectives and Methodology

To finalize this introductory section, and to comply with the new regulations for doctoral studies of the University of Santiago de Compostela, we include here as two separate sections the global objectives of this thesis and the summary of the methodologies employed, that have been already mentioned above and that will be fully developed in the corresponding chapters.

1.3.1 Objectives

The objective of this thesis are the following:

1. **Formal aspects of the Improved Opacity Expansion**: We extend the Improved Opacity Expansion framework beyond the first non-trivial order to explore its properties in the asymptotic regions and thus ensure that this framework has a solid formal basis;

2. **Efficient quantum simulation of QFTs**: We set the goal to introduce a new approach to simulate ϕ^4 scalar QFT in a quantum computer, essential for future studies of more complex QFTs as QCD;

3. **First principle formulation of parton evolution in a QCD background in a quantum computer**: We aim at providing the key ingredients for describing the evolution of jets in a medium. Our focus will be single parton evolution, neglecting particle branching.

1.3.2 Methodology

The topics explored in this thesis cover two different subfields of physics: one is concerned with QCD and, in general, QFT; the other is related to quantum digital computation and its applications. As such, we borrow different analytical tools and techniques from both these areas in order to reach the goals set in the previous section. In more detail, the methods used can be divided as:

1. **Perturbative QCD and other aspects of QFT**: The first part of this thesis requires the usage of perturbative QCD techniques. In addition, formal aspects related to path integral representations are used.

2. **Digital quantum computation elements**: In a second part, we make use of elements of digital quantum computing.

The first method is used to study the first objective in this thesis. The second and third objectives require the usage of QFT and quantum computing methods.

2

Hard parton propagation in a QCD medium

Based on the discussion in chapter 1, we now proceed to study the propagation of a high energy parton in the presence of an underlying strong classical gluon field. The goal of this chapter is to introduce the results that form the basis for the work shown in chapters 3 and 6. Since all the information in this chapter is part of the common knowledge of the jet quenching community, we will try to put more focus on the underlying physics, rather than provide extremely rigorous and longer derivations of the results, which can be easily found in the literature (see [81–83] for some recent reviews).

In what follows, we assume that the medium is weakly-coupled, consisting of a collection of static scattering centers. This assumption is necessary to ensure that perturbative techniques are applicable. In addition, since we are not interested in exploring different spacetime profiles for the medium, we take it to be a homogeneous and static slab (plasma brick model).

For energetic jets/probes, the relevant mechanism for transporting energy from the large energy scale corresponding to the initial parton energy $p^+ \gg |\boldsymbol{p}|$ down to the medium temperature scale $|\boldsymbol{p}| \gg T \gtrsim \Lambda_{\rm QCD}$ is medium induced radiation [81, 84–88]. This is in contrast with the low energy regime, where collisional energy loss [49, 89] dominates. Although, several formalisms exist to describe how the probe propagates in the medium (mainly differing on details such as the exact treatment of the medium; see [90] for a detailed comparison between models) in this thesis we focus on the approaches by Baier, Dokshitzer, Mueller, Peigné, Schiff – Zakharov [91–98], with the respective phenomenological implementation by Armesto, Salgado, Wiedemann [99,100], BDMPS-Z/ASW, and

the one by Gyulassy, Levai, Vitev – Wiedemann [101,102] (GLV/W). With respect to the GLV/W approach, W provided an all order result in the number of scatterings, which in the limit of soft momentum exchanges reduces to the BDMPS-Z/ASW result, once resummed. Thus, one can recover the GLV/W result using the BDMPS-Z/ASW formalism. As such, we devote this section to introduce the BDMPS-Z/ASW formalism (more inline with more modern treatments; see for example [103–106]) and latter discuss which physical regions are better captured by the different approaches.

In particular, we will first consider eikonal parton propagation in the medium, which allows to define the first object we wish to study further below: the single particle momentum broadening distribution. We then introduce next-to-eikonal corrections to the phases, allowing the probe to do a random walk in transverse space and study how branching takes place in-medium. All these results are summarized in a set of *effective* in-medium jet quenching Feynman rules. We conclude the chapter by reviewing the typical solutions for the medium induced energy gluon spectrum.

Some results introduced in this chapter, related to the in-medium scattering potential models, overlap with [2, 6].

2.1 Eikonal propagation

As a first step, we consider the simplest case of an energetic quark[1], originated from a hard (in-medium) scattering process, which then propagates inside a medium of length L before entering the vacuum. As mentioned previously in chapter 1, we assume that hard and soft processes can be factorized, and thus we will ignore the details of the initial state hard matrix element.

We want to construct the effective in-medium (massless) quark propagator in the eikonal limit, i.e. ignoring power corrections $O(\boldsymbol{p}^2/p^+)$. In this limit, it turns out to be simple to compute the in-medium propagator, taking into account multiple soft gluon exchanges between probe and medium. The resummed S matrix taking into account all possible n gluon exchanges is given by

$$S = \sum_{n=0}^{\infty} S_n \,, \tag{2.1}$$

where S_n is the S matrix for n scatterings in the medium, with $n = 0$ the vacuum solution. The diagrams contributing for $n = 1, 2$ and generic n are given in Fig. 2.1.

The first non-trivial contribution comes at $n = 1$, where the hard probe scatters once in the field, leading to a single field insertion $\sim A_\mu(x) \cdot t$. S_1 can be written using the standard Feynman rules for QCD [23, 24, 38] (see Fig. 2.1)

$$S_1 = \int_x \mathrm{e}^{iq\cdot x} A_\mu(x) \cdot t\, \bar{u}(p_f)(ig\gamma^\mu)u(p_f - q) \,, \tag{2.2}$$

[1]The case for a gluon is analogous, and can be obtained from the quark result by adjusting the color factors.

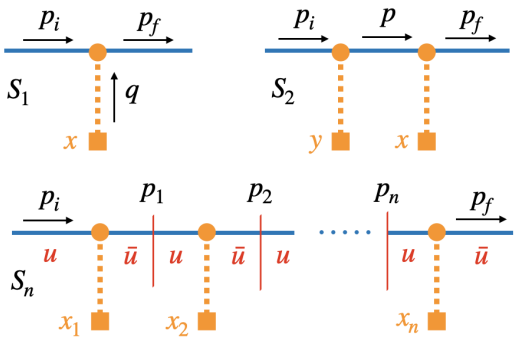

Figure 2.1: Diagrammatic representation of the contributions to S_1 (top left), S_2 (top right) and S_n (bottom). For the generic case, we have highlighted the decomposition used in Eq. (2.13) to simplify the Dirac algebra. Blue lines (color online) denote the hard parton vacuum propagator with the respective momentum given above and the yellow vertical lines denote the field insertion at position x_i.

where $\int_x = \int d^4x$, $q = p_f - p_i$ is the momentum transfer with the medium and we contracted the color indices. In the eikonal limit, the large component of the quark momentum is $p_f^+ \gg |\boldsymbol{p}_f|$ (see appendix 2.A),

$$p_f^\mu = (p_f^+, \boldsymbol{p}_f, p_f^-) \approx \left(p_f^+, \boldsymbol{p}_f, \frac{\boldsymbol{p}_f^2}{2p_f^+} \right) . \tag{2.3}$$

Thus, in this highly-boosted regime, the propagation of this almost on-shell quark occurs over the future pointing light-cone, along the + direction. As a consequence, the quark is only sensitive to physics occurring locally at $x^- = 0$. Thus, we can simplify the spacetime dependence of the background field to $A^\mu(x^+, \boldsymbol{x}, x^-) \approx A^\mu(x^+, \boldsymbol{x}, 0) \equiv A^\mu(x^+, \boldsymbol{x})$. Also, in this boosted regime and recalling that we always consider the light-cone gauge $A^+ = 0$, the framework to describe the parton evolution is the same as the one used in saturation physics [38,107,108], and thus all the ensuing results can be seen as a particular application of Light Cone Perturbation Theory (LCPT) [109, 110]. The advantage of working on the light-front will become evident in the following sections.

With these approximations, the physics in x^- becomes frozen and the corresponding integral can be easily performed. Furthermore, at high energies the Dirac structure of the above amplitude simplifies considerably. This can be seen directly from the LCPT Dirac matrix elements [38, 110] or by using Gordon's identity [23, 24]

$$\bar{u}(q)\gamma^\mu u(p) = \bar{u}(q) \left\{ \frac{(q+p)^\mu}{2m} - \frac{1}{2}[\gamma^\mu, \gamma^\nu] \frac{(q-p)_\nu}{2m} \right\} u(p) \,, \tag{2.4}$$

and recalling that $\bar{u}^\sigma(p)\bar{u}^\lambda(p) = 2m\,\delta^{\sigma\lambda}$ and using $u(p_f - q) \approx u(p_f)$. We then obtain

$$\frac{1}{2} \sum_{\lambda\sigma} \bar{u}^\lambda(p_f)(ig\gamma^\mu)u^\sigma(p_f - q) \approx 2igp_f^\mu \,, \tag{2.5}$$

where we averaged over the initial spin and summed over final state spin. Finally, only the A^- component of the field survives, since the transverse component couples to the small components of p. We then obtain

$$S_1 = 2p_f^+(2\pi)\delta(p_f^+ - p_i^+)\int_{\boldsymbol{x}} \mathrm{e}^{-i(\boldsymbol{p}_f-\boldsymbol{p}_i)\cdot\boldsymbol{x}}\int_{x^+} igA^-(x^+,\boldsymbol{x})\cdot t\,, \tag{2.6}$$

where light-one energy is explicitly conserved. The scattering matrix S_2 can be computed similarly and reads (see Fig. 2.1)

$$S_2 = \int_{x,y,p} \mathrm{e}^{ix\cdot(p_f-p)}\mathrm{e}^{iy\cdot(p-p_i)}(ig)^2 A_\mu(x)\cdot t A_\nu(y)\cdot t\,\bar{u}(p_f)\gamma^\mu\frac{i\not{p}}{p^2+i\varepsilon}\gamma^\nu u(p_i)\,, \tag{2.7}$$

where p is an internal momentum. The Dirac structure can be easily simplified in the eikonal limit

$$\frac{1}{2}\sum_{\lambda,\sigma}\bar{u}^\lambda(p)\gamma^\mu\not{p}\gamma^\nu u^\sigma(p) = p^\nu\bar{u}^\lambda(p)\gamma^\mu u^\lambda(p) = (2p^\mu)(2p^\nu)\,. \tag{2.8}$$

where in the intermediate step we used the commutation relation of the gamma matrices and then used the massless Dirac equation $\not{p}u(p)=0$. In addition, the x^- and y^- integrals are also easy to perform and lead to the conservation of the $+$ component of momentum. We can thus write

$$S_2 = (2p_f^+)^2(ig)^2\int_{\vec{x},\vec{y},p} A^-(x)\cdot tA^-(y)\cdot t\,\frac{i}{p^2+i\varepsilon}\mathrm{e}^{-i\vec{p}\cdot(\vec{x}-\vec{y})}\mathrm{e}^{i\vec{x}\cdot\vec{p}_f}\mathrm{e}^{-i\vec{y}\cdot\vec{p}_i}\,, \tag{2.9}$$

where we have not explicitly written the delta functions $(2\pi)^2\delta(p_f^+-p^+)\delta(p^+-p_i^+)$ imposing conservation of the $+$ component of the momentum and in the phases we used $\vec{p}\cdot\vec{x} = p^-x^+ - \boldsymbol{p}\cdot\boldsymbol{x}$ and $\vec{x}=(x^+,\boldsymbol{x})$ (see appendix 2.A). The only non-trivial integration is over p^-, for which we get

$$\int\frac{dp^-}{2\pi}\frac{\mathrm{e}^{-ip^-(x^+-y^+)}}{2p^+}\frac{1}{p^- - \frac{\boldsymbol{p}^2}{2p^+}+i\varepsilon'} = \frac{-i}{2p^+}\mathrm{e}^{-i\frac{\boldsymbol{p}^2}{2p^+}(x^+-y^+)}\theta(x^+-y^+) \approx \frac{-i}{2p^+}\theta(x^+-y^+)\,, \tag{2.10}$$

where we used Cauchy's theorem, closing the path on the lower half plane (and included the -1 due to the path index) and in the last line we have used the eikonal approximation to neglect the exponential factor. It is easy to observe that the remaining $\boldsymbol{p}$ integral gives a delta function $(2\pi)^2\delta^{(2)}(\boldsymbol{x}-\boldsymbol{y})$ while the p^+ integration removes one of the energy delta functions (that are not written explicitly above) to yield an overall conservation factor $(2\pi)\delta(p_f^+-p_i^+)$. We thus obtain

$$\begin{aligned} S_2 &= 2p_f^+(2\pi)\delta(p_f^+-p_i^+)(ig)^2\int_{\boldsymbol{x}}\mathrm{e}^{-i(\boldsymbol{p}_f-\boldsymbol{p}_i)\cdot\boldsymbol{x}}\int_{x^+,y^+}\theta(x^+-y^+)A^-(x^+,\boldsymbol{x})\cdot tA^-(y^+,\boldsymbol{x})\cdot t \\ &= 2p_f^+(2\pi)\delta(p_f^+-p_i^+)\int_{\boldsymbol{x}}\mathrm{e}^{-i(\boldsymbol{p}_f-\boldsymbol{p}_i)\cdot\boldsymbol{x}}\frac{1}{2!}\mathcal{P}\left[\int_{x^+} ig\,A^-(x^+,\boldsymbol{x})\cdot t\right]^2\,, \end{aligned} \tag{2.11}$$

where we again neglect any energy suppressed contributions to the phases and in the last step introduced the path ordering operator $\mathcal{P}$ using the identity

$$\int_{x_1^+,x_2^+,\cdots x_n^+} \theta(x_n^+ - x_{n-1}^+)\theta(x_{n-1}^+ - x_{n-2}^+)\cdots\theta(x_2^+ - x_1^+) = \frac{1}{n!}\mathcal{P}\left(\int_{x^+}\right)^n . \tag{2.12}$$

The remaining step is to show that given S_n then one can obtain S_{n+1} iteratively. Clearly the only complicated step is to deal with the more evolved Dirac algebra, but this also turns out to be simple. We first recall that in the massless limit one has $\not{p} = \sum_\lambda u^\lambda(p)\bar{u}^\lambda(p)$, thus in general case with n insertions (and also true for $n = 2$ situation above) one would have (see Fig. 2.1)

$$\begin{aligned}
&\frac{1}{2}\sum_{\lambda,\sigma}\bar{u}^\lambda(p)\gamma^\mu\not{p}\gamma^\nu\not{p}\gamma^\alpha\cdots u^\sigma(p)\\
=&\frac{1}{2}\sum_{\lambda,\sigma}\sum_{\langle s\rangle}\bar{u}^\lambda(p)\gamma^\mu u^{s_1}(p)\bar{u}^{s_1}(p)\gamma^\nu u^{s_2}(p)\bar{u}^{s_2}(p)\gamma^\alpha\cdots u^\sigma(p)\\
=&(2p^+)^n ,
\end{aligned} \tag{2.13}$$

where $\langle s\rangle$ denotes the sum over all spinor indices pairs and in the last step we have applied the Gordon identity multiple times and anticipated that only the + component survives. More rigorously, each momentum should have a different label, but at leading order it can be dropped. The integrations over the internal momenta follow as before and at the end one can always write S_n as

$$S_n = 2p_f^+(2\pi)\delta(p_f^+ - p_i^+)\int_{\boldsymbol{x}} \mathrm{e}^{-i(\boldsymbol{p}_f-\boldsymbol{p}_i)\cdot\boldsymbol{x}}\frac{1}{n!}\mathcal{P}\left[\int_{x^+} ig\,A^-(x^+,\boldsymbol{x})\cdot t\right]^n , \tag{2.14}$$

so that the full S matrix reads

$$\begin{aligned}
S &= 2p_f^+(2\pi)\delta(p_f^+ - p_i^+)\int_{\boldsymbol{x}} \mathrm{e}^{-i(\boldsymbol{p}_f-\boldsymbol{p}_i)\cdot\boldsymbol{x}}\,\mathcal{P}\exp\left[\int_0^L dx^+\, ig\,A^-(x^+,\boldsymbol{x})\cdot t\right]\\
&\equiv 2p_f^+(2\pi)\delta(p_f^+ - p_i^+)\int_{\boldsymbol{x}} \mathrm{e}^{-i(\boldsymbol{p}_f-\boldsymbol{p}_i)\cdot\boldsymbol{x}}\,\mathcal{W}(L,\boldsymbol{x}) .
\end{aligned} \tag{2.15}$$

where in the last line we introduced the Wilson line, in the fundamental representation, along the + direction and at $\boldsymbol{x}$ in the transverse plane. It resums the multiple t-channel gluon exchanges between the medium and the hard parton and we assumed that propagation started at a time $x^+ = 0$ and ended at $x^+ = L$. Thus, we learn that, up to factors, the S matrix is the Fourier transform of the Wilson line.

The above formula deserves some comments.

1. The overall $2p^+$ factor in Eq. (2.15) implies that the in-medium effective rules must include a $1/(2p^+)$ pre-factor.

2. The multiple p^- integrations generate phases $\sim \boldsymbol{p}_i^2/(2p^+)(x_{i+1}^+ - x_i)$ we neglected due to the apparent power suppression in energy. Nonetheless, the remaining integrations in the transverse and longitudinal momenta are not kinematically restricted, and thus the phase could become important. This would (parametrically) be relevant once

$$\frac{\boldsymbol{p}_i^2}{2p^+} L \sim 1\,, \tag{2.16}$$

where we used that $x_{i+1}^+ - x_i^+ \sim L$. Thus as long as $\frac{\boldsymbol{p}^2}{2p^+} L \ll 1$, with $\boldsymbol{p}$ here some typical transverse scale, the phases can be neglected. The factor[2] $t_f^{-1} \equiv \frac{\boldsymbol{p}^2}{2p^+}$, when associated to a particle being radiated with transverse momentum $\boldsymbol{p}$ and energy p^+, is the typical quantum formation time for the particle to be resolved [111] (put on-shell). This leads one to conclude that the eikonal approximation is insufficient to study medium-induced radiation, since it always requires that $t_f \gg L$, i.e. the gluon is never resolved in the times scales it takes to traverse the medium. This is not the most relevant region for jet quenching phenomenology, and thus one needs to consider next-to-eikonal corrections to the in-medium propagator in order to capture the scenario where the gluon is resolved by the medium. This is done in section 2.4.

2.2 Medium averages

When computing any observable, in the eikonal limit, one needs to deal with the combination of several Wilson lines. On top of that, in the previous section all the calculations were done for a fixed configuration of the background field. Thus, to extract meaningful cross-sections, one needs to perform an average over all possible field configurations, the so called *medium average*, for the relevant combination of $\mathcal{W}$ operators.

It is common to find the averaging procedure done in two different ways. The first, which is extensively used for example in the GLV/W approach (see also [112]), is to write the field A^μ as a Fourier superposition of the individual fields generated by the several scattering centers in the medium, i.e. $A^\mu(p) = \sum_i \mathrm{e}^{ipx_i} a_i^\mu(p)$. The form of a_i^μ can be calculated for a given model for the in-medium interaction cross-section [38, 101, 113]. Then, in the limit of a large number of uncorrelated centers, the summation can be replaced by a spatial integral that results in an average over all positions.

Another approach, which leads to the same end results, is to consider that the background field A^μ is generated by a classical ensemble of color charges ρ[3]. In the highly

[2] A simple way to see this is to realize that if a particle propagates for a time t then (classically) it would be seen at a transverse position $\boldsymbol{x} \sim \theta t$, with θ its emission angle. To linear order $\boldsymbol{x} \sim t\theta \sim t\boldsymbol{k}/k^+$. Using the Heisenberg uncertainty principle $\boldsymbol{k} \cdot \boldsymbol{x} \sim 1$, one obtains $t \sim k^+/\boldsymbol{k}^2$. See also the discussion related to the Ioffe time in chapter 1.

[3] The fact that the field is classical is justified by the small value of the coupling and in accordance with the previous chapter.

boosted frame considered, and in the light-cone gauge, the color current must take the form [38, 114]

$$\mathcal{J}^{\mu a} = \delta^{\mu -} \rho^a(x^+, \boldsymbol{x}) \,, \tag{2.17}$$

along the $-$ light-cone direction. Indeed, in the $A^+ = 0$ gauge (similar arguments also follow in the Lorentz gauge [38,115]), one can obtain this result directly from the covariant conservation of the color current

$$D_\mu \mathcal{J}^\mu \equiv \partial_\mu \mathcal{J}^\mu - ig[A_\mu, \mathcal{J}^\mu] = \partial^+ \mathcal{J}^- = \frac{\partial}{\partial x^-} \mathcal{J}^- = 0 \,, \tag{2.18}$$

and the (pure gauge) transverse field component can be taken to be zero [81, 108, 116]. Eq. (2.18) ensures that the current is well localized in around $x^- = 0$. Physically, this means that color charges do not rescatter on the field they self generate, leading to a clear separation between the degrees of freedom associated with the color current and the ones associated with the gauge field. In this sub-gauge choice, the Yang-Mills equations simplify considerably and lead to a Poisson law for the gauge field [107, 108]

$$\partial^2_{\boldsymbol{x}} A^{-a}(x^+, \boldsymbol{x}) = -g\rho^a(x^+, \boldsymbol{x}) \,, \tag{2.19}$$

which is easily solved to give

$$A^{-a}(x^+, \boldsymbol{x}) = g \int_{\boldsymbol{y}} \int_{\boldsymbol{k}} \frac{\mathrm{e}^{i\boldsymbol{k}\cdot(\boldsymbol{x}-\boldsymbol{y})}}{\boldsymbol{k}^2} \rho^a(x^+, \boldsymbol{y}) = g \int_{\boldsymbol{k}} \frac{\mathrm{e}^{i\boldsymbol{k}\cdot\boldsymbol{x}}}{\boldsymbol{k}^2} \rho^a(x^+, \boldsymbol{k}) \,. \tag{2.20}$$

In the Mclerran-Venugopalan (MV) model [117–119], one further treats the classical color charges stochastically, assuming that they obey a Gaussian distribution, as a consequence of the central limit theorem and recognizing that in a dense system the field is generated due to the incoherent combination of a large number of uncorrelated sources. This is of course a very simple picture, but it satisfies the constraints that the overall color charge should be zero and describes an isotropic medium. This can be easily verified by extracting the field auto-correlators, which can be done using standard methods [120].

A simple outline of the calculation goes as follows. The probability to generate the field configurations ρ (we will drop spacetime indices in most of what follows to simplify notation) is given in the Gaussian *ansatz* by

$$\mathrm{Prob}[\rho] \propto \exp\left[-\int_{\boldsymbol{x}} \int_{x^+} \frac{\rho \cdot \rho}{2n(x^+)} \right] \,, \tag{2.21}$$

where $n\, dx^+ \sim g^2$ is the density of color charges in the transverse plane in an infinitesimal longitudinal slice of time and the factor 2 is chosen to have the usual normalization. The overall normalization is fixed by requiring that $\int D\rho \mathrm{Prob}[\rho] = 1$. We can thus define the generating function $Z[J]$

$$Z[J] = \int D\rho \mathrm{Prob}[\rho] \exp\left(\int_{\vec{x}} J \cdot \rho \right) \,, \tag{2.22}$$

where as usual taking the n^{th} functional derivative with respect to J at $J=0$ gives

$$\left.\frac{\delta^n Z[J]}{(\delta J)^n}\right|_{J=0} = \int D\rho \text{Prob}[\rho]\rho^n \equiv \langle \rho^{a_1}(x_1^+, \boldsymbol{x}_1)\rho^{a_2}(x_2^+, \boldsymbol{x}_2)\cdots\rho^{a_n}(x_n^+, \boldsymbol{x}_n)\rangle\,, \tag{2.23}$$

where the spacetime and color indices were only made explicit in the last term. Since the integrations are Gaussian, Eq. (2.22) is easily simplified

$$Z[J] = \int D\rho \exp\left(-\int_{\boldsymbol{x},x^+}\frac{1}{2n}\left[\rho\cdot\rho - 2nJ\cdot\rho\right]\right) = \exp\left(\int_{\boldsymbol{x},x^+}\frac{n}{2}J\cdot J\right)\,, \tag{2.24}$$

thus we learn by taking the first derivative that

$$\langle \rho^{a_1}(x_1^+, \boldsymbol{x}_1)\rangle = n(x_1^+)JZ[J]_{J=0} = 0\,, \tag{2.25}$$

which physically corresponds to the statement that the net color charge is zero. The two-point correlator gives

$$\langle \rho^{a_1}(x_1^+, \boldsymbol{x}_1)\rho^{a_2}(x_2^+, \boldsymbol{x}_2)\rangle = n(x_1^+)\delta^{a_1,a_2}\delta(x_1^+ - x_2^+)\delta(\boldsymbol{x}_1 - \boldsymbol{x}_2)\,, \tag{2.26}$$

where we already removed all terms proportional to J. As mentioned above, this is the mathematical equivalent of stating that correlations between charges are local in color and spacetime, with an isotropic profile in the transverse plane.

It is easy to realize that higher order odd correlators always vanish, while even correlators only have a single non-vanishing component which can be written as the sum over all permutations of two-point correlators. In the literature devoted to the study of stochastic systems [120] this prescription for the correlators is typically referred to as *white noise*. In addition, one can show that strategy followed in, for example, the GLV/W approach recovers Eqs. (2.25) and (2.26) [121, 122].

Combining Eqs. (2.20) and (2.26), one obtains

$$\langle A^{-a_1}(x_1^+, \boldsymbol{x}_1)A^{-a_2}(x_2^+, \boldsymbol{x}_2)\rangle = g^2 n(x_1^+)\delta^{a_1,a_2}\delta(x_1^+ - x_2^+)\gamma(\boldsymbol{x}_1 - \boldsymbol{x}_2)\,, \tag{2.27}$$

where

$$\gamma(\boldsymbol{x}) = \int_{\boldsymbol{q}}\frac{\mathrm{e}^{-i\boldsymbol{q}\cdot\boldsymbol{x}}}{\boldsymbol{q}^4}\,, \tag{2.28}$$

which is just the Fourier transform of the Coulomb potential. In the presence of a background however, this potential is naturally regulated in the infrared by the medium Debye mass m_D, such that the integration in $\boldsymbol{q}$ is bounded from below by this scale. The way γ is regulated is model dependent and typically done using some phenomenological model[4]. For the independent scattering picture we developed in the previous section to be valid one must require that the free mean path of the parton inside the medium, λ, satisfies

[4]The regulator could already have been introduced in Eq. (2.19) by adding a mass term. As we will argue, the exact way the regularization of γ is done is not important at leading order in $\boldsymbol{x}$.

$L \geq \lambda \gg 1/m_D$, otherwise one can not ignore the color correlations between different scattering centers, where the above arguments are no longer valid.

Using Eq. (2.27), one can easily extract the many point correlator of Wilson lines, which appear when computing observables. Due to linearity, the Gaussian form still holds for higher order correlators of $\mathcal{W}$ and it is sufficient to work up to quadratic order in the fields. We thus find for the two-point function

$$\begin{aligned}
&\frac{\mathrm{Tr}\langle \mathcal{W}^\dagger(\boldsymbol{y})\mathcal{W}(\boldsymbol{x})\rangle}{N_c} = \mathcal{P}\Big\langle 1 - \frac{g^2}{2}\int_{x^+,y^+} \mathrm{Tr}A(x^+,\boldsymbol{y})\cdot tA(y^+,\boldsymbol{y})\cdot t \\
&-\frac{g^2}{2}\int_{x^+,y^+} \mathrm{Tr}A(x^+,\boldsymbol{x})\cdot tA(y^+,\boldsymbol{x})\cdot t + g^2\int_{x^+,y^+} A(y^+,\boldsymbol{y})\cdot tA(x^+,\boldsymbol{x})\cdot t\Big\rangle \frac{1}{N_c} + O(\langle A^4\rangle) \\
&= \mathcal{P}\left(1 + g^4 C_F \int_{x^+} n(x^+)(\gamma(\boldsymbol{y}-\boldsymbol{x}) - \gamma(\boldsymbol{0}))\right) \\
&= \exp\left(-g^4 C_F \int_{x^+} n(x^+)\int_{\boldsymbol{q}} \frac{1-\mathrm{e}^{-i\boldsymbol{q}\cdot(\boldsymbol{y}-\boldsymbol{x})}}{\boldsymbol{q}^4}\right),
\end{aligned} \tag{2.29}$$

where we used $C_F = \frac{1}{N_c}\mathrm{Tr}(t^a t^a) = \frac{4}{3}$ and in the last step we re-exponentiated the linearized solution, which is valid due to the iterative structure of the Wilson line shown in the previous section and the Gaussian approximation. In practice, and as mentioned above, the Coulomb singularity gets regularized by providing some model for the local interactions. One usually introduces the so called *dipole cross-section* σ [85, 105]

$$\frac{\mathrm{Tr}\langle \mathcal{W}(\boldsymbol{y})^\dagger \mathcal{W}(\boldsymbol{x})\rangle}{N_c} = \exp\left(-C_F \int_{x^+} \sigma(\boldsymbol{y}-\boldsymbol{x}, x^+)\right), \tag{2.30}$$

where

$$\sigma(\boldsymbol{x}, x^+) = g^4 n(x^+)\int_{\boldsymbol{q}} \left(1-\mathrm{e}^{-i\boldsymbol{q}\cdot\boldsymbol{x}}\right)\bar{\gamma}(\boldsymbol{q}), \tag{2.31}$$

where $\bar{\gamma}$ is a regularized form for γ. It is constrained to reproduce the ultraviolet Coulomb behavior.

The dipole cross-section, already entails both virtual and real contributions; the first correspond to the factor 1 in Eq. (2.29), which are unable to resolve the dipole transverse dimensions, while the real terms depend on the dipole size $|\boldsymbol{y}-\boldsymbol{x}|$. The advantage of this treatment of real and virtual contributions in the same footing should be contrasted with the treatment for example followed in [101, 123], which requires the explicit calculation and resummation of both virtual and real terms.

2.3 Momentum broadening

The results from the previous two sections are enough to study the leading order (α_s^0) medium effect: *momentum broadening*. From a theoretical point of view, this effect can

be studied at the level of the single particle broadening distribution $\mathcal{P}(\boldsymbol{k}, L)$

$$\mathcal{P}(\boldsymbol{k}, L) = \int_{\boldsymbol{x}} \mathrm{e}^{-i\boldsymbol{k}\cdot\boldsymbol{x}} \exp\left(-C_R \int_0^L dx^+ \, \sigma(\boldsymbol{x}, x^+)\right) , \tag{2.32}$$

which is easily related to the the relevant partonic cross-section [85]. Although not being a physical observable, the broadening probability is a key theoretical piece to describe full in-medium jet evolution in phenomenological Monte-Carlo models [51,52] and can be also found in saturation physics models [124].

Here we assumed that the parton is in a color representation R. The $\mathcal{P}(\boldsymbol{k}, L)$ distribution gives the probability for the parton to acquire a transverse momentum $\boldsymbol{k}$ due to the propagation in the medium for a time L and it is normalized to unity since $\sigma(\boldsymbol{0}) = 0$. A more physical understanding of the broadening distribution can be gained by considering the related kinetic form. This is easily obtained by taking the derivative of Eq. (2.32) with respect to L

$$\frac{\partial}{\partial L}\mathcal{P}(\boldsymbol{k}, L) = C_R \int_{\boldsymbol{q}} \Gamma(\boldsymbol{q}, L) \left[\mathcal{P}(\boldsymbol{k}-\boldsymbol{q}, L) - \mathcal{P}(\boldsymbol{k}, L)\right] , \tag{2.33}$$

where $\Gamma(\boldsymbol{q}, x^+) = g^4 n(x^+)\gamma(\boldsymbol{q})$ is the (model dependent) scattering kernel. This kinetic equation is open to a simple physical interpretation. The probability to observe a particle in the momentum mode $\boldsymbol{k}$, due to a small time evolution, is equal to the probability of starting with a particle with momentum $\boldsymbol{k}-\boldsymbol{q}$ that acquires momentum $\boldsymbol{q}$ due to the interaction with the medium. Since the process must be conservative, i.e. the probability of finding the particle $\int_{\boldsymbol{k}} \mathcal{P}(\boldsymbol{k}, L)$ must be conserved, one also needs to take into account the states which start with $\boldsymbol{k}$ and diffusive to some other momentum mode.

To go further, one needs to know the form of the in-medium scattering cross-section, encapsulated by Γ. In jet quenching phenomenology, usually two models for the medium are considered. In terms of Γ these are given as follows:

1. **Hard Thermal Loop (HTL) model** [125]: When the background is modeled as a thermally equilibrated QCD plasma, then one can use HTL theory to compute the interaction rate Γ. It reads

$$\Gamma^{\mathrm{HTL}}(\boldsymbol{q}) = \frac{g^2 m_D^2 T}{\boldsymbol{q}^2\,(\boldsymbol{q}^2 + m_D^2)} , \tag{2.34}$$

   where $m_D^2(T) = (1 + \frac{n_\mathrm{f}}{6}) g^2 T^2$ is the Debye mass of the medium and here we give the leading order dependence on the medium temperature T and number of active light flavors n_f.

2. **Gyulassy-Wang (GW) model** [113]: Another model, based on perturbative QCD, assumes that the medium is formed by an ensemble of static centers with an Yukawa potential. At leading order, the scattering potential reads

$$\Gamma^{\mathrm{GW}}(\boldsymbol{q}) = \frac{g^4 n}{(\boldsymbol{q}^2 + \mu^2)^2} , \tag{2.35}$$

where now the infrared regulator is $\mu \equiv \mu^{\rm GW}$, which is the Yukawa screening mass. This form for Γ is a direct consequence of the fact that the t-channel gluons exchanged between the medium and the parton have a large transverse component, thus when squaring the amplitude one obtains the squared gluon propagator.

Both these models agree in the ultraviolet (UV), behaving as $1/\boldsymbol{q}^4$. However in the infrared (IR) the GW model predicts a constant value for the scattering rate (since the probe is not able to resolve scales smaller than $1/\mu$) while the HTL model predicts that $\Gamma \sim \boldsymbol{q}^{-2}$. Below we will show nonetheless that one can create a map between all possible physical models and an universal Γ, with deviations only becoming important when the dipole size becomes large than $1/\mu$.

In this thesis we will always consider the so called plasma brick model, which assumes that the medium is a static and homogeneous slab of size L, with all its evolution frozen. This means that $n(x^+) = n\Theta(L - x^+)$ and the time integrations become trivial. In this simple case the broadening distribution is given by

$$\mathcal{P}(\boldsymbol{k}, L) = \int_{\boldsymbol{k}} \mathrm{e}^{-i\boldsymbol{x}\cdot\boldsymbol{k}} \mathrm{e}^{-v(\boldsymbol{x})L} \equiv \int_{\boldsymbol{k}} \mathrm{e}^{-i\boldsymbol{x}\cdot\boldsymbol{k}} S(\boldsymbol{x}, L)\,, \tag{2.36}$$

where we refer to $v(\boldsymbol{x}) = C_R\sigma(\boldsymbol{x})$ as the (scattering) potential

$$v(\boldsymbol{x}) = C_R \int_{\boldsymbol{q}} \left(1 - \mathrm{e}^{-i\boldsymbol{q}\cdot\boldsymbol{x}}\right) \Gamma(\boldsymbol{q})\,, \tag{2.37}$$

where the time dependence is implicit. Assuming the GW model, it reads

$$v^{\rm GW}(\boldsymbol{x}) = \frac{\hat{q}_0}{\mu^2} \left(1 - \mu|\boldsymbol{x}| K_1(\mu|\boldsymbol{x}|)\right)\,, \tag{2.38}$$

where we introduced the *bare* jet quenching parameter $\hat{q}_0$, which is given by

$$\hat{q}_0 = 4\pi\alpha_s^2 C_R n\,. \tag{2.39}$$

For the HTL model the calculation is slightly more evolved but still possible. One obtains

$$v^{\rm HTL}(\boldsymbol{x}) = \frac{2\hat{q}_0}{m_D^2} \left(K_0(m_D|\boldsymbol{x}|) + \log\left(\frac{m_D|\boldsymbol{x}|}{2}\right) + \gamma_E \right)\,, \tag{2.40}$$

where in this case we define the jet quenching parameter as

$$\hat{q}_0 = \alpha_s C_R m_D^2 T\,. \tag{2.41}$$

The details on the derivation of these formulas can be found in [2, 6] and are replicated in appendix 3.A. In the above formulas K_0 and K_1 are Bessel functions, $\gamma_E = 0.577(2)$ is the Euler-Mascheroni constant and T is the plasma temperature.

One subtle point is that the broadening probability is not well defined for these potentials. This is because at large values of the dipole size $\boldsymbol{x}$ (i.e. at small $\boldsymbol{k}$) the GW and HTL potentials do not grow sufficiently fast, such that $\exp(-v(\boldsymbol{x})L)$ is not integrable in the Fourier sense (see Fig. 2.2 right). In fact, they asymptotically saturate so that one gets an undesired delta function, related to a no-broadening contribution. Therefore, in these cases we update the definition of the broadening probability to be given by

$$\mathcal{P}(\boldsymbol{k},L)=\int_{\boldsymbol{x}}(S(\boldsymbol{x},L)-S(\infty,L))\mathrm{e}^{-i\boldsymbol{x}\cdot\boldsymbol{k}}\,, \tag{2.42}$$

where it is easy to see that the extra term removes the undesired singular contribution proportional to $\delta^{(2)}(\boldsymbol{k})$. The cost of using this definition is that the normalization has to be altered, as can be verified

$$\int_{\boldsymbol{k}}\mathcal{P}(\boldsymbol{k},L)=1-\exp(-v(\infty)L)\,. \tag{2.43}$$

This is just expressing the fact that the broadening probability only takes into account contributions where there is a modification of the particle's momentum. Nonetheless, for all practical purposes it turns out that this extra term has very little impact on any numerical results, since $v(\infty)L$ can be a reasonably large number.

Although the Fourier pair of the broadening distribution, $S(\boldsymbol{x},L)$, is known exactly in the two above models, the distribution itself does not admit a closed form expression. However, in many applications it is common to expand the potentials in powers of the dipole size $\mu^2\boldsymbol{x}^2$ ($m_D^2\boldsymbol{x}^2$); we shall refer to this as the *Twist* (T) expansion, with the first terms being the leading twist (LT) contribution and so on. This choice of nomenclature, inspired by [126], is used to distinguish this expansion, which beyond LT order generates non-universal and model dependent contributions, from the universal expansion scheme to be detailed in the next chapter.

Expanding Eqs. (2.38) and (2.40) to LT order we obtain

$$v^{\mathrm{GW}}(\boldsymbol{x})=\frac{\hat{q}_0}{4}\,\boldsymbol{x}^2\log\left(\frac{4\mathrm{e}^{1-2\gamma_E}}{\boldsymbol{x}^2\mu^2}\right)+O(\hat{q}_0\boldsymbol{x}^4\mu^2)\,, \tag{2.44}$$

and

$$v^{\mathrm{HTL}}(\boldsymbol{x})=\frac{\hat{q}_0}{4}\,\boldsymbol{x}^2\log\left(\frac{4\mathrm{e}^{2-2\gamma_E}}{\boldsymbol{x}^2m_D^2}\right)+O(\hat{q}_0\boldsymbol{x}^4m_D^2)\,. \tag{2.45}$$

We thus observe that at this leading logarithmic (LL)[5] order both potentials have the same functional form. In fact, it is easily realized that this must be the functional form of any physical potential, by noticing that for $|\boldsymbol{k}|\gg\mu$ one has

$$\int_{\boldsymbol{x}}e^{-i\boldsymbol{k}\cdot\boldsymbol{x}}\boldsymbol{x}^{2n}\log\left(\frac{1}{Q^2\boldsymbol{x}^2}\right)=i^{2n}4\pi\frac{(2n+1)!}{\boldsymbol{k}^{2n+2}}\,, \tag{2.46}$$

[5]We use the LT and LL notations interchangeably, referring to the expansion of the in-medium potentials to first order.

which for $n = 1$ implies that $\sim \boldsymbol{x}^2 \log(\boldsymbol{x}^2)$ is nothing but the Fourier pair of a microscopic Coulomb potential. Since all physical potentials must be of the Coulomb form in the UV, this implies that at LT (LL) accuracy one can construct an universal potential $v^{\rm LT}$, and a map between this potential and any model. The universal potential is defined as

$$v^{\rm LT}(\boldsymbol{x}) = \frac{\hat{q}_0}{4}\,\boldsymbol{x}^2 \log\left(\frac{1}{\boldsymbol{x}^2\mu_\star^2}\right) . \tag{2.47}$$

Here the infrared scale $\mu_\star$ should be seen as the *physical* screening mass of the system. The importance of having this prescription is that it allows for a systematic and well calibrated comparison between calculations employing different models for the non-perturbative part of the potential. In fact, if this is not done then there is no meaningful way of doing model comparisons, since there is *a priori* no good reason to take $\mu = m_D$, for example. In the literature (see for example [127]), this last prescription is indeed the typical procedure, i.e. to fix the mass regulators to be the same in all models and the comparison between models is done by just updating the functional form. As was noted in [127] (see also Fig. 2.2 left), even though the difference between the GW and HTL is small at the level of the potential v, it can become important at the observable level. This type of analysis is however not completely correct, since in fact the physics being described is not the same, and thus one should not expect to observe similar results at the observable level. Said in another way, the prescription $\mu = m_D$ does not lead to the same physical description.

Thus, to circumvent this issue, we propose a LT accuracy map between the mass regulator in each model and the universal scale $\mu_\star$. This is the statement that whatever the model one chooses, the physics being observed should be the same. Of course, one might find that to describe some medium the obtained mass is unphysical (too large or too small). This simply implies that the medium can not be reasonably described by that model. The map between the GW and HTL to the physical scale is given by

$$\mu_\star^2 = \begin{cases} \dfrac{\mu^2}{4}\,\mathrm{e}^{-1+2\gamma_E} & \text{for the GW model} \\ \dfrac{m_D^2}{4}\,\mathrm{e}^{-2+2\gamma_E} & \text{for the HTL model} \end{cases} , \tag{2.48}$$

where implicitly $m_D^2 = \mathrm{e}\mu^2$.

It is interesting to go to NLT accuracy and study how large these contributions can be. The NLT contribution to the GW and HTL models reads

$$v_{\rm NLT}^{\rm GW}(\boldsymbol{x}) = \frac{\hat{q}_0 \boldsymbol{x}^4 \mu^2}{64} \log\left(\frac{16 e^{5-4\gamma_E}}{\boldsymbol{x}^4\mu^4}\right) , \tag{2.49}$$

and

$$v_{\rm NLT}^{\rm HTL}(\boldsymbol{x}) = \frac{\hat{q}_0 \boldsymbol{x}^4 m_D^2}{128} \log\left(\frac{16 e^{6-4\gamma_E}}{\boldsymbol{x}^4 m_D^4}\right) . \tag{2.50}$$

At this order, we observe that there is no consistent way to construct a map between different models; this is a consequence that starting at NLT order the expansion explicitly depends on the infrared scale, unlike the LT order. Nonetheless, even in this case one can construct an universal LT + NLT potential

$$v^{\mathrm{LT+NLT}}(\boldsymbol{x}) = \frac{\hat{q}_0 \boldsymbol{x}^2}{4} \log\left(\frac{1}{\mu_\star^2 \boldsymbol{x}^2}\right) + \frac{\hat{q}_0 \boldsymbol{x}^4 \mu_\star^2}{c_1} \log\left(\frac{c_2}{\mu_\star^4 \boldsymbol{x}^4}\right) \equiv v^{\mathrm{LT}}(\boldsymbol{x}) + v^{\mathrm{NLT}}(\boldsymbol{x})\,, \tag{2.51}$$

where the constants c_1 and c_2 are model dependent. Using the map given by Eq. (2.48), they read for the GW and HTL models

$$c_1^{\mathrm{GW}} = 64\frac{\mu^2}{\mu_\star^2}\,, \quad c_2^{\mathrm{GW}} = 16\mathrm{e}^{5-4\gamma_E}\frac{\mu^4}{\mu_\star^4}\,, \tag{2.52}$$

$$c_1^{\mathrm{HTL}} = 128\frac{m_D^2}{\mu_\star^2}\,, \quad c_2^{\mathrm{HTL}} = 16\mathrm{e}^{6-4\gamma_E}\frac{m_D^4}{\mu_\star^4}\,. \tag{2.53}$$

In Fig. 2.2 (right) we plot the GW and HTL potentials (Eqs. (2.38) and (2.40)) comparing to the LT/LL accuracy forms (Eqs. (2.44) and (2.45)) with and without using the map given in Eq. (2.48). We clearly observe that up to the scale $\boldsymbol{x} \sim 1/m_D$, using the universal map we provide, the GW and HTL agree considerably well. This is compared to the more usual prescription $\mu = m_D$ [127], which even for small dipoles sizes gives a considerable difference between the models.

With all these considerations regarding the scattering potential, we can construct the LT $S(\boldsymbol{x}, L)$ function as

$$S^{\mathrm{LT}}(\boldsymbol{x}) = \exp\left[-\frac{1}{4}Q_{s0}^2\,\boldsymbol{x}^2\,\log\frac{1}{\boldsymbol{x}^2\mu_\star^2}\right]\,. \tag{2.54}$$

where we introduced the *bare* saturation scale $Q_{s0}^2 = \hat{q}_0 L$.

So far the only simplifications we have made relates to the fact that smaller dipoles give the dominant contribution to momentum broadening and it is natural to power expand in the dipole size. Nonetheless, it is still impossible to express the $\mathcal{P}^{LT}$ distribution in a closed form. The second set of simplifications one can adopt are related to the energy of the probe. From Eq. (2.54) one observes that the dipole size $\boldsymbol{x}^2 \sim 1/\boldsymbol{k}^2$ competes with the saturation scale Q_{s0}^2. In the case where the transverse momentum acquired by the probe is much larger than the saturation scale of the medium, $\boldsymbol{k}^2 \gg Q_{s0}^2$, one expects that the dominant contribution comes from a single hard scattering, rather than due to multiple soft parton-medium interactions. Indeed, in this case we can expand S^{LT} in a Taylor series to give

$$S^{\mathrm{LT}}(\boldsymbol{x})\Big|_{|\boldsymbol{x}|\ll 1/Q_{s0}} = 1 - \frac{1}{4}Q_{s0}^2\,\boldsymbol{x}^2\,\log\frac{1}{\boldsymbol{x}^2\mu_\star^2} + O\left(\boldsymbol{x}^4 Q_{s0}^4\right)\,. \tag{2.55}$$

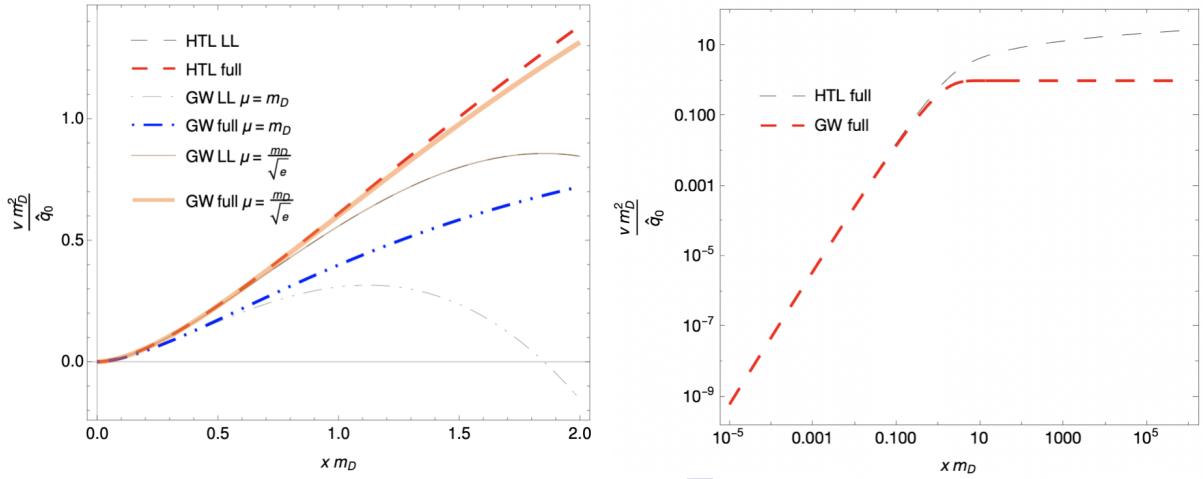

Figure 2.2: Plot of the potential v for the HTL and GW models, with the normalization $\frac{m_D^2}{\hat{q}_0}$ and $|\boldsymbol{x}|$ given in units of the Debye mass m_D. **Left**: Dashed curves correspond to the HTL model, the dash-dotted lines give the GW model potential when $\mu_{\rm GW} = m_{\rm D}$ and the full lines correspond to the GW model solution in the Leading Logarithmic (LL) approximation (full thin curve) and for the full potential (full crosser line) when one makes use of the matching proposed in Eq. (2.48). The LL curves for both the HTL and GW model show that this approximation breaks down when $|\boldsymbol{x}| \sim \frac{1}{m_{\rm D}}$, as expected. Figure taken from [2]. **Right**: The full HTL and GW potentials at large dipole sizes, where the evolution in the dipole size is slow.

The first term can be neglected since it does not contribute to $\mathcal{P}$ and we see that the broadening distribution is proportional to the dipole cross-section, i.e. it is dominated by a *single hard* (SH) scattering. We define the corresponding broadening distribution as

$$\mathcal{P}^{\rm SH}(\boldsymbol{k}, L) = -\frac{1}{4} Q_{s0}^2 \int_{\boldsymbol{x}} \mathrm{e}^{-i\boldsymbol{x}\cdot\boldsymbol{k}}\, \boldsymbol{x}^2 \log \frac{1}{\boldsymbol{x}^2 \mu_\star^2} = \frac{1}{4} Q_{s0}^2\, \vec{\nabla}_{\boldsymbol{k}}^2 \frac{4\pi}{\boldsymbol{k}^2} = 4\pi \frac{Q_{s0}^2}{\boldsymbol{k}^4}\,, \tag{2.56}$$

where we used the $n = 0$ case of Eq. (2.46) and as expected we recover a hard Coulomb $1/\boldsymbol{k}^4$ tail.

On the other end, when $\boldsymbol{k}^2 \ll Q_{s0}^2$, the logarithm in Eq. (2.54) is slowly varying with $\boldsymbol{x}$ and can be regulated by a large momentum scale $Q^2 \sim Q_{s0}^2$, making the integrations in $\mathcal{P}$ Gaussian and allowing to resum all orders in the *effective* saturation scale $Q_s^2 = Q_{s0}^2 \log \frac{Q^2}{\mu_\star^2}$. The broadening distribution reads in this case

$$\mathcal{P}^{\rm MS}(\boldsymbol{k}, L) = \int_{\boldsymbol{x}} \mathrm{e}^{-\frac{1}{4}\boldsymbol{x}^2 Q_s^2}\, \mathrm{e}^{-i\boldsymbol{x}\cdot\boldsymbol{k}} = \frac{4\pi}{Q_s^2}\, \mathrm{e}^{-\frac{\boldsymbol{k}^2}{Q_s^2}}\,. \tag{2.57}$$

Here MS stands for *multiple soft*, since $Q_{s0}^2 \gg \mu_\star^2 \implies \chi \sim L/\lambda \sim Q_{s0}^2/\mu_\star^2 \gg 1$, where χ is easily recognized to be the medium opacity. In this approximation, the net momentum transfer is due to the multiple scatterings of the probe in the medium, $\chi \gg 1$, and the

soft approximation comes from neglecting the logarithm in Eq. (2.54), suppressing large momentum transfers.

In chapter 3 section 3.2, we go beyond this dicotomic description between MS and SH broadening distributions, providing a closed form solution that includes both the SH and MS results. Although the full LT broadening distribution can be easily computed numerically, the previous simpler forms are sometimes preferable since, for example, they speed up numerical calculations or allow for an analytic treatment.

2.4 Next-to-eikonal propagation and branching

So far, we have worked in the eikonal approximation, where terms $O(\boldsymbol{p}^2/p^+)$ are neglected. However, as argued at the end of section 2.1, to study processes where medium induced radiation is produced, one needs to go beyond eikonal accuracy in order for radiation to be resolved. Capturing all order corrections to the eikonal result in a systematic manner is a difficult problem; see for example [128–130] and references therein, focused on next-to-eikonal accuracy calculations.

For the present discussion, from the previous sections, it should be clear that the minimal but most important correction one should implement is at the level of the phase structure, which was drastically simplified before. In particular, we will not neglect next-to-eikonal phases generated from the integration over the $-$ component of momenta. However, next-to-eikonal corrections appearing anywhere but in the phases are neglected.

The only important simplification we took was in Eq. (2.10), where now we do not neglect the phase factor but rather keep it. Recall that, as we outlined, for multiple field insertions after simplifying the Dirac algebra the momentum integrations decouple and it is thus sufficient just to consider the lowest order contribution. Keeping this new phase term, the integration over transverse momenta gets modified and reads (with $x^+ - y^+ > 0$)

$$G_F(\boldsymbol{x}, x^+; \boldsymbol{y}, y^+) \equiv \int_{\boldsymbol{p}} \mathrm{e}^{-i\frac{\boldsymbol{p}^2}{2p^+}(x^+-y^+)} \mathrm{e}^{i\boldsymbol{p}\cdot(\boldsymbol{x}-\boldsymbol{y})} = \frac{p^+}{2\pi i(x^+-y^+)} \mathrm{e}^{i\frac{p^+}{2}\frac{(\boldsymbol{x}-\boldsymbol{y})^2}{(x^+-y^+)}}\,, \tag{2.58}$$

where we introduced G_F which can be recognized as the free propagator for a single particle moving in two dimensions between space time points $(\boldsymbol{y}, y^+)$ and $(\boldsymbol{x}, x^+)$; a perhaps more enlightening way of seeing this is by inseting back the p^- integration

$$\frac{1}{2p^+} G_F(\boldsymbol{x}, x^+; \boldsymbol{y}, y^+)\Theta(x^+ - y^+) = \int_{p^-,\boldsymbol{p}} \frac{i}{p^2 + i\varepsilon} \mathrm{e}^{-i\vec{p}\cdot(\vec{x}-\vec{y})}\,, \tag{2.59}$$

which shows that indeed G_F is the Fourier transform of the (retarded) propagator (where again we also have the extra $2p^+$ factor).

Going back to the eikonal case, we see that each $\boldsymbol{p}$ integral in the generic n case would give rise to a delta function which eliminated one of the momentum integrations. In the

next-to-eikonal case, between each field insertion one inserts a free propagator, thus S_n must be of the form

$$S_n \propto \prod_{i=1}^{n+1} \int_{\vec{x}_i} \Theta(x_i^+ - x_{i-1}^+) G_F(\boldsymbol{x}_i, x_i^+; \boldsymbol{x}_{i-1}, x_{i-1}^+)(igA^-(\boldsymbol{x}_i, x_i^+) \cdot t)\,, \tag{2.60}$$

where the overall constants and energy conservation are not included, $(\boldsymbol{x}_0, x_0^+) \equiv (\boldsymbol{y}, y^+)$ is the initial position, $(\boldsymbol{x}_{n+1}, x_{n+1}^+) \equiv (\boldsymbol{x}, x^+)$ is the final position and the final field insertion should be set $(igA^-(\boldsymbol{x}_{n+1}, x_{n+1}^+) \cdot t) \to 1$, see Fig. 2.3.

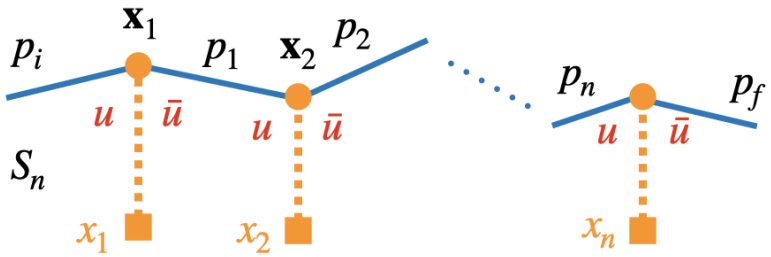

Figure 2.3: Diagrammatic representation S_n given in Eq. (2.60).

Up to linear order in the fields (in accordance to the above discussion when expanding the Wilson lines), it is easily recognized the full S matrix can be written in terms of a path integral [131]

$$S = 2p_f^+(2\pi)\delta(p_f^+ - p_i^+) \int_{\boldsymbol{x}} \mathrm{e}^{-i(\boldsymbol{p}_f\cdot\boldsymbol{x} - \boldsymbol{p}_i\cdot\boldsymbol{y})} \int_{\boldsymbol{r}(y^+)=\boldsymbol{y}}^{\boldsymbol{r}(x^+)=\boldsymbol{x}} D\boldsymbol{r}(s^+) \exp\left(\frac{ip_f^+}{2}\int_0^L ds \left[\frac{d\boldsymbol{r}}{ds^+}\right]^2\right) \mathcal{W}(L,\boldsymbol{r})\,, \tag{2.61}$$

starting at $(\boldsymbol{y}, y^+)$ and with endpoint at $(\boldsymbol{x}, x^+)$. This form for the S matrix indicates that when doing perturbation theory for processes fully embedded in the medium, one should consider exactly the same diagrams as in the vacuum case, but use instead for the propagator between vertices

$$\frac{1}{2p^+}\mathcal{G}(\boldsymbol{x}, x^+; \boldsymbol{y}, y^+)\,, \tag{2.62}$$

where $\mathcal{G}$ denotes either the vacuum propagator G_F, the eikonal propagator $\mathcal{W}$ or the next-to-eikonal propagator

$$G(\boldsymbol{x}, x^+; \boldsymbol{y}, y^+|p^+) = \int_{\boldsymbol{r}(y^+)=\boldsymbol{y}}^{\boldsymbol{r}(x^+)=\boldsymbol{x}} D\boldsymbol{r}(s^+) \exp\left(\frac{ip^+}{2}\int_0^L ds \left[\frac{d\boldsymbol{r}}{ds^+}\right]^2\right) \mathcal{W}(L,\boldsymbol{r})\,. \tag{2.63}$$

Since G is an unitary time evolution operator, it obeys a simple composition law, which in a basis free form reads

$$G(x^+; y^+) = G(x^+; z^+)G(z^+; y^+)\,. \tag{2.64}$$

Projecting to the position basis and inserting the identity operator $\int_{\boldsymbol{z}} |\boldsymbol{z}\rangle \langle \boldsymbol{z}|$, we obtain

$$\langle \boldsymbol{x}| \, G(x^+; y^+) \, |\boldsymbol{y}\rangle \equiv G(\boldsymbol{x}, x^+; \boldsymbol{y}, y^+) = \int_{\boldsymbol{z}} G(\boldsymbol{x}, x^+; \boldsymbol{z}, z^+) G(\boldsymbol{z}, z^+; \boldsymbol{y}, y^+) \, , \tag{2.65}$$

which is sometimes referred to as the Chapman-Kolmogorov composition law in the context of stochastic systems [120], and it just says that at any time the particle must be situated at some spatial point. This could also have been directly obtained from the partition of the above path integral.

Finally, we have so far only considered the case where the parton propagates fully inside the medium. However, one is typically interested in partons being produced inside a medium and emerging out of it after a finite amount of time has passed. Therefore, we consider now the case where the parton leaves the medium at $(\boldsymbol{z}, L)$, and then undergoes some further branching in the vacuum at $(\boldsymbol{x}, x^+)$. Using Eqs. (2.59) and (2.65) and recalling that the extra splitting will introduce an energy-momentum conservation delta function, the relevant object to consider is

$$\begin{aligned} \int_{\vec{x}} \mathrm{e}^{i\vec{p}\cdot\vec{x}} G(\boldsymbol{x}, x^+; \boldsymbol{y}, y^+) &= \int_{\vec{x}} \mathrm{e}^{i\vec{p}\cdot\vec{x}} \int_{\boldsymbol{z}} G_F(\boldsymbol{x}, x^+; \boldsymbol{z}, L) G(\boldsymbol{z}, L; \boldsymbol{y}, y^+) \\ &= \int_{\vec{x}} \mathrm{e}^{i\vec{p}\cdot\vec{x}} \int_{\boldsymbol{z}} \int_{\vec{p}'} \frac{2p^{+\prime} i}{p'^2 + i\varepsilon} \mathrm{e}^{-i\vec{p}'\cdot(\vec{x}-\vec{z})} G(\boldsymbol{z}, L; \boldsymbol{y}, y^+) \\ &= \frac{2p^+ i}{p^2 + i\varepsilon} \int_{\boldsymbol{z}} \mathrm{e}^{-i\,\vec{p}\cdot\vec{z}} G(\boldsymbol{z}, L; \boldsymbol{y}, y^+) \, . \end{aligned} \tag{2.66}$$

In conclusion, one can decouple vacuum and in-medium propagators by using a mixed representation: vacuum propagators follow the usual momentum prescription, while in-medium propagators are more conveniently written in configuration space. Additionally, we see that each medium-vacuum crossing adds a $2p^+$ contribution.

To complete the set of *effective* Feynman rules for in-medium propagation, one needs to describe in-medium branching. Locally, one assumes that all splitting processes are the same as in vacuum. The only important difference comes from the fact that in vacuum the momentum out off a vertex is the same as the measured momentum, while in the medium this is no longer true in general.

First, it is convenient to rewrite the splitting matrix elements just in terms of their transverse components. These are the only terms that matter for any practical calculation, since as illustrated in the previous sections, only the transverse modes are dynamical[6]. We consider the leading branching processes: $g \to g + g$ and $q \to q + g$, ignoring the energy suppressed four gluon vertex and all other processes easily obtained by similarity transformations.

In the pure gluonic case, using standard Feynman rules, and considering an incoming state with momentum k_1 and color a and outgoing gluon with momenta k_2 and k_3 (and

[6]The results that follow are easily derived in LCPT [110].

color indices b and c, respectively), the vertex reads (see Fig. 2.5)

$$V^{abc\,,\alpha\beta\gamma} = -gf^{abc}((k_1+k_3)^\beta g^{\alpha\gamma} + (k_2-k_3)^\alpha g^{\beta\gamma} - (k_2+k_1)^\gamma g^{\alpha\beta}) \equiv -gf^{abc}\Gamma^{\alpha\beta\gamma}\,. \quad (2.67)$$

In the light-cone gauge, propagating modes have $\varepsilon^+(k) = 0$, which when combined with the constraints

$$\varepsilon(k)^\lambda_\mu k^\mu = 0\,, \quad \varepsilon^\lambda_\mu(k)\varepsilon^{\lambda\star\mu}(k) = -\delta^{\lambda,\lambda'}\,, \quad (2.68)$$

yield

$$\varepsilon^\lambda(k) = \left(0, \frac{\boldsymbol{\varepsilon}^\lambda\cdot\boldsymbol{k}}{k^+}, \boldsymbol{\varepsilon}^\lambda\right)\,, \quad (2.69)$$

where the transverse polarization vector can be written (in a circular polarization form) as $\boldsymbol{\varepsilon}^{\pm1} = (1,\pm i)/\sqrt{2}$, such that $\boldsymbol{\varepsilon}^{\lambda\star}\cdot\boldsymbol{\varepsilon}^{\lambda'} = \delta^{\lambda,\lambda'}$. Contracting $\Gamma^{\alpha\beta\gamma}$ with the respective polarization vectors we obtain (dropping helicity indices)

$$\Gamma^{\alpha\beta\gamma}\varepsilon^\alpha(k_1)\varepsilon^\beta(k_2)\varepsilon^\gamma(k_3) = 2(k_1\cdot\varepsilon_2)(\varepsilon_1\cdot\varepsilon_3) + 2(k_2\cdot\varepsilon_1)(\varepsilon_2\cdot\varepsilon_3) - (k_1+k_2)\cdot\varepsilon_3(\varepsilon_1\cdot\varepsilon_2)\,, \quad (2.70)$$

where $\cdot$ here means contraction on all four-momentum components, with $\varepsilon_\mu(k_n)\equiv\varepsilon_n$ and we used $k_1 = k_2 + k_3$. Defining the energy fractions $zk_1^+ = k_2^+$ and $(1-z)k_1^+ = k_3^+$, with the explicit decomposition for the momenta and polarizations given above, after some simple algebra one finds that the only non-vanishing components of the vertex are given by

$$V^{abc}_{ijl} = 2gf^{abc}\left[\frac{\boldsymbol{\mathfrak{k}}^l\delta^{ij}}{(1-z)} + \frac{\boldsymbol{\mathfrak{k}}^j\delta^{il}}{z} - \boldsymbol{\mathfrak{k}}^i\delta^{jl}\right]\,, \quad (2.71)$$

where we have introduced the relative transverse momentum of the splitting $\boldsymbol{\mathfrak{k}} \equiv \boldsymbol{k}_2 - z\boldsymbol{k}_1$.

In the case of the $q\to q+g$ splitting, one essentially follows a similar calculation, now taking into account the Dirac structure. The calculation is made simpler by considering an incoming quark with momentum $p_i = (p_i^+, \mathbf{0}, 0)$ that splits into a gluon with momentum k and a quark with momentum p, and adjust for the most generic case by introducing $\boldsymbol{\mathfrak{k}}$ at the end. The vertex is defined as (see Fig. 2.5)

$$V^a_{s',s,\lambda}(p,k,p_i) = \bar{u}_s(p)igt^a\not{\varepsilon}^\lambda(k)u_{s'}(p_i)\,. \quad (2.72)$$

and we already anticipate that $s = s'$, as seen before. Again we define $zp_i^+ = k^+$ and $(1-z)p_i^+ = p^+$ and we decompose the Dirac structure in right/left (R/L) handed components, with $\boldsymbol{\varepsilon}^{+1} = \boldsymbol{\varepsilon}^R$ and $\boldsymbol{\varepsilon}^{-1} = \boldsymbol{\varepsilon}^L$. Using the typical decomposition of the gamma matrices in this component basis [23, 24]

$$\gamma^\mu = \begin{pmatrix} 0 & \sigma^\mu \\ \bar{\sigma}^\mu & 0\,, \end{pmatrix} \quad (2.73)$$

with $\sigma^\mu \in \{1, \sigma^x, \sigma^y, \sigma^y\}$, $\bar{\sigma}^\mu \in \{1, -\sigma^x, -\sigma^y, -\sigma^y\}$, with $\sigma^{x,y,z}$ the x, y, z Pauli matrices and noticing that the splitting is collinear (i.e. $\boldsymbol{k} = -\boldsymbol{p}$), after some lengthy algebra one obtains

$$V^a_{s',s,\lambda}(p,k,p_i) = -\frac{2gt^a\delta^{s,s'}}{z\sqrt{1-z}}\left(\delta^{s,\lambda} + (1-z)\delta^{s,-\lambda}\right)\boldsymbol{k}\cdot\boldsymbol{\varepsilon}^\lambda\,, \quad (2.74)$$

where in the general case one should replace $\boldsymbol{k} \to \mathfrak{k} \equiv \boldsymbol{k} - z\boldsymbol{p}_i$.

Finally, the vertex structure in-medium needs to be altered since the measured momentum is not $\mathfrak{k}$; rather it only matches the momentum off the vertex if the particles propagate eikonally. Following the logic above, we consider now the $q \to q + g$ branching but with the outgoing quark scattering once before exiting the medium. It should be clear that including more field insertions will not qualitatively change the solution since, as outlined above, each new insertion factorizes from the other ones. In this case, the matrix element is proportional to (see Fig. 2.4)

$$\propto \int_{x,x_b,p} \left[\bar{u}(p_f)\not{A}(x)\cdot t u_s(p)\right] \frac{i}{p^2+i\varepsilon} \left[\bar{u}_s(p)\not{\epsilon}(k) t^b u(p_i)\right] \mathrm{e}^{ix(p_f-p)} \mathrm{e}^{ix_b(p+k-p_i)} \,. \tag{2.75}$$

The second $[\,.\,]$ was computed above and is proportional to the vector $\boldsymbol{k}(1-z) - z\boldsymbol{p}$, the

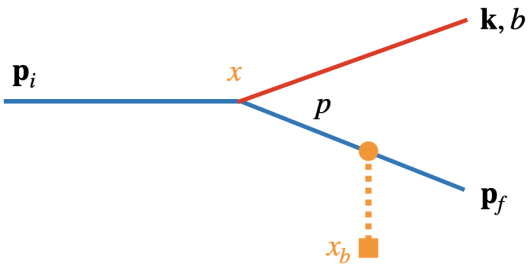

Figure 2.4: Diagram used to explicitly show how to modify the vertex structure in the medium. Gluons are given by red lines and quark by blue lines.

relative transverse momentum of the vertex. The first term in $\boldsymbol{k}$ is not relevant for the present calculation since the outgoing gluon propagates as in vacuum, and thus the only important piece remaining involves

$$\propto \int_{x_b} \mathrm{e}^{ix_b(k-p_i)} \int_{x,p} \left[\bar{u}(p_f)\not{A}(x)\cdot t u_s(p)\right] \frac{i}{p^2+i\varepsilon} \mathrm{e}^{ip(x_b-x)} \mathrm{e}^{ixp_f} \boldsymbol{p} \,. \tag{2.76}$$

The itegration over p^- can be performed as in section 2.1, yielding at next-to-eikonal accuracy a transverse integration

$$\begin{aligned} \propto \int_{\boldsymbol{p}} \boldsymbol{p} \mathrm{e}^{i\frac{\boldsymbol{p}^2}{2p^+}(x^+-x_b^+)} \mathrm{e}^{-i\boldsymbol{p}\cdot(\boldsymbol{x}-\boldsymbol{x}_b)} \Theta(x^+-x_b^+) &= \int_{\boldsymbol{p}} (-i\partial_{\boldsymbol{x}_b}) \mathrm{e}^{i\frac{\boldsymbol{p}^2}{2p^+}(x^+-x_b^+)} \mathrm{e}^{-i\boldsymbol{p}\cdot(\boldsymbol{x}-\boldsymbol{x}_b)} \Theta(x^+-x_b^+) \\ &= (-i\partial_{\boldsymbol{x}_b}) G_F(\boldsymbol{x}, x^+; \boldsymbol{x}_b, x_b^+) \Theta(x^+-x_b^+) \,, \end{aligned} \tag{2.77}$$

where the derivative is understood to only act on G_F, but not on the Fourier phase we omitted. Thus, we see that one must replace, in the vertex, the transverse vectors by derivate operators, which are just the position space representation of the momentum operator $\boldsymbol{p} = -i\partial_{\boldsymbol{x}}$.

This is perhaps better realized starting from a coordinate free form and taking into account multiple field insertions in all legs. The matrix element should be proportional to

$$\propto \int_{x_b^+} G(L; x_b^+) V(x_b^+) G(x_b^+; x_i^+) G^A(L; x_b^+) \tag{2.78}$$

where G^A denotes the in-medium gluon propagator, in the adjoint color representation. Projecting to a position basis we obtain

$$\propto \int_{x_b^+, \boldsymbol{x}_b, \boldsymbol{z}, \boldsymbol{y}} G(\boldsymbol{x}_b, x_b^+; \boldsymbol{x}_i, x_i^+) \langle \boldsymbol{x}_b | V(x_b^+) | \boldsymbol{y}, \boldsymbol{z} \rangle G(\boldsymbol{x}, L; \boldsymbol{z}, x_b^+) G^A(\boldsymbol{x}_g, L; \boldsymbol{y}, x_b^+) \,, \tag{2.79}$$

where we have ignored additional integrations on the external outgoing states. Inserting the $q \to q + g$ vertex (ignoring pre-factors), we obtain

$$\propto \int_{x_b^+, \boldsymbol{x}_b} G(\boldsymbol{x}_b, x_b^+; \boldsymbol{x}_i, x_i^+)(-i) \left[\partial_{\boldsymbol{z}} - z\partial_{\boldsymbol{y}}\right]_{\boldsymbol{z}=\boldsymbol{x}_b}^{\boldsymbol{y}=\boldsymbol{x}_b} G(\boldsymbol{x}, L; \boldsymbol{z}, x_b^+) G^A(\boldsymbol{x}_g, L; \boldsymbol{y}, x_b^+) \,. \tag{2.80}$$

The above *effective* Feynman rules for jet quenching are summarized in Fig. 2.5. We omitted rules which are common to *standard* perturbative calculations. Also, one must integrate over the vertices spacetime arguments as well over any remaining explicit spacetime position dependence, which is easily deduced by writing any amplitude in a free basis and projecting to the configuration space, as we outlined before.

Finally, we would like to note that the form in Eq (2.63) implies that G is the Green's function of a Schrodinger equation

$$\left(i\partial_t + \frac{\partial_{\boldsymbol{x}}^2}{2\omega} + gA^-(t, \boldsymbol{x}) \cdot T\right) G(t, \boldsymbol{x}; 0, \boldsymbol{y}) = i\delta(t)\delta(\boldsymbol{x} - \boldsymbol{y}) \,, \tag{2.81}$$

which will make use of in chapter 6. Also, the eikonal limit where $G \to \mathcal{W}$, is obtained by neglecting the term containing $\partial_{\boldsymbol{x}}$ in the previous equation.

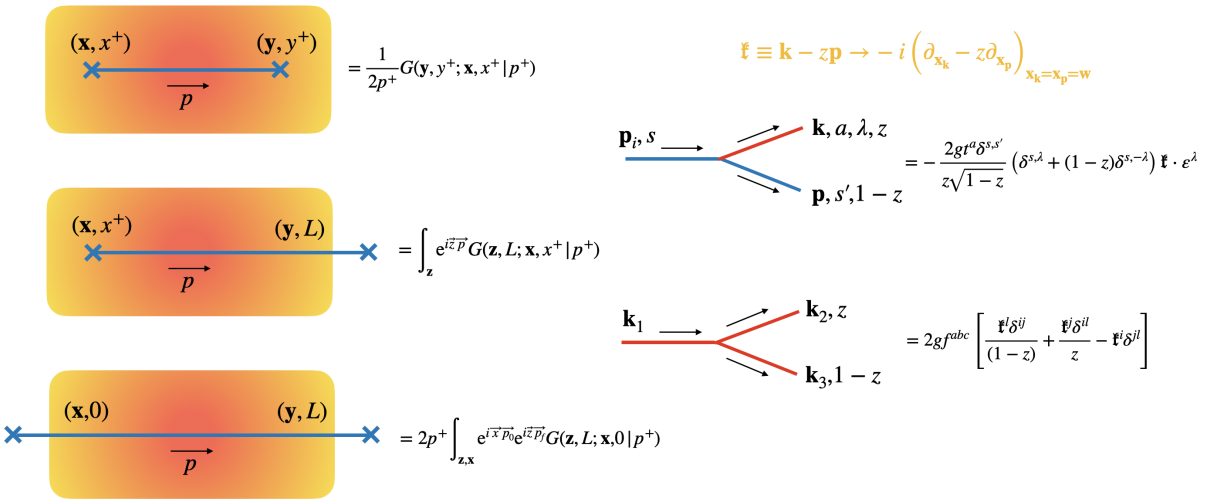

Figure 2.5: Effective Feynman rules for jet quenching. **Left**: Propagator structure depending on the end and starting point, valid for both gluons and quarks and for eikonal or next-to-eikonal propagation. The momentum appearing in the integrals refer to the final or initial state momentum. Notice that the + component is always conserved. **Right**: Branching rules with quarks denoted by blue lines and gluons by red lines. On top, we highlight that in the case of extra non-eikonal propagation one must update the transverse structure, with the splitting occurring at position w.

2.5 Medium induced gluon energy spectrum

Equipped with the set of rules outlined in the previous sections, one can compute more interesting observables. Arguably, the most important observable for jet quenching phenomenology at this level is the medium induced radiation spectrum[7]. To study the radiation pattern, we consider the propagation of a hard (eikonal) parton (in color representation R) that emits a soft gluon with transverse momentum $\boldsymbol{k}$ and energy ω; in the present approach this leads to the BDMPS-Z/ASW result (see Fig. 2.6). This can be generalized to the case where the emitter is not eikonal [103, 105] (see also [132] for the GLV approach).

In this thesis, we only consider the energy spectrum, integrating over the gluon transverse momentum $\boldsymbol{k}$. In Fig. 2.6, we outline the single diagram contributing to spectrum, with the choice that the branching time in the amplitude t_1 is smaller than the branching time in the conjugate amplitude t_2. Although one can directly apply all the rules detailed in the previous section to compute the spectrum[8], one can obtain the general form of the

[7] As for the broadening distribution, the radiation spectrum is strictly speaking not an observable.

[8] We do not do this in this thesis since the exact derivation, even with the effective Feynman, is still quite lengthy and unimportant for what follows. Derivations following similar notation and strategy to the one we outlined can be found, for example, in [104, 105, 133, 134].

spectrum by direct inspection of the diagrams shown in Fig. 2.6.

Due to the time locality of the medium averages (see previous section 2.2) one can analyze the process by splitting it into three different regions: $(0, t_1)$, (t_1, t_2) and (t_2, L). In the first time region, the initial hard parton propagates eikonally at the same transverse position both in amplitude and conjugate amplitude, and thus the respective dipole $\mathrm{Tr}(\mathcal{W}^\dagger\mathcal{W}) = N_c$[9]. In the last time step, when both gluons have been emitted, the system evolution is dominated by the dynamics of the gluon dipole (where the emitter plays no role). Clearly in this last step, only broadening effects matter, but since broadening conserves energy and only shuffles the momentum modes, after integrating over $\boldsymbol{k}$ all contributions from this sector vanish. Thus one expects the only non-trivial contribution to come from the middle section.

Here, the gluon contributes with a propagator G. The other contribution is easily obtained for the case of an initial quark by using Eq. (2.65) to split the propagators into each region and the relation between fundamental $\mathcal{U}$ and adjoint $\mathcal{W}$ Wilson lines [83, 135]

$$\mathcal{W}^{\dagger ab}(\mathbf{x}) = \mathcal{W}^{ba}(\mathbf{x}) = 2\mathrm{Tr}[t^b\mathcal{U}^\dagger(\mathbf{x})t^a\mathcal{U}(\mathbf{x})]\,, \tag{2.82}$$

such that by a quick analysis of the color flow one finds that the middle sector gives a term proportional to $\mathrm{Tr}(G\mathcal{W}^\dagger)$.

The overall factors must be α_s (one emission), C_R (the strength of the emission) and $2\Re$ to take into account all time orderings. There must be an ordered integration in t_1 and t_2 and the vertices in the eikonal limit must generate a differential operator with respect to the gluon. Also, on dimensional grounds the spectrum must be proportional to $1/\omega^2$. Finally, the integrations can run beyond the medium length L, and thus in its full generality the spectrum will include (divergent) vacuum-like pieces which one can remove by subtracting the vacuum version of the operator $\mathrm{Tr}(G\mathcal{W}^\dagger)$.

Indeed, an exact calculation of the spectrum leads to so called Zakharov formula [94, 102] (see also [136])

$$\omega\frac{dI}{d\omega} = \frac{\alpha_s C_R}{\omega^2} 2\Re \int_0^\infty dt_2 \int_0^{t_2} dt_1\; \boldsymbol{\partial}_{\boldsymbol{x}}\cdot\boldsymbol{\partial}_{\boldsymbol{y}}\left[\mathcal{K}(\boldsymbol{x}, t_2; \boldsymbol{y}, t_1) - \mathcal{K}_0(\boldsymbol{x}, t_2; \boldsymbol{y}, t_1)\right]_{\boldsymbol{x}=\boldsymbol{y}=0}\,, \tag{2.83}$$

where the gluon frequency is assumed much smaller than the initial energy of the initiating parton[10]. This is in agreement with the direct analysis of the diagrams.

The branching kernel $\mathcal{K}(\boldsymbol{x}, t_2; \boldsymbol{y}, t_1) = \frac{1}{N_c^2-1}\mathrm{Tr}(G(\boldsymbol{x}, t_2; \boldsymbol{y}, t_1|\omega)\mathcal{W}^\dagger(\boldsymbol{0}, t_2 - t_1))$[11] is given in the path integral formalism by

$$\mathcal{K}(\boldsymbol{x}, t_2; \boldsymbol{y}, t_1) = \int_{\mathbf{y}}^{\mathbf{x}} \mathcal{D}\mathbf{r}(t) \exp\left[\frac{i\omega}{2}\int_{t_1}^{t_2} dt\, \dot{\mathbf{r}}^2 - \int_{t_1}^{t_2} dt\, v(\boldsymbol{x}-\boldsymbol{y}, t)\right]\,, \tag{2.84}$$

[9] Here all propagators, except for this region, are in the adjoint representation.

[10] In what follows, we will use $\bar{\alpha} = \alpha_s C_R/\pi$.

[11] Here we denote light-cone times x^+ and t.

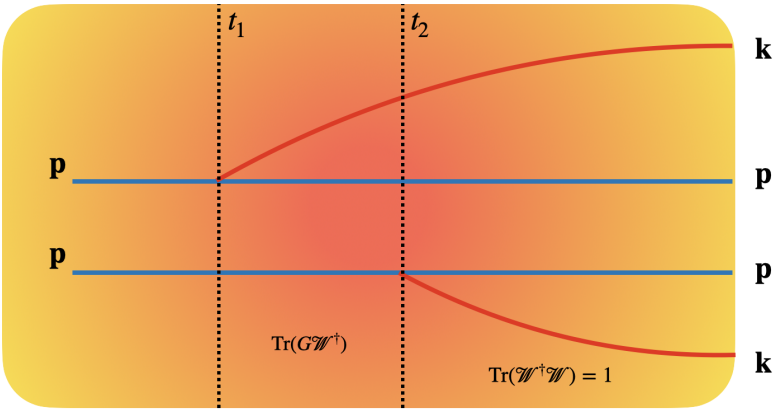

Figure 2.6: Structure of the diagrams contributing to the medium induced energy spectrum, in the soft gluon approximation. The top figure represents the amplitude diagram and the bottom figure represents conjugate amplitude diagram with the choice $t_2 > t_1$, as in the text. In the bottom, we sketch the color structure associated with each time slice, where all objects are taken to be in the adjoint representation. We note that the structure of the last time slice is only valid for the energy spectrum and in the soft gluon limit. Note that the transverse position of the quark lines should match in amplitude and conjugate, so that the result is inclusive with respect to it, while the endpoints of the gluons do not match in both terms.

where we used Eqs. (2.30) and (2.63). The vacuum case $\mathcal{K}_0$ was already considered in Eq. (2.58)

$$\mathcal{K}_0(\boldsymbol{x}, t_2; \boldsymbol{y}, t_1) = \frac{\omega}{2\pi i(t_2 - t_1)} \mathrm{e}^{i\frac{\omega}{2}\frac{(\boldsymbol{x}-\boldsymbol{y})^2}{(t_2-t_1)}} . \tag{2.85}$$

In what follows, we make use of the fact that $\mathcal{K}$ is the Green's function to a Schrodinger equation with an imaginary potential $v(\boldsymbol{x})$ (see Eq. (2.37) with $C_R = C_A$)

$$\left[i\partial_{t_2} + \frac{\boldsymbol{\partial}_{\boldsymbol{x}}^2}{2\omega^2} + iv(\boldsymbol{x}) \right] \mathcal{K}(\boldsymbol{x}, t_2; \boldsymbol{y}, t_1) = i\delta(\boldsymbol{x} - \boldsymbol{y})\delta(t_2 - t_1) . \tag{2.86}$$

We see that indeed v enters as an imaginary potential, leading to a non-unitary time evolution of the system. Evolution does not preserve probabilities since when obtaining $v(\boldsymbol{x})$ one performs a classical average over the configurations of the background field. Therefore, large dipoles sizes, where v is large, are exponentially suppressed in favor of small dipoles that can resolve the structure of the medium.

In general, solutions to Eq. (2.86) are not known. Nonetheless, there are two special cases, most relevant for jet quenching phenomenology, where one can solve the spectrum analytically. We detail such approaches in what follows. Numerical methods to solve Eq. (2.86) exactly also exist and have been the topic of great interest in recent years [3, 4, 137–139].

BDMPS-Z/ASW

The first case we explore is the situation where one takes $v(\boldsymbol{x}) = v^{\rm MS}(\boldsymbol{x})$ and corresponds to the BDMPS-Z/ASW model. In this case, Eq. (2.86) can be solved exactly since the potential is harmonic. This spectrum takes into account multiple soft interactions between the medium and probe, at the cost, as detailed above, of neglecting the exact form of the potential, effectively missing the physics associated to large momentum transfers. Thus the BDMPS-Z/ASW solution captures the multiple soft scattering regime.

An explicit form for $\mathcal{K}$ can be found directly by applying the steepest descent approximation to Eq. (2.84) (which in this case is exact because the potential is quadratic, see [103, 131]). We consider instead an equivalent method, essentially based on solving the path integral by considering fluctuations around the classical path [131], which was first introduced, in the jet quenching language, in [140]. In the MS approximation, one can write Eq. (2.86) as

$$\left[i\partial_{t_2} + \frac{\partial^2_{\boldsymbol{x}}}{2\omega^2} - \frac{\omega\Omega^2(t_2)}{2}\boldsymbol{x}^2\right]\mathcal{K}_{\rm HO}(\boldsymbol{x},t_2;\boldsymbol{y},t_1) = i\delta(\boldsymbol{x}-\boldsymbol{y})\delta(t_2-t_1)\,, \tag{2.87}$$

with

$$\Omega(t) = \frac{1-i}{2}\sqrt{\frac{\hat{q}_0(t)\log\frac{Q^2}{\mu_\star^2}}{\omega}}, \tag{2.88}$$

where Q is the UV cutoff introduced for the MS prescription and here we consider the universal IR model, with a regulator $\mu_\star$. The subscript HO denotes that the potential is harmonic. Formally, the solution to Eq. (2.87) is given by [92, 103, 131, 140, 141]

$$\begin{aligned}\mathcal{K}_{\rm HO}(\boldsymbol{x},t_2;\boldsymbol{y},t_1) = \frac{\omega}{2\pi i S(t_2,t_1)}\exp\Big\{&\partial_{t_2}S(t_2,t_0)\boldsymbol{x}^2 - \partial_{t_1}S(t_2,t_1)\boldsymbol{y}^2 - (\partial_s S(t_2,s)_{s=t_2}\\ &- \partial_s S(s,t_1)_{s=t_1})\boldsymbol{x}\cdot\boldsymbol{y}\Big\}\,,\end{aligned} \tag{2.89}$$

where the function S satisfies

$$\left[\frac{d^2}{d^2t} + \Omega^2[t]\right]S(t,t_0) = 0\,,\quad S(t_0,t_0) = 0\,,\quad \partial_t S(t,t_0)_{t=t_0} = 1\,. \tag{2.90}$$

It is well known from the theory of linear ordinary differential equations that any given solution can be written as a linear combination of a complete and orthogonal set of other solutions. Since this is a second order equation we take the orthogonal solution to the harmonic equation to satisfy

$$\left[\frac{d^2}{d^2t} + \Omega^2[t]\right]C(t,t_0) = 0\,,\quad C(t_0,t_0) = 1\,,\quad \partial_t C(t,t_0)_{t=t_0} = 0\,, \tag{2.91}$$

with $C(t,s) = \partial_s S(s,t) = -\partial_s S(t,s)$, where we used the fact that S is odd in the arguments. These solutions are related by the determinant of the Wronskian matrix (W), giving

$$W = C(t,s)\partial_t S(t,s) - \partial_t C(t,s) S(t,s) = 1\,, \tag{2.92}$$

where we used the initial conditions above. In particular, we obtain the useful formula

$$\partial_t \frac{C(t,s)}{S(t,s)} = -\frac{C(t,s)\partial_t S(t,s) - \partial_t C(t,s) S(t,s)}{S^2(t,s)} = -\frac{1}{S^2(t,s)}\,. \tag{2.93}$$

With these results, Eq. (2.89) can be written as

$$\mathcal{K}_{\text{HO}}(\boldsymbol{x},t_2;\boldsymbol{y},t_1) = \frac{\omega}{2\pi i S(t_2,t_1)} \exp\left[\frac{i\omega}{2S(t_2,t_1)}\left\{C(t_1,t_2)\,\boldsymbol{x}^2 + C(t_2,t_1)\,\boldsymbol{y}^2 - 2\boldsymbol{x}\cdot\boldsymbol{y}\right\}\right]. \tag{2.94}$$

Finally, S and C can always be written as linear combinations of other solutions to the equations of motion. In particular, for the time order $t > t_1 > t_0$ any solution in (t,t_1) can be written as a superposition of solutions in (t,t_0). Using the above boundary conditions, one finds [140]

$$\begin{aligned} S(t,t_1) &= C(t_1,t_0)S(t,t_0) - S(t_1,t_0)C(t,t_0)\,,\\ C(t,t_1) &= -\partial_{t_1}C(t_1,t_0)S(t,t_0) + \partial_{t_1}S(t_1,t_0)C(t,t_0)\,, \end{aligned} \tag{2.95}$$

where it is explicit that S is odd. Taking $t = +\infty$, $t_1 = s > L$ and $t_0 = L$, and using the fact that the vacuum solutions ($\Omega = 0$) read $S(t,s) = t - s$ and $C(t,s) = 1$, one sees that the first term dominates, leading to the handy formula

$$\frac{C(\infty,s)}{S(\infty,s)} = -\frac{\partial_s C(s,L)}{C(s,L)} = \Omega^2(s)\frac{S(s,L)}{C(s,L)}\,, \tag{2.96}$$

where the last equality only holds if C is even. In the next section, we also make use of the notation $C(t,s) = C_{t,s}$ and $C(t_2,t_1) = C_{2,1}$.

In the case of the plasma brick model we consider in this thesis, the S and C functions satisfy inside the medium

$$S(t,t_0) = \frac{1}{\Omega}\sin(\Omega(t-t_0)) \quad , \quad C(t,t_0) = \cos(\Omega(t-t_0))\,, \tag{2.97}$$

so that the propagator reads

$$\mathcal{K}_{\text{HO}}(\boldsymbol{x},t;\boldsymbol{y},t_1) = \frac{\omega\Omega}{2\pi i\sin(\Omega(t-t_1))} \exp\left[\frac{i\omega\Omega}{2\sin(\Omega(t-t_1))}\left\{\cos(\Omega(t-t_1))\,(\boldsymbol{x}^2+\boldsymbol{y}^2) - 2\boldsymbol{x}\cdot\boldsymbol{y}\right\}\right], \tag{2.98}$$

where one can explicitly take the limit $\Omega \to 0$ and obtain Eq. (2.85).

With the above discussion, one can directly compute the emission spectrum. Using Eq. (2.94) in Eq. (2.83), one finds[12]

$$\omega\frac{dI^{\rm HO}}{d\omega} = -2\bar{\alpha}\Re\left[\int_0^\infty dt_2\int_0^{t_2} dt_1 \frac{1}{S^2(t_2,t_1)} - \frac{1}{(t_2-t_1)^2}\right] . \tag{2.99}$$

One can cancel the explicit collinear divergence between medium and vacuum contributions using the above properties of the S and C functions

$$\begin{aligned}\omega\frac{dI^{\rm HO}}{d\omega} &= -2\bar{\alpha}\Re\left[\int_0^\infty dt_1\ \frac{C(t_1,t_1)}{S(t_1,t_1)} - \frac{C(\infty,t_1)}{S(\infty,t_1)} - \frac{1}{t_1-t_1}\right] \\ &= 2\bar{\alpha}\Re\left[\int_0^\infty dt_1\ \frac{C(\infty,t_1)}{S(\infty,t_1)}\right] = 2\bar{\alpha}\Re\left[\int_0^\infty dt_1\ -\frac{\partial_{t_1}C(t_1,L)}{C(t_1,L)}\right] \\ &= 2\bar{\alpha}\log C(0,L)\,,\end{aligned} \tag{2.100}$$

which in the brick case reduces to

$$\omega\frac{dI^{\rm HO}}{d\omega} = 2\bar{\alpha}\log|\cos(\Omega L)|\,. \tag{2.101}$$

The scale $\Omega L \propto \sqrt{\omega_c/\omega}$, where $\omega_c \equiv \frac{1}{2}\hat{q}_0\log\left(\frac{Q^2}{\mu_\star^2}\right)L^2 = \frac{1}{2}\hat{q}L^2$ is the typical frequency of gluons with a formation time of the order of the medium length, controls the behavior of the spectrum. The limiting behaviors, for small and large frequencies read

$$\omega\frac{dI^{\rm LO}}{d\omega} = 2\bar{\alpha}\begin{cases}\sqrt{\dfrac{\omega_c}{2\omega}} & ,\ \omega\ll\omega_c \\ \dfrac{1}{12}\left(\dfrac{\omega_c}{\omega}\right)^2 & ,\ \omega\gg\omega_c\end{cases} . \tag{2.102}$$

Thus we observe that the spectrum is dominated by soft gluons with $\omega \ll \omega_c$, while hard modes are power suppressed.

The form of this spectrum is intrinsically related to the QCD Landau-Pomerantchuk-Migdal (LPM) effect [142–144]. One way to see this is to recall that the formation time of the gluon, i.e. the typical time it takes to put it on-shell (to be quantum mechanically resolved) is given by (see section 2.1)

$$t_f \equiv \frac{2\omega}{\boldsymbol{k}^2}\,. \tag{2.103}$$

During a time interval t, the gluon can acquire an extra transverse momentum component due to interactions with the medium of the order

$$\boldsymbol{k}^2 \sim \hat{q}t_f\,, \tag{2.104}$$

[12] In what follows, we denote the BDMPS-Z/ASW either using HO or LO.

thus equating the previous identities one obtains $t_f^2 \sim \omega/\hat{q}$, and the formation time is only a function of the gluon frequency and the medium properties. The radiation spectrum must be proportional to the number of gluon whose emission is resolved inside the medium. Thus one expects that in the regime where the gluon frequency is smaller than ω_c (which from above we observe that $t_f(\omega_c) = L$) that

$$\omega \frac{dI}{d\omega} \propto \alpha_s \frac{L}{t_f} \sim \alpha_s \sqrt{\frac{\omega_c}{\omega}}\,, \tag{2.105}$$

Thus, we observe that when $1/\mu_\star < t_f < L$, different scattering centers act coherently, leading to a suppression of harder gluons. In addition, one notices that the transverse momentum acquired during the branching $\boldsymbol{k}^2 \sim \sqrt{\hat{q}\omega}$ is smaller than the saturation scale $Q_s^2 = \hat{q}L$[13]. Thus, in this regime of highly localized branchings ($t_f < L$) the splitting can be seen as being almost collinear, with the gluons being transported to the large angle region due to final state broadening [51, 85].

In the previous argument, we have also assumed that $t_f \gg \lambda$ (recall λ is the mean free path). In the regime where each scattering in the medium is responsible for the formation of a soft gluon $\lambda \sim t_f$, the BDMPS-Z/ASW spectrum is no longer valid, but rather the correct behavior is captured by the incoherent Bethe-Heitler (BH) spectrum [146]. In this regime, each scattering acts as a single radiation source, and thus one obtains

$$\omega \frac{dI}{d\omega} \propto \alpha_s \frac{L}{\lambda} \sim \alpha_s N_{\text{scat.}}\,, \tag{2.106}$$

leading to a flat spectrum in energy, corresponding to the incoherent superposition of $N_{\text{scat.}}$ single scattering contributions, with the momentum transfer of the order $\boldsymbol{k}^2 \sim \hat{q}_0\lambda \sim \mu_\star^2$. In terms of the gluon frequency, the BH regime is only reached when the gluon frequency is smaller than $\sim \lambda\mu_\star^2 = \frac{\mu_\star^4}{\hat{q}_0} \equiv \omega_{\text{BH}}$[14].

GLV/W

The second approach to solving Eq. (2.83) consists in expanding $\mathcal{K}$ order by order in opacity, i.e. adding a single scattering at the time. At leading order in opacity, the spectrum is dominated by a single large momentum transfer, due to tails present in the full form for $v(\boldsymbol{x})$. As mentioned before, this regime was first explored by GLV/W. Since

[13] In fact, this observation gives a way to estimate the arbitrary cut-off scale Q^2 [145]. In the regime $\omega < \omega_c$ it is natural to identify $Q^2 \sim \boldsymbol{k}^2 \sim \sqrt{\hat{q}\omega} = \sqrt{\hat{q}_0\omega \log Q^2/\mu_\star^2}$. In the regime $\omega > \omega_c$, the UV regulator should be controlled by the saturation scale $Q^2 \sim Q_s^2 \sim \hat{q}L = \hat{q}_0 L \log \hat{q}_0 L/\mu_\star^2$, where notice that the logarithm becomes energy independent. In the BDMSP-Z/ASW model this is however a sort of *educated* parametric estimate rather than a necessary condition one should impose. In the next chapter, we will show that when merging the MS and SH regimes under a single framework, the determination of Q^2 becomes critically important.

[14] Notice that in the definition of ω_{BH} we used $\hat{q}_0$ instead of $\hat{q}$, unlike the definition for ω_c. For reasons that will become obvious in the next chapter, it is convenient to define ω_c also with $\hat{q}_0$; the exact numerical value of this scale is not of extreme importance and thus logarithmic difference is not critical.

then, the calculation as been extended beyond ninth order in opacity [147], at a cost of extremely cumbersome computations.

Here we follow W's approach, which obtains the GLV result from the BDMPS-Z/ASW formalism used so far. The kernel obeys a simple Dyson-like relation [131]

$$\mathcal{K}(\boldsymbol{x},x^+;\boldsymbol{y},y^+)=\mathcal{K}_0(\boldsymbol{x},x^+;\boldsymbol{y},y^+)-\int_{\boldsymbol{z}}\int_{y^+}^{x^+}dt\,\mathcal{K}_0(\boldsymbol{x},x^+;\boldsymbol{z},t)v(\boldsymbol{z},t)\mathcal{K}(\boldsymbol{z},t;\boldsymbol{y},y^+)\,, \tag{2.107}$$

where each iteration introduces a scattering off the field followed by vacuum-like evolution, similar to the all order derivations detailed in the previous sections. Plugin in Eq. (2.83) and after some algebra one finds that the energy spectrum can be written as[15]

$$\omega\frac{dI}{d\omega}=\frac{\bar{\alpha}\hat{q}_0L^2}{\omega}\int_0^\infty dx\,\frac{1}{x+y}\frac{x-\sin(x)}{x^2}\,. \tag{2.108}$$

Here $y=\mu^2L/(2\omega)$ and we also alert that μ is the GW infrared scale, since the GLV/W result is usually derived assuming this form for the medium. Here the relevant cut scale is $\bar{\omega}_c=\frac{1}{2}\mu^2L\ll\hat{q}_0L$, so that one obtains

$$\omega\frac{dI^{\mathrm{GLV/W}}}{d\omega}=\bar{\alpha}\frac{\hat{q}_0L}{\mu^2}\begin{cases}\log\dfrac{\mu^2L}{2\omega}\,, & \omega\ll\bar{\omega}_c\\ \dfrac{\pi}{4}\left(\dfrac{\mu^2L}{2\omega}\right)\,, & \omega\gg\bar{\omega}_c\end{cases}\,. \tag{2.109}$$

One can see that at small frequencies the spectrum predicted by GLV/W (to first opacity order) does not capture the expected correct behavior, based on the previous heuristic discussion. Of course, this is expected since coherence effects between different scatterings centers are not fully taken into account at this fixed order.

Let us now consider the regime $\omega\gg\omega_c$, where $t_f\geq L$. In this case, the medium is seen as a single hard scattering center. The first condition can be written as $\boldsymbol{k}^2\geq\frac{\omega}{L}$ and the second one imposes that $\boldsymbol{k}^2$ must be much larger than the saturation scale. Thus, using the LT form for the potential v, the spectrum reduces to

$$\omega\frac{dI}{d\omega}\propto\alpha_s\int_{\sqrt{\omega/L}}^\infty d|\boldsymbol{k}|\frac{|\boldsymbol{k}|}{\boldsymbol{k}^4}\sim\alpha_s\frac{\omega_c}{\omega}\,, \tag{2.110}$$

as predicted by the GLV/W result, but not the BDMPS-Z/ASW result since it misses the $1/\boldsymbol{k}^4$ tail.

[15] A detailed derivation can be found in [141]. In the following chapter, we will present a similar calculation, which reduces to this result in a special limit. Thus, to not over extend this section, we refer the reader to the next chapter.

Beyond BDMPS-Z/ASW *vs* GLV/W Similar to the discussion in section 2.3, we see that the full energy spectrum is sectioned intro three regions, without any analytic approach being able to describe them all correctly in a closed form (see Fig. 2.7). For jet quenching phenomenology, the BH sector is not relevant, but it is important to have control over the contributions coming either from the BDMPS-Z/ASW or GLV/W regions. Thus, having an approach that encapsulates both these regimes would be of extreme importance.

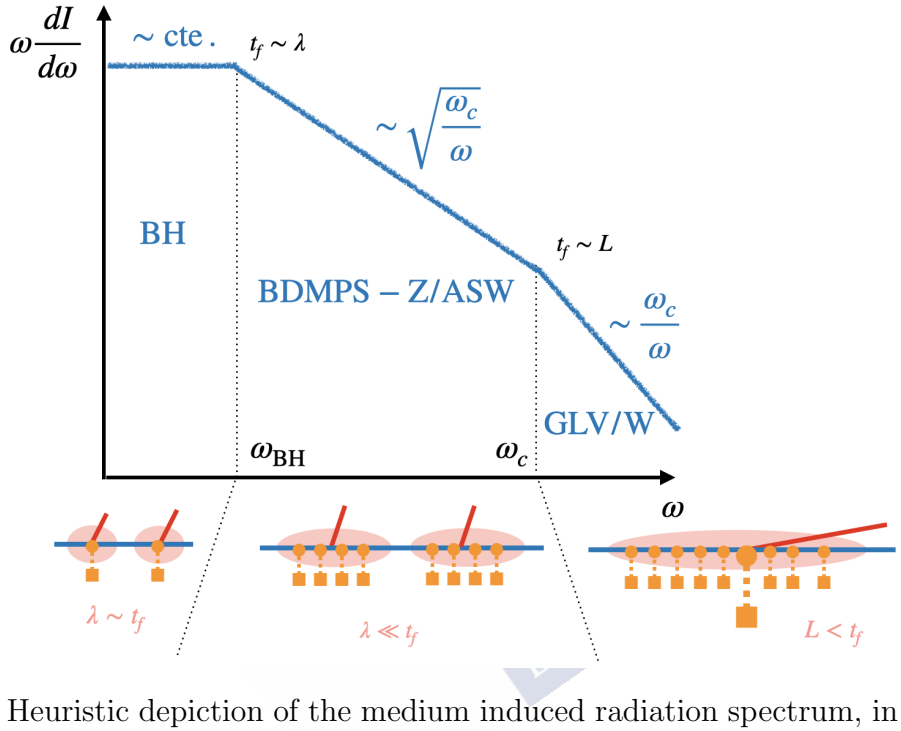

Figure 2.7: Heuristic depiction of the medium induced radiation spectrum, in accordance with the discussion in the main text. In the bottom, we give a simplified depiction of the local medium-probe interactions controlling the dominant physics in each region.

In the next chapter, we introduce a new approach [141,148] that interpolates between the BDMPS-Z/ASW and GLV/W solutions, based on Molière's theory of multiple scattering [149,150]. In particular, we expand this program, so far either named **Improved Opacity Expansion** (IOE) or, more deservedly, **Molière** (M), beyond first order in opacity and show that it can be generalized to momentum broadening in a simple manner.

2.A Light-cone coordinates and notation

In this appendix we clarify some of the notation and conventions used.

We always work in the light-cone gauge with $A^+ = 0$ and the parton being a right-mover. The four-vector $a^\mu = (a^0, a^1, a^2, a^3)$ is written in light-cone coordinates as $a^\mu =$

$(a^+, \boldsymbol{a}, a^-)$, with $\sqrt{2}a^+ = a^0 + a^3$, $\sqrt{2}a^- = a^0 - a^3$ and $\boldsymbol{a} = (a^1, a^2)$. We sometimes denote $\vec{a} = (a^+, \boldsymbol{a})$ if a is a spacetime point and $\vec{a} = (a^-, \boldsymbol{a})$ if a denotes a particle's momentum. With this choice $\vec{x} \cdot \vec{p} = x^+ p^- - \boldsymbol{x} \cdot \boldsymbol{p}$. To simplify notation we also denote $x_\mu p^\mu = x \cdot p$ in the main text, when obvious.

The metric tensor $\eta^{\mu\nu}$, for the ordering $x = (x^+, \boldsymbol{x}, x^-)$, reads

$$\eta^{\mu\nu} = \begin{pmatrix} 0 & 0 & 0 & 1 \\ 0 & -1 & 0 & 0 \\ 0 & 0 & -1 & 0 \\ 1 & 0 & 0 & 0 \end{pmatrix} . \tag{2.111}$$

This implies that the product of two four-vectors is given by

$$a^\mu b_\mu = a^+ b^- + a^- b^+ - \mathbf{a} \cdot \boldsymbol{b} \, . \tag{2.112}$$

A particular case of the previous identity is $k^2 = 0 \implies k^- = \boldsymbol{k}^2/(2k^+)$, which we use extensively. We also recall that $a^+ = a_-$, since the metric is not diagonal. Also, the medium L differs by a factor of $\sqrt{2}$ from the medium length measured in cartesian coordinates (which is what one would naturally call the length of the medium).

Position space integrals are represented, per dimension as, $\int_x \equiv \int_{-\infty}^{\infty} dx$, or with omitted boundaries if they are evident. Momentum space integrals then read $\int_p = \int_{-\infty}^{\infty} (2\pi)^{-1} dp$.

2.B Dipole cross-section in the GW and HTL models: useful integrals

Combining Eqs. (2.34) and (2.35) with Eq. (2.31) and recalling that $v(\boldsymbol{x}) = C_R \sigma(\boldsymbol{x})$, one concludes that the computation of the GW and HTL potentials boils down to solving

$$\int_0^\infty du \, \frac{u}{(u^2 + b^2)\,(u^2 + a^2)} \, (1 - J_0(ux)) \, , \tag{2.113}$$

with $b = a = \mu$ and $b = 0$ for the GW model, $a = m_{\mathrm{D}}$ for HTL, see Eq. (2.37).

This integral can be done explicitly as follows. Separating the denominators we obtain

$$\frac{1}{(a^2 - b^2)} \int_0^\infty du \, \left[\frac{u}{(u^2 + b^2)} - \frac{u}{(u^2 + a^2)} \right] (1 - J_0(ux)) \, , \tag{2.114}$$

which is simplified using the identities

$$\int_0^\infty du \, \left[\frac{u}{(u^2 + a^2)} \right] J_0(xu) = K_0(ax) \, , \tag{2.115}$$

and

$$\int_0^\infty du \, \frac{u}{(u^2 + b^2)\,(u^2 + a^2)} = \frac{\log a^2 - \log b^2}{2(a^2 - b^2)} \, . \tag{2.116}$$

These yield

$$\int_0^\infty du\ \frac{u}{(u^2+b^2)\,(u^2+a^2)}\,(1-J_0(ux)) = \frac{1}{(a^2-b^2)}\,[K_0(ax)-K_0(bx)+\log a-\log b]\ . \tag{2.117}$$

Taking $a=b$, one obtains the GW result

$$\int_0^\infty du\ \frac{u}{(u^2+a^2)^2}\,(1-J_0(ux)) = \frac{1}{2a^2}\,[1-axK_1(ax)]\ , \tag{2.118}$$

while for $b=0$ and for small dipoles sizes, where $K_0(bx)\approx -\log(bx/2)-\gamma_E$, one obtains

$$\int_0^\infty du\ \frac{1}{u\,(u^2+a^2)}\,(1-J_0(ux)) = \frac{1}{a^2}\,[K_0(ax)+\log(ax/2)+\gamma_E]\ , \tag{2.119}$$

which is the result quoted in the main text.

3

Aspects of the Improved Opacity Expansion/Molière approach

In this chapter, we introduce the Improved Opacity Expansion/Molière (IOE/M) framework [141, 148–150] to compute the medium induced radiation spectrum and the momentum broadening distribution. We first explore the structure of the energy spectrum beyond first order in opacity. Then, we apply the same scheme to compute the single particle broadening probability $\mathcal{P}$, such that the end result can describe both the MS and SH regimes.

The work presented in this chapter is based on [2, 6].

3.1 The all order structure of the IOE/M gluon energy spectrum

In this section, we apply the IOE/M framework to compute the gluon energy spectrum. Before, let us first review the mains aspects of this approach.

3.1.1 General remarks on the IOE/M approach

The first step in the IOE/M strategy is to work with the LT potential $v(\boldsymbol{x})$, thus ignoring small corrections (in the twist expansion introduced before), and to split it using a

matching scale Q^2 as

$$v^{\mathrm{LT}}(\boldsymbol{x}) = \frac{\hat{q}_0}{4}\,\boldsymbol{x}^2 \log\left(\frac{1}{\boldsymbol{x}^2\mu_\star^2}\right) = \frac{\hat{q}_0}{4}\,\boldsymbol{x}^2\left\{\log\frac{Q^2}{\mu_\star^2} + \log\frac{1}{Q^2\boldsymbol{x}^2}\right\} \equiv v_{\mathrm{MS}}(\boldsymbol{x}) + \delta v(\boldsymbol{x})\,, \tag{3.1}$$

where the time dependence is implicit. This splitting does not change the potential but it allows to identify a first piece which is just the MS potential with an ultraviolet regulator Q and a remaining piece δv that has the information regarding the tail behavior of v. This splitting becomes useful if one wants to treat δv as a perturbative parameter, which is valid as long as

$$\log\frac{1}{\boldsymbol{x}^2Q^2} \ll \log\frac{Q^2}{\mu_\star^2} \implies Q^2 \gg \mu_\star^2\,. \tag{3.2}$$

One can then see that at small frequencies, $\omega \ll \omega_c$, δv becomes a perturbation around v_{MS}, while at large frequencies, one can not neglect δv, but rather the dominant physical picture is set by taking $v = \delta v$.

Eq. (3.2) is so far the only condition on Q. It indeed matches the BDMPS-Z/ASW prescription to regulate the logarithm, and thus when trying to extract information from data, this scale always introduces a certain degree of ambiguity, since although it is natural to take Q to be the largest/most relevant energy scale in problem, there is no theoretical constraint on possible numerical pre-factors[1]. Although this also seems to be the case in the IOE/M approach we will show that in fact Q can not be a constant scale and it must obey a transcendental equation. This extra constraint comes from requiring that observables can not depend on the matching scale.

The second, and more ingenious step of the IOE/M framework, is to promote in Eq. (2.107) $\mathcal{K}_0 \to \mathcal{K}_{\mathrm{HO}}$ and replace v by δv. This corresponds to doing the traditional opacity expansion, but instead of in between each scattering the parton propagating as in vacuum, one resums all soft gluon exchanges into the harmonic propagator and includes the hard part of the potential perturbatively. Then the Dyson equation for $\mathcal{K}$ now reads

$$\mathcal{K}(\boldsymbol{x},x^+;\boldsymbol{y},y^+) = \mathcal{K}_{\mathrm{HO}}(\boldsymbol{x},x^+;\boldsymbol{y},y^+) - \int_{\boldsymbol{z}}\int_{y^+}^{x^+} ds\; \mathcal{K}_{\mathrm{HO}}(\boldsymbol{x},x^+;\boldsymbol{z},s)\delta v(\boldsymbol{z},s)\mathcal{K}(\boldsymbol{z},s;\boldsymbol{y},y^+)\,. \tag{3.3}$$

In the limit $\omega \gg \omega_c$, one has that $\mathcal{K}_{\mathrm{HO}} \to \mathcal{K}_0$ and the physics is dominated by hard scatterings in the medium. Thus, in this limit one expects that this expansion recovers the GLV/W result. On the other end, when $\omega \ll \omega_c$, higher order terms when expanding this equation will give sub-leading contributions in energy, and thus $\mathcal{K} \to \mathcal{K}_{\mathrm{HO}}$, i.e. one should recover the BDMPS-Z/ASW result.

In conclusion, the IOE/M is formally very similar to the GLV/W approach, but instead of expanding around the vacuum solution, one expands around the harmonic

[1]Indeed, in the original formulation of the IOE/M approach it was used $Q^2 \sim \sqrt{\hat{q}\omega}$, with the *dressed* jet quenching parameter defined as $\hat{q} = \hat{q}_0 \log\frac{Q^2}{\mu_\star^2}$. This choice is discussed in further at the end of this section.

solution. Naturally, one then expects that both the MS and SH regime are already encoded in this strategy. In [148], it was attempted to also include the BH regime, but as shown in [4], the obtained result it not correct. The main issue seems to be that expanding around the harmonic solution, automatically rules out the possibility of going to the multiple incoherent scattering regime. This aspect of the IOE/M strategy deserves a more in-depth study.

3.1.2 Medium induced energy spectrum in the IOE/M approach

Formally, the energy spectrum in the IOE/M framework can be recast as

$$\omega\frac{dI}{d\omega} = \omega\frac{dI^{\mathrm{HO=LO}}}{d\omega} + \omega\frac{dI^{\mathrm{NLO}}}{d\omega} + \cdots = \omega\frac{dI^{\mathrm{LO}}}{d\omega} + \sum_{m=1}^{\infty}\omega\frac{dI^{\mathrm{N}^m\mathrm{LO}}}{d\omega}\,. \tag{3.4}$$

We use the nomenclature $\mathrm{N^nLO}$, but this should not be confused with the more traditional use of these terms in the context of higher loop order calculations, which is not the case of the present calculation. In particular, the LO result is the BDMPS-Z/ASW result, NLO corresponds to $m = 1$ hard scatterings, and so on.

Expanding out the Dyson equation (Eq. (3.3)) and inserting it into Eq. (2.83) we obtain that the m^{th} term in the series reads (for $m > 1$)

$$\begin{aligned}\omega\frac{dI^{\mathrm{N}^m\mathrm{LO}}}{d\omega} = (-1)^m\frac{\bar{\alpha}\pi}{\omega^2}2\Re\Bigg[\int_0^\infty dt_2\int_0^{t_2}dt_1\int_{\boldsymbol{z}_1}\int_{\boldsymbol{z}_2}\cdots\int_{\boldsymbol{z}_m}\int_{t_1}^{t_2}ds_m\int_{t_1}^{s_m}ds_{m-1}\cdots\int_{t_1}^{s_2}ds_1\\ \times\boldsymbol{\partial}_{\boldsymbol{x}}\cdot\boldsymbol{\partial}_{\boldsymbol{y}}\,\mathcal{K}_{\mathrm{HO}}(\boldsymbol{x},t_2;\boldsymbol{z}_m,s_m)\delta v(\boldsymbol{z}_m,s_m)\mathcal{K}_{\mathrm{HO}}(\boldsymbol{z}_m,s_m;\boldsymbol{z}_{m-1},s_{m-1})\delta v(\boldsymbol{z}_{m-1},s_{m-1})\\ \times\mathcal{K}_{\mathrm{HO}}(\boldsymbol{z}_{m-1},s_{m-1};\boldsymbol{z}_{m-2},s_{m-2})\cdots\times\mathcal{K}_{\mathrm{HO}}(\boldsymbol{z}_1,s_1;\boldsymbol{y},t_1)\Bigg]_{\boldsymbol{x}=\boldsymbol{y}=0},\end{aligned} \tag{3.5}$$

where we ordered the times of each scattering center from t_1 to t_2 in increasing order of the sub-index, running from 1 to m. The transverse position of the i^{th} scattering center $\boldsymbol{z}_i$ is also ordered from the first scattering center ($\boldsymbol{z}_1$) to the last one ($\boldsymbol{z}_m$). The two external propagators can be integrated using the following useful identity

$$\begin{aligned}\int_0^{x^+}ds\,\partial_{\boldsymbol{y}}\mathcal{K}_{\mathrm{HO}}(\boldsymbol{x},x^+;\boldsymbol{y},s)_{\boldsymbol{y}=\boldsymbol{0}} &= -\frac{\omega^2}{2\pi}\int_0^{x^+}ds\,\frac{\boldsymbol{x}}{S^2(x^+,s)}\exp\left(-\frac{i\omega}{2}\frac{C(s,x^+)}{S(s,x^+)}\right)\\ &= \frac{\omega}{i\pi}\frac{\boldsymbol{x}}{\boldsymbol{x}^2}\exp\left(-i\frac{\omega}{2}\frac{C(0,x^+)}{S(0,x^+)}\boldsymbol{x}^2\right),\end{aligned} \tag{3.6}$$

where we used the properties of the S and C functions detailed in the previous chapter and neglected infinite frequency terms. A similar identity holds for the other integral in time [141]

$$\int_{z^+}^{\infty}ds\,\partial_{\boldsymbol{x}}\mathcal{K}_{\mathrm{HO}}(\boldsymbol{x},s;\boldsymbol{z},z^+)_{\boldsymbol{x}=\boldsymbol{0}} = \frac{\omega}{i\pi}\frac{\boldsymbol{z}}{\boldsymbol{z}^2}\exp\left(i\frac{\omega}{2}\frac{C(\infty,z^+)}{S(\infty,z^+)}\boldsymbol{z}^2\right)\,. \tag{3.7}$$

Taking the convolution of the time integrations to the form

$$\begin{aligned}&\int_0^\infty dt_2 \int_0^{t_2} dt_1 \int_{t_1}^{t_2} ds_m \int_{t_1}^{s_m} ds_{m-1} \cdots \int_{t_1}^{s_2} ds_1 = \\ &= \int_0^\infty ds_1 \int_{s_1}^\infty ds_2 \cdots \int_{s_{m-1}}^\infty ds_m \int_{s_m}^\infty dt_2 \int_0^{s_1} dt_1 \,,\end{aligned} \tag{3.8}$$

the two above identities can be directly applied, leaving only dependencies on the times and position of the intermediate scatterings. Then introducing the exact representation for the remaining $\mathcal{K}_{\text{HO}}$ (see Eq. (2.94)), after some algebra one eventually obtains

$$\begin{aligned}\omega \frac{dI^{\text{N}^m\text{LO}}}{d\omega} = \frac{\bar{\alpha}\hat{q}_0^m}{2^{3m-2}\pi^m} \Re\Bigg[\left[\frac{\boldsymbol{z}_1 \cdot \boldsymbol{z}_m}{\boldsymbol{z}_1^2 \boldsymbol{z}_m^2}\right] \prod_{j=1}^{m} \fint_{\boldsymbol{z}_j} \int_{s_{j-1}}^{L} ds_j \; \boldsymbol{z}_j^2 \log\left(\frac{1}{Q^2 \boldsymbol{z}_j^2}\right) \\ \times \sigma_{j+1,j} \exp\left[k_j^2 \boldsymbol{z}_j^2\right] \exp\left[-\sigma_{j+1,j} \boldsymbol{z}_{j+1} \cdot \boldsymbol{z}_j\right] \Bigg] \,,\end{aligned} \tag{3.9}$$

where we use the prescriptions: $s_0 = 0$, $\sigma_{m+1,m} = 1$ and $\boldsymbol{z}_{m+1} = 0$. The factor depending on $\boldsymbol{z}_m$ and $\boldsymbol{z}_1$ outside the product should be understood to be integrated over (i.e. the factor enters the $\boldsymbol{z}_1$ and $\boldsymbol{z}_m$ integrals; this is denoted by the slashed integral symbol). The factor π^m comes from the m factors of $\mathcal{K}_{\text{HO}}$ present in the general formula and the factor $\hat{q}_0^m$ is due to the presence of m δv terms. The 2^{3m} appears as a combination of the $\mathcal{K}_{\text{HO}}$ normalization factors and the terms in δv. In addition, we introduced the following functions

$$k_j^2 = \frac{i\omega}{2}\left[\frac{C_{j,j-1}}{S_{j,j-1}} + \frac{C_{j+1,j}}{S_{j+1,j}}\right], \tag{3.10}$$

with the boundary properties $C_{1,0} = C_{\infty,1}$ and $C_{m+1,m} = C_{m,0}$ and the same for the S function. Also

$$\sigma_{k,j} = \frac{i\omega}{S_{k,j}} \,. \tag{3.11}$$

Eq. (3.9) is hard to compute analytically beyond $m = 2$, due to the angular integrations. Nonetheless, for the present calculation it is enough to work at $m = 2$ order and one does not even have to fully simplify the NNLO solution to get the results we seek.

NLO contribution

Setting $m = 1$, one recovers the result obtained in [141]

$$\omega \frac{dI^{\text{NLO}}}{d\omega} = \frac{\bar{\alpha}\hat{q}_0}{2\pi} \Re\left[\int_{\boldsymbol{z}} \int_0^L ds \; \log\left(\frac{1}{Q^2 \boldsymbol{z}^2}\right) \exp\left[k^2(s) \boldsymbol{z}^2\right] \right], \tag{3.12}$$

with

$$k^2(s) = \frac{i\omega}{2}\left[\frac{C_{1,0}}{S_{1,0}} + \frac{C_{2,1}}{S_{2,1}}\right] = \frac{i\omega}{2}\left[\frac{C_{\infty,s}}{S_{\infty,s}} + \frac{C_{s,0}}{S_{s,0}}\right], \tag{3.13}$$

where in the last step we rewrote the time dependence in terms of the variables appearing in Eq. (3.12). This expression can be easily simplified by using the identity

$$\int_0^\infty du \log\left(\frac{1}{u}\right) e^{-bu} = \frac{1}{b}\left(\log(b) + \gamma_E\right) , \tag{3.14}$$

to eliminate the integration over $\boldsymbol{z}$. This gives

$$\omega \frac{dI^{\rm NLO}}{d\omega} = \frac{1}{2}\bar{\alpha}\hat{q}_0 \Re\left[\int_0^L ds\ \frac{-1}{k^2(s)}\left(\log\left(-\frac{k^2(s)}{Q^2}\right) + \gamma_E\right)\right] , \tag{3.15}$$

which is the final result obtained in [141][2]. As argued above, this term should become dominant at large energies and recover the GLV/W result. Let us then follow the same procedure as for the BDMPS-Z/ASW and GLV/W spectra and compute the asymptotic form.

When $\omega \to 0$, one gets that $k^2(s) \to -\omega\Omega$. The NLO term then reduces to

$$\begin{aligned}\lim_{\omega\to 0}\omega\frac{dI^{\rm NLO}}{d\omega} &= \frac{\bar{\alpha}}{2}\hat{q}_0\Re\left[\int_0^L \frac{2}{(1-i)\sqrt{\omega\hat{q}}}\left(\log\left(\frac{(1-i)\sqrt{\omega\hat{q}}}{2Q^2}\right) + \gamma_E\right)\right] \\ &= \frac{\bar{\alpha}}{2}\left(\frac{\hat{q}_0}{\hat{q}}\right)\sqrt{\frac{\hat{q}L^2}{\omega}}\left[\gamma_E + \log\left(\frac{\sqrt{\omega\hat{q}}}{\sqrt{2}Q^2}\right) + \frac{\pi}{4}\right] \sim \omega\frac{dI^{\rm LO}}{d\omega}\left(\frac{\hat{q}_0}{\hat{q}}\right) ,\end{aligned} \tag{3.16}$$

where $\frac{\hat{q}_0}{\hat{q}} \sim \log^{-1}\left(\frac{Q^2}{\mu_\star^2}\right) = \log^{-1}\left(\frac{\sqrt{\hat{q}\omega}}{\mu_\star^2}\right)$, is the formal expansion parameter of the series, corresponding to ratio between the hard and soft scales in the problem. Here we have used that

$$Q^2 = \sqrt{\hat{q}_0\omega\log\frac{Q^2}{\mu_\star^2}} \approx \sqrt{\hat{q}_0\omega\log\frac{\sqrt{\hat{q}_0\omega}}{\mu_\star^2}} , \tag{3.17}$$

which emerges from noting that the natural large scale in the MS regime is $Q^2 \sim \langle \boldsymbol{k}^2\rangle$. Here we defne the *dressed* jet quenching parameter $\hat{q} \equiv \hat{q}_0 \log\frac{Q^2}{\mu_\star^2}$. We discuss more the importance of this choice below.

Thus, as long as the hard Q^2 and soft $\mu_\star^2$ scales are sufficiently well separated, then the IOE/M expansion is meaningful. Interestingly, we observe in Eq. (3.16) that at small frequencies the spectrum reduces back to the LO form, with a pre-factor.

At high energies, $k^2(s) \to \frac{i\omega}{2s}$. Using this in Eq. (3.15), we obtain

$$\lim_{\omega\to\infty}\omega\frac{dI^{\rm NLO}}{d\omega} \sim \bar{\alpha}\hat{q}_0\frac{\pi}{4}\frac{L^2}{2\omega} = \frac{\bar{\alpha}\hat{q}_0 L}{\mu^{\star 2}}\frac{\pi}{4}\frac{\bar{\omega}_c}{\omega} = \frac{\pi}{4}\chi\,\bar{\alpha}\frac{\bar{\omega}_c}{\omega} , \tag{3.18}$$

which matches the asymptotic behavior of GLV/W result. We introduced the medium opacity $\chi \equiv \frac{\hat{q}_0 L}{\mu^{\star 2}}$ that becomes larger the denser the system is. Notice that unlike the BDMPS-Z/ASW result that decays as ω^{-2}, this term is power enhanced and thus dominates the $\omega \gg \omega_c$ region of the spectrum.

[2] In [141, 148] there is an incorrect − sign. This slightly changes the spectrum in the soft region, but does not change the result qualitatively.

NNLO contribution and beyond

Let us now try to see what is the formal structure of the IOE/M spectrum, i.e. if its features do not get spoiled at higher orders. Taking $m = 2$ in Eq. (3.9), and integrating over the angles one obtains

$$\omega\frac{dI^{\text{NNLO}}}{d\omega} = -\frac{\bar{\alpha}}{4}\Re\Bigg[\hat{q}_0^2\int_0^L ds_2\int_{s_2}^L ds_1\ \sigma_{s_1,s_2}\int_{z_1z_2}\log\left(\frac{1}{Q^2z_1^2}\right)\log\left(\frac{1}{Q^2z_2^2}\right)z_1^2z_2^2 \\ \times e^{k_1^2z_1^2}e^{k_2^2z_2^2}J_1(z_1z_2\sigma_{s_1,s_2})\Bigg], \tag{3.19}$$

and we introduced the simplified notation

$$k_1^2 = \frac{i\omega}{2}\left(\frac{C_{1,2}}{S_{1,2}}+\frac{C_{\infty,1}}{S_{\infty,1}}\right) \quad , \quad k_2^2 = \frac{i\omega}{2}\left(\frac{C_{1,2}}{S_{1,2}}+\frac{C_{2,0}}{S_{2,0}}\right) \quad , \quad \sigma_{s_1,s_2}\equiv\sigma = \frac{i\omega}{S_{1,2}}\,. \tag{3.20}$$

As before, we now consider the asymptotic forms of this contribution to the spectrum.

At high energies, $\omega \gg \omega_c$, such that $\omega\to\infty\equiv\Omega\to(1-i)\times 0$ and k_1, k_2 and σ can be simplified using that in this regime $C_{s_a,s_b}\to 1$ and $S_{s_a,s_b}\to s_a - s_b$, giving

$$\sigma\to\frac{i\omega}{s_1-s_2} \quad , \quad k_1^2\to\frac{i\omega}{2(s_1-s_2)} \quad , \quad k_2^2\to\frac{i\omega}{2}\frac{s_1}{s_2(s_1-s_2)}\,. \tag{3.21}$$

We (naively) expand the Bessel function in Eq. (3.19), assuming for now that all the integrals are convergent so that one can formally swap the summation and integral symbols. We obtain

$$\omega\frac{dI^{\text{NNLO}}}{d\omega} = -\frac{\bar{\alpha}}{8}\hat{q}_0^2\Re\Bigg[\int_0^L ds_2\int_{s_2}^L ds_1\sum_{n=0}^{\infty}\frac{(-1)^n}{n!(n+1)!}\sigma^{2(n+1)}\left(\frac{1}{4}\right)^n \\ \times\int_{z_1z_2}\log\left(\frac{1}{Q^2z_1^2}\right)\log\left(\frac{1}{Q^2z_2^2}\right)z_1^{2n+3}z_2^{2n+3}e^{k_1^2z_1^2}e^{k_2^2z_2^2}\Bigg]. \tag{3.22}$$

The integrals in the positions can be performed using the following identity

$$\int_x\log\left(\frac{1}{Q^2x^2}\right)x^{2n+3}e^{k^2x^2} = \frac{(n+1)!}{2}\left(-\frac{1}{k^2}\right)^{n+2}\log\left(-\frac{k^2}{Q^2E\psi(n+2)}\right), \tag{3.23}$$

where $E\psi(n) = \exp(\psi(n))$, $\psi(n) = \Gamma'(n)/\Gamma(n)$ and Γ is the gamma function. After some simple algebra one obtains

$$\omega\frac{dI^{\text{NNLO}}}{d\omega} = \frac{\omega}{32}\hat{q}_0^2\Im\Bigg[\int_0^L ds_2\int_{s_2}^L ds_1\ \frac{\sigma}{S_{12}}\left(\frac{1}{k_1^2k_2^2}\right)^2\sum_{n=0}^{\infty}\frac{(-1)^n(n+1)}{4^n}\sigma^{2n} \\ \times\left(\frac{1}{k_1^2k_2^2}\right)^n\log\left(-\frac{k_1^2}{Q^2E\psi(n+2)}\right)\log\left(-\frac{k_2^2}{Q^2E\psi(n+2)}\right)\Bigg]. \tag{3.24}$$

For this expression to make sense the series must be convergent. For this to happen, we analyse the terms depeding on n, namely

$$\sim \frac{n+1}{4^n}\left(\frac{\sigma^2}{k_1^2k_2^2}\right)^n \psi(n+2)\psi(n+2) \overset{n\gg 1}{\sim} n\left(\frac{\sigma^2}{4k_1^2k_2^2}\right)^n \log^2(n)\,. \tag{3.25}$$

One clearly sees that this can only lead to a convergent series if $\frac{\sigma^2}{4k_1^2k_2^2}$ is under control. In the high energy limit this expression reduces to

$$n\left(\frac{\sigma^2}{4k_1^2k_2^2}\right)^n \log^2(n) \sim \left(\frac{s_2}{s_1}\right)^n n\log^2(n)\,, \tag{3.26}$$

which leads to a convergent series, since $s_2 < s_1$. However, as one takes into account energy suppressed contributions, it becomes clear that the series should diverge as $\omega \to \omega_c$, thus we now restrict ourselves to $\omega \gg \omega_c$.

Using the high energy approximation, Eq. (3.24) reduces to

$$\begin{aligned}\lim_{\omega\to\infty}\omega\frac{dI^{\mathrm{NNLO}}}{dLd\omega} = \frac{\bar{\alpha}}{2\omega^2}\hat{q}_0^2\Re\Bigg[\int_0^L ds_2\,\left(\frac{s_2}{L}\right)^2(L-s_2)^2\sum_{n=0}^{\infty}(-1)^n(n+1)\left(\frac{s_2}{L}\right)^n \\ \times\log\left(-i\frac{\omega}{2(L-s_2)Q^2E\psi(n+2)}\right)\log\left(-i\frac{\omega L}{2s_2(L-s_2)Q^2E\psi(n+2)}\right)\Bigg],\end{aligned} \tag{3.27}$$

where the real part can be easily extracted

$$\begin{aligned}\lim_{\omega\to\infty}\omega\frac{dI^{\mathrm{NNLO}}}{dLd\omega} = \frac{\bar{\alpha}}{2\omega^2}\hat{q}_0^2\Bigg[\int_0^L ds_2\,\left(\frac{s_2}{L}\right)^2(L-s_2)^2\sum_{n=0}^{\infty}(-1)^n(n+1)\left(\frac{s_2}{L}\right)^n \\ \times\left(\log\left(\frac{\omega}{2(L-s_2)Q^2E\psi(n+2)}\right)\log\left(\frac{\omega L}{2s_2(L-s_2)Q^2E\psi(n+2)}\right)-\frac{\pi^2}{4}\right)\Bigg].\end{aligned} \tag{3.28}$$

In the previous two equations, we have considered the rate rather than the energy spectrum. In general, this simplification is not allowed, since the derivative operator does not commute with the limit, this is however not the case at high energies, where the dependence on L is always trivial (see [4] for a more rigorous treatment of this aspect, giving the same solution).

At leading order in the logarithms $\sim \log(\frac{\omega}{Q^2L})$, enhanced by an energy factor, we obtain

$$\begin{aligned}\lim_{\omega\to\infty}\omega\frac{dI^{\mathrm{NNLO}}}{dLd\omega} &= \frac{\bar{\alpha}L^3}{2\omega^2}\hat{q}_0^2\int_0^1 du\; u^2(1-u)^2\sum_{n=0}^{\infty}(-1)^n(n+1)u^n \\ &\quad\times\log\left(\frac{\omega}{2L(1-u)Q^2}\right)\log\left(\frac{\omega}{2Lu(1-u)Q^2}\right) \\ &\sim \frac{\bar{\alpha}}{L}\chi\left(\frac{\bar{\omega}_c}{\omega}\right)^2\log^2\left(\frac{\omega}{Q^2L}\right),\end{aligned} \tag{3.29}$$

where we neglected all the terms that do get a double logarithm enhancement and numerical factors coming from the remaining series and integral. Remarkably we observe that the structure observed at NLO continues: the spectrum is again proportional to the opacity (the explicit L dependence here appears since we are considering the rate), but now the spectrum scales with $\sim (\omega_c/\omega)^2$, at the same order of the LO term. Thus, in this kinematic region, the NLO term becomes dominant and gives the leading order behavior that matches GLV/W. The remaining logarithmic dependence, that we observe to change from order to order, is slowly evolving with ω and so does not dominate.

This pattern holds to higher orders in the expansion. This is easily recognized by noticing that each order in the IOE/M expansion will contribute with a term proportional to $\delta v(\boldsymbol{x}) \sim \boldsymbol{x}^2 \log\left(\frac{1}{\boldsymbol{x}^2 Q^2}\right)$, where $\boldsymbol{x}$ is the transverse position of the vertex. Each $\boldsymbol{x}$ is conjugate to some transverse momentum $\boldsymbol{k}$ (see Eqs. (3.19) and (3.21)). In the high energy limit, $\boldsymbol{k}^2 \sim \frac{\omega}{L}$, thus each new vertex introduces a suppression factor $\sim \frac{\bar{\omega}_c}{\omega} \log\left(\frac{\omega}{LQ^2}\right)$, which leads to an order by order power suppression.

To make this statement more rigorous, one would need to construct the formal series for the high frequency limit of the spectrum, by expanding the k's and σ's functions in powers of $1/\omega$. However, a simple analysis suffices to see that indeed the NLO term dominates. First, when $Q^2 = \mu_\star^2$, one recovers the traditional opacity expansion [102]. In the more general case, this is no longer true. However, consider as an example the terms scaling as $(\omega_c/\omega)^2$. In addition to the contribution of the NNLO term as shown in Eq. (3.29) and the first term in the high energy expansion of the LO term (see Eq. (2.102)), one needs to consider the next order term in the expansion of the NLO contribution. The NNLO term has a double logarithm of the form $\log^2\left(\frac{\omega}{LQ^2}\right)$, the LO $\log^2\left(\frac{Q^2}{\mu^{\star 2}}\right)$ and the NLO is easily realized that has a sub-leading energy term with a logarithmic coefficient $\log\left(\frac{Q^2}{\mu^{\star 2}}\right)\log\left(\frac{\omega}{LQ^2}\right)$. Summing all contributions, the logarithmic dependence in Q^2 vanishes. However, we note that the leading NLO term is always independent of Q^2, since there is no analogous term in the all order expansion of the LO piece, thus ensuring that the NLO is always the (power) dominant contribution to the spectrum when $\omega \gg \omega_c$.

In Fig. 3.1 (left) we present the numerical computation of the LO, NLO (already shown in [141]) and the NNLO terms in the IOE. In addition, we present the GLV spectrum. The NNLO term is obtained by direct numerical implementation of Eq. (3.24), and thus this result is only valid for sufficiently large ω (in this case, we summed the first 11 terms of the series; see Fig. 3.1 (right) for the comparison of different truncation values).

The numerical results depict exactly what was argued before. At large ω, the NLO term becomes the dominant contribution to the spectrum. The NNLO at LO lines become almost parallel at large ω, thus showing that these two terms give the same asymptotic contribution (this is not strictly true, since they will differ by sub-leading logarithmic terms). Moreover, we also notice that the actual numerical values assumed by the NNLO curve are at their best only an order of magnitude smaller than the NLO contribution. This shows, that for practical purposes, in this regime, the NLO truncation already offers

an excellent approximation to the full spectrum, and sub-leading corrections do not change the behavior of the IOE/M spectrum.

To sum up, in the high energy spectrum the spectrum takes the form

$$\omega\frac{dI}{d\omega} \sim \underbrace{\omega\frac{dI^{\mathrm{GLV/W}}}{d\omega}}_{O\left(\frac{\omega_c}{\omega}\right)} + \underbrace{\left(\omega\frac{dI^{\mathrm{HO=LO}}}{d\omega} + \omega\frac{dI^{\mathrm{NNLO}}}{d\omega}\right)}_{O\left(\left(\frac{\omega_c}{\omega}\right)^2\right)} + O\left(\left(\frac{\omega_c}{\omega}\right)^3\right) , \tag{3.30}$$

where one understands that each term is expanded to leading order in $\frac{\omega_c}{\omega}$, thus preventing us from writing a strict equality.

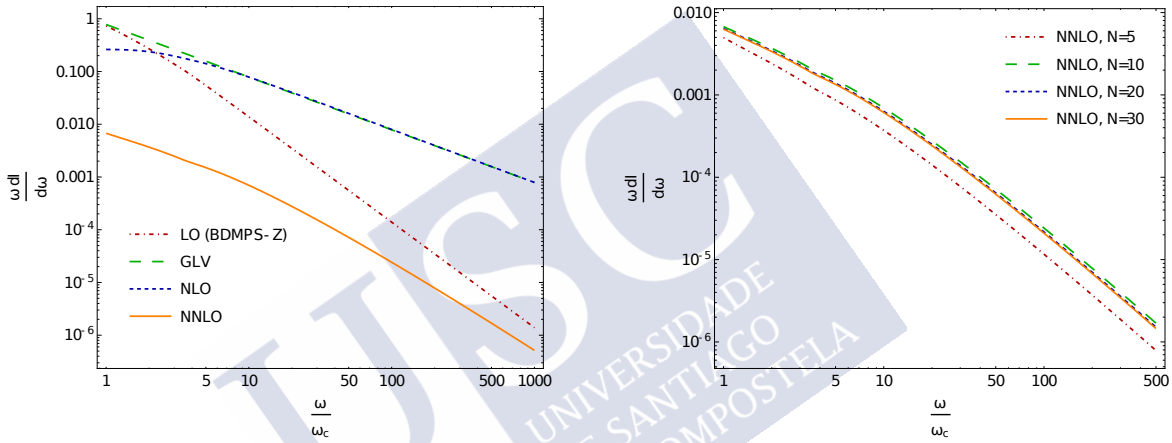

Figure 3.1: **Left:** LO, NLO and NNLO contributions to the spectrum, compared to the GLV/W spectrum, in the high frequency regime ($\omega \gtrsim \omega_c$). We take $\bar{\alpha} = 1$ and use the following set of numerical parameters: $\hat{q}_0 = 0.1$ GeV^3, $\mu_\star = 0.2$ GeV and $L = 6$ fm. The same parameters are used for the remainder of this section, unless otherwise stated and in all plots ω_c is defined using $\hat{q}_0$. Figure taken from [2]. **Right:** The NNLO term computed using Eq. (3.24), changing the cut-off (N) on the summation of the series. We consider N= 5, N= 10, N= 20 and N=30. The plots that follow in the rest of this paper use N= 10, since it shows an extremely good convergence and small computational time.

Now let us consider the opposite limit when $\omega_{\mathrm{BH}} \ll \omega \ll \omega_c$, where the lower bound avoids entering the single soft scattering region, which is not properly described in the IOE/M. Also, formally the BDMPS-Z/ASW solution diverges (slowly) in this regime and thus one must introduce a cut-off scale; the main challenge boils down to the proper treatment of this divergence at each order in the expansion which becomes somewhat more intricate starting at NNLO order. Nonetheless, the correct treatment of the divergences leads the self-consistency of the IOE/M approach and reveals an interesting IR structure, unlike the ultraviolet behavior studied above.

Formally we are taking the limit $\omega \to 0 \equiv \Omega \to (1-i)\times\infty$, while keeping $\log Q^2/\mu^2 \gg$

1. Using the limiting forms

$$\lim_{\omega/\omega_c\to 0}\Omega\frac{\cos(\Omega x)}{\sin(\Omega x)}=i\Omega\quad,\quad\lim_{\omega/\omega_c\to 0}\frac{1}{\Omega}\frac{\sin(\Omega x)}{\cos(\Omega x)}=-\frac{i}{\Omega}\,,\tag{3.31}$$

one can simplify the spectrum significantly. We note however that these limits can not be taken straightforwardly on the functions depending on the time difference $s_1-s_2\equiv\tau$. The support for such functions will be roughly order of the formation time of the gluon, $s_1-s_2\sim t_f$, while $\Omega\sim\frac{1}{t_f}$, thus if one naively applied the above identities one would obtain a divergent result. So the full time dependence is kept in those cases. Thus, in the spectrum, we replace the phases by

$$\lim_{\omega/\omega_c\to 0}k_1^2=k_2^2=\frac{i\omega\Omega}{2}\left(i+\frac{C_{12}}{\Omega S_{12}}\right)\,,\tag{3.32}$$

with σ unchanged. This leads to

$$\begin{aligned}\lim_{\omega/\omega_c\to 0}\frac{dI^{\text{NNLO}}}{d\omega}=-\hat{q}_0^2\frac{\bar{\alpha}}{4}\Bigg[\int_0^L ds_1\int_0^{s_1}ds_2\;\sigma(\Omega(s_1-s_2))\int_{zz'}\log\left(\frac{1}{Q^2z_1^2}\right)\log\left(\frac{1}{Q^2z_2^2}\right)\\ \times z_1^2z_2^2\exp\left[\frac{i\omega\Omega}{2}\left(i+\frac{C_{12}}{\Omega S_{12}}\right)(z_1^2+z_2^2)\right]J_1(z_1z_2\sigma)\Bigg]\,.\end{aligned}\tag{3.33}$$

Changing now the integration variables $(s_1,s_2)\to(s_1,\tau)$ and using that $\tau\sim t_f$, one can further simplify the spectrum. Firstly, since the support of the τ integral is highly localized, the sensitivity to the upper bound should be small, and thus one can replace $L-s_1\to\infty$ (which is consistent that at small frequencies $t_f\ll L$), eliminating one of the time integrations. Secondly, we rescale $\tau\to t=\sqrt{\frac{\hat{q}}{4\omega}}\tau$, in order to factor out all physical scales. Finally, we perform the Wick-rotation $-iT=(1-i)t$, so that the remaining phases no longer have a complex argument. The net result of all these operations is

$$\begin{aligned}\lim_{\omega/\omega_c\to 0}\omega\frac{dI^{\text{NNLO}}}{d\omega}=-2\bar{\alpha}\frac{\hat{q}_0^2}{\hat{q}^2}\sqrt{\frac{\hat{q}}{\omega}}L\Re\Bigg[\int_{TUV}\frac{i}{\sinh(T)}\log\left(\frac{\sqrt{\hat{q}\omega}}{2Q^2V^2}\right)\log\left(\frac{\sqrt{\hat{q}\omega}}{2Q^2U^2}\right)\\ \times U^2V^2J_1\left(UV(1+i)i\frac{1}{\sinh(T)}\right)e^{\frac{-1+i}{2}(\coth(T)+1)(U^2+V^2)}\Bigg]\,,\end{aligned}\tag{3.34}$$

with $U=\left(\frac{\hat{q}\omega}{4}\right)^{1/4}z_1$ and $V=\left(\frac{\hat{q}\omega}{4}\right)^{1/4}z_2$, and where the U and V integrals span the entire real positive axis and the time integral goes up to L. This formula is almost in a simple enough form, except for the $\sqrt{\hat{q}\omega}/Q^2$ dependence. However, we recall that at leading order in energy $Q^2\sim\sqrt{\hat{q}\omega}$, and thus with this choice and using

$$\begin{aligned}\Re\Bigg[\int_{TUV}\frac{-2i}{\sinh(T)}\log\left(\frac{1}{2V^2}\right)\log\left(\frac{1}{2U^2}\right)U^2V^2\\ \times J_1\left(UV(1+i)i\frac{1}{\sinh(T)}\right)e^{\frac{-1+i}{2}(\coth(T)+1)(U^2+V^2)}\Bigg]\approx 0.0293246\,,\end{aligned}\tag{3.35}$$

one finally obtains

$$\lim_{\omega/\omega_c\to 0}\omega\frac{dI^{\rm NNLO}}{d\omega}\sim\bar{\alpha}\left(\frac{\hat{q}_0}{\hat{q}}\right)^2\sqrt{\frac{\hat{q}L^2}{\omega}}=\omega\frac{dI^{\rm LO}}{d\omega}\left(\frac{\hat{q}_0}{\hat{q}}\right)^2. \tag{3.36}$$

Interestingly, we observe that in the small frequency limit and using $Q^2=\sqrt{\omega\hat{q}}\equiv Q_c^2$ the NNLO term reduces to the LO form, multiplied by the expansion parameter (squared since it is the second order term in the expansion). This is unlike the high energy limit, where we saw that the NLO term was (power) enhanced compared to all other orders. In particular, this result means that the spectrum seems to take a rather simple all order form, namely

$$\begin{aligned}\lim_{\omega/\omega_c\to 0}\omega\frac{dI}{d\omega}&=\omega\frac{dI^{\rm LO}}{d\omega}\left(1+\frac{c_{1,0}}{\log\left(\frac{Q_c^2}{\mu_\star^2}\right)}+\frac{c_{2,0}}{\log^2\left(\frac{Q_c^2}{\mu_\star^2 2}\right)}+\cdots\right)\\&=\omega\frac{dI^{\rm LO}}{d\omega}\left(1+\frac{0.508}{\log\left(\frac{Q_c^2}{\mu_\star^2}\right)}+\frac{0.029}{\log^2\left(\frac{Q_c^2}{\mu_\star^2}\right)}+\cdots\right),\end{aligned} \tag{3.37}$$

where the LO term is understood to be taken in the small frequency limit and the $c_{i,0}$ coefficients (where i indicates the power of the logarithmic coefficient) are real numbers computable order by order in perturbation theory. Although we did not find a generic formula that generates them, this is not relevant for the ensuing argument. A major difference between the logarithms $\log\left(\frac{Q_c^2}{\mu_\star^2}\right)$, compared with $\sim\log\omega$ found in the high energy limit, is that they can become large and thus require an all order treatment, while at large energies the strict ordering in powers of energy prevented this from happening. In practice, this means that one must be more careful about the previous expansion, in particularly with respect to how the matching scale is fixed.

Let us explore this question more in depth. If Q is left free, one would have obtained the more general result

$$\begin{aligned}\lim_{\omega/\omega_c\to 0}\omega\frac{dI}{d\omega}&=\omega\frac{dI^{\rm LO}}{d\omega}\left(1+\frac{c_{1,0}+c_{1,1}\log\left(\frac{\sqrt{\omega\hat{q}}}{Q^2}\right)}{\log\left(\frac{Q^2}{\mu^{\star 2}}\right)}\right.\\&\left.+\frac{c_{2,0}-c_{2,1}\log\left(\frac{\sqrt{\omega\hat{q}}}{Q^2}\right)-c_{2,2}\log^2\left(\frac{\sqrt{\omega\hat{q}}}{Q^2}\right)}{\log^2\left(\frac{Q^2}{\mu^{\star 2}}\right)}+\cdots\right)\\&=\omega\frac{dI^{\rm LO}}{d\omega}\left(1+\frac{0.508+0.5\log\left(\frac{\sqrt{\omega\hat{q}}}{Q^2}\right)}{\log\left(\frac{Q^2}{\mu^{\star 2}}\right)}\right.\\&\left.+\frac{0.029-0.026\log\left(\frac{\sqrt{\omega\hat{q}}}{Q^2}\right)-0.028\log^2\left(\frac{\sqrt{\omega\hat{q}}}{Q^2}\right)}{\log^2\left(\frac{Q^2}{\mu^{\star 2}}\right)}+\cdots\right),\end{aligned} \tag{3.38}$$

where again all the numeric coefficients are computable order by order. Here the notation for the coefficients $c_{i,j}$ introduced above becomes evident: the first index denotes the power of the expansion in $\log\left(\frac{Q_c^2}{\mu_\star^2}\right)$, while the second index indicates the dependence on the slower $\log\left(\frac{\sqrt{\hat{q}\omega}}{Q^2}\right)$.

In this form of the spectrum, it seems that the full dependence on Q^2 is unwieldy. However, we know that resuming all orders must yield an expression which is independent of Q^2, because as shown before the dependence on this scale is not physical, but only emerges since we are truncating the IOE/M scheme at a fixed order in perturbation theory. Taking into account all orders is trivial in this limit, since all orders scale with the LO solution, which itself depends on Q^2. Thus, the net effect of the series in $\log\left(\frac{Q_c^2}{\mu_\star^2}\right)$ multiplying the LO spectrum is to cancel this fictitious dependence on the matching scale. This implies that, the full spectrum must take the form

$$\lim_{\omega/\omega_c\to 0}\omega\frac{dI}{d\omega}\equiv\omega\frac{dI^{\mathrm{LO}}}{d\omega}\sqrt{\frac{W(\sqrt{\omega\hat{q}}/\mu_\star^2)}{\log\left(\frac{Q^2}{\mu_\star^2}\right)}}=\bar{\alpha}\sqrt{\frac{\hat{q}_0 W(\sqrt{\omega\hat{q}}/\mu_\star^2)}{\omega}}\,, \tag{3.39}$$

where in the second equality we introduced the W function which resums all orders, and the denominator logarithm cancels explicitly with the implicit logarithm in the LO term. The final equality, makes this explicit, with the only scales being $\hat{q}_0/\omega$ and $\sqrt{\hat{q}\omega}/\mu_\star^2\gg 1$ (recall $\omega\gg\omega_{\mathrm{BH}}$). Again, we reiterate that this results follows from the invariance of the spectrum with respect to Q^2, and can also be obtained by just requiring that the derivative of the full spectrum with respect to $\log Q^2/\mu_\star^2$ is vanishing.

The practical net effect of noticing the invariance of the spectrum with respect to Q^2 and that all orders scale with the LO solution, with some logarithmic enhancement, is to generate the all order equation obeyed by Q^2, we have advertised in the beginning of this section. Let us detail how to construct such an equation.

Going back to Eq. (3.38), let us suppose that Q^2 can be fixed, as in the BDMPS-Z/ASW approach, to some fixed energy scale, namely $Q^2\equiv\hat{q}_0 L$. Then, the logarithms scaling with $\frac{Q^2}{\mu_\star^2}$ are fixed and the evolution with ω is encoded in the logarithms that appear in the numerators. This means that at small enough ω, but still $\omega>\omega_{\mathrm{BH}}$, $\mathrm{N}^m\mathrm{LO}/\mathrm{LO}\sim\log^m\left(\frac{\sqrt{\omega\hat{q}}}{Q^2}\right)\gtrsim 1$, and thus the series will diverge in the infrared. This is not a physical divergence, but rather a fictitious divergence introduced due to the incorrect choice for the matching scale, so that $\omega\sim\hat{q}_0L^2/\log\left(\frac{Q^2}{\mu_\star^2}\right)>\omega_{\mathrm{BH}}\sim\hat{q}\lambda^2$, the series is not well defined since the LO term is constant but all other orders strongly diverge. Thus, unlike the BDMPS-Z/ASW prescription, the matching scale plays an important role in getting the physically meaningful spectrum.

A way to remove this divergence is of course to take $Q^2\equiv Q^2(\omega)$. More concretely, one wants the numerators to remain finite, and thus the natural choice for the matching scale is $Q^2\equiv Q_c^2(\omega)\sim\sqrt{\omega\hat{q}}$, which should guarantee convergence up to around $\omega\sim\omega_{\mathrm{BH}}$. With this choice the numerator logarithms only give small finite contributions to the

spectrum and non-trivial cancellations between different orders in the IOE lead to that at a given truncation, the spectrum only depends on the concrete choice made for Q_c^2 in the first neglected truncated contribution. Again, one quickly realizes that this is the order by order (perturbative) form of requiring that the full spectrum is independent on the matching scale. If different choices of Q_c lead to the difference between the respective spectrums be of the order of the largest considered power in $\log Q^2/\mu_\star^2$, then the overall spectrum would depend on Q^2. We make this observation now evident both analytically in Eq. (3.40) and numerically in Fig. 3.2.

First, consider that we take $Q^2 \equiv a^2 Q_c^2$, where a is dimensionless factor that rescales $Q_c^2 = \sqrt{\omega \hat{q}}$. Then, to leading logarithmic accuracy, Eq. (3.38) becomes

$$\begin{aligned}
\lim_{\omega/\omega_c \to 0} \omega \frac{dI}{d\omega} &= \bar{\alpha} \sqrt{\frac{\hat{q}_0 L^2 \log\left(\frac{Q_c^2 a^2}{\mu_\star^2}\right)}{\omega}} \left[1 + \frac{1}{2} \frac{c_{1,0} - \log\left(a^2\right)}{\log\left(\frac{Q_c^2 a^2}{\mu_\star^2}\right)} + O\left(\log^{-2}\left(\frac{Q^2}{\mu_\star^2}\right)\right)\right] \\
&= \bar{\alpha} \sqrt{\frac{\hat{q} L^2}{\omega}} \left(1 + \frac{1}{2} \frac{\log\left(a^2\right)}{\log\left(\frac{Q_c^2}{\mu_\star^2}\right)}\right) \left[1 + \frac{1}{2} \frac{c_{1,0} - \log\left(a^2\right)}{\log\left(\frac{Q_c^2}{\mu_\star^2}\right)} \left(1 - \frac{\log\left(a^2\right)}{\log\left(\frac{Q_c^2}{\mu_\star^2}\right)}\right)\right. \\
&\quad \left. + O\left(\log^{-2}\left(\frac{Q^2}{\mu_\star^2}\right)\right)\right] \\
&= \bar{\alpha} \sqrt{\frac{\hat{q} L^2}{\omega}} \left[1 + \frac{1}{2} \frac{c_{1,0} - \log\left(a^2\right) + \log\left(a^2\right)}{\log\left(\frac{Q_c^2}{\mu_\star^2}\right)} + O\left(\log^{-2}\left(\frac{Q^2}{\mu_\star^2}\right)\right)\right] \\
&= \bar{\alpha} \sqrt{\frac{\hat{q} L^2}{\omega}} \left[1 + \frac{1}{2} \frac{c_{1,0}}{\log\left(\frac{Q_c^2}{\mu_\star^2}\right)} + O\left(\log^{-2}\left(\frac{Q^2}{\mu_\star^2}\right)\right)\right] = \lim_{\omega \to 0} \left(\omega \frac{dI}{d\omega}\right)_{Q^2 = Q_c^2},
\end{aligned} \tag{3.40}$$

where we neglected the a in the logarithmic correction in the NLO term, since it is easily seen that it only contributes at higher orders. Thus, with the truncation at the NNLO order, we see that different choices for Q^2 contribute only at NNLO order, but not NLO. This is easily seen to generalize to all orders due to the structure of the spectrum in the IR.

Perhaps more illuminating is to repeat the same exercise but by numerically evaluating the spectrum. In Fig. 3.2 we compute the spectrum at NLO accuracy, fixing the scale $Q^2 \equiv Q_c^2$ and then varying it by factors of 2. At low energies, we observe that although the LO and NLO terms change dramatically as the choice for the matching scale varies, we observe that the overall LO+NLO spectrum remains roughly the same, in accordance with the previous discussion. Also, compared to the case where one sets the matching to a constant value, we observe that the spectrum does not have any divergence, as long as $\omega > \omega_{\mathrm{BH}}$. Another important remark is that the choice for Q^2 shows that the interpolation between the BDMPS-Z/ASW (multiple soft) and GLV/W (single hard) regimes is not

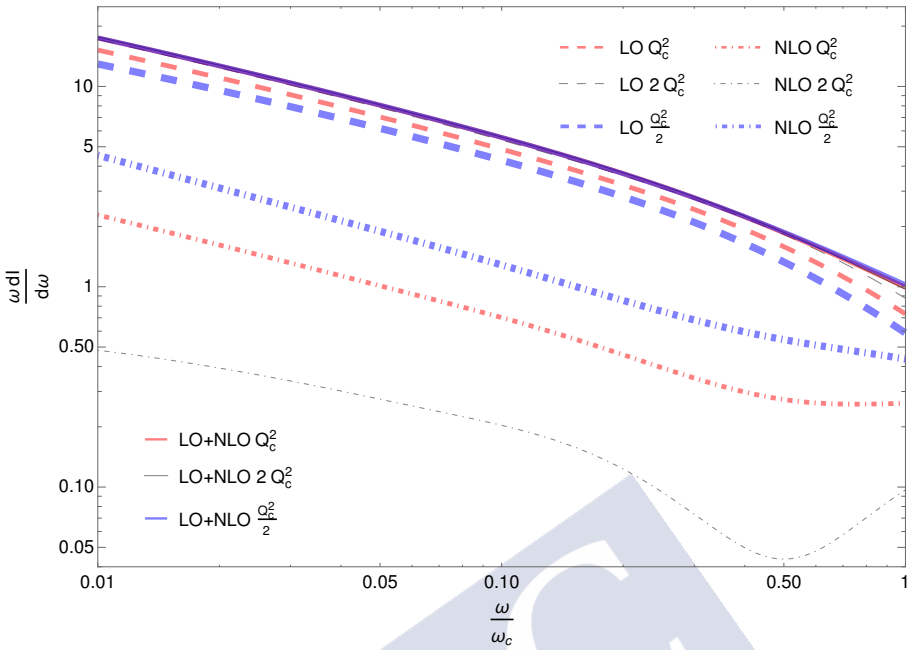

Figure 3.2: Calculation of the IOE at NLO accuracy, while fixing the matching scale $Q^2 = Q_c^2 = \sqrt{\hat{q}\omega}$ and varying this by $Q_c^2 \to 2Q_c^2$ or $Q_c^2 \to \frac{1}{2}Q_c^2$, where $\hat{q} = \hat{q}_0 \log\left(\frac{Q_0^2}{\mu^2}\right)$ and $Q_0^2 = \hat{q}_0 L$. Figure taken from [2].

trivial, i.e. one can not just fix a scale below/above which the appropriate spectrum is selected.

Another important aspect is to understand the importance of the NNLO term as the ratio between the large and small scales in the problem, $Q^2/\mu_\star^2$, evolves. This measures the sensitivity of the spectrum to the BH frequency $\omega_{\rm BH} \sim \mu_\star^4/\hat{q}_0$. Clearly if $Q^2 \to \mu_\star^2$ (or equivalently $\omega \to \omega_{\rm BH}$), the series diverges order by order, in accordance with our initial assumptions. To make this study more systematic beyond this limiting case, we take Eq. (3.37), normalizing to the LO result, obtaining

$$\lim_{\omega/\omega_c \to 0} \omega \frac{dI}{d\omega}_{\rm norm.} = 1 + \left(\frac{0.508}{\beta}\right) + \left(\frac{0.029}{\beta^2}\right) , \tag{3.41}$$

with $\beta = \log\left(Q_c^2/\mu_\star^2\right) = \frac{1}{2}\log(\omega/\omega_{\rm BH})$. Comparing the NNLO term to the LO+NLO piece boils down to studying

$$\frac{Q_c^2}{\mu^{\star 2}} = \exp\left(-0.254 + 0.002\sqrt{16129 + \frac{7256}{\alpha}}\right) , \tag{3.42}$$

where $\alpha \equiv \frac{\rm NNLO}{\rm 1+NLO}$ gives the percentile contribution of the NNLO term compared to the LO+NLO (up to NNNLO corrections). This relation can be written just in term of the

gluon frequency scales (using $\omega_{\rm BH} \equiv \mu_\star^4/\hat{q}_0$ and $Q^2/\mu_\star^2 = \sqrt{\omega/\omega_{\rm BH}}$), to give

$$\omega = \exp\left(-0.508 + 0.004\sqrt{16129 + \frac{7256}{\alpha}}\right)\omega_{\rm BH}\,, \tag{3.43}$$

where we only take the root which is physically meaningful. If $\alpha = 1\%$, $\omega \geq 18.83\ \omega_{\rm BH}$; $\alpha = 10\%$, $\omega \geq 1.98\,\omega_{\rm BH}$ and $\alpha = 50\%$, $\omega \geq 1.21\ \omega_{\rm BH}$, where the inequality is due to the fact that we are only looking at the lower bound, below which the ratio NNLO/(1 + NLO) exceeds the value of α. The evolution in α is rather fast, ensuring that roughly after $O(10\omega_{\rm BH})$, the obtained spectrum is already quite accurate and insensitive to the infrared details.

This aspect was perhaps better elucidated in recent results from parallel efforts to compute the single gluon emission spectrum exactly, by solving the associated Boltzmann equation [3,4]. In Fig. 3.3, we reproduced one of the numerical results shown in [4], where the IOE/W approach is compared against the exact solution for the spectrum. One can clearly see that at roughly $\sim 10\,\omega_{\rm BH}$ the spectrum breaks down, inline with our estimates. In addition, the work done in [4] confirms the analytic behavior of the full spectrum is identical in the two regions explored in this chapter, thus showing that the LO+NLO accuracy spectrum provides a good approximation to the spectrum, going beyond the BDMPS-Z/ASW and GLV/W limitations.

In summary, in the soft regime, the full spectrum can be written as

$$\omega\frac{{\rm d}I}{{\rm d}\omega{\rm d}L} = \bar{\alpha}\sqrt{\frac{\hat{q}_{\rm eff}(Q_c)}{\omega}}\,, \tag{3.44}$$

where the effective transport coefficient is calculated to NNLO in the IOE/M framework to give

$$\hat{q}_{\rm eff}(Q_c) = \hat{q}_0 \log\left(\frac{Q_c^2}{\mu^{\star 2}}\right)\left[1 + \frac{1.016}{\log\left(\frac{Q_c^2}{\mu^{\star 2}}\right)} + \frac{0.316}{\log^2\left(\frac{Q_c^2}{\mu^{\star 2}}\right)} + \mathcal{O}\left(\log^{-3}\left(\frac{Q_c^2}{\mu^{\star 2}}\right)\right)\right]\,, \tag{3.45}$$

and the matching scale is determined by the transcendental relation

$$Q_c^2 = \sqrt{\hat{q}_0\,\omega \log\left(\frac{Q_c^2}{\mu^{\star 2}}\right)}\,. \tag{3.46}$$

3.1.3 A brief summary

Fig. 3.4 summarizes the findings presented in this section. At large frequencies $\omega \gg \omega_c$, the NLO contribution to the IOE/M spectrum dominates, matching the GLV/W result. The NNLO and LO terms are seen to contribute at the same power suppressed order. At small frequencies $\omega_{\rm BH} \ll \omega \ll \omega_c$, the dominant term is the LO contribution, with the

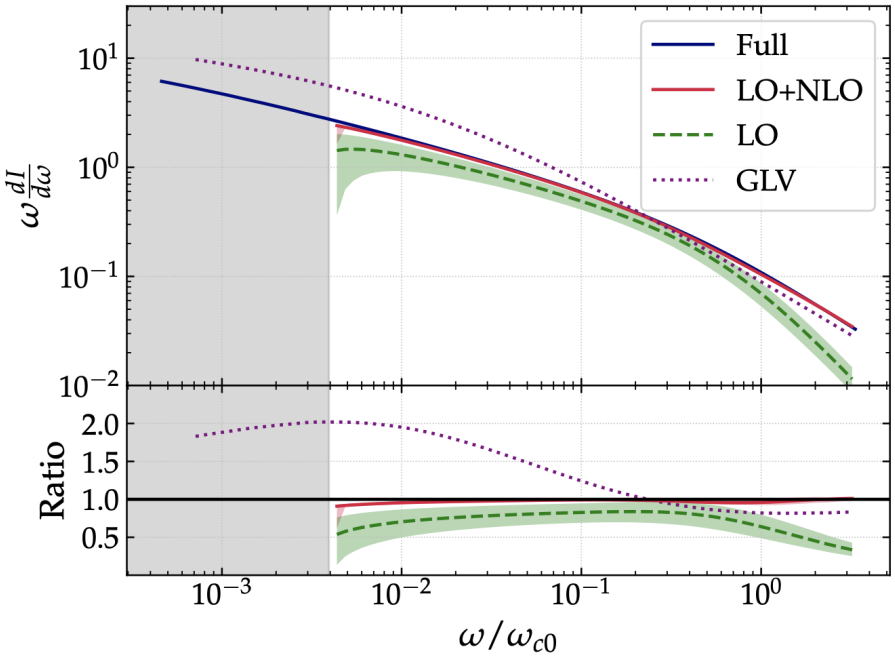

Figure 3.3: Comparison between the full emission spectrum (Full) computed in [3,4], the IOE/W result up to NLO and the GLV/W results. The gray band denotes the BH region, where the IOE is not valid. Figure taken from [5], with $\omega_{c0} = \hat{q}_0 L^2$. See reference for the values used for the physical constants.

NNLO term giving a small correction. As a consequence, one finds that truncating the IOE/M series at NLO accuracy gives a good approximation to the full emission spectrum, outperforming the GLV/W and BDMPS-Z/ASW solutions.

In Fig. 3.4 we have used the matching scale Q_c^2, thus ensuring that the spectrum is well behaved at small frequencies; at large frequencies the form of the matching is less relevant. In particular, this shows that the matching between the GLV/W and BDMPS-Z/ASW regions is not straightforward, but rather it requires a detailed treatment to avoid fake divergences in the spectrum. More importantly, the study shown in this chapter guarantees that the IOE/M is well defined at higher orders in opacity and is thus a legitimate analytic strategy to compute the medium induced gluon spectrum.

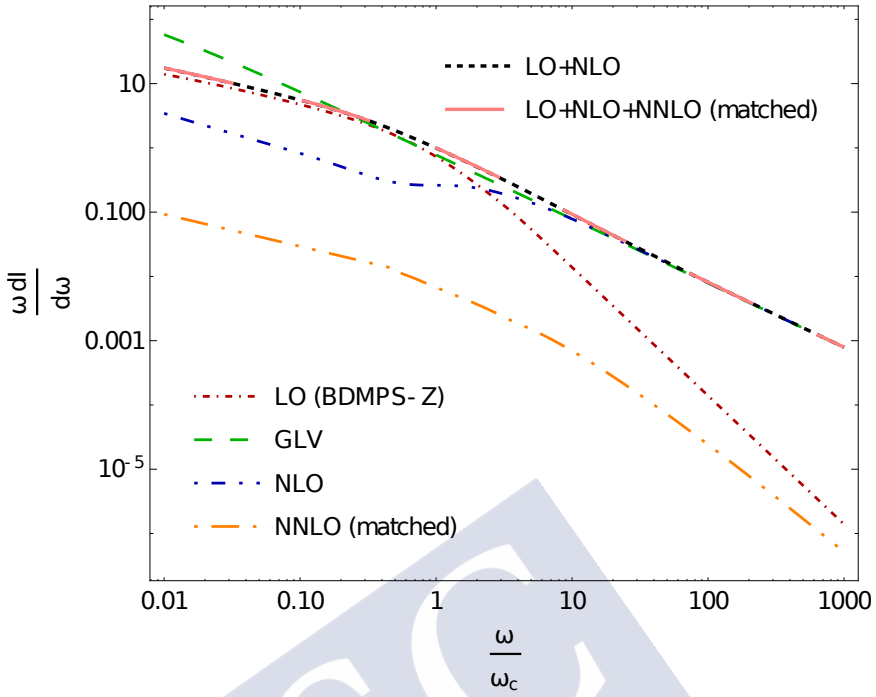

Figure 3.4: Comparison between BDMPS-Z/ASW, GLV/W and IOE/M up to NNLO accuracy in the MS and SH frequency domain. The NNLO term is computed in the asymptotic regions and matched at $\omega \sim \omega_c$. Figure taken from [2].

3.2 IOE/M approach to momentum broadening

The IOE/M approach can also be applied to momentum broadening. More generally, one can apply the IOE to any n-point function made out of propagators G, as long as a Dyson-like relation is known for such objects and there is a closed form solution in the MS regime.

The discussion in this section follows from the results in section 2.3. Here we will work mainly at LT accuracy, but we study the contributions coming from the NLT terms.

3.2.1 IOE/M broadening distribution at LT accuracy

We again consider the decomposition given in Eq. (3.1) and apply it directly to Eq. (2.54). Expanding in powers of δv results in the following LT momentum broadening distribution

$$\mathcal{P}^{\mathrm{LT}}(\boldsymbol{k}, L) = \sum_{n=0}^{\infty} \int_{\boldsymbol{x}} \mathrm{e}^{-i\boldsymbol{x}\cdot\boldsymbol{k}} \mathrm{e}^{-\frac{1}{4}\boldsymbol{x}^2 Q_s^2} \frac{(-1)^n Q_{s0}^{2n}}{4^n n!} \boldsymbol{x}^{2n} \log^n \frac{1}{\boldsymbol{x}^2 Q^2} \equiv \mathcal{P}^{\mathrm{LO}} + \mathcal{P}^{\mathrm{NLO}} + \mathcal{P}^{\mathrm{NNLO}} + \cdots , \tag{3.47}$$

where we note that the IOE/M scheme results in an expansion in powers of $\sim Q_{s0}^2 \boldsymbol{x}^2 \gg \mu_\star^2 \boldsymbol{x}^2$. Here we define the *dressed* saturation scale equivalently to the Q_c[3] scale introduced in the previous sections

$$Q_s^2 \equiv \langle \boldsymbol{k}^2 \rangle_{\text{typ}} = \hat{q}_0 L \, \log \frac{Q^2}{\mu_\star^2} \,, \tag{3.48}$$

which trivially relates to the matching scale

$$Q^2 = a Q_s^2 \,, \tag{3.49}$$

where we always take $a = 1$ in what follows, corresponding to Molière's prescription [149]. Although other values for a were studied, they do not seem to lead to any better numerical results. Additionally, in the previous section we showed that varying a only leads to sub-leading contributions. We also define the *effective* jet quenching parameter

$$Q_s^2 = \hat{q}_0 L \, \log \frac{a Q_s^2}{\mu_\star^2} \,, \tag{3.50}$$

with the *bare* jet quenching parameter $\hat{q}_0$, associated to the *bare* saturation scale $Q_{s0}^2 = \hat{q}_0 L$.

It is easy to check that truncating Eq. (3.47) still preserves $\int_{\boldsymbol{k}} \mathcal{P}(\boldsymbol{k}) = 1$, since all terms but the LO vanish once integrated over $\boldsymbol{k}$ and $\boldsymbol{x}$. Formally, the series is divergent. However, one must recall that this divergence is in the full LT case also present if the potential is not regulated in the infrared. Thus, the regulation of the integral translates into a truncaton of the series, $n < n_{\max} \sim Q_{s0}^2/\mu_\star^2$, with higher order terms being divergent (see [126] for a similar conclusion). As for the gluon spectrum, the expansion parameter is given by

$$\lambda \equiv \frac{\hat{q}_0}{\hat{q}} = \frac{1}{\log(Q^2/\mu_\star^2)} \ll 1 \,. \tag{3.51}$$

The momentum distribution $\mathcal{P}$ can be formally recast as

$$(4\pi)^{-1} Q_s^2 \, \mathcal{P}(\boldsymbol{k}, L) \equiv f\,(x, \lambda) = \sum_{n=0}^{\infty} \lambda^n f^{(n)}(x) \,, \tag{3.52}$$

where $x \equiv \boldsymbol{k}^2/Q_s^2$. The LO term reads

$$f^{(0)} = (4\pi)^{-1} \, Q_s^2 \, I_1(x) = \mathrm{e}^{-x} \,, \tag{3.53}$$

[3] If one wants to merge broadening and the energy spectrum, a sensible prescription to select either Q_c or Q_s has to be made, see [151,152]. Importantly, Q_s is independent of energy, and thus this prescription does not cancel any divergences at small frequencies.

while the NLO contribution gives [149]

$$\begin{aligned}\lambda f^{(1)} &= -\frac{1}{16\pi}Q_{s0}^2 Q_s^2 \int_{\boldsymbol{x}} \mathrm{e}^{-i\boldsymbol{x}\cdot\boldsymbol{k}}\mathrm{e}^{-\frac{1}{4}Q_s^2\boldsymbol{x}^2}\,\boldsymbol{x}^2 \log\frac{1}{\boldsymbol{x}^2Q^2} \\ &= \frac{Q_s^4}{16\pi}\lambda\vec{\nabla}_{\boldsymbol{k}}^2 \int_{\boldsymbol{x}} \mathrm{e}^{-i\boldsymbol{x}\cdot\boldsymbol{k}}\mathrm{e}^{-\frac{1}{4}Q_s^2\boldsymbol{x}^2}\,\log\frac{1}{\boldsymbol{x}^2Q^2} \\ &= \frac{\lambda Q_s^2}{4\pi}\frac{\partial}{\partial x}x\frac{\partial}{\partial x}\,I_2(x,a) \\ &= \lambda\,\Delta_x\, e^{-x}\,\left(\mathrm{Ei}\,(x) - \log(4x\,a)\right)\,,\end{aligned} \tag{3.54}$$

where we used the reduced Laplacian operator $\Delta_x \equiv \partial_x(x\,\partial_x)$ and $\vec{\nabla}_{\boldsymbol{k}}^2 = 4/Q_s^2\Delta_x$ with $x \equiv \boldsymbol{k}^2/Q_s^2$. The special integrals $I_1(x)$ and $I_2(x,a)$ are detailed in appendix 3.A. Putting all LO and NLO contributions together, we recover Molière's [149, 150] formula (derived in QED)

$$\mathcal{P}^{\mathrm{LO+NLO}}(\boldsymbol{k},L) = \frac{4\pi}{Q_s^2}\mathrm{e}^{-x}\Big\{1-\lambda\left(\mathrm{e}^x - 2 + (1-x)\,\left(\mathrm{Ei}\,(x) - \log(4x\,a)\right)\right)\Big\}\,, \tag{3.55}$$

with $x \equiv \frac{\boldsymbol{k}^2}{Q_s^2}$.

By construction, for $\boldsymbol{k}^2 \ll Q_s^2$, we recover the MS solution, which is flat in $\boldsymbol{k}^2$. In the opposite limit, when $\boldsymbol{k}^2 \gg Q_s^2$, the LO term decays exponentially and is thus suppressed. The typical momentum transfer due to this piece is then $\langle\boldsymbol{k}^2\rangle_{\mathrm{typ}} \sim Q_s^2$, in accordance with previous discussions.

The NLO piece can be simplified in the high energy limit using the (divergent) asymptotic expansion $x \to \infty$, $\mathrm{Ei}(x) \approx \mathrm{e}^x(1/x + 1/x^2 + 2/x^3)$, which reduces the NLO to

$$\mathcal{P}^{\mathrm{NLO}}(\boldsymbol{k},L)\Big|_{\boldsymbol{k}^2\gg Q_{s0}^2} = 4\pi\frac{Q_{s0}^2}{\boldsymbol{k}^4} + O\left(\frac{Q_{s0}^4}{\boldsymbol{k}^6}\right)\,. \tag{3.56}$$

This is exactly the asymptotic SH behavior seen in section 2.3 (Eq. (2.56)), encoding the hard $1/\boldsymbol{k}^4$ Coulomb tail. As for the energy spectrum, the LO term is suppressed in the distribution tail, and thus the NLO becomes the dominant contribution. In the opposite limit, for small momentum transfers we have that the NLO piece reduces to

$$\mathcal{P}^{\mathrm{NLO}}(\boldsymbol{k},L)\Big|_{\boldsymbol{k}^2\ll Q_{s0}^2} = \frac{4\pi\lambda}{Q_s^2}\log(4\,a\,\mathrm{e}^{1-\gamma_E})\,, \tag{3.57}$$

which, up to logarithms, is just the MS solution suppressed by a power of λ, analogous to the behavior we observed for the gluon spectrum in the previous section, ensuring that LO+NLO contribution is well behaved.

In conclusion, using the LO+NLO terms in the IOE/M scheme to compute $\mathcal{P}$, one is capable of capturing the correct physics at small and large $\boldsymbol{k}$, thus outperforming the MS and SH approximations. This can be seen in Fig. 3.5 left, where we plot the LO,

NLO and LO+NLO terms, comparing to the full solution using the GW model. We take a small value for $\lambda = 0.1$, so that the we are well within the region of validity of the IOE/M scheme. As detailed, we observe that the LO+NLO solution qualitatively captures the correct behavior of the full distribution, while the LO (MS) term completely fails to describe the hard tail, leading to a too strong suppression of the tails.

In Fig. 3.5 (right), we study the behavior of the IOE/M framework as λ increases, also including the NNLO (numerically computed) corrections to estimate how significant they are. The values of λ explored correspond roughly to the values at LHC, RHIC and the future EIC, in increasing order. We observe that at $\lambda = 0.2$ there are already 40% deviations with respect to the exact result, and thus at higher values one expects the IOE/M approach require higher order corrections beyond NLO. Indeed, in the bottom panel we observe that including the NNLO term leads to a significant improvement of the results. This seems to be in contradiction with the findings of the previous sections, where we found NNLO corrections to the energy spectrum to be suppressed by at least an order of magnitude. We recall however that the broadening and energy spectrum depend on different two-point functions, and such a direct comparison is not entirely meaningful. For the *best* choice for $\lambda = 0.1$, we observe that at NLO the IOE/M solution is already quite close to the full GW result, with the larger deviations coming from the regions which will contribute less to any integrated quantities. We see however, that at small $\boldsymbol{k}$ there is a constant deviation with respect to the GW model, which in the MS approach is never present since one can adjust Q^2 (not a matching scale) in that case to reproduce the exact results in the small $\boldsymbol{k}$ region; this deviation is nonetheless not extremely relevant in practice.

3.2.2 The role of NLT terms in the IOE/M expansion

In the previous section, we have fixed the accuracy of the expansion at NLO in the IOE/M scheme and at LT in the expansion of the dipole cross-section. In this section, we explore the contributions due to NLT contributions, making use of the discussion introduced in section 2.3. We recall that these are two competing expansions, one in powers of $Q_{s0}^2 \boldsymbol{x}^2$ and the other in powers of $\mu_\star^2 \boldsymbol{x}^2$, thus one expects that the twist expansion plays a minor role. In this section we fix $Q_s^2 = Q_{s0}^2 = 4.8$ GeV^2, so that we are only sensitive to the infrared corrections due to the NLT term.

Using the LT+NLT form for the dipole cross-section introduced in section 2.3, we first compare the LT+NLT broadening distributions to the full GW and HTL results, see Fig. 3.6. As shown in appendix 3.C, at large values of the IR regulator, the LT map fails to reproduce the exact result. This is due to the fact that in such cases λ is large and thus higher orders in the IOE/M expansion need to be taken into account. We note that for both models the LT+NLT result is remarkably close the LT one, thus ensuring a minimal dependence on the IR details of each potential (recall that the NLT contribution is not universal, see section 2.3). Thus, this suggests that jet quenching phenomenology should have little sensitivity to the non-perturbative model dependent details of the scattering

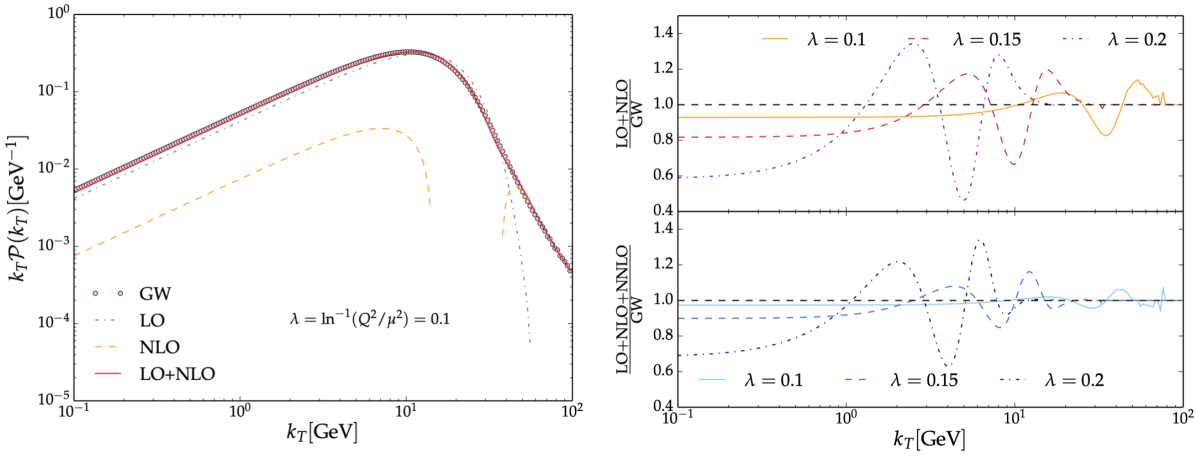

Figure 3.5: **Left**: Momentum broadening probability distribution obtained from the IOE/M scheme (LO,NLO and LO+NLO contributions), compared to the full GW model solution. Here we take $\lambda = 0.1$ corresponding to ($Q_{s0}^2 = 30$ GeV^2, $m_D^2 = 0.13$ GeV^2). In this and following figures $k_T \equiv |\boldsymbol{k}|$. **Right, Top**: ratio between the LO+NLO result and the exact GW for $\lambda = 0.1, 0.15, 0.2$. **Right Bottom**: same but for the LO+NLO+NNLO result. $\lambda = 0.15, 0.2$ corresponds to ($Q_{s0}^2 = 4$ GeV^2, $m_D^2 = 0.3$ GeV^2), ($Q_{s0}^2 = 4$ GeV^2, $m_D^2 = 0.5$ GeV^2), respectively. Figures taken from [6].

potentials. We note however that the GW comparison leads to a larger discrepancy between the LT and LT+NLT curves. This can be traced back to the fact that we fix m_D and the use the universal map to generate the respective μ. This map is only valid at LT accuracy and thus, it is expected that larger deviations occur in the GW result.

Finally, we incorporate the NLT expansion into the IOE/M approach by shifting the expansion point $v^{\rm MS}(\boldsymbol{x}) \to v^{\rm MS}(\boldsymbol{x}) + v^{\rm NLT}(\boldsymbol{x})$ and continue treating $\delta v(\boldsymbol{x})$ as a perturbation. An analytic treatment Eq. (3.47) to NLO is possible if one also notices that the NLT corrections are always small when compared to the NLO ones, and thus one can also keep track of corrections up to linear order in $\mu_\star^2$. The respective broadening distribution is given by

$$\mathcal{P}^{\rm NLO+\delta NLT}(\boldsymbol{k}, L) = \lambda \Delta_x \, I_2(x, a) - \frac{32\lambda\mu_\star^2}{c_1 Q_s^2} \Delta_x^2 \, I_2\left(x, \frac{\mu_\star^2}{\sqrt{c_2} Q_s^2}\right) , \tag{3.58}$$

where δNLT denotes that we also expand to linear order the non-universal contribution. Notice that $\mathcal{P}$ is no longer just a function of λ, but it depends explicitly on $\mu_\star^2$ and the coefficients c_1 and c_2 (see section 2.3), thus showing that indeed the result is model dependent. In Fig. 3.7 we compare the LO+NLO+NLT[4] distribution $\mathcal{P}$ to the GW (top) and HTL (bottom) exact results. We clearly observe that the effect of including the NLT

[4]Here we do not use the linearized version δNLT, although it was numerically checked that the difference to the figure shown is negligible.

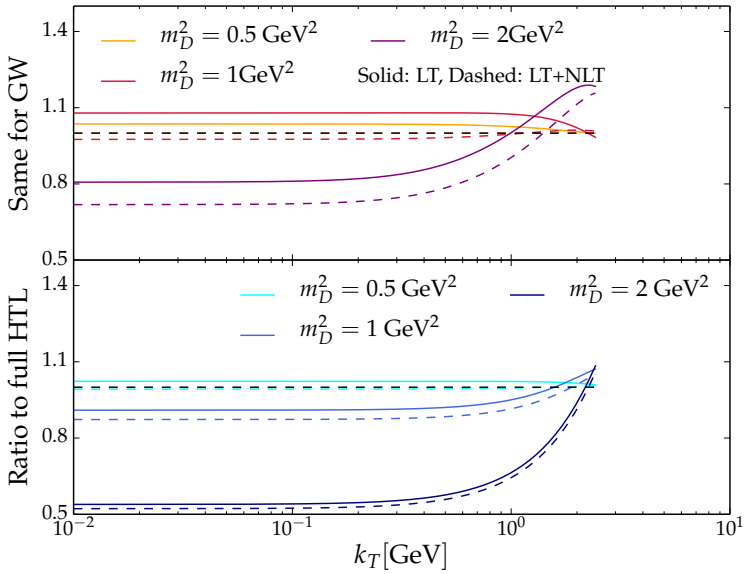

Figure 3.6: Ratio between the LT (solid) and NLT expansions to the full GW (top) and HTL (bottom) potentials for different values of m_D^2. The orange, dashed line in the top panel fully overlaps with the reference black line denoting unity. Figure taken from [6].

contribution is always smaller than 3%, only becoming relevant for already relatively large values of m_D. This confirms the small dependence on the infrared modeling, although the agreement at small $|\boldsymbol{k}|$ to the exact solution increases by including the NLT term, as expected.

3.2.3 Broadening distribution in the IOE/M approach at LHC, RHIC and EIC

In this final section, we apply the IOE/M scheme at NLO accuracy, in the parameter region to be explored at LHC, RHIC and EIC. We fix the medium length $L = 6$ fm roughly corresponding to the radius of both Pb and Au nuclei. For RHIC and LHC, we use the same temperature estimate as the one in [153], and we assume the medium can be described by the HTL model (the temperature is fixed, with no time evolution). The saturation scale Q_{s0}^2 is then deduced using $\hat{q}_0 = 18\pi\alpha_s^2 T^3$, where we take $\alpha_s = 1/\pi$. For the EIC, the HTL model can not be directly applied since the medium is not thermal[5]. The relevant scale probed the propagating parton is size of the nucleons, we take to be of order $1/\Lambda_{\rm QCD}$. Thus, in the GW model, one obtains that $\mu = \Lambda_{\rm QCD} = 200\,\text{MeV}$ and using the estimate provided in [154] in the context of Color Glass Condensate physics,

[5]We note however that at LT order there is no difference between the GW and HTL models, and thus one could simply consider one of them.

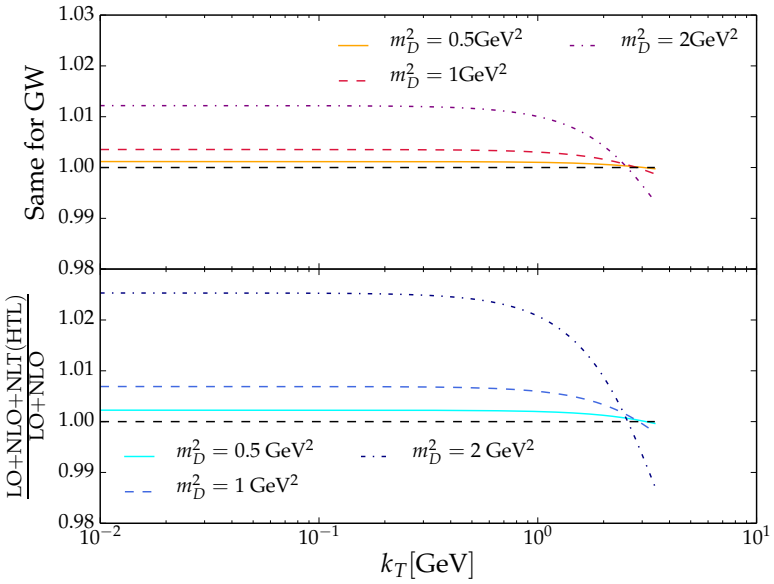

Figure 3.7: Comparison between HTL/GW to LO+NLO+NLT broadening distributions for different values of m_D^2. Figure taken from [6].

we obtain $\hat{q}_0 L = 0.35\,\text{GeV}^2$, similar to the values used in [155]. The values used in result shown in Fig. 3.8 are detailed in table 3.1.

Table 3.1: Relevant parameters for the three different setups.

Collider	T[MeV]	m_D^2 [GeV^2]	Q_s^2[GeV^2]	$\hat{q}$ [GeV^2/fm]	λ
LHC	470	1.33	120.2	20.03	0.15
RHIC	360	0.78	51.5	8.58	0.16
Collider	μ[MeV]	$\mu_\star^2$[GeV^2]	Q_s^2[GeV^2]	$\hat{q}$ [GeV^2/fm]	λ
EIC	200	0.01	1.8	0.29	0.2

For the LHC results, we observe that the IOE/M approximation captures the GW solution up to a 5% accuracy at $|\boldsymbol{k}| > 20$ GeV, while the LO term fails to describe this region. The universal map between potentials leads to minimal differences between the GW and HTL models, as expected for this set-up. In the IR, we see that for $|\boldsymbol{k}| < 1$ GeV there is a $\sim 20\%$ deviation for the LO+NLO term that gets greatly improved by the LO+NLO+NNLO term, as observed in the previous sections. Around the peak there is a 15% deviations to the exact solution, which get improved when adding the NNLO term. We note that although these fluctuations disappear in the case of the LO approach (by adjusting Q^2), this is at the cost of losing the hard tail, which is physically meaningful. Plus, for a phenomenological application, this fluctuations will not dominate the physics or the uncertainty of the result. Similar results are found for RHIC, the

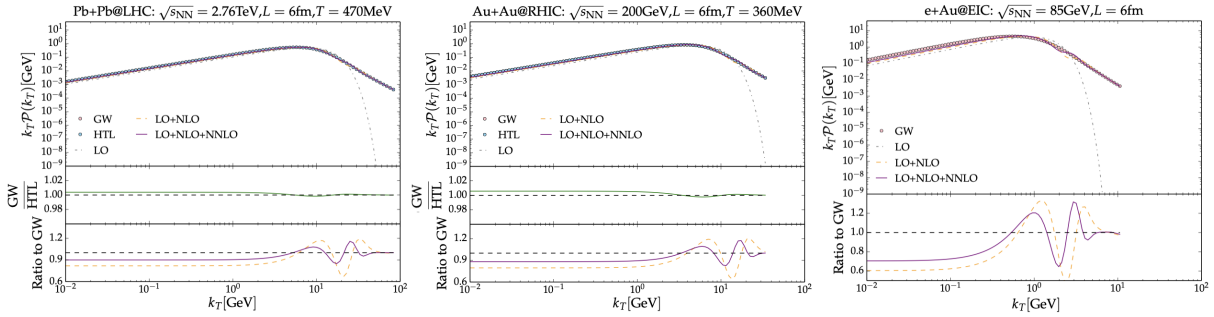

Figure 3.8: Results obtained for the expected parameters selection at LHC (left), RHIC (center) and EIC (right), see table 3.1. For LHC and RHIC, we plot the momentum distribution for the GW and HTL models, and for the LO, LO+NLO and LO+NLO+NNLO terms in the IOE/M approach (top). The middle panel shows the ratio between the GW and HTL models using the universal map in Eq. 2.48 and the bottom panel shows the LO+NLO (orange) and LO+NLO+NNLO (purple) to the GW result. For EIC, the legend is the same, except we do not provide a comparison to the GW model. Figure taken from [6].

most important difference being a more noticeable distinction between the GW and HTL results, due the to larger λ value. For the EIC set-up we find a *dressed* saturation scale $Q_s^2 = 1.8\,\mathrm{GeV}^2$, justifying the application of the GW model and perturbation theory. Although the value the saturation scale is significantly smaller, so is the IR scale, due to the fact that the expected medium is not a thermal plasma but rather a dense cold gluonic system. Thus, we observe that although the value for λ is slightly larger, its evolution is slow. Nonetheless, the application of the IOE/M approach is less successful in this set-up and it is better suited for only semi-quantitative analysis.

3.2.4 A brief summary

In this section we have shown that using the IOE/M approach to computing the single particle momentum broadening distribution leads at NLO accuracy to a closed form expression that captures both the MS and SH regimes. The major result of this section, Eq. (3.55), was already known to Molière 70 years ago (in the QED context), and it is surprising that for so long phenomenological studies either focus on the MS, SH regimes or treat the problem exactly. A downside of the IOE/M approach is that it requires a big separations between the hard (Q_s^2) and soft ($\mu_\star^2$) scales in the problem. We observed that this is well satisfied in the LHC and RHIC regimes, but it does not hold so well for EIC conditions.

A secondary result in the previous study was the realization that non-perturbative and model dependent contributions to the broadening distribution seem to have a very small effect, specially when compared with higher order contributions in the IOE/M scheme. The reason for this is the fact that the IOE/M is an expansion in $Q_{s0}^2\boldsymbol{x}^2$, while the model

dependent contributions come from an expansion in $\mu_\star^2 \boldsymbol{x}^2$. Thus, if one uses the map given in Eq. (2.48), a meaningful and controllable comparison between models for the in-medium scattering cross-sections is possible, unlike previous approaches [127].

3.A Useful integrals to compute the NLO broadening term in the IOE/M approach

In this appendix, we compute the two Fourier integrals used to compute the single particle broadening distribution in the IOE/M scheme. They read

$$I_1 = \int_{\boldsymbol{x}} \mathrm{e}^{-i\boldsymbol{x}\cdot\boldsymbol{k}}\, \mathrm{e}^{-\frac{1}{4}Q_s^2\,\boldsymbol{x}^2}\ , \tag{3.59}$$

and

$$I_2 = \int_{\boldsymbol{x}} \mathrm{e}^{-i\boldsymbol{x}\cdot\boldsymbol{k}}\ \mathrm{e}^{-\frac{1}{4}Q_s^2\,\boldsymbol{x}^2}\, \log\frac{1}{Q^2\boldsymbol{x}^2}\,. \tag{3.60}$$

I_1 is trivial to obtain since it is Gaussian

$$I_1(x) = \frac{4\pi}{Q_s^2}\,\mathrm{e}^{-x}\,. \tag{3.61}$$

with $x = \boldsymbol{k}^2/Q_s^2$. I_2 requires one to decompose the logarithm as the sum of two indefinite integrals

$$\log\frac{1}{\boldsymbol{x}^2Q^2} = -\lim_{\epsilon\to 0}\int_\epsilon^\infty \frac{dt}{t}\left(\mathrm{e}^{-t} - \mathrm{e}^{-\boldsymbol{x}^2Q^2t}\right)\,. \tag{3.62}$$

This representation is particularly useful since it reduces the computation of a hard integral to the sum of two Gaussian integrations. Using $a = Q^2/Q_s^2$

$$\begin{aligned} I_2 &= -I_1\int_\epsilon^\infty \frac{dt}{t}\mathrm{e}^{-t} + \int_\epsilon^\infty\frac{dt}{t}\int_{\boldsymbol{x}}\mathrm{e}^{-i\boldsymbol{x}\cdot\boldsymbol{k}}\mathrm{e}^{-\frac{1}{4}(1+4at)Q_s^2\boldsymbol{x}^2} \\ &= -I_1\int_\epsilon^\infty\frac{dt}{t}\mathrm{e}^{-t} + \frac{4\pi}{Q^2}\int_\epsilon^\infty\frac{dt}{t(1+4at)}\,\mathrm{e}^{-\frac{\boldsymbol{k}^2}{(1+4at)Q_s^2}}\,. \end{aligned} \tag{3.63}$$

Performing the change of variables $u + x = x/(1+4at)$, the last integral in Eq. (3.63) yields

$$-\mathrm{e}^{-x}\int_{-x}^{-4ax\epsilon}\frac{du}{u}\mathrm{e}^{-u} = \mathrm{e}^{-x}\left[\mathrm{Ei}(x) - \mathrm{Ei}(4ax\epsilon)\right]\,. \tag{3.64}$$

Taking the limit $\epsilon\to 0$, the first term in Eq. (3.63) and the last term in Eq. (3.64) combine to give

$$-\int_\epsilon^\infty\frac{dt}{t}\mathrm{e}^{-t} - \mathrm{Ei}(4ax\epsilon) = \mathrm{Ei}(\epsilon) - \mathrm{Ei}(4ax\epsilon) = -\log 4ax\ + O(\epsilon)\,, \tag{3.65}$$

where we used that $\mathrm{Ei}(\epsilon)\simeq\gamma_E + \log\epsilon$, with $\gamma_E = 0.577(2)$ the Euler-Mascheroni constant. Putting back in the I_1 overall factor, one obtains the exression in the main text

$$I_2(x,a) = I_1(x)\Big[\mathrm{Ei}(x) - \log 4ax\Big]\,. \tag{3.66}$$

3.B Kinetic formulation of momentum broadening

In the main text, the momentum broadening distribution was computed by solving the associated kinetic equation in Fourier space. Nonetheless, we observed that the kinetic formulation somehow better displays the underlying physics, and thus it would be interesting to see how it simplifies in the MS, SH and IOE/M solutions.

One can write Eq. (2.33) as

$$\frac{\partial}{\partial L}\mathcal{P}(\boldsymbol{k},L)=-\int_{\boldsymbol{q}}v(\boldsymbol{q})\mathcal{P}(\boldsymbol{k}-\boldsymbol{q},L)\,. \tag{3.67}$$

In the SH regime, this equation can be solved iteratively and only the first iteration contributes. It reads in that case

$$\mathcal{P}^{\mathrm{SH}}(\boldsymbol{k},L)=-\int_{\boldsymbol{q}}v(\boldsymbol{q})(2\pi)^2\delta^{(2)}(\boldsymbol{k}-\boldsymbol{q})\,, \tag{3.68}$$

which is satisfied by Eq. (2.56).

When multiple soft effects become important, one can neglect the slow logarithms which only become important in the tails of the distribution, and thus $v(\boldsymbol{x})\sim\boldsymbol{x}^2$. This reduces Eq. (3.67) to a diffusion (Fokker-Planck) equation, with $\hat{q}$ the diffusion parameter,

$$\frac{\partial}{\partial L}\mathcal{P}^{\mathrm{MS}}(\boldsymbol{k},L)=\frac{\hat{q}}{4}\vec{\nabla}^2_{\boldsymbol{k}}\mathcal{P}^{\mathrm{MS}}(\boldsymbol{k},L)\,, \tag{3.69}$$

which can be easily shown to reproduce the solution in the main text.

In the IOE/M approach, one expects to recover the diffusion equation at leading order. Since formally, the broadening distribution can be written as a series in λ, one can expand Eq. (3.67). This leads to a hierarchy of (trivially) coupled diffusion equations with a source term. Using Eqs. (3.1) and (3.47) combined with Eq. (3.67), leads to ($\mathrm{i}\geq 1$)

$$\frac{\partial}{\partial L}\mathcal{P}^{\mathrm{N^iLO}}(\boldsymbol{k},L)=\frac{Q_s^2}{4L}\vec{\nabla}^2_{\boldsymbol{k}}\mathcal{P}^{\mathrm{N^iLO}}(\boldsymbol{k},L)+\frac{4\pi Q_{s0}^2}{L}\int_{\boldsymbol{q}}\frac{1}{\boldsymbol{q}^4}\mathcal{P}^{\mathrm{N^{i-1}LO}}(\boldsymbol{k}-\boldsymbol{q},L)\,, \tag{3.70}$$

with the leading order term satisfying Eq. (3.69). Eq. (3.70), besides its interesting coupled structure, offers no clear computational advantage over the approach followed in the main text.

3.C Universal map between GW and HTL at the level of the broadening distribution

In this appendix we study the quality of the LT map between the GW and HTL model introduced in section 2.3 at the level of the broadening distribution. Here we fix m_D and use the universal map given in Eq. (2.48) to obtain the respective μ; we then compute

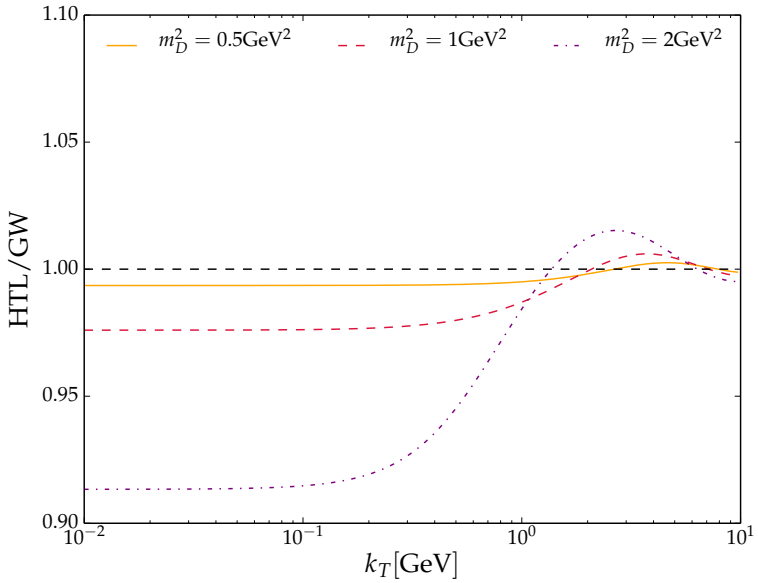

Figure 3.9: Ratio between $\mathcal{P}^{\text{HTL}}(\boldsymbol{k}, L)$ and $\mathcal{P}^{\text{GW}}(\boldsymbol{k}, L)$ as a function of the Debye mass m_D^2 for $Q_{s0}^2 = 4.8$ GeV^2. Figure taken from [6].

the broadening distributions for the GW and HTL models. In Fig. 3.9, we show the ratio of the respective distributions, and we observe that for small values of the masses the universal map works well. When the m_D tends to the large momentum scale Q_{s0}, then the mapping becomes worse, as expected. Notice, that at small $|\boldsymbol{k}|$ one observes a $\sim 10\%$ deviation, in accordance with the fact that this is a LT (small dipole) map. These results agree with the ones shown in the previous chapter.

USC
UNIVERSIDADE
DE SANTIAGO
DE COMPOSTELA

4

Digital quantum computing for quantum simulation

In this chapter we introduce the quantum circuit model [156] and respective notation. This is followed by an overview of the quantum simulation algorithm [58, 70, 71]. This chapter is primarily aimed at introducing the main concepts and notation used in chapters 5 and 6, and more detailed and complete discussion can be found in relevant books and reviews [74, 157].

4.1 Quantum bits and quantum gates

In this section we introduce the usual notation and basic results found in quantum computing.

In classical digital computation, the smallest object that can hold any information is called a *bit*. A bit can be in either one of two states – 0 or 1 – and the only non-trivial operation that one can perform on a bit is the negation operation: $1 \to 0$ and $0 \to 1$. Although bits are represented in the real world by, for example, the discrete values of tension in an electrical wire, we consider them as purely mathematical objects in this thesis.

In the quantum world, bits get promoted to *quantum bits* or *qubits* for short. As bits, qubits can be in a (pure) state $|0\rangle$ or $|1\rangle$, but since they are quantum, in general a bit $|\psi\rangle$ can be written as a superposition of the two basis states

$$|\psi\rangle = \alpha\,|0\rangle + \beta\,|1\rangle\ , \tag{4.1}$$

where α and β are complex numbers and the only constraint is that $|\alpha|^2 + |\beta|^2 = 1$, which follows from the fact the Quantum Mechanics (QM) is unitary. Like classical bits, qubits can also be represented in physical devices, for example, as combinations of the discrete eigenstates of a harmonic oscillator (see chapter 1). Although we do not discuss the physical realizations of qubits, it is convenient to think of a qubit as a 1/2-spin, where the usual convention in quantum computing[1] is that the state $|0\rangle = |\uparrow\rangle = [1,0]^T$ and $|1\rangle = |\downarrow\rangle = [0,1]^T$ are the eigenstates of the spin operator S_z.

As is well known in QM, any transformation done to a single qubit can be decomposed as a linear combination of Pauli operators with unity, i.e. $\{1, \sigma^x, \sigma^y, \sigma^z\}$. In the computational basis, i.e. in the $\{|0\rangle, |1\rangle\}$ basis, these gates (operators) read

$$1 = \begin{pmatrix} 1 & 0 \\ 0 & 1 \end{pmatrix}, \quad \sigma^x = \begin{pmatrix} 0 & 1 \\ 1 & 0 \end{pmatrix}, \quad \sigma^y = \begin{pmatrix} 0 & -i \\ i & 0 \end{pmatrix}, \quad \sigma^z = \begin{pmatrix} 1 & 0 \\ 0 & -1 \end{pmatrix}. \tag{4.2}$$

It is also useful to introduce the two following gates (operators)

$$H = \frac{1}{\sqrt{2}} \begin{pmatrix} 1 & 1 \\ 1 & -1 \end{pmatrix}, \quad S = \begin{pmatrix} 1 & 0 \\ 0 & i \end{pmatrix}, \tag{4.3}$$

where the first gate is usually referred to as Hadamard gate and the second as phase gate. Finally, since we are interested in quantum simulation, which requires at some level the implementation of the exponential of some of the previous operators, we recall that the exponential of the Pauli matrices is easily computed by writing the exponential map explicitly. One obtains for σ^z

$$R_z(\theta) \equiv \exp\left(-i\frac{\theta}{2}\sigma^z\right) = \begin{pmatrix} \mathrm{e}^{-i\frac{\theta}{2}} & 0 \\ 0 & \mathrm{e}^{i\frac{\theta}{2}} \end{pmatrix}. \tag{4.4}$$

The other two rotation matrices are easily obtained from this one by noticing that

$$H\sigma^x H = \sigma^z, \quad HS^\dagger \sigma^y S H = H\sigma^x H = \sigma^z. \tag{4.5}$$

Then we have, for example,

$$R_x(\theta) \equiv \exp\left(-i\frac{\theta}{2}\sigma^x\right) = \exp\left(-i\frac{\theta}{2}H\sigma^x H\right) = H\exp\left(-i\frac{\theta}{2}\sigma^z\right)H = HR_z(\theta)H. \tag{4.6}$$

The usefulness of this formula will become apparent later. In conclusion and unlike the classical counterpart, where the only single bit operation is the NOT operation, the quantum scenario allows for an infinite set of discrete transformations to be performed on a single qubit.

Another difference with respect to the classical case is the act of measurement. In the classical world, one is able to measure the bit at any moment without disrupting the

[1] Not the usual convention in QM [158].

stored state. In the quantum world this is no longer true, due to the special character of the act of measurement in QM. In particular, if a qubit is measured its state will collapse to either $|0\rangle$ or $|1\rangle$, with the probability of such transitions occurring given by the coefficient associated to each basis state. Since the output state is always classical, and it is not usually used for any further operations (although it can be used to control classical operations), one can consider the qubit after measurement as being a classical bit.

Finally, similar to the classical case, one can represent the set of operations acting on a single qubit state via a circuit representation, inherited from Penrose's diagrammatic calculus. One can show that such a model is complete, in the sense that any possible operation can be represented [74]. In Fig. 4.1, we introduce the usual notation for denoting the single qubit operations. Notice that the incoming state comes from the left (to a reader) and the output state leaves through the right. This is unlike the matrix notation where the order is reversed (i.e. matrices act on vectors coming from the right). Thus, when going from a matrix to a circuit representation one needs to reverse the order of the operations.

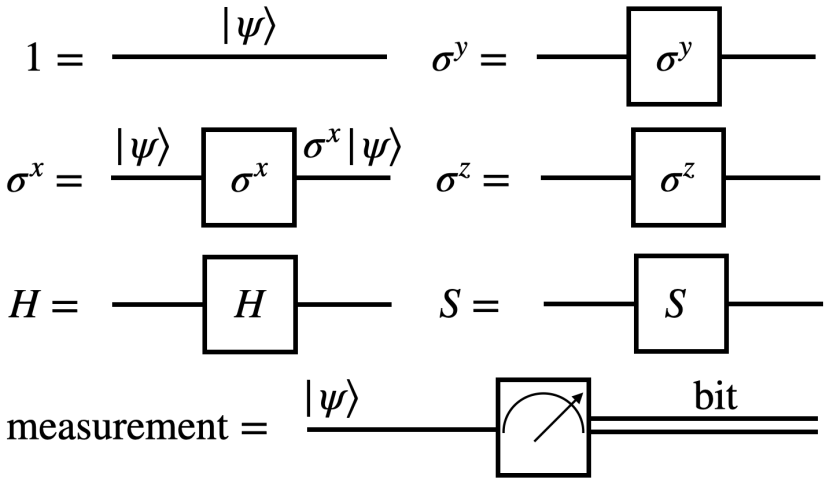

Figure 4.1: Circuit notation for single qubit operations. We introduce an fictitious input state, denoted by $|\psi\rangle$, just to highlight how the operations act, i.e. from left to right. Qubits are denoted by single lines, while classical bits are denoted by double lines.

The generalization of the previous results to a multi-(qub)bit system is immediate. It is enough to detail the two (qu)bit scenario, while larger systems can always be written in terms of single or two (qu)bit operations.

In the classical scenario, with two bits the state space is span by $\{00, 01, 10, 11\}$. There are many operations that use two bits; here we consider the NAND gate, which given two inputs, outputs the negation of the logical adding operation. It is possible to show that any multi-bit operation can be decomposed just in terms of NAND gates; in this sense the NAND gate is an *universal* gate [159].

In the quantum world, there is also a large variety of two-qubits gates. In this case, the Hilbert space is spanned by the computational basis states $\{|00\rangle, |01\rangle, |10\rangle, |11\rangle\}$, where our notation implicitly means $|ab\rangle = |a\rangle \otimes |b\rangle$, i.e. extra qubits can be added via a tensor product of the respective Hilbert spaces. Thus, in this case the single qubit gate U should explicitly read $U \otimes 1$. We only employ this explicit but heavy notation when operations are not completely clear.

The prototypical two-qubit gate is the CNOT gate, where the C stands for controlled and the NOT operation is nothing but the application of σ^x. In the computational basis, the CNOT gate is given by

$$\text{CNOT} = \begin{pmatrix} 1 & 0 & 0 & 0 \\ 0 & 1 & 0 & 0 \\ 0 & 0 & 0 & 1 \\ 0 & 0 & 1 & 0 \end{pmatrix}, \tag{4.7}$$

i.e. it applies the single qubit operation σ^x only when the input state is of the form $|10\rangle$ or $|11\rangle$. One can generalize this and define a generalized controlled gate CU, as applying the single qubit gate U, depending on the value of the input qubit. Usually, if one wants to apply the gate on the *target* qubit when the *control* is in the state $|1\rangle$, then one uses a ● on the control qubit line, with a vertical line down to the controllable gate. On the other hand, if one wants to activate the gate if the control qubit is in the state $|0\rangle$, then one uses the symbol ◯ $= \sigma^x$ ● σ^x. This notation can be extended to circuits with more qubits, where one can have more than one control qubit at a time and also act on more than one target qubit. Such gates can always be written in terms of CNOT and the single qubits gates [74], i.e. the set formed by the CNOT and single qubit gates is universal. It is however easily realized that decomposing any multi-qubit gate in terms of CNOT and single qubit gates is not efficient, since it will require an exponential number of such basic gates[2]. Nonetheless, one can show that a discrete set of gates can approximate any circuit constructed using CNOT and single qubit unitaries, with only a sub-exponential overhead in the number of gates. This result is one of the most important results in quantum computing and is known as the Solovay-Kitaev theorem [161]. An advantage of using a discrete set of gates (versus a continuum set of gates) is that fault tolerance and quantum error correction techniques can be easily applied, since they also require discrete sets of gates to correct an infinite set of errors [160].

Coming back to the classical scenario, a natural question is if one can construct a NAND quantum gate. It is easily realized that it is impossible to construct such a gate since all operations in QM have to be unitary. This requires that every gate maps each input to a different output. In the case of the classical NAND gate this is not possible because the inputs 00, 01 and 10 are mapped to the same output. Thus, only *reversible* classical gates have a quantum analog. Also, as a corollary, there can be no universal gate analog to the classical NAND in the quantum context.

[2]In such implementations, fault-tolerance and efficient quantum error correction is also not guaranteed [160].

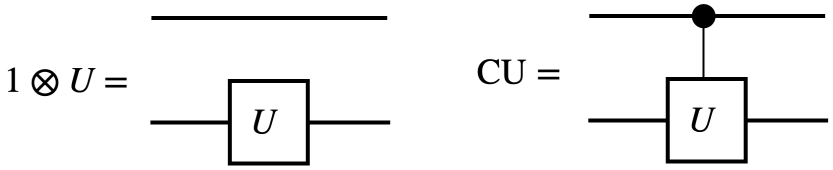

Figure 4.2: **Left**: Diagrammatic representation of the two-qubit operator $1 \otimes U$. **Right**: Generic CU operation, where the gate $\boxed{U}$ is only applied if the control qubit is in the state $|1\rangle$.

Other two important examples of classical operations which are not allowed in the quantum context are the FANIN and FANOUT classical gates. The first operation, takes two inputs and merges them into a single bit output; the second gate does the opposite by splitting a single input bit to two bits, each holding a copy of the input. A quantum FANIN operation would clearly not be possible since we are mapping larger (finite) Hilbert spaces to smaller ones, the FANOUT operation is forbidden by the so called no-cloning theorem of QM [74], which is just a consequence of unitarity. Another type of operation which is also forbidden are FEEDBACKs, where forward information in the circuit can loop back to a previous point in the circuit. This is forbidden because QM is linear, and clearly FEEDBACK operations are not linear, see Fig. 4.3.

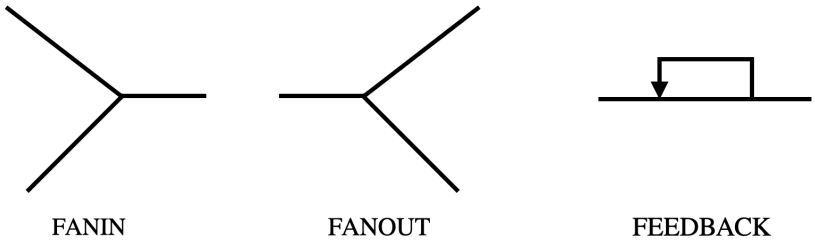

Figure 4.3: FANIN, FANOUT and FEEDBACK diagrammatic representations, which are not allowed by QM.

With the above definitions and concepts (with the respective extension to higher qubits systems), we can give the notion of quantum computer that we use in the rest of this thesis.

A quantum computer is a physical device which can be theoretically represented using the circuit model. In addition, we require that a quantum computer satisfies the following conditions [73]:

1. It is a quantum device where one can recognize the different qubits, the couplings between each of them and the system Hamiltonian. For our purposes, we consider that there is no limit on the number of qubits and that each qubit is coupled to all other qubits. We also do not care about the details of the system natural time evolution, and assume that one can implement an universal set of gates.

2. The underlying Hilbert space for n_Q qubits has dimension 2^{n_Q}, where we assume that the Hilbert space is always finite dimensional. The computational basis is defined as being given by states of the form $|x_1 x_2 \cdots x_{n_Q}\rangle = |x\rangle$, where $x_i \in \{0, 1\}$ and the tensor product corresponds to the binary decomposition of the number x. One also assumes that the fiducial state $|x = 0\rangle$ can always be prepared.

3. One is able to perform single qubit measurements in the computational basis. Coupled with the hypothesis that an universal set of quantum gates can be implemented, then one can measure in different basis, by doing the adequate set of transformations between different basis.

4. We finally require that there is a *sea* of qubits, which largely surpasses the number of qubits necessary to run a certain circuit. In particular, this means if an algorithm needs auxiliary qubits – referred to as ancilla qubits – to perform a side step calculation, then we assume that such qubits are always available. We also assume that ancillas can be used more than once, provided adequate erasure procedures are implemented.

4.2 The quantum simulation algorithm

In the previous section, we gave the basic elements of the quantum circuit model, which effectively define the theoretical representation for a quantum computer. Let us now apply the above definitions and concepts to quantum simulation.

The quantum simulation algorithm tries to simulate the time evolution of a complex and inaccessible quantum system, by using an simpler and accessible quantum system. In practice, one wants to simulate dynamics of the target system according to the Schrodinger equation

$$i\partial_t |\psi\rangle = H |\psi\rangle \ , \tag{4.8}$$

whose formula solution for a time independent Hamiltonian is

$$|\psi(t)\rangle = \exp(-iHt) |\psi(0)\rangle \ , \tag{4.9}$$

where $|\psi(0)\rangle$ is the initial condition of the system at time $t = 0$.

One way to simulate the dynamics of the system would be to construct an initial state $|\psi(0)\rangle$ and then solve the differential equation given in Eq. (4.8). However, this would require solving an exponential number of equations, and it would therefore in general require an exponential time to solve the problem. However, Eq. (4.9) tells us that instead of solving a set of differential equations, one can simply construct an approximation to the time evolution operator $\exp(-iHt)$ of the target system in the quantum computer. Since this is an unitary operator, based on the previous section, we know that in principle an efficient implementation of such an operator could exist.

Another important observation is that for physical systems, the form of H is restricted by, for example, symmetry or other physical criteria. Thus, the class of physical Hamiltonians is much smaller than the full space of Hamiltonians. In particular, the Hamiltonians we are interested can always be written as

$$H = \sum_i H_i \,, \tag{4.10}$$

where each H_i only acts on a sub-space of the full Hilbert space. Indeed, we know, for example, that interactions in a physical system are always local, and thus one expects that the respective Hamiltonian reflects this property. We note however that this is a basis dependent statement; for example in a momentum basis the interaction terms are highly delocalized (since they are roughly the Fourier pair of a local term), and thus their implementation would not be efficient.

Even assuming the form in Eq. (4.10), it is not trivial to implement the time evolution operator, unless for all $i \neq k$ one has that $[H_i, H_k] = 0$, which is not typically the case. However the Baker–Campbell–Hausdorff (BCH) formula tells us that for any operators A and B, one has that

$$\mathrm{e}^{iAt}\mathrm{e}^{iBt} = \mathrm{e}^{iAt+iBt-\frac{t^2}{2}[A,B]} + O(t^3) \,, \tag{4.11}$$

thus truncating at order t^2

$$\mathrm{e}^{iAt}\mathrm{e}^{iBt} \approx \mathrm{e}^{iAt+iBt} \,. \tag{4.12}$$

Identifying the exponent on the right hand side with $-iHt$, this gives a formula to approximate the time evolution operator. Here A and B should be seen as local Hermitian operators, which are easier to implement than the Hamiltonian, since they only act on sub-spaces of the full Hilbert space.

However, the error for such a formula is $\frac{t^2}{2}[A, B]$, which grows quadratically in time, and thus if the simulation time is large, than the error becomes of the order of the first order term we track. A generalization of the BCH formula to solve this issue consists in subdividing the simulation time into n small evolution steps. This leads to the famous Trotter formula [162]

$$\lim_{n\to\infty} \left(\mathrm{e}^{i\frac{At}{n}}\mathrm{e}^{i\frac{Bt}{n}}\right)^n = \mathrm{e}^{i(A+B)t} \,, \tag{4.13}$$

which holds since in an infinitesimal step all operators commute to linear order.

The leading order approximation to the Trotter formula is known as first order Trotter-Suzuki formula [163, 164] and reads

$$\mathrm{e}^{i(A+B)t} = \left(\mathrm{e}^{i\frac{At}{n}}\mathrm{e}^{i\frac{Bt}{n}}\right)^n + O\left(\frac{t^2}{n^2}\right) \tag{4.14}$$

The previous equation says that the full Hamiltonian can be implemented by slicing time in n small steps. In each step, all operators commute and thus one can implement the infinitesimal time evolution operator as a product of several (simpler) time evolution

operators. The error of such an approximation is quadratic in the infinitesimal time step[3]. Although higher order product formulas can be constructed [163, 164], we will consider only the first order Trotter-Suzuki formula in this thesis. Although recent efforts have lead to more efficient and accurate ways of implementing the time evolution operator [72, 167, 168], it turns out that for many applications, due to the characteristics of physical Hamiltonians, the Trotter-Suzuki approximation works remarkably well. Another advantage of this strategy, compared to some of the most recent approaches, is that it allows to explore the symmetries and properties of the underlying Hamiltonian directly, leading to a very straightforward way to simulate the desired system.

With the above considerations we can outline the steps involved in the quantum simulation algorithm.

1. **Input**: The Hamiltonian $H = \sum_i H_i$ describing the dynamics of the target system, where we assume H is given in terms of local Hamiltonians H_i. In addition, one needs a template for the initial state of the system $|\psi(0)\rangle$.

2. **Encoding/Digitization**: In a digital quantum computer, one will need a map between the degrees of freedom of the target system and the qubits in the quantum computer. In addition, one needs to find a decomposition of the local Hamiltonians H_i in terms of basic gate operations.

3. **Initial State Preparation**: Given the template and an initial fiducial state $|0\rangle$, one performs $|0\rangle \to |\tilde{\psi}(0)\rangle$, where the tilde denotes that this is the discrete version of the physical state $|\psi(0)\rangle$.

4. **Time evolution:** Once the initial state is prepared, one time evolves it using an approximation to the exact time evolution operator.

5. **Measurement**: After the time evolution step is performed, one extracts the information of the system by measuring the adequate qubits, typically according to some protocol.

6. **Output**: In this thesis we are interested in outputs corresponding to the expectation value of operators, i.e. given the final state $|\tilde{\psi}(t)\rangle$ we want $\langle\tilde{\psi}(t)| V |\tilde{\psi}(t)\rangle$.

It is useful here to give a typical example of simulating local Hamiltonians, which we will use in the next chapter. Suppose first that one has a one-qubit system which evolves according to the Hamiltonian $H = \sigma^z$. Then, supposing $|\tilde{\psi}(0)\rangle = |0\rangle$, the time evolution operator is simply $R_z(2t)$. If we had instead two qubits, then the straightforward generalization of the Hamiltonian is $H = \sigma^z \otimes \sigma^z$, which is not immediately exponentiated.

[3]One can find a detailed discussion on Trotter-Suzuki formulas and their accuracy and exact error bounds in [165]. Such estimates are important for implementation in Noisy Intermediate-Scale Quantum (NISQ) [166] devices.

The usual trick is to notice that the Hamiltonian simply measures the parity of the state, i.e.

$$\sigma^z\otimes\sigma^z\,|00\rangle = |00\rangle\ , \quad \sigma^z\otimes\sigma^z\,|01\rangle = -\,|01\rangle\ , \quad \sigma^z\otimes\sigma^z\,|10\rangle = -\,|10\rangle\ , \quad \sigma^z\otimes\sigma^z\,|11\rangle = |11\rangle\ . \tag{4.15}$$

Thus, if the qubits have different parity one has to change the phase by a -1 factor. One can implement such a time evolution operator as detailed in Fig. 4.4. The initial two CNOT gates determine the parity of the input, determining the sign of the phase. The last two gates erase the action of the initial parity determination, erasing all the information from the ancilla qubit. This symmetric structure is typically found every time one needs to erase a previous operation.

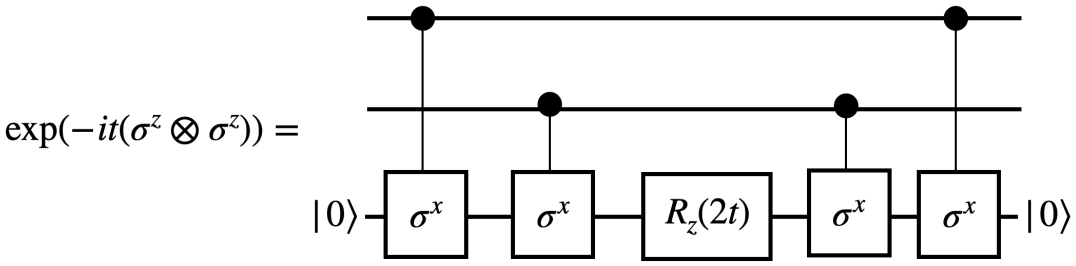

Figure 4.4: Implementation of the time evolution operator associated to he Hamiltonian $H = \sigma^z \otimes \sigma^z$.

This strategy is easily seen to generalize to larger qubit systems. Using Eqs. (4.5) and (4.6), one realizes that if instead of σ^z one had, for example, σ^x, then on the line of the corresponding qubit one would previously apply a Hadamard gate (and respectively one at the end), so that it suffices to know how to exponentiate the σ^z gate. The importance of this strategy is that it gives a brute force way of implementing any local Hamiltonian. For example, in the harmonic quantum oscillator the number operator $\sim a^\dagger a$ can be easily mapped to a spin system, corresponding to the operator $\sim S^+S^-$. It is well known [158] that the raising S^+ and lowering S^- 1/2-spin operators can always be written in terms of Pauli matrices. Thus, expanding out S^+S^- into a sum of products of Pauli operators one could easily apply the above algorithm. However, it is also clear that, for a generic operator, the number of local operators one needs to implement can be exponentially large, thus this brute force approach to implementing the time evolution operator is usually not adequate and smarter strategies need to be found. Nonetheless, for NISQ era implementations, the overhead due to using this strategy is typically small and thus it is useful in practice.

4.A The (symmetric) quantum Fourier transform algorithm

In this appendix we introduce the quantum Fourier transform [74] (qFT) and the symmetric quantum Fourier transform [10] algorithms. Although the qFT is not strictly necessary to quantum simulate a system, it is nonetheless useful in order to transform between different basis, where implementing the time evolution operator might be more convenient. More importantly, the qFT will play an important role in the next chapters.

Given a register with n_Q qubits and denoting a generic state as

$$|x\rangle = |\sum_{i=0}^{n_Q-1} x_i 2^i\rangle \ , \tag{4.16}$$

with $x_i \in \{0,1\}$, the qFT algorithm performs the following operation

$$|x\rangle \to \frac{1}{\sqrt{2^{n_Q}}} \sum_{k=0}^{2^{n_Q}-1} e^{2\pi i \frac{xk}{2^{n_Q}}} |k\rangle \ . \tag{4.17}$$

To construct the circuit implementing this operation one just needs to realize that the exponents can be written as (up to terms leading to trivial phases)

$$\begin{aligned}\frac{xk}{2^{n_Q}} &= (x_0 + 2x_1 + 4x_2 + \cdots + 2^{n_Q-1}x_{n_Q-1})(k_0 + 2k_1 + 4k_2 + \cdots + 2^{n_Q-1}k_{n_Q-1})\frac{1}{2^{n_Q}} \\ &= k_0\left(\frac{x_{n_Q-1}}{2} + \frac{x_{n_Q-2}}{4} + \cdots + \frac{x_0}{2^{n_Q}}\right) + k_1\left(\frac{x_{n_Q-2}}{2} + \frac{x_{n_Q-3}}{4} + \cdots + \frac{x_0}{2^{n_Q-1}}\right) \\ &+ \cdots + k_{n_Q-1}\frac{x_0}{2}\,.\end{aligned} \tag{4.18}$$

Thus one can rewrite Eq. (4.17) explicitly as

$$\begin{aligned}|x\rangle = &\frac{|0\rangle + e^{2\pi i\left(\frac{x_{n_Q-1}}{2} + \frac{x_{n_Q-2}}{4} + \cdots + \frac{x_0}{2^{n_Q}}\right)}|1\rangle}{\sqrt{2}} \otimes \frac{|0\rangle + e^{2\pi i\left(\frac{x_{n_Q-2}}{2} + \frac{x_{n_Q-3}}{4} + \cdots + \frac{x_0}{2^{n_Q-1}}\right)}|1\rangle}{\sqrt{2}} \otimes \\ &\otimes \cdots \otimes \frac{|0\rangle + e^{2\pi i\frac{x_0}{2}}|1\rangle}{\sqrt{2}}\,.\end{aligned} \tag{4.19}$$

Introducing the single qubit gate operator $R_t \equiv \mathrm{diag}(1, \exp\{-2\pi i/2^t\})$[4], one can easily realize that the qFT is implemented by the circuit shown in Fig. 4.5.

[4]This definition differs from the typical one [74].

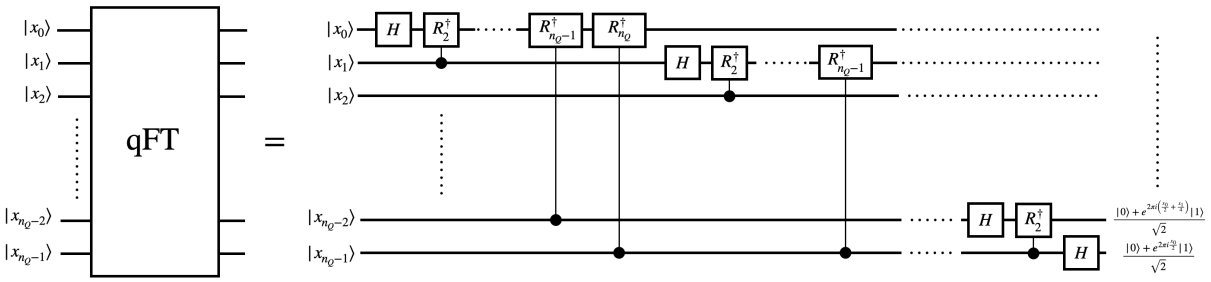

Figure 4.5: Implementation of the quantum Fourier transform algorithm.

The symmetric qFT is defined as

$$|x\rangle \to \frac{1}{\sqrt{2^{n_Q}}} \sum_{k=-\frac{2^{n_Q}-1}{2}}^{\frac{2^{n_Q}-1}{2}} e^{2\pi i \frac{xk}{2^{n_Q}}} |k\rangle \ . \tag{4.20}$$

It is obtained from the standard qFT by subtracting the x dependent phase $\exp(-2\pi i \frac{(2^{n_Q}-1)x}{2^{n_Q+1}})$ to each state $|k\rangle$. This can be implemented by an overall phase shift applied before the standard qFT, as shown in Fig. 4.6.

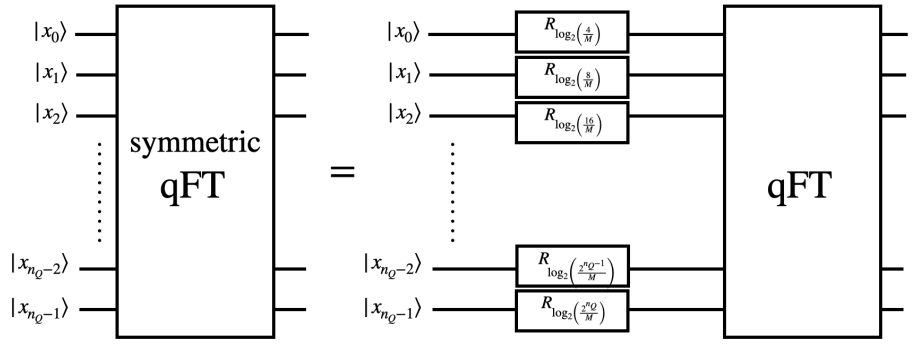

Figure 4.6: Implementation of the symmetric quantum Fourier transform algorithm. Here $M = 2^{n_Q} - 1$.

USC
UNIVERSIDADE
DE SANTIAGO
DE COMPOSTELA

5

Quantum simulating scattering of ϕ^4 scalar theory in $d+1$ dimensions

In this chapter we introduce a new strategy towards quantum simulating scattering in ϕ^4 scalar QFT in $d+1$ dimensions, following the seminal work of Jordan, Lee and Preskill (JLP) [64, 65]. The fundamental difference between these two approaches lies on the encoding/digitization of the QFT. Thus, after setting up the familiar picture of high energy scattering [23, 24], we review JLP's approach and introduce our strategy. After, we detail the several steps involved in a quantum simulation algorithm (see previous chapter), presenting how our strategy might be realized, while comparing to JLP and its implementation [10].

This chapter is based on [7].

5.1 Setting up the problem: high energy scattering

Let us first revisit the formulation of scattering experiments in the QFT context. The relevant object to consider is the S-matrix, which relates in/out asymptotic states

$$S_{\beta\alpha} \equiv \langle \Psi_\beta^{\text{out}} | \Psi_\alpha^{\text{in}} \rangle \,, \tag{5.1}$$

where $|\Psi_\alpha^{\text{in}}\rangle$ is an asymptotic in-state and $|\Psi_\beta^{\text{out}}\rangle$ an asymptotic out-state, both being time independent eigenstates of the full Hamiltonian H.

We assume that the Hamiltonian of the system can always be written as a sum of a *free* part H_0 and an interacting potential V, i.e. $H = H_0 + V$. If the energy spectrum

is continuous, then if at early/late times the state is described by an eigenstate of the free Hamiltonian with energy E, $H_0\,|\phi_\alpha\rangle = E_\alpha\,|\phi_\alpha\rangle$, then there must exist an eigenstate of the full Hamiltonian satisfying $H\,|\Psi_\alpha\rangle = (H_0+V)\,|\Psi_\alpha\rangle = E_\alpha\,|\Psi_\alpha\rangle$. This leads to the Lippmann-Schwinger equation [169, 170],

$$|\Psi_\alpha^{\text{in/out}}\rangle = |\phi_\alpha\rangle + G_0V|\Psi_\alpha^{\text{in/out}}\rangle = (V - VG_0V)^{-1}V|\phi_\alpha\rangle\,, \tag{5.2}$$

with $G_0^{-1} = E_\alpha - H_0 + i\varepsilon$. This equation formally gives the connection between the free wave-function and the system wave-function in the full theory. As usual, one can isolate the scattering terms from the non-scattering terms

$$S_{\beta\alpha} = \delta_{\alpha\beta} - 2\pi i\,\delta(E_\alpha - E_\beta)\,T_{\beta\alpha}\,, \tag{5.3}$$

where the $T-$matrix is the object entering the calculation of physical cross-sections [23, 24]. It is formally defined by the condition $T\,|\phi_\alpha\rangle = V\,|\Psi_\alpha\rangle$, which in components reads

$$T_{\beta\alpha} = \langle\phi_\beta|V|\Psi_\alpha^{\text{out}}\rangle = \langle\Psi_\beta^{\text{in}}|V|\phi_\alpha\rangle = \langle\Psi_\beta^{\text{in}}|(V - VG_0V)|\Psi_\alpha^{\text{out}}\rangle\,. \tag{5.4}$$

Squaring the previous expression

$$|T_{\beta\alpha}|^2 = \langle\Psi_\alpha^{\text{in}}|\,(V - VG_0V)|\Psi_\beta^{\text{out}}\rangle\langle\Psi_\beta^{\text{out}}|(V - VG_0V)^\dagger\,|\Psi_\alpha^{\text{in}}\rangle\,, \tag{5.5}$$

and inserting the necessary kinematical pre-factors gives an exact way to compute any cross-section. In practice, the operator $V - VG_0V$ is not known exactly or in a closed form, and thus one either makes uses of perturbation theory to expand Eq. (5.2) order by order in the potential (similar to usual QM perturbation theory) [170] or one can use variational/numerical approaches [169, 171, 172]. Although quantum formulations of such algorithms have been considered [173], we proceed by using the Schrodinger picture, where the time dependence is put in the system state.

In the Schrodinger picture, one assumes that the asymptotic states are eigenstates of H_0, i.e. $|\Psi_g^{\text{in}}(-\infty)\rangle = |\phi_g(-\infty)\rangle$ and $|\Psi_g^{\text{out}}(+\infty)\rangle = |\phi_g(+\infty)\rangle$. A state in this picture is related to the respective state in the Heisenberg picture via time dependent wave-packets

$$|\Psi_g^{\text{in/out}}(t)\rangle \equiv \int d\alpha\, g(\alpha)e^{-iE_\alpha t}\,|\Psi_\alpha^{\text{in/out}}\rangle\,, \tag{5.6}$$

and

$$|\phi_g(t)\rangle \equiv \int d\alpha\, g(\alpha)e^{-iE_\alpha t}\,|\phi_\alpha\rangle\,. \tag{5.7}$$

The Lippmann-Schwinger equation can be written for these time dependent states as

$$|\Psi_g^{\text{in/out}}(t)\rangle = |\phi_g(t)\rangle + \int_0^\infty dT\, e^{\pm i(H_0\mp i\epsilon)T}\,V|\Psi_g^{\text{in/out}}(t\mp T)\rangle\,, \tag{5.8}$$

where $V(T) \equiv Ve^{-\epsilon|T|}$ can be seen as adiabatically turning on the interaction to obtain $|\Psi^{\text{in}}(t)\rangle$ from the initial condition $|\phi_g(-\infty)\rangle$. Thus, the formulation of scattering in the Schrodinger picture, tells us that one can prepare an initial eigenstate of the free Hamiltonian in the infinite past and then slowly turn-on the interactions such that after a finite amount of time one has prepared the eigenstate of the full Hamiltonian with the same eigenvalue. Then, one time evolves this state according to the full time evolution operator (thus allowing for interactions to occur) until the wave-packet of the final state has been obtained.

With this more abstract discussion in mind, let us introduce the theory we want to study: real scalar ϕ^4 theory in d spatial dimension. The Hamiltonian reads

$$\bar{H} = \int \mathrm{d}^d\mathbf{x}\Big[\frac{\pi_{\mathbf{x}}^2}{2} + \frac{1}{2}(\nabla\phi_{\mathbf{x}})^2 + \frac{\overline{m}^2}{2}\phi_{\mathbf{x}}^2 + \frac{\overline{\lambda}}{4!}\phi_{\mathbf{x}}^4\Big]\,, \tag{5.9}$$

where $\overline{m}$ and $\overline{\lambda}$ are the (bare) mass and quartic coupling, and ∇ is the spatial gradient operator in d dimensions. The Heisenberg field operators are[1]

$$\phi_{\boldsymbol{x}} = \int \frac{\mathrm{d}^d\boldsymbol{p}}{(2\pi)^d}\frac{1}{\sqrt{2\,\overline{\omega}_{\boldsymbol{p}}}}\Big[a_{\boldsymbol{p}} + a_{-\boldsymbol{p}}^\dagger\Big]e^{i\boldsymbol{p}\cdot\boldsymbol{x}}\,, \tag{5.10}$$

satisfying the canonical commutation relations $[\phi_{\boldsymbol{x}}, \pi_{\mathbf{y}}] = i.\delta^{(d)}(\boldsymbol{x}-\mathbf{y})$. The annihilation (creation) operators $a_{\boldsymbol{p}}$ ($a_{\boldsymbol{p}}^\dagger$) are momentum-space Fock operators, corresponding to a set of harmonic oscillators with frequency $\overline{\omega}_{\boldsymbol{p}} = \sqrt{\boldsymbol{p}^2 + \overline{m}^2}$ and commutation relations $[a_{\boldsymbol{p}}, a_{\mathbf{k}}^\dagger] = (2\pi)^d\delta^{(d)}(\boldsymbol{p}-\mathbf{k})$, $[a_{\boldsymbol{p}}, a_{\mathbf{k}}] = [a_{\boldsymbol{p}}^\dagger, a_{\mathbf{k}}^\dagger] = 0$.

To study these theory in a digital quantum computer, one needs to discretize the degrees freedom so that the infinite dimensional Hilbert space of the QFT can be mapped to the finite Hilbert space where the qubits live. We begin by discretizing the theory in space, by introducing a lattice with $\mathcal{V} \equiv N_s^d$ sites (N_s per dimension), such that the (dimensionless) Hamiltonian $\bar{H}$ can be written as

$$H \equiv a_s\bar{H} = \sum_{\mathbf{n}}\Big[\frac{1}{2}\pi_{\mathbf{n}}^2 + \frac{1}{2}(\nabla\phi_{\mathbf{n}})^2 + \frac{m^2}{2}\phi_{\mathbf{n}}^2 + \frac{\lambda}{4!}\phi_{\mathbf{n}}^4\Big]\,, \tag{5.11}$$

where $m = \overline{m}\,a_s$, $\lambda = \overline{\lambda}\,a_s^{4-d}$ are dimensionless bare mass and coupling parameters, a_s the lattice spacing and $\mathbf{n} = (n_1, \ldots, n_d)$, $n_i \in [0, N_s - 1]$ labels a point $\boldsymbol{x} = \mathbf{n}a_s$ on the lattice. We will likewise define a momentum space lattice vector $\mathbf{q} = (q_1, \ldots, q_d)$, $q_i \in [-\frac{N_s}{2}, \frac{N_s}{2} - 1]$. The lattice field operators read

$$\phi_{\mathbf{n}} = \frac{1}{\sqrt{\mathcal{V}}}\sum_{\mathbf{q}}\frac{1}{\sqrt{2\omega_{\mathbf{q}}}}\Big[a_{\mathbf{q}} + a_{-\mathbf{q}}^\dagger\Big]e^{i2\pi\mathbf{n}\cdot\mathbf{q}/N_s}\,,\quad \pi_{\mathbf{n}} = \frac{-i}{\sqrt{\mathcal{V}}}\sum_{\mathbf{q}}\sqrt{\frac{\omega_{\mathbf{q}}}{2}}\Big[a_{\mathbf{q}} - a_{-\mathbf{q}}^\dagger\Big]e^{i2\pi\mathbf{n}\cdot\mathbf{q}/N_s}\,. \tag{5.12}$$

[1] In this chapter, unlike previous ones, the usage of $\cdot$ is applied to denote any contraction indices, regardless of dimension. From the context, it should be easy for a reader to deduce what each contraction denotes.

Here we have introduced the lattice volume $\mathcal{V} = N_s^d$ and the dimensionless energy factor $\omega_{\mathbf{q}} = \overline{\omega}_{\mathbf{q}}\, a_s^{-1}$ is the dimensionless energy. We use the same notation for continuous and discrete Fock operators and respective indices, which should not create any confusion taken into context.

Even with this digitization, it is clearly seen that that for each lattice point the associated Hilbert space is infinite dimensional. Therefore, another discretization step is necessary in order to have a finite dimensional Hilbert space. We now detail the approach of JLP and an alternative strategy.

Field based picture: Jordan-Lee-Preskill approach

The approach of JLP consists in noticing that after discretizing the full Hilbert space $\mathcal{H}$ into a spatial lattice one can focus on a single spatial position, since $\mathcal{H} = \bigotimes_{\boldsymbol{x}} \mathcal{H}_{\boldsymbol{x}}$. For each position, the associated Hilbert space has infinite dimensions. Also, after spatial discretization, the field operator $\phi(\boldsymbol{x})$ gets replaced by N_s^d local field operators $\phi_{\boldsymbol{x}}$, which are defined in terms of a coherent basis for each position: $\hat{\phi}_{\boldsymbol{x}} \left|\boldsymbol{x}\right\rangle = \phi_{\boldsymbol{x}} \left|\boldsymbol{x}\right\rangle$ or by their Fourier conjugate $\hat{\pi}_{\boldsymbol{x}} \left|\boldsymbol{x}\right\rangle = \pi_{\boldsymbol{x}} \left|\boldsymbol{x}\right\rangle$. Therefore, if one further imposes a truncation in the local operator basis for each $\boldsymbol{x}$, i.e. $\phi_{\boldsymbol{x}}$ can only take values between $[\phi_{\text{min.}}, \phi_{\text{max.}}]$ (respectively for π), than the full Hilbert space becomes finite dimensional.

With these discretizations, it easy to compute the number of necessary qubits. If the maximum value for the field ϕ at each position is N_ϕ, and if one dedicates a register of qubits for each $\boldsymbol{x}$ to store the value of the field, then one would need in total $O(\mathcal{V} \log_2 N_\phi)$ qubits. Thus, we see that increasing the size of the spatial lattice leads to a linear increase in the number of necessary qubits, while allowing for the field to take larger values at each position only grows logarithimically. A diagrammatic representation of JLP discretization is given in Fig. 5.1.

Particle based picture

Another way of decomposing the Hilbert space, first suggested in [174] and then implemented in [7], is to first decompose $\mathcal{H}$ in single particle sectors $\mathcal{H} = \bigotimes_{l=0}^{\infty} \mathcal{H}^l$, where to each sector we reserve a register to represent either the momentum or the position of the particle in a binary basis. Single particle states are defined as

$$\left|\boldsymbol{p}\right\rangle^{\text{phys}} \equiv \sqrt{2\,\overline{\omega}_{\boldsymbol{p}}} a_{\boldsymbol{p}}^\dagger |\text{vac}\rangle\,, \tag{5.13}$$

which satisfy the relativistic normalization condition $\langle \boldsymbol{p}|\mathbf{k}\rangle^{\text{phys}} = 2\,\overline{\omega}_{\boldsymbol{p}}\, \delta^{(3)}(\boldsymbol{p} - \mathbf{k})$, where $|\text{vac}\rangle$ denotes the Fock vacuum.

In addition, we reserve an extra qubit for each sector to denote whether the particle exists or if the state is in the single particle vacuum $|\Omega\rangle^{(l)}$. Then, each particle sector is spanned by the single particle vacuum and the collection of occupied states, i.e.

$$\mathcal{H}^l = \text{span}\{|\Omega\rangle^{(l)}, \{|\mathbf{q}\rangle^{(l)}\}\}\,, \tag{5.14}$$

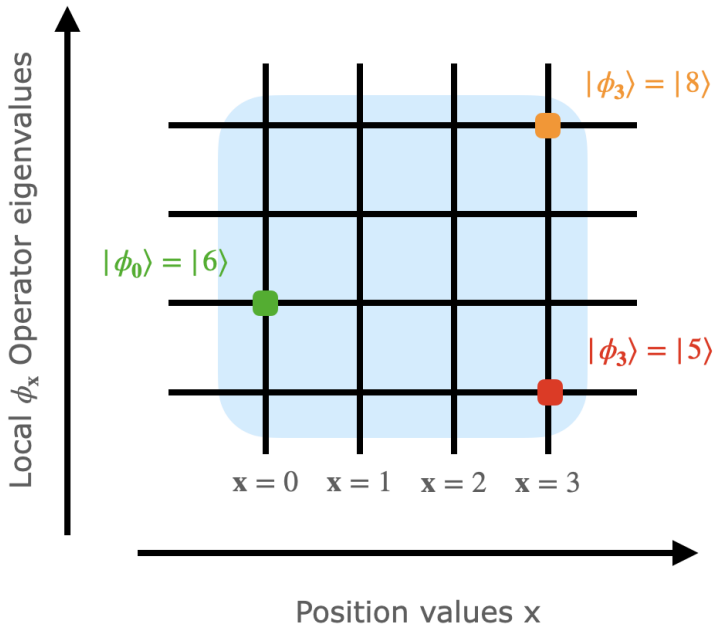

Figure 5.1: A simple example of JLP's digitization strategy. Here the light blue square outlines the region fo the Hilbert space represented in the quantum computer, where the spatial lattice terminates at $\boldsymbol{x} = 5$ and the maximum field value is $\phi_{\boldsymbol{x}} = 8$. Three lattice points were highlighted, with each vertical line being represented in the quantum computer by an array (register) of $\sim \log_2(8)$ qubits, storing the value of the field operator.

$|\mathbf{q}\rangle$ denotes the occupied states in a momentum representation. For the same reason in JLP's approach one could choose between $|\phi\rangle$ or $|\pi\rangle$ basis, here one can also opt between a position $|\boldsymbol{x}\rangle^{(l)}$ or momentum $|\mathbf{q}\rangle^{(l)}$ basis.

In more detail, each register requires $N \equiv \log_2 \mathcal{V} + 1$ qubits, to represent a relativistic particle state with momentum $\mathbf{q} = (\mathbf{q}_1, \ldots, \mathbf{q}_d)$, reading

$$|\mathbf{q}\rangle^{(l)} \equiv \left|\mathbf{q}_1, \ldots, \mathbf{q}_d\right\rangle \left|\uparrow\right\rangle, \tag{5.15}$$

where one qubit $|\uparrow\rangle$ denotes that the single-particle state is occupied. Furthermore, since position and momentum states are signed, we choose to represent the value of momentum/position by reserving a single qubit to denote the sign and multi-qubit register to hold the absolute value (per dimension)

$$|q_i\rangle \equiv |s_i\rangle||q_i|\rangle\,. \tag{5.16}$$

where each component requires $(N-1)/d$ qubits, $s_i = \text{sign}(q_i)$ is the sign (one qubit) and $|q_i|$ the absolute value (abs). We define an empty single-particle state as a state where abs, sign and occupation number qubits are all in the $|\downarrow\rangle$ state,

$$|\Omega\rangle^{(l)} \equiv |\downarrow^{\otimes d \cdot N^{\text{abs}}}, \downarrow^{\otimes d}, \downarrow\rangle\,, \tag{5.17}$$

and the full vacuum is defined as $|\text{vac}\rangle = \bigotimes_l |\Omega\rangle^{(l)}$.

It is easily realized that one needs $N^{\text{abs}} = \frac{N-1}{d} - 1 = \frac{\log_2(\mathcal{V}/2^d)}{d}$ qubits to represent the absolute value of the momentum/position per dimension, with an extra qubit per dimension to store the sign and an overall qubit per single particle sector to store the occupancy. In the approach we take, there is an ambiguity in representing the state of zero momentum or at the spatial origin, thus one must avoid such a point. Another way to avoid this issue would be to use complement-two digitization, which is the usual way to digitally represent signed numbers. Although this encoding avoids the issues with the doubling of the zero state, it would require a non-trivial modification of standard gate operations (such as the qFT), and is therefore undesirable. The discretization approach described is diagrammatically represented in Fig. 5.2.

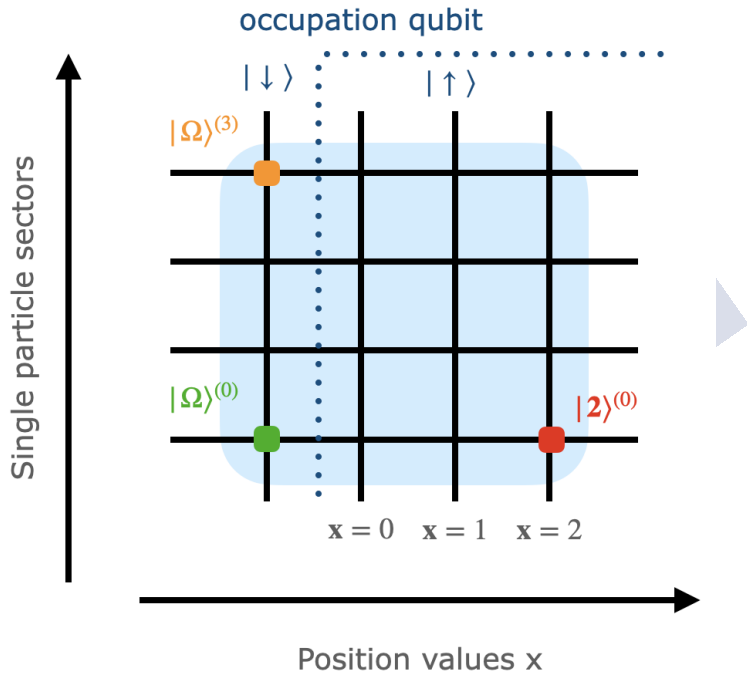

Figure 5.2: A simple example of the single particle approach to discretizing the Hilbert space. The blue square denotes the subspace captured in the quantum computer, while the dotted line denotes the values of the occupancy qubit. Here we consider that one can have at most 4 single-particle states. Each one of them can be in the single vacuum or up to position $\boldsymbol{x} = 2$. If we had included the sign qubit, then a mirror image with respect to the vacuum vertical line, would appear to the left.

We can now compare the representation of the full state of the system $|\Psi\rangle$ in these two discretizations. In the JLP basis, this would be given by

$$|\Psi\rangle = \prod_{i=1}^{\mathcal{V}} \int_{-\infty}^{\infty} d\phi_i \Psi(\phi_1, \cdots, \phi_{\mathcal{V}}) \, |\phi_1 \cdots \phi_{\mathcal{V}}\rangle \ , \tag{5.18}$$

with the limits of integrations replaced by finite boundaries, once the local Hilbert space at each position is truncated and by sums after discretization. In the single particle basis, this would simply read

$$|\Psi\rangle = \bigotimes_{l=1}^{\infty} |\psi\rangle^{(l)} \,, \tag{5.19}$$

where, after discretizaion, each component can be written as (in a momentum representation)

$$|\psi\rangle^{(l)} = \mathfrak{a}_0 |\Omega\rangle^{(l)} + \sum_{\mathbf{q}} \mathfrak{a}_{\mathbf{q}} |\mathbf{q}\rangle^{(l)} \,, \tag{5.20}$$

with $|\mathfrak{a}_0|^2 + \sum_{\mathbf{q}} |\mathfrak{a}_{\mathbf{q}}|^2 = 1$. Notice that the normalization $\langle \mathbf{q}|\mathbf{q}'\rangle = \delta_{\mathbf{q},\mathbf{q}'}$ of these basis states differs from the usual relativistic normalization, with $|\mathbf{q}\rangle = |\boldsymbol{p}\rangle^{\text{phys}}/\sqrt{2\omega_{\mathbf{q}}}$.

The final digitization step comes from replacing ∞ in the previous product by a single particle sector cut-off M, i.e. the maximum number of particle at any given point in the simulation, which we discuss below. An important question is how to define the full momentum space Fock operators in terms of the single particle sector Fock operators. These can be defined as

$$a_{\mathbf{q}} \equiv \lim_{M\to\infty} \frac{1}{\sqrt{M}} \sum_{l=0}^{M-1} a_{\mathbf{q}}^{(l)} \,, \tag{5.21}$$

with $a_{\mathbf{q}}^{(l)}, a_{\mathbf{q}}^{(l)\dagger}$ denoting chains of spin raising and lowering operators for each $\mathbf{q}$, and $(a_{\mathbf{q}}^{(l)\dagger})^2 = (a_{\mathbf{q}}^{(l)})^2 = 0$. However, once the Hilbert space in the number of single particle sectors, it is easily realized that this definition implies that the Fock operators do not obey the usual canonical relations. Nonetheless, for sufficiently large M, much larger than the typical occupancy of a momentum state, the bosonic commutation algebra is realized.

To observe this, let us give a small example. The single particle Fock operators can be represented as products of spin raising (lowering) operators $S^{\pm} = 1/2(\sigma^x \pm i\sigma^y)$. Besides having to obey the canonical commutation relations and the being vanishing when squared, they also must satisfy $a_{\mathbf{q}}^{(i)\dagger}|\Omega^{(i)}\rangle = |\mathbf{q}^{(i)}\rangle$, which provides a simple way to explicitly construct such operators. Fixing $N = 4$ qubits per register and $d = 1$, and working in a momentum basis, the particle can have momentum $\mathbf{q} \in [-7/2, 7/2]$. We have that

$$\begin{aligned} |\pm 1/2\rangle &\equiv |\downarrow\downarrow;\uparrow / \downarrow;\uparrow\rangle \,, \quad |\pm 3/2\rangle \equiv |\downarrow\uparrow;\uparrow / \downarrow;\uparrow\rangle \,, \\ |\pm 5/2\rangle &\equiv |\uparrow\downarrow;\uparrow / \downarrow;\uparrow\rangle \,, \quad |\pm 7/2\rangle \equiv |\uparrow\uparrow;\uparrow / \downarrow;\uparrow\rangle \,, \end{aligned} \tag{5.22}$$

and the empty state $|\Omega\rangle = |\downarrow\downarrow;\downarrow;\downarrow\rangle$. By direct inspection one has that the single particle momentum Fock operators read

$$a_{-1/2}^{(i)\dagger} \equiv S_0^+ \,, \qquad a_{-3/2}^{(i)\dagger} \equiv S_2^+ S_0^+ \,, \qquad a_{-5/2}^{(i)\dagger} \equiv S_3^+ S_0^+ \,, \qquad a_{-7/2}^{(i)\dagger} \equiv S_3^+ S_2^+ S_0^+ \,, \tag{5.23}$$

where $a^{(i)\dagger}_{+|\mathbf{q}|} = S^+_1 a^{(i)\dagger}_{-|\mathbf{q}|}$, and we label 0 as the occupancy qubit and 1 the sign qubit and lowest digit in the abs register 2 and 3 the highest value digit. The position space representation is identical. Using this map, it is simple to check that $a^{(i)\dagger}_{\mathbf{q}}|\Omega^{(i)}\rangle = |\mathbf{q}^{(i)}\rangle$ and $(a^{(i)\dagger}_{\mathbf{q}})^2 = (a^{(i)}_{\mathbf{q}})^2 = 0$, so that Eq. (5.21), at finite M, implies

$$[a_{\mathbf{q}}, a^\dagger_{\mathbf{q}}] = \frac{1}{M}\sum_{i=0}^{M-1}\left[\{a^{(i)}_{\mathbf{q}}, a^{(i)\dagger}_{\mathbf{q}}\} - 2a^{(i)\dagger}_{\mathbf{q}}a^{(i)}_{\mathbf{q}}\right] = 1 + O\left(\frac{\mathfrak{n}_{\mathbf{q}}}{M}\right), \tag{5.24}$$

where 1 is a unit matrix in the space spanned by $|\mathbf{q}\rangle$ and $|\Omega\rangle$, as well as $[a_{\mathbf{q}}, a^\dagger_{\mathbf{q}'}] = O(\mathfrak{n}_{\mathbf{q}}/M)$ where $\mathfrak{n}_{\mathbf{q}}$ is the occupation number of the mode $\mathbf{q}$. Thus, as long as M is much larger than the occupancy of a given momentum mode, then the canonical relations hold.

An important point is that not all available states are physical. For example, states with occupation $|\downarrow\rangle$ but finite $\mathbf{q}$ are unphysical and are excluded. Thus, one must ensure that any operation acting on the system never connects physical and unphysical states. Also, any physical state needs to be Bose-symmetric. Although, as is known from conventional QFT calculations, Bose-symmetry only leads to overall combinatorial factors, it turns out, as we detail below, that simulating the symmetrized wave-functions is easier, since the free Hamiltonian is diagonal in the Bose-symmetrized basis.

Finally, we can compare this basis with the one from JLP. This approach requires $O(M\log_2\mathcal{V})$ qubits, so unlike JLP it scales logarithimically with the simulation volume. Thus, for dilute systems where $M \ll \mathcal{V}$, this approach seems preferable to JLP. In particular, it seems ideal for scattering at high energy in QCD, where the number of partons is not large, but they can explore widely separated momentum modes. Here we recall, that although at high energy it would seem that one can generate arbitrarily large numbers of particles (i.e. to go from a n particle sector to a $n+1$ particle costs an infinitesimal amount of energy), we recall that in theories like QCD, other scales become important. This point was already made for DIS in chapter 1, where we saw the emergence of the Ioffe time scale, much larger than the typical interaction time scale. In addition, at high energies a partonic description of QCD emerges, where the above time scales fix the relevant number of degrees of freedom.

5.2 The quantum algorithm

As outlined in the previous chapter, given the above digitization of the QFT in terms of a spin chain/qubits, we are now in position to outline the several steps of the quantum simulation algorithm, already introduced. Here we will focus on the implementation of the single particle basis approach, and a broad comparison to JLP's approach is provided.

The implementation of the quantum simulation algorithm is depicted in Fig. 5.3. We give a detail discussion of each component in the following sections.

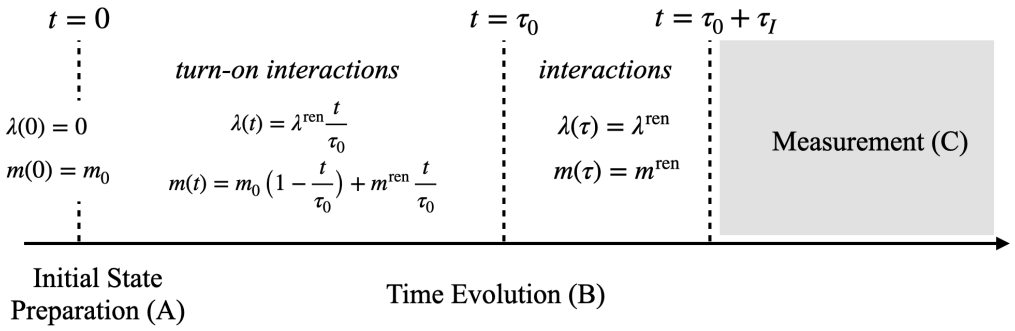

Figure 5.3: Diagrammatic representation for the overall quantum strategy to simulate a scattering process. One initially prepares a collection of wave packets (A) in the free theory that are then evolved to wave packets of the full theory. These are then time evolved according to the full Hamiltonian (B), after which one applies a sensible measurement protocol to extract the physical cross-sections (C). On top of this, one must relate the bare and renormalized parameters of the theory, which is done via a linear map, to be discussed. Figure taken from [7].

5.2.1 Initial state preparation

Initial state preparation, unlike the JLP approach, is remarkably simple in the single particle basis. It can be divided in the following steps.

1. Prepare $\mathfrak{n} \ll M$ wave-packets in the free theory, centered around $\boldsymbol{x} = 0$ and $\boldsymbol{p} = 0$. The parameter $\mathfrak{n}$ stands for the typical number of initial state particles, thus $\mathfrak{n} \sim 2$. In case one would like to prepare two colliding proton states then the lowest value would be $\mathfrak{n} \sim 6$.

2. Each wave-packet is characterized by position and momentum space widths $(\Delta\boldsymbol{x}, \Delta\boldsymbol{p})$[2]. We require that $\Delta\boldsymbol{x} \sim 1/m$, so that the wave-packet is macroscopically well resolved. Although considering Gaussian wave-packets is sufficient, in fact the particular shape of the wave-packet is not important as long as it decays (at least) exponentially at the asymptotic regions.

3. After each wave-packets is prepared, one displaces the wave-packets in position and momentum space to the correct initial conditions. In the typical case $\mathfrak{n} = 2$, one would locate one of the wave-packets at spatial position $L \gg 1$ and with the initial particle momentum $\boldsymbol{p}$, while the other wave-packet would be located at $-L$, with momentum $\sim -\boldsymbol{p}$. In a more generic case, the only condition one should require is that the supports of different wave-packets do not overlap.

[2]These are related by the Heisenberg relation.

4. The next step consists in Bose-symmetrizing the wave-packets. In the single particle basis, as we will show below, this is particularly simple since occupied and vacuum states form the computational basis.

5. Finally, the wave-packets must be let to evolve by slowly turning on the coupling and linearly displacing the parameters from the bare to the dressed values. After this process is concluded, one has prepared the initial state wave-packets in the full theory.

Let us now detail each of these steps. Wave-packets comprised of single-particle states $|\mathbf{q}\rangle$, located at the origin $(\bar{\mathbf{x}}_i, \bar{\mathbf{p}}_i) = (0, 0)$, can be written as

$$|\Psi\rangle = \frac{1}{\sqrt{\mathcal{V}}} \sum_{\mathbf{q}} \Psi_{\mathbf{q}} |\mathbf{q}\rangle \,, \tag{5.25}$$

where we have dropped the (l) super-index to simplify notation. Here $\Psi_{\mathbf{q}}$ is a real, positive and strongly localized distribution. The exact shape of $\Psi_{\mathbf{q}}$ is not relevant, as long as it decays sufficiently fast in the asymptotic regions, and we assume that its width $\boldsymbol{\Delta}\mathbf{p}$ ($|\Delta\mathbf{x}| \sim |\Delta\mathbf{p}|^{-1}$) is order m.

To generate such a distribution we assume that we have access to a fiducial state corresponding to a register representing a single particle in the vacuum state $|\Omega\rangle$ (see (5.17)). Several algorithms [175–177] exist that can exactly load such a template distribution, as long as it is integrable, but they require an exponential number of basic gate operations (i.e. they require at least $O(\mathcal{V})$ gate operations). In the present case, the fact that the exact shape of the distribution is not critically important means that a simpler algorithm can be implemented which only requires a logarithmic large number of basic operations.

In $d = 1$ the algorithm can be easily detailed[3]. The first step consists in flipping the occupation qubit using a σ^x gate and the sign qubit by a Hadamard gate

$$|\Omega\rangle = |\downarrow^{\otimes N^{\text{abs}}}, \downarrow, \downarrow\rangle \xrightarrow{\sigma^x, H} \frac{1}{\sqrt{2}} \Big[|\downarrow^{\otimes N^{\text{abs}}}, \uparrow, \uparrow\rangle + |\downarrow^{\otimes N^{\text{abs}}}, \downarrow, \uparrow\rangle \Big] \,. \tag{5.26}$$

This splits the state into a negative and positive branch, so that in what follows the algorithm can be applied in each branch independently. Considering the positive branch, the remaining $N^{\text{abs}} \sim \log_2(N_s)$ qubits get rotated by an angle $\theta_k = \pi/4 - \epsilon_k$,

$$|\downarrow\rangle^{(k)} \to \cos(\theta_k) |\downarrow\rangle^{(k)} + \sin(\theta_k) |\uparrow\rangle^{(k)} \,. \tag{5.27}$$

where $k \in [0, N^{\text{abs}} - 1]$ and $\epsilon_k \in [0, \pi/4)$. Thus for each $|\downarrow\rangle^{(k)}$ the state gets a $\cos(\theta_k)$ coefficient, while each $|\uparrow\rangle^{(k)}$ receives a $\sin(\theta_k)$ contribution; an illustrative example of the algorithm can be found in appendix 5.A.

[3] It is easily extended to higher dimensions.

Once each wave-packet has been prepared we displace them, such that they are widely separated from each other and their centers are set accordingly with the kinematics of the problem. This operation is achieved by using the translation operator $T_{\mathbf{n}}$ ($T_{\mathbf{q}}$) in position space (momentum space), defined as

$$T_{\mathbf{n}}|\mathbf{q}\rangle = e^{-i\,2\pi\mathbf{n}\cdot\mathbf{q}/N_s}|\mathbf{q}\rangle\,, \qquad T_{\mathbf{n}}|\Omega\rangle = |\Omega\rangle\,, \tag{5.28}$$

where $\mathbf{x} = \mathbf{n}a_s$ and $\mathbf{n} = (n_1, \dots n_d)$. The translation operator can be written as a combination of several one-dimensional translation operators, $T_{\mathbf{n}} \equiv \bigotimes_{k=1}^{d} T_{n_k}^{(k)}$, each of which can be further decomposed in terms of the composition of single step translations, i.e. $T_{n_k}^{(k)} = (T_1^{(k)})^{n_k}$ ($T_{n_k}^{(k)} = (T_1^{(k)\dagger})^{|n_k|}$) if $n_k > 0$ ($n_k < 0$). Therefore, it is enough to know how to implement $T_1^{(k)}$.

In Fig. 5.4 (a) we first detail the generic form of the translation operator in $d = 1$. Notice that one has two gates since depending on the sign of the momentum, the translation operator acts differently. This is taken into account by the control qubits. In Fig. 5.4 (b) we illustrate the implementation of the $T_1^{(k)}$ (dropping the label k, since we consider $d = 1$) operator in terms of basic gate operations. Here we introduced the gate $R_t \equiv \mathrm{diag}(1, \exp\{-2\pi i/2^t\})$, and the particular decomposition of the single step translation operator in terms of this basic gate follows from the binary decomposition of the phase in Eq. (5.28). The construction for the Fourier pair operator $T_{\mathbf{q}}$ is done using exactly the same circuit, after one has changed from $|\mathbf{q}\rangle \to |\mathbf{n}\rangle$.

By iterative composition of the above operators, the full translation operator can be constructed in d dimensions. Since one has to apply these operations for each occupied particle register and in each dimension, the overall number of basic gate operations is $O(M\log(\mathcal{V}))$[4], where we assume that the lattice is sufficiently large, such that one never reaches the boundaries, where the treatment would fail.

Once the initial state wave-packets have been prepared and translated to the adequate initial positions, the state being stored $|\Psi_i\rangle$ is comprised by $M - \mathfrak{n} \approx M$ empty particle registers and the remaining registers storing the translated wave-packets. The state explicitly reads

$$|\phi\rangle \equiv |\Psi_0, \Psi_1, \dots \Psi_{\mathfrak{n}-1}, \Omega, \dots, \Omega, \dots\rangle\,. \tag{5.29}$$

The ordering of the individual particle registers is arbitrary, and all permutations are physically equivalent. Combining them all into a single equidistributed state corresponds to preparing the Bose-symmetrized state from the un-symmetrized one in Eq. (5.29). It is convenient to work with Bose-symmetrized states since, as it will become apparent in the next section, the Hamiltonian action becomes easier to compute when acting on the sub-space of Bose-symmetrized states. Thus, we want to prepare the state

$$|\phi_B\rangle \equiv \frac{1}{\sqrt{\mathcal{N}}}\sum_P \hat{P}|\phi\rangle\,, \tag{5.30}$$

[4]In fact, it one should replace M by $\mathfrak{n} \ll M$, but this difference is not important since this cost is already sub-leading.

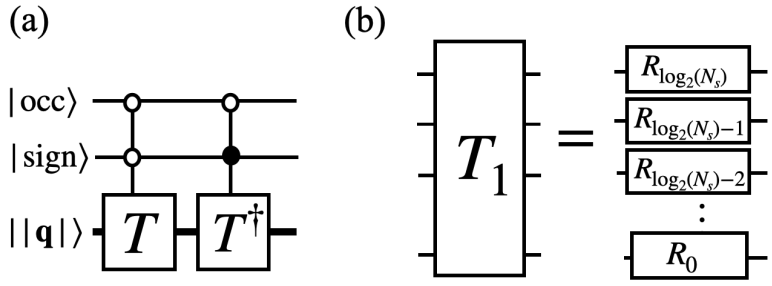

Figure 5.4: (a) Translation operator for $d = 1$, where we abbreviate $T \equiv T_{n_1}^{(1)} = (T_1^{(1)})^{|n_1|}$ for $n_1 > 0$ and $(T_1^{(1)\dagger})^{|n_1|}$ for $n_1 < 0$. A white (black) circle indicates control by the $|\uparrow\rangle$ ($|\downarrow\rangle$) state. (b) Single step translation operator decomposition in terms of basic single qubit gates. Figure taken from [7].

where $\hat{P}$ is the Bose permutation operator and $\mathcal{N} = M!/(M - \mathfrak{n})!$ is the number of Bose permutations.

To get $|\phi_B\rangle$ from $|\phi\rangle$ we present an algorithm that consists in introducing an ancilla register which generates a set of code words (binary numbers), each corresponding to a set of SWAP operations one has to apply on the physical particle registers. We discuss this algorithm in detail in appendix 5.A; here we detail the almost trivial case of $\mathfrak{n} = 1$, $M = 2$, where the set of necessary operations would read

$$\begin{aligned} |\Psi,\Omega\rangle|0\rangle \xrightarrow{H} |\Psi,\Omega\rangle\frac{1}{\sqrt{2}}\big[|0\rangle + |1\rangle\big] \xrightarrow{\text{CSWAP}} \frac{1}{\sqrt{2}}\big[|\Psi,\Omega\rangle|0\rangle + |\Omega,\Psi\rangle|1\rangle\big] \\ \xrightarrow{\text{CNOT}} \frac{1}{\sqrt{2}}\big[|\Psi,\Omega\rangle + |\Omega,\Psi\rangle\big]|0\rangle = |\phi_B\rangle\,. \end{aligned} \tag{5.31}$$

The generic case is similar to this simple example, however in general the algorithm is stochastic since $\mathcal{N}$ is not an integer power of two. Thus one will generate extra states that need to be eliminated using non-unitary operations. This is discussed in depth in the appendix associated to this section. Apart from this point, the general algorithm does not differ much from the example given here.

In a final step, after symmetrization is completed, one would slowly turn-on the interaction such that the analogous wave-packets of the full theory are prepared. We discuss how the turn-on is performed further in the renormalization section, but we would like to point out that while doing this Bose-symmetry is not broken and more importantly the previously empty registers start to get populated, since the wave-function in the full theory will consist of a superposition of different Fock space's contributions[5].

This algorithm can be contrasted with the one presented by JLP [64, 65]. In this case, one would first prepare a non-interacting vacuum Gaussian state (using an adequate

[5]We note that in the QCD/DIS context it would be natural to identify the turn-on time τ_0 with the Ioffe time. The algorithm is however agnostic to these details and thus we refrain from further discussing this topic, already detailed above.

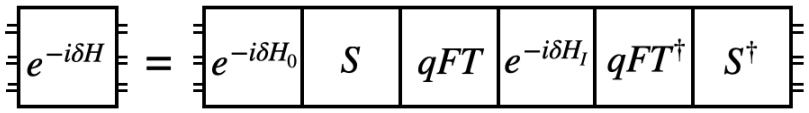

Figure 5.5: Implementation of the time evolution operator, here given for a single Trotter step δ. Here S denotes the squeezing transformation and qFT the quantum Fourier transform. Figure taken from [7].

algorithm to load the Gaussian template). In a second step, a Trotter-Suzuki scheme is applied to provide an unitary realization of the action of the Fock operators on the vacuum state. These operators can be parametrized as a linear combination of $\phi_{\mathbf{x}}$ and $\pi_{\mathbf{x}}$, with the exact form of the linear combination determining the form of the final wave-packet. In addition, Bose-symmetry is ensured by the explicit construction of the field operators[6]. Thus our approach differs from JLP's mainly on the fact that the vacuum is a computational basis state in our approach and Bose-symmetrization has to be explicitly imposed in our case. In addition, no Trotter-Suzuki scheme is needed in our construction.

5.2.2 Time evolution

Once the initial state in the full theory is prepared one can time evolve it, allowing for interactions to occur. As mentioned in the previous chapter, we consider a first order Trotter-Suzuki scheme, with $N_\delta = (t-t_0)/\delta$ steps to implement the time evolution operator,

$$U(t,t_0) \equiv e^{-iH(t-t_0)} = \left(e^{-iH\delta}\right)^{N_\delta} + O(\delta^2) = (e^{-iH_I\delta}e^{-iH_0\delta})^{N_\delta} + O(\delta^2) \equiv (U_I U_0)^{N_\delta} + O(\delta^2)\,. \tag{5.32}$$

Here we split the evolution operator in a non-interacting piece $U_0 \equiv \exp\{-iH_0\delta\}$ and an interacting one $U_I \equiv \exp\{-iH_I\delta\}$, where H_0 is given by the quadratic terms and H_I by the ϕ^4 interaction term in Eq. (5.11). The free part of the evolution operator is naturally implemented in momentum basis, while, due to the locality of interactions, the interacting piece is more naturally implemented in the position basis. Thus, we implement each term in these two different basis, performing a basis transformation in between, consisting in the application of squeezing operation and Fourier transform. This approach is detailed in Fig. 5.5, and we now proceed to detail each step in more detail. Further discussion is provided in appendices 5.B, 5.C and 5.D.

[6]It is difficult to give a more quantitative discussion, since the original proposal [64, 65] is itself only given at a rather conceptual level, unlike our construction.

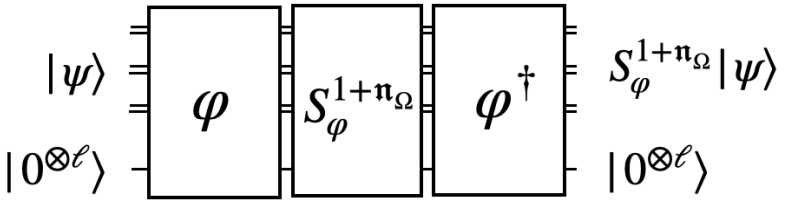

Figure 5.6: Quantum circuit implementing U_0. It required $O(M \mathrm{poly}\log(\mathcal{V}))$ basic gate operations and 2ℓ ancilla qubits. Double lines indicate particle registers (including $|\mathbf{q}|$, sign and occupation number qubits). Figure taken from [7].

Free part U_0

The infinitesimal time evolution operator U_0 is given by

$$U_0 \equiv \exp\Big\{ -i\delta \sum_{\mathbf{q}} \omega_{\mathbf{q}}\, a^\dagger_{\mathbf{q}} a_{\mathbf{q}} \Big\} = \exp\Big\{ -\frac{i\delta}{M} \sum_{\mathbf{q}} \omega_{\mathbf{q}} \Big[\sum_{i=0}^{M-1} a^{(i)\dagger}_{\mathbf{q}} a^{(i)}_{\mathbf{q}} + \sum_{i\neq j=0}^{M-1} a^{(i)\dagger}_{\mathbf{q}} a^{(j)}_{\mathbf{q}} \Big] \Big\}\,. \tag{5.33}$$

where U_0 is diagonal in the momentum space representation, and Bose-symmetrization has been explicitly taken into account. A simple calculation leads that the application of U_0 to a state gives rise to a phase

$$U_0\,|\psi\rangle = e^{-\frac{i\delta}{M}\sum_{\mathbf{q}} \omega_{\mathbf{q}} \mathfrak{n}_{\mathbf{q}}(1+\mathfrak{n}_\Omega)} |\psi\rangle = S_\varphi^{1+\mathfrak{n}_\Omega} |\psi\rangle\,, \tag{5.34}$$

where $S_\varphi \equiv \exp\{-i\frac{\delta}{M}\varphi\}$, $\varphi \equiv \sum_{\bar{n}} \omega_{\mathbf{q}} \mathfrak{n}_{\mathbf{q}}$ is the total energy of all occupied states, and $\mathfrak{n}_{\mathbf{q}}$ ($\mathfrak{n}_\Omega$) the number of registers with momentum $\mathbf{q}$ (empty registers), while $\omega_{\mathbf{q}}$ is the continuum dispersion relation. The factor $\mathfrak{n}_{\mathbf{q}}(1+\mathfrak{n}_\Omega)$ is a consequence of the decomposition in the last equality in Eq. (5.33), where we split the operator $a^\dagger_{\mathbf{q}} a_{\mathbf{q}}$ into a diagonal term $\{i,i\}$ and a off-diagonal contribution $\{i,j\}$. The diagonal term only gives a phase if the state is occupied, thus accounting for the 1 contribution to the phase in the last equality in Eq. (5.34). The off-diagonal piece only contributes if i is an empty register and j is occupied (or vice-versa). Although by itself this term swaps the content of the two registers (and thus leading to a non-diagonal action of U_0) it is easy to show that since we are working with Bose-symmetric state, the overall action of U_0 is diagonal[7]. The number of times one can get such a phase is given by the number of combinations between each occupied state and all empty registers; i.e. $\mathfrak{n}_\Omega$. In Fig. 5.6 we illustrate the circuit implementing U_0 (see Eq. (5.34)).

The idea is to first compute the phase φ, storing it in an ancilla register (quantum memory) using 2ℓ ancilla qubits. See Fig. 5.7 for the sub-circuit performing this operation and the discussion in appendix 5.B. In the diagram shown, the circuit $\boxed{\omega}$ that computes

[7]This makes clear why it is advantageous to work with Bose-symmetrized states.

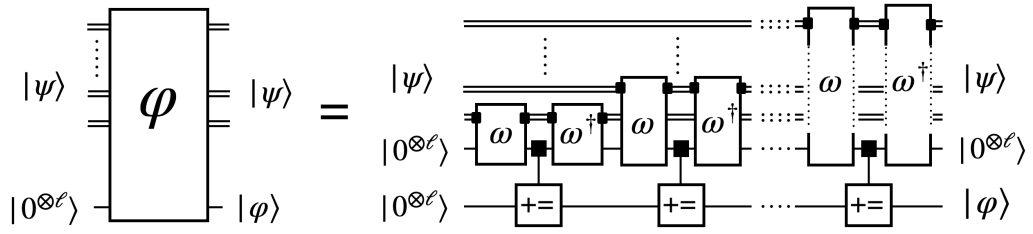

Figure 5.7: Quantum sub-circuit that computes and stores φ in memory. As mentioned in the text and respective appendix, $\boxed{\omega}$ is an (arithmetic) oracle computing $\omega(\mathbf{q})$ given an input $|\mathbf{q}\rangle$, and $\boxed{+=}$ is the quantum-addition circuit [8, 9]. The ■ symbol appearing in the gate $\boxed{+=}$ denotes that the associated register is an input. The relevant particle register input for the $\boxed{\omega}$ gates is denoted by (small) black boxes accordingly. Figure taken from [7].

$\omega_{\mathbf{q}}$ is treated as a quantum "oracle". The number of ancilla registers 2ℓ is determined by the precision with which we wish to compute $\omega_{\mathbf{q}}$ from $\mathbf{q}$, which should be similar to the number of qubits necessary to realize $\mathbf{q}$ in one dimension, i.e. $\ell \sim O(\log(\mathcal{V})/d)$. The number of gate operations included in $\boxed{\omega}$ is $O(\text{poly}\log(\mathcal{V}))$.

In a second step, once φ is stored in memory, one applies $O(M)$ diagonal phase rotations $S_{\varphi}^{1+\mathfrak{n}_\Omega}$. The details of this operation are discussed in appendix 5.B. Finally, one clears the memory register, leading to a total of $O(M)$ $\boxed{+=}$ and $\boxed{\omega}$ gates. Thus, the overall gate complexity of the circuit implementing U_0 is $O(M\,\text{poly}\log(\mathcal{V}))$, per Trotter step[8].

Squeezing Transformation

As mentioned above, after applying U_0 in each infinitesimal time step, one must perform a transformation from the single-particle representation in momentum space to position space. In relativistic theories, these two spaces are not simply related by a Fourier transform[9], rather one must perform a squeezing operation [179] followed by a (quantum-) Fourier transformation.

This construction can be formulated as follows. The position space Fock operators

[8] In essence, the algorithm introduced here was first proposed by Zalka [178], in a somewhat simpler form.

[9] This is can be seen from, for example, the relation

$$|\boldsymbol{x}\rangle = \phi_{\boldsymbol{x}}\,|\Omega\rangle = \int \frac{d^d\boldsymbol{p}}{(2\pi)^d}\frac{e^{i\boldsymbol{p}\cdot\boldsymbol{x}}}{\sqrt{2E_{\boldsymbol{p}}}}a^\dagger_{-\boldsymbol{p}}\,|\Omega\rangle\ ,$$

where the energy factor prevents the last relation to be a direct Fourier transform.

are given by

$$a_{\mathbf{n}} \equiv \frac{1}{\sqrt{2}}\big(\phi_{\mathbf{n}} + i\pi_{\mathbf{n}}\big)\,, \qquad a^{\dagger}_{\mathbf{n}} \equiv \frac{1}{\sqrt{2}}\big(\phi_{\mathbf{n}} - i\pi_{\mathbf{n}}\big)\,, \tag{5.35}$$

with the commutation relations $[a_{\mathbf{n}}, a^{\dagger}_{\mathbf{n}'}] = \delta_{\mathbf{n},\mathbf{n}'}$, and the single-particle decomposition $a_{\mathbf{n}} \equiv \sum_i a^{(i)}_{\mathbf{n}}/\sqrt{M}$, $a^{\dagger}_{\mathbf{n}} \equiv \sum_i a^{(i)\dagger}_{\mathbf{n}}/\sqrt{M}$.

Let us introduce the Fourier conjugate operators $A_{\mathbf{q}}$ of $a_{\mathbf{n}}$ as

$$a_{\mathbf{n}} \equiv \frac{1}{\sqrt{\mathcal{V}}} \sum_{\mathbf{q}} A_{\mathbf{q}}\, e^{i2\pi \mathbf{n}\cdot\mathbf{q}/N_s}\,, \tag{5.36}$$

with an analogous relation holding for the Hermitian conjugate pairs. The $\{A_{\boldsymbol{q}}\}$ operators are related [179] to the momentum space Fock operators $a_{\mathbf{q}}$, $a^{\dagger}_{\mathbf{q}}$ by

$$A_{\mathbf{q}} \equiv \frac{1}{2}\big[\omega_{\mathbf{q}}^{-\frac{1}{2}} + \omega_{\mathbf{q}}^{\frac{1}{2}}\big] a_{\mathbf{q}} + \frac{1}{2}\big[\omega_{\mathbf{q}}^{-\frac{1}{2}} - \omega_{\mathbf{q}}^{\frac{1}{2}}\big] a^{\dagger}_{-\mathbf{q}}\,, \tag{5.37}$$

and an analogous relation for the Hermitian conjugate. This transformation is known in the literature [180–182] to be a (two-mode) squeezing transform. In appendix 5.C we show that the momentum space Fock operators can be obtained by a similarity transformation involving the squeezing operator S

$$A_{\mathbf{q}} = S a_{\mathbf{q}} S^{\dagger}, \qquad A^{\dagger}_{\mathbf{q}} = S a^{\dagger}_{\mathbf{q}} S^{\dagger}, \tag{5.38}$$

where $S \equiv \prod_{\mathbf{q}} S_{\mathbf{q}}$ and

$$S_{\mathbf{q}} \equiv \exp\big\{ - z_{\mathbf{q}} [a^{\dagger}_{\mathbf{q}} a^{\dagger}_{-\mathbf{q}} - a_{-\mathbf{q}} a_{\mathbf{q}}]\big\}\,, \tag{5.39}$$

is an unitary operator with $z_{\mathbf{q}} \equiv \frac{1}{2}\log(\omega_{\mathbf{q}})$. Thus, implementing the circuit for Eq. (5.39), followed by a qFT, gives the correct transformation between single particle sectors in position and momentum space, which we proceed to detail.

The circuit implementing $S_{\mathbf{q}}$ is given in Fig.5.9, which is simply a decomposition over all $\mathcal{V}$ momentum modes. A further step consists in factoring, for each $\boldsymbol{q}$, the squeezing operator into $M(M-1)/2$ squeezing operators over particle pairs $i \neq j$, $i, j = 0, \ldots M-1$. This decomposition is used within a Trotter-Suzuki scheme with an error $O([\mathfrak{n}_{\mathbf{q}} z_{\mathbf{q}}/M]^2)$, where $\mathfrak{n}_{\mathbf{q}}$ is the occupation number of the mode $\mathbf{q}$ of the state the operator acts on. This leads to a decomposition with $O(M^2\mathcal{V})$ terms

$$S = \prod_{\mathbf{q},\langle i\neq j\rangle} S_{\mathbf{q},ij}\,, \tag{5.40}$$

where

$$S_{\mathbf{q},ij} \equiv \exp\big\{ - \frac{z_{\mathbf{q}}}{M} [a^{(i)\dagger}_{\mathbf{q}} a^{(j)\dagger}_{-\mathbf{q}} - a^{(j)}_{-\mathbf{q}} a^{(i)}_{\mathbf{q}}]\big\}\,. \tag{5.41}$$

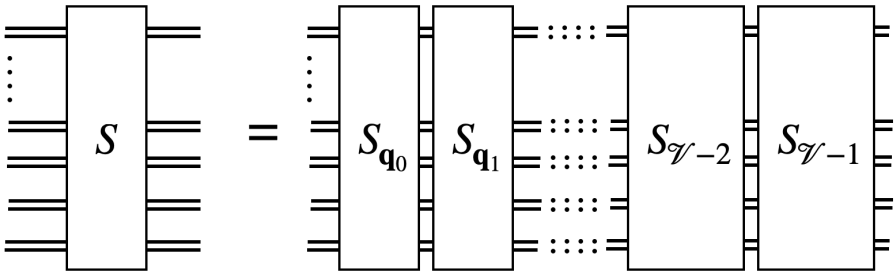

Figure 5.8: Squeezing operator S decomposition in terms of squeezing operators acting on single momentu modes $S = \prod_{\mathbf{q}=\mathbf{q}_0}^{\mathbf{q}=\mathbf{q}_{\mathcal{V}-1}} S_{\mathbf{q}}$. The Trotter error in this factorization in zero, since the Fock operators of different momentum modes always commute. Figure taken from [7].

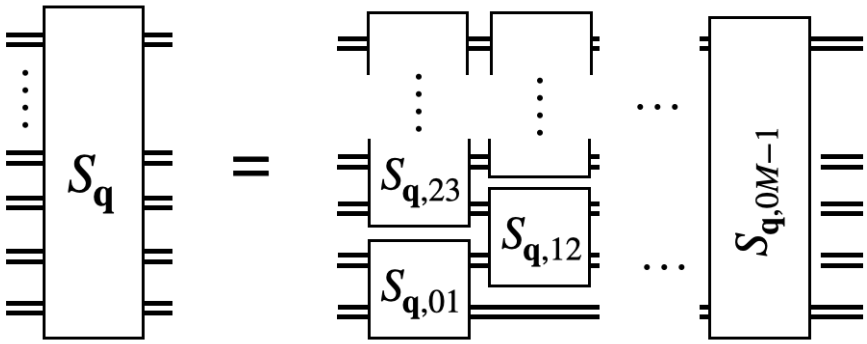

Figure 5.9: Decomposition of $S_{\boldsymbol{q}}$ into $M(M-1)/2$ pair-wise squeezing operators $S_{\mathbf{q},ij}$ with $i \neq j$. Note that each operator is even in $\{i,j\}$ and thus $S_{\mathbf{q},ij}(z_{\mathbf{q}})S_{\mathbf{q},ji}(z_{\mathbf{q}}) = S_{\mathbf{q},ij}(2z_{\mathbf{q}})$. Figure taken from [7].

The circuit decomposition is given in Fig. 5.9.

Using the mapping between spin raising and lowering operators and the creation and annihilation operators detailed in section 5.1, $S_{\mathbf{q},ij}$ can be written as

$$S_{\mathbf{q},ij} \equiv \exp\big\{ -i\frac{z_{\mathbf{q}}}{M}\sigma^y_{\mathbf{q},ij}\big\}\,, \tag{5.42}$$

where $\sigma^y_{\mathbf{q},ij} \equiv (-i)[a^{(i)\dagger}_{\mathbf{q}}a^{(j)\dagger}_{-\mathbf{q}} - a^{(j)}_{-\mathbf{q}}a^{(i)}_{\mathbf{q}}]$. In the matrix representation of the $\mathfrak{N}$ occupation and momentum qubits spanning $\{|\mathbf{q}\rangle \otimes |-\mathbf{q}\rangle\ ,\ |\Omega\rangle \otimes |\Omega\rangle\}$, this can be written as

$$\sigma^y_{\mathbf{q},ij} = \begin{pmatrix} 0 & \dots & 0 & -i \\ 0 & \ddots & & 0 \\ \vdots & & \ddots & \vdots \\ i & 0 & \dots & 0 \end{pmatrix} \equiv \sigma^y_{\mathfrak{N}}\,. \tag{5.43}$$

We note that $\mathfrak{N}$ here depends on the pair $\{i,j\}$ and on $\boldsymbol{q}$, and it stands for the effective dimension of the associated spin space, depending on the decomposition in terms of spin operators.

Implementing Eq. (5.42) can be done using a strategy similar to the one mentioned in section 4.2. First, one transforms Eq. (5.43) to a block-diagonal form $\sigma^y_{\mathfrak{N}}$, using the binary increment operator $I_{\mathfrak{N}}$ ($I_1 = \sigma^x$, see appendix 5.C)

$$I^\dagger_{\mathfrak{N}} \sigma^y_{\mathfrak{N}} I_{\mathfrak{N}} = \begin{pmatrix} 0 & \dots & \dots & 0 \\ \vdots & 0 & & 0 \\ \vdots & & \ddots & i \\ 0 & 0 & -i & 0 \end{pmatrix} \equiv \tilde{\sigma}^y_{\mathfrak{N}} \,. \tag{5.44}$$

It is easy to notice that this operator satisfies the recursion law

$$\tilde{\sigma}^y_{\mathfrak{N}} = \frac{1}{2}(1-\sigma^z) \otimes \tilde{\sigma}^y_{\mathfrak{N}-1} \,, \tag{5.45}$$

where $\tilde{\sigma}^y_1 = -\sigma^y$. Expanding this relation we obtain

$$\tilde{\sigma}^y_{\mathfrak{N}} = \Big[\bigotimes_{i=2}^{\mathfrak{N}} \frac{1}{2}(1-\sigma^z) \Big] \otimes \tilde{\sigma}^y_1 \,. \tag{5.46}$$

The operator $(1-\sigma^z)$ is diagonal, thus one only needs to diagonalize $\tilde{\sigma}^y_1 = -\sigma^y = -\bar{S} H \sigma^z H \bar{S}^\dagger$, which follows from Eq. (4.5)[10]. The end results then reads

$$S_{\mathbf{q},ij} = I_{\mathfrak{N}} \, (1 \otimes \dots 1 \otimes H\bar{S}^\dagger) \, R\left[\frac{z_{\mathbf{q}}}{M}\right] (1 \otimes \dots 1 \otimes \bar{S}H) \, I^\dagger_{\mathfrak{N}} \,, \tag{5.47}$$

where $R[\frac{z_{\mathbf{q}}}{M}] \equiv \exp\{ i \frac{z_{\mathbf{q}}}{M} \left[\otimes_{i=2}^{\mathfrak{N}} \frac{1}{2} [1-\sigma^z]_i \right] \otimes \sigma^z \}$ is a simple controlled (diagonal) σ^z-rotation. This construction is depicted in Fig. 5.10.

Overall, the implementation of the squeezing transformation entails $O(M^2 \mathcal{V} \operatorname{poly}\log(\mathcal{V}))$ elementary gate operations (per Trotter step). The $\operatorname{poly}\log(\mathcal{V})$ contribution comes from the complexity of the bit increment $I_{\mathfrak{N}}$ and controlled z-rotation $R(z_{\mathbf{q}}/M)$. The M^2 factor is due to the loop over pairs of particle registers, while $\mathcal{V}$ is due to the decomposition in the momentum modes $\mathbf{q}$.

Quantum Fourier Transform

The next step is to apply the quantum Fourier Transform algorithm, following Eq. (5.36). This can be done using the algorithm implementation discussed in appendix 4.A, but adjusting for the specific characteristic of our digitization. The qFT algorithm is only applied if the particle register is occupied and it needs to be applied once per dimension

[10] Notice that here $\bar{S}$ denotes the phase gate, to avoid confusion with the squeezing operator S.

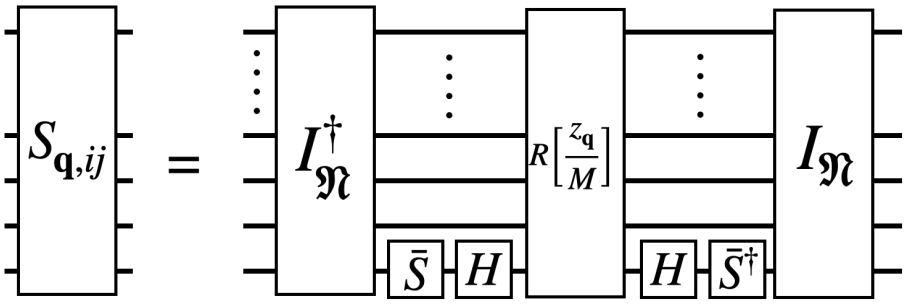

Figure 5.10: Circuit implementation of $S_{\mathbf{q},ij}$, using the bit-increment operator $I_{\mathfrak{N}}$ and the diagonal single qubit rotation $\exp\{i\frac{z_{\mathbf{q}}}{M}\sigma^z\}$. The circuit involves $\mathfrak{N}$ qubits that make up $(-i)[a^{(i)\dagger}_{\mathbf{q}}a^{(j)\dagger}_{-\mathbf{q}} - a^{(j)}_{-\mathbf{q}}a^{(i)}_{\mathbf{q}}]$. Figure taken from [7].

and per register. In addition, since we are dealing with signed integers, we should consider instead the symmetric qFT algorithm introduced in [10].

To apply this transformation, we first bring the states (see Eqs. (5.14) and (5.20)) to the standard form for the symmetric qFT. This is done by first rotating the sign qubits, and then using them as controls (i.e. deciding if the number is positive or negative) over the qubits storing the absolute value. This operation is detailed in Fig. 5.11 and it requires $O(M\text{poly}\log(\mathcal{V}))$ elementary gate operations.

Interaction part U_I

Once the transformation to the single-particle position space basis has been performed, one can apply the U_I evolution operator, using the locality of interactions.

The ϕ^4 interaction term can be decomposed into $\mathcal{V}$ Trotter steps per time step, leading to

$$U_I = \exp\{-i\delta\sum_{\mathbf{n}}\frac{\lambda}{4!}\phi^4_{\mathbf{n}}\} = \prod_{\mathbf{n}}\exp\{-i\frac{\delta\lambda}{4!}\phi^4_{\mathbf{n}}\} \equiv \prod_{\mathbf{n}}U_{I,\mathbf{n}}\,, \tag{5.48}$$

where $U_{I,\mathbf{n}}$ is a decomposition over $\mathcal{V}$ positions. To implement each one of these operators, we use that the field operator can be written as $\phi_{\mathbf{n}} \equiv \sum_{i=0}^{M-1}\phi^{(i)}_{\mathbf{n}}/\sqrt{M}$, where

$$\phi^{(i)}_{\mathbf{n}} \equiv \frac{a^{(i)}_{\mathbf{n}} + a^{(i)\dagger}_{\mathbf{n}}}{\sqrt{2}} = \frac{1}{\sqrt{2}}\begin{pmatrix} 0 & \dots & 0 & 1 \\ 0 & \ddots & & 0 \\ \vdots & & \ddots & \vdots \\ 1 & 0 & \dots & 0 \end{pmatrix} \equiv \frac{1}{\sqrt{2}}\sigma^x_{\mathfrak{N}}\,, \tag{5.49}$$

with $\sigma^x_{\mathfrak{N}}$ the $\mathfrak{N}$-qubit operator decomposition of $\phi^{(i)}_{\mathbf{n}}$, comprised of the qubits that span $\{|\mathbf{n}\rangle, |\Omega\rangle\}$, as outlined in section 5.1. Thus we observe that the strategy to follow should

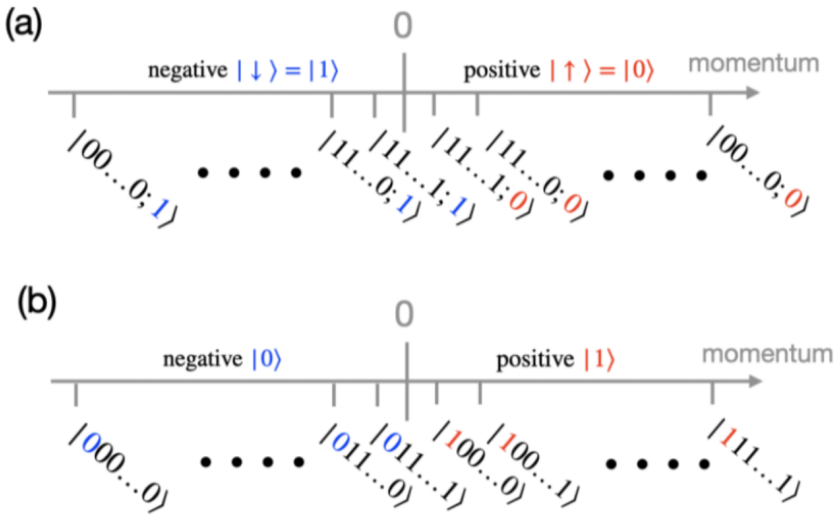

Figure 5.11: Depiction on how to transform the digitized states to the form suitable to apply the symmetric qFT algorithm [10]. In (a) we represent the basis states in the convention used in the main text, where the last qubit is considered to be the sign qubit. In a first step, one applies the σ^x gate to the sign qubit in order for it to be in the usual quantum computing convention. Then, one interprets the sign qubit as the first qubit which acts as a control: if it is in the state $|1\rangle$, one rotates all the remaining qubits (b). This last step orders the positive branch correctly and brings it to the form considered in [10]. After applying the symmetric qFT, one reverses this operation to go back to the basis used in the main text.

be similar to the one employed for the squeezing operator. We again write the evolution operator in terms of a diagonal one as

$$U_{I,\mathbf{n}} \equiv V_{\mathbf{n}} U_{I,\mathbf{n}}^{\text{diag}} V_{\mathbf{n}}^{\dagger}\,, \tag{5.50}$$

where $U_{I,\mathbf{n}}^{\text{diag}}$ is given by

$$U_{I,\boldsymbol{n}}^{\text{diag}} \equiv e^{-i\Delta \sum_{\langle i,j,k,l\rangle} \phi_{\mathbf{n}}^{(i)\,\text{diag}} \phi_{\mathbf{n}}^{(j)\,\text{diag}} \phi_{\mathbf{n}}^{(k)\,\text{diag}} \phi_{\mathbf{n}}^{(l)\,\text{diag}}}\,, \tag{5.51}$$

with $\Delta \equiv \delta\lambda/(96M^2)$ and $V_{\mathbf{n}} \equiv \prod_{i=0}^{M-1} V_{\mathbf{n}}^{(i)}$. The diagonalizing matrix is easily seen to be similar to the one found for the squeezing operator, but now with respect to σ^x, i.e.

$$V_{\mathbf{n}}^{(i)} = I_{\mathfrak{N}}(1 \otimes \ldots 1 \otimes H)\,, \tag{5.52}$$

where similar to the discussion for the squeezing operator one has that $\phi_{\boldsymbol{n}}^{(i)\,\text{diag}} \equiv V_{\mathbf{n}}^{(i)\dagger} \phi_{\mathbf{n}}^{(i)} V_{\mathbf{n}}^{(i)}$, which can be decomposed as $\phi_{\boldsymbol{n}}^{(i)\,\text{diag}} = \bigotimes_j \frac{1}{2}(1-\sigma^z)_j \otimes \sigma^z$.

In Fig. 5.12 we outline the implementation of $U_{I,\mathbf{n}}$. The operator $U_{I,\mathbf{n}}^{\text{diag}}$ can be implemented using the techniques detailed in section 4.2. Although one can obtain $U_{I,\mathbf{n}}^{\text{diag}}$ by

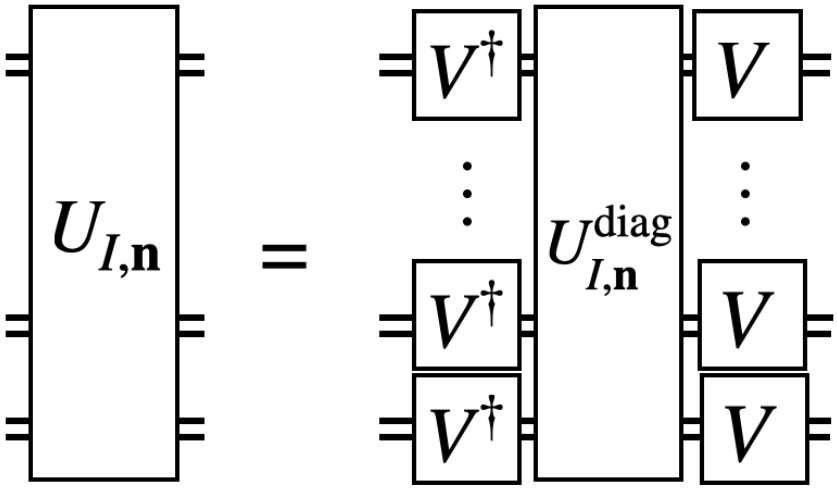

Figure 5.12: Circuit implementing $U_{I,\mathbf{n}}$. Figure taken from [7].

summing over $\langle i,j,k,l\rangle$ in Eq. (5.51), this is in general a difficult task. In general, this summation can be simplified to considering only five distinct cases: either the four particle's indices match, three indices match, two indices match, two pairs of indices match independently or they all differ, leading to a small number of operators that need to be exponentiated. Besides this, one also needs to take into account all the combinatorial factors; in appendix 5.D we exemplify this exercise for the simple case of $M = 4$ and $\mathbf{n} = -1/2$, and provide further discussion for the generic case.

The implementation of U_I involves $O(M^4\mathcal{V}\,\mathrm{poly}\log(\mathcal{V}))$ elementary gate operations, where the M^4 dependence originates from the loop over four-tuples of particle registers. We expect that this bound can be lowered down to $O(M)$, provided a smarter way of dealing with the combinatorics is found. As for the squeezing operator, there is a dependence in $\mathcal{V}$ due to the loop over all position modes, each entailing an additional computation requiring $O(\mathrm{poly}\log(\mathcal{V}))$ gate operations. Thus, this section of the algorithm gives the dominant cost to the implementation of the time evolution operator. Compared to JLP's proposal (see [10] for the explicit implementation of the time evolution operator) we see that indeed the scaling with $\mathcal{V}$ is the same; this a consequence of the *brute force* approach used to implement the algorithms in terms of Pauli gates. To obtain a more meaningful comparison, one would require a comparative numerical study, where one also has to take into account that the comparison depends on the exact scattering process at study. In addition, issues related, for example, with quantum error correction [74, 183] have to be taken into account in such comparisons in currently available devices. A particularly relevant error that can occur, consists in mapping the physical and unphysical spaces (i.e. map Bose-symmetric states to an un-symmetrized ones), whose probability of occurring grows with M. This question is somewhat similar to problems found in quantum simu-

lation of gauge theories [184–188], and thus one hopes that some techniques used in that area can be employed for our digitization.

5.2.3 Measurement

In this section we detail the measurement protocols to be applied once the time evolved state has been prepared. The wave-function of the system can be written in the most general form as

$$|\Psi(t)\rangle = \sum_{\ell} \alpha_{\ell}(t)|\Psi_{\ell}\rangle \equiv \sum_{\text{basis states}} \frac{\alpha_{(\mathbf{q},\mathbf{q}',\dots)}(t)}{\sqrt{\mathcal{N}_{(\mathbf{q},\mathbf{q}',\dots)}(t)}} \left[|\mathbf{q},\mathbf{q}',\dots,\Omega\rangle + \text{symm.}\right], \tag{5.53}$$

where we introduced the unknown coefficients $\alpha_{(\mathbf{q},\mathbf{q}',\dots)}(t)$, 'symm' denotes Bose-symmetric permutations and $\mathcal{N}_{(\mathbf{q},\mathbf{q}',\dots)} \equiv M!/[\mathfrak{n}_{\Omega}! \prod_{\mathbf{q}} \mathfrak{n}_{\mathbf{q}}!]$ is a generalization of the Bose-symmetric factor $\mathcal{N}$ introduced in section 5.2.1 for the M single-particle registers, now also accounting for the possibility of degenerate momenta among particle registers.

When measuring all the qubits from the particle registers, the wave-function will collapse to a state with well defined particle number for every mode $\mathbf{q}$ with probability $|\alpha_{(\mathbf{q},\mathbf{q}',\dots)}|^2$. This is to be contrasted with JLP's procedure, where particle number measurement requires additional gate operations. We would like to emphasize that the above wave-function does not guarantee that the different particles are well separated and localized, thus one might want to further evolve the state for a time τ_f, during which interactions are slowly turn-off (mirroring initial state preparation), until the final states are well separated.

If one measures all the qubits in the particle registers available, then up to kinematical factors, this defines the differential cross-section

$$\frac{\mathrm{d}^{d\mathfrak{n}}\sigma}{\mathrm{d}^d\mathbf{p}_0 \dots \mathrm{d}^d\mathbf{p}_{\mathfrak{n}}}, \tag{5.54}$$

of $\mathfrak{n} = \sum_{\mathbf{q}} \mathfrak{n}_{\mathbf{q}}$ particles for a given outcome. This shows that running the quantum algorithm is equivalent to accumulating events in a particle physics experiment, with the output requiring a classical analysis in both cases. However, on a quantum computer one has direct access to more integrated quantities more straightforwardly than in a experimental set-up, since the full physical information is stored in $|\Psi\rangle$ and different measurement protocols can extract different information from this state. For example, measuring only the occupancy qubits, one obtains the integrated cross-section

$$\sigma_{\mathfrak{n}} \equiv \int \mathrm{d}^d\mathbf{p}_0 \dots \mathrm{d}^d\mathbf{p}_{\mathfrak{n}} \frac{\mathrm{d}^{d\mathfrak{n}}\sigma}{\mathrm{d}^d\mathbf{p}_0 \dots \mathrm{d}^d\mathbf{p}_{\mathfrak{n}}}. \tag{5.55}$$

In theories where particles are described by more discrete quantum numbers, such as electric charge, spin or color, the occupancy qubit (which in this case *works* as a quantum

number to distinguish the vacuum from other states) would be replaced by a register tracking all values of the different quantum numbers. Measuring only these array would give rise to integrated cross-sections, as in this example.

Another advantage of using a quantum computer is the fact that phase space cuts can be applied directly at the quantum level, and not on the post-classical analysis of data. A simple example would be to restrict the particles' momenta to a region $\boldsymbol{p} \in [\boldsymbol{p}^{\min}, \boldsymbol{p}^{\max}]$. This can be done by employing $2d$ auxiliary registers (of size $\log_2(\mathcal{V})$) set to kinematic bounds $\boldsymbol{p}^{\min/\max}$ in d dimensions. Then, using a quantum comparator circuit [189–191] (using $\log_2(\mathcal{V})$ ancilla qubits and $O(\log(\mathcal{V}))$ gate operations), one can determine if the register stores a momentum within the above region or not. The result would be stored in $2d$ ancilla qubits with outcome $|11\rangle^{\otimes d}$ if the momentum is within the kinematical range, thus splitting the Hilbert space into two non-overlapping regions, with a tag identifying each state. The application of techniques such as (Oblivious) Amplitude Amplification [192–195] could, in principle, then be used to bias the system towards being within the allowed phase space.

In general, it might not be possible to adiabatically go from an eigenstate of the free theory to that of the full theory. This is the case in QCD, where the eigenstates of the full theory are hadrons (bound states) and not the quarks and gluons. The transition between the free and confine phases is important in the hadronization stage of the scattering experiment [196–199]. In ϕ^4 scalar, for example, it is also known that for $d < 4$ there exists a phase transition [200–202]. In case the free and full theory are not adiabatically connected, one omits the time τ_f, during which there was a turn-off interactions, and one should keep the interaction time τ_I long enough to include the physical time it takes to form such a bound state. This issue is also present JLP approach and a comparison between both approaches would require a numerical analysis, trying to recover the continuum limit.

Once bound states are sufficiently separated, one can proceed s before and measure their respective quantum numbers. An example, consists in extracting the expectation value of the momentum operator, which is defined as

$$P^i_{\tilde{\mathcal{V}}_{\mathbf{p}}} \equiv \int_{\tilde{\mathcal{V}}_{\mathbf{p}}} d^d\mathbf{p}\, \mathbf{p}^i\, a^\dagger_{\mathbf{p}} a_{\mathbf{p}}\,, \tag{5.56}$$

where $i = 1, \ldots, d$ and $\tilde{\mathcal{V}}_{\mathbf{p}}$ stands for a region in momentum space. Since the final state is an eigenstate of the momentum operator (since the final state should correspond to a bound state with well defined momenta) one could extract the momentum expectation value by employing strategies based on the phase estimation algorithm (PEA) [74, 203–206]. The PEA algorithm makes uses of repeated applications of the operator $U \equiv \exp\left(-iP^i_{\tilde{\mathcal{V}}_{\mathbf{p}}}\right)$, giving with a probability (within precision ε) the expectation value $\langle P^i_{\tilde{\mathcal{V}}_{\mathbf{p}}} \rangle$, requiring an extra $O(\log(\varepsilon^{-1})) \sim O(\log(\mathcal{V})/d)$ ancilla qubits, taking the precision to be the same as the one used for the momentum discretization. It requires $O(\log(\varepsilon^{-1}))$ applications of the controlled-U gate, which can be easily constructed following the discussion regarding the free time evolution operator implementation, with a

quantum comparator being employed to verify if the physical state is within $\tilde{\mathcal{V}}_{\mathbf{p}}$. The same construction can be extended to the energy operator

$$H_{\tilde{\mathcal{V}}_{\mathbf{p}}} \equiv \int_{\tilde{\mathcal{V}}_{\mathbf{p}}} d^d\mathbf{p}\, H_{\mathbf{p}} = \int_{\tilde{\mathcal{V}}_{\mathbf{p}}} d^d\mathbf{p}\, H_{0,\mathbf{p}} + \int_{\tilde{\mathcal{V}}_{\mathbf{p}}} d^d\mathbf{p}\, H_{I,\mathbf{p}}\,, \tag{5.57}$$

where $H_{0,\mathbf{p}}$ and $H_{I,\mathbf{p}}$ are the Fourier transforms of the Hamiltonian densities $H_{0,\mathbf{x}}$ and $H_{I,\mathbf{x}}$, with $H_0 = \int d^d\mathbf{x}\, H_{0,\mathbf{x}}$ and $H_I = \int d^d\mathbf{x}\, H_{I,\mathbf{x}}$. Again one can apply the PEA to estimate expectation value of this operator; a more detailed discussion on the extraction of this expectation value can be found in [7].

5.2.4 Renormalization

In this section we detail how to take into account renormalization in the single-particle basis strategy we adopted. Essentially this amounts to employing the renormalization group (RG) procedure in the Hamiltonian formalism, which in the present case is similar to the one found in classical lattice computations in the (Euclidean) path integral formalism. This approach differs from the perturbative strategy employed by JLP. We note however that a perturbative approach, solely from a computational standpoint, is perhaps not a suitable procedure since it requires one to perform classical computations as complex as the ones being simulated in the quantum computer.

We begin by formulating the renormalization procedure in the operator formalism [207], which amounts to finding and effective Hamiltonian with a UV cutoff. These are of course related to the lattice discretization and the respective truncation of the Hilbert space due to the digitization. Here we outline the formulation of the RG procedure in the operator formalism for single-particle strategies, which has been extensively studied [208–210].

We recall that the computational basis corresponds to the eigenbasis of the free Hamiltonian H_0 (and the full Hamiltonian if there they are addiabatically connected). One can write the full Hamiltonian in a such a basis as

$$H = \begin{pmatrix} H_{ll} & H_{lh} \\ H_{hl} & H_{hh} \end{pmatrix}, \tag{5.58}$$

where we implicitly introduced a cut-off energy scale Λ, with the matrix elements in this representation are between states with energies $E = \sum_{\mathbf{p}} \omega_{\mathbf{p}} \mathfrak{n}_{\mathbf{p}}$, either below (l) or above (h). From this Hamiltonian we would like to define an effective Hamiltonian H^{eff}, where (l) and (h) can not communicate. Such a RG transformation can be written as

$$H^{\text{eff}} \equiv THT^\dagger\,, \tag{5.59}$$

where $T \equiv \exp(i\eta)$ block-diagonalizes H. Then it is easily seen that if one is below the scale Λ, in the diagonal basis H^{eff}_{ll} defines an effective field theory.

To do this one, one needs to determine T (η). This can be done perturbatively, by applying the Schrieffer-Wolf transformation [211] (see appendix 5.E), giving the elements

of H_{eff} order by order in λ. As mentioned, this is however not the desired approach since, as outlined in appendix 5.E , the computational complexity of such calculation grows factorially with λ and also breaks down if there is a phase transition.

In our algorithm, a non-perturbative formulation of the RG can nonetheless be followed. First, we recall that renormalization enters in the algorithm when turning-on interaction after the initial state preparation algorithm is finished, as shown in Fig. 5.3. Renormalization enters in the determination of

$$\lambda(\tau_0) = \lambda^{\text{ren}}\,, \qquad m(\tau_0) = m^{\text{ren}}\,, \tag{5.60}$$

The intermediate time theories $H(t) = H(\lambda(t), m(t))$ at $t < \tau_0$, including the initial values

$$\lambda(0) = 0\,, \qquad m(0) = m_0\,, \tag{5.61}$$

are not renormalized because there is simply no physical renormalization for them. Instead, one simply works with a linear interpolation

$$\lambda(t) = \lambda^{\text{ren}}\frac{t}{\tau_0}\,, \qquad m(t) = m_0\big(1 - \frac{t}{\tau_0}\big) + m^{\text{ren}}\frac{t}{\tau_0}\,, \tag{5.62}$$

for $t \in [0, \tau_0]$ and constant thereafter, where m_0 can be taken to be the bare quark mass in QCD.

The renormalized values for the bare parameters $\lambda(t)$ and $m(t)$ at $t \geq \tau_0$ can be obtained by computing a static property and then use the result as the input for the computation of a scattering process. This can be done non-perturbatively following the strategy commonly found in lattice calculations

1. Compute a static physical quantity for a given a_s and M. Then, repeat the calculation adjusting the bare parameters λ, m so that the physical value is reproduced for that a_s and M. Algorithms to implement this procedure [203–206, 212–217] can be adapted to the single-particle approach.

2. The previous step is repeated for a different a_s, M towards the continuum limit, i.e. $a_s \to 0$ and $M \to \infty$, along the line of constant physics. The determination of this path should be determined using a minimization procedure.

3. Once one has obtained the values of the renormalized parameters for several (a_s, M) points, the quantum scattering algorithm is run using the obtained values. Notice that this also includes the renormalization of operators measured in section 5.2.3, $\langle O^{\text{eff}}\rangle$, which in the simplest case read $O = ZO^{\text{eff}}$, where Z can be determined as the other parameters.

4. Finally, one extrapolates the expectation values obtained to the continuum limit, which is known to be a computationally demanding task even in a quantum computer.

5.3 A brief summary

In this chapter, we introduced a novel strategy to quantum simulate high energy scattering problems. The main idea was the decomposition of the Hilbert space in terms of single-particle sub-spaces, which when truncated allow one to simulate processes up to M particles. With the additional discretization of phase space into a lattice with volume $\mathcal{V}$, the algorithm requires $O(M \log \mathcal{V})$ qubits, thus ideally suited for dilute systems that can explore a large lattices.

	Elementary gate operations		Ancilla qubits
Initial State preparation	$O(M^{\mathfrak{n}} \log(\mathcal{V}))$	$p_{\text{success}} = 1$ [exact*] $p_{\text{success}} > 1/2$ [probabilistic*]	$\log(M!/(M-\mathfrak{n}!))$ [exact*] $O(\log(M^{\mathfrak{n}}))$ [probabilistic*]
Time Evolution	Free part U_0	$O(M \text{poly}\log(\mathcal{V})\, t)$	$O(\log(\mathcal{V})/d)$
	Squeezing transform S	$O(M^2\mathcal{V} \text{poly}\log(\mathcal{V})\, t)$	0
	quantum Fourier transform	$O(M \text{poly}\log(\mathcal{V})\, t)$	0
	Interaction part U_I	$O(M^4\mathcal{V} \text{poly}\ \log(\mathcal{V})\, t)$	$O(\log(\mathcal{V})/d)$
	Total	$O(M^4\mathcal{V} \text{poly}\ \log(\mathcal{V})\, t)$	$O(\log(\mathcal{V})/d)$
Measurement	Particle number	0	0
	Momentum density	$O(M \text{ poly}\log(\mathcal{V}))$ (PEA**)	$O(\log(\mathcal{V})/d)$
	Energy density	$O(M^4\mathcal{V}_{\mathbf{x}} \text{ poly}\log(\mathcal{V}))$ (PEA**)	$O(\log(\mathcal{V})/d)$

Table 5.1: Gate and ancilla cost in order to implement the algorithm introduced in this chapter. We recall the notation used: number of particle registers M, volume $\mathcal{V}$, occupied registers in initial state $\mathfrak{n}$, dimension d, Trotter time steps t. (*) If $\log_2(M!/(M-\mathfrak{n}))$ is not an integer, the initial state is prepared with probability $p_{\text{success}} > 1/2$, depending **only** on M and $\mathfrak{n}$. (**) Measurements of (localized) energy and momentum densities are via the phase estimation algorithm (PEA) [203–206]. The cost estimate for the localized energy density includes a factor $\mathcal{V}_{\mathbf{x}} \subset \mathcal{V}$ denoting a small sub-volume of the total $\mathcal{V}$.

In table 5.1 we detail the gate and ancilla cost associated to each section of the algorithm. The dominant cost to the number of basic gate operations comes from the time evolution section associated with the interacting Hamiltonian. Nonetheless, we note that this cost is comparable with the one in JLP's approach [10,64,65], thus we see either no clear advantage/disadvantage when using our discretization strategy. However, for initial state preparation we were able to provide a complete and explicit algorithm, scaling logarithmically with the volume. In addition, compared to JLP's approach, measurement is conceptually much closer to what is done experimentally. In particular, we showed that one can devise simple and cost free protocols to extract different cross-sections, possibly more efficiently than what is done experimentally.

5.A Details of state preparation

In this appendix we give some details and simple examples on the algorithms necessary for the initial state preparation. We discuss first the algorithm to prepare a single localized wave-packet in the free theory and then discuss the Bose-symmatrization algorithm.

As mentioned in the main text, the first steps of the wave-packet preparation algorithm consist in splitting the positive and negative branches and flipping the occupation qubit. Assuming that $d = 1$, as in the main text, and that all these two operations have already been performed, we can solely focus on the positive branch and only act on the qubits storing the absolute value for the momentum.

The fiducial state in this case is simply $N^{\text{abs}} \equiv 2^{n_Q}$ qubits in the state $|0\rangle$[11]. Applying the procedure detailed in the main text, each one gets rotated by an angle

$$|0\rangle \to \cos\theta_k|0\rangle + \sin\theta_k|1\rangle \tag{5.63}$$

for all $k = 0, \ldots, n_Q - 1$ qubits. As mentioned in the main text, each $|1\rangle$ acquires a sine and each $|0\rangle$ acquires a cosine. The full state after the transformation, for n_Q qubits, can be written as

$$|0,0,\cdots,0\rangle \to \sum_{p=0}^{2^{n_Q}-1} \left\{ \prod_{k=0}^{n_Q-1} \left(\cos^{(1-p_k)}(\theta_k)\sin^{(p_k)}(\theta_k)\right) \right\} |p\rangle = \sum_{p=0}^{2^{n_Q}-1} \psi_p|p\rangle \equiv |\Psi\rangle\,, \tag{5.64}$$

where $|p\rangle$ here stands for the n_Q qubits storing the absolute value of a single particle momenta and $p_k \in \{0,1\}$.

Thus one can see that providing the adequate map between k and θ_k, one can load different distributions on to the produced state. The most straightforward one is to set all the angles to the same value up to some k, after which they all vanish. This generates a square wave function, which although it is well localized in momentum space, it is not well localized in position space (the Fourier pair decays as $\sim 1/x$, i.e. sub-exponentially). Thus, this particular solution is not desirable. It is however not difficult to come up with better solutions, by noticing that large momentum values are associated to binary numbers where the higher digits are all 1's, while smaller numbers all have higher digits equaling 0's. Thus, it is natural to require that the larger angles for the θ_k occur for small values of k, while larger values for k are dominated by smaller angles. With this in mind, we give here three simple polynomial examples, explicitly reading

$$\begin{aligned}
\theta_k^{\text{linear}} &= \frac{\pi}{4} - \epsilon + \frac{2\epsilon - \frac{\pi}{4}}{n_Q - 1}k\,,\\
\theta_k^{\text{quadratic}} &= \frac{\pi}{4} - \epsilon + \left(2\epsilon - \frac{\pi}{4} - c_0(n_Q-1)^2\right)\frac{k}{n_Q-1} + c_0k^2\,,\\
\theta_k^{\text{cubic}} &= \frac{\pi}{4} - \epsilon + \left(2\epsilon - \frac{\pi}{4} - c_1(n_Q-1)^2 - c_2(n_Q-1)^3\right)\frac{k}{n_Q-1} + c_1k^2 + c_2k^3\,.
\end{aligned} \tag{5.65}$$

Here the c_i parameters are adjusted such that the resulting distribution is smoothed (in the sense of having less and smaller peaks); for the numerical results we took $c_0 = -0.01325$, $c_1 = -0.0195$, $c_2 = 0.0005905$, the numerical regulator $\epsilon = 0.015$ and $n_Q = 10$. These

[11] Here we use the inverted basis with respect to the main text

maps are fixed at the initial point $p = 0$ where $\theta_0 = \pi/4 - \epsilon$ and $\theta_{n_Q-1} = \epsilon$ is the smallest possible value. In Fig. 5.13 we illustrate the generated distributions, comparing to an exponentially decaying function $\sim \exp(-p/\sigma)$. Indeed, we see that even these low ordered polynomials, easily derived by hand, already give rise to a well localized distribution, at the cost of losing some control over its shape. In particular, we observe that while increasing the degree of the polynomial map, the bumpy profile of ψ_p gets smoother, thus in practice one is hopeful that designing a more sophisticated numerical routine (going further than the polynomial maps shown) could lead to much smoother distributions. Finally, notice that this approach only requires n_Q qubits, unlike [175, 176] which uses exponentially many more resources.

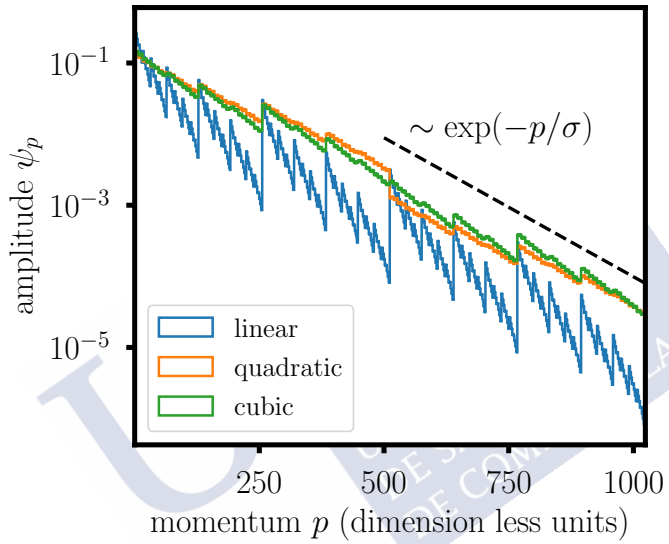

Figure 5.13: Induced distributions for ψ_p (see Eq. (5.64)) using the polynomial maps detailed in the text. To guide the eye, we provided the profile of an off-set decaying exponential distribution, with $\sigma = 100$. Figure taken from [7].

Let us now discuss the Bose-symmetrization algorithm introduced in the main text. The idea of the algorithm consists in starting with an un-symmetrized state and then, using an auxiliary register, generate a code that symmetrizes the initial state. The idea of the code is to associate each Bose permutation to a binary number (the code) represented in the ancilla register; knowing the associated word is tantamount to knowing which permutations to do in order to generate the correct state. Finally, once the desired state has been generated, one erases the ancilla register. The exact algorithm depends on M and $\mathfrak{n}$, but the generic structure can be described as

1. Apply Hadamard gates to all the ancilla registers, so that all possible code words are generated. In general, this will generate more states than the number of desired

Bose permutations.

2. Define a code that relates each one of the states in the ancilla register to a set of operations. Each code word details a SWAP operation between different particle registers. After the correct number of SWAP operations has been generated, one should have generated at least one of the Bose permutations of the un-symmetrized initial state, but usually not in equal probabilities.

3. In order to be a Bose-symmetric state, all permutations must equally likely, thus one must eliminate the extra states via non-unitary measurements of extra ancillas, preceded by an adequate detection algorithm.

4. Once all extra states are eliminated, one needs to erase the ancilla register; this can in principle be done using only a small number of qubits of the particle registers as controls.

The algorithm is best illustrated by giving the first non-trivial example, for $\mathfrak{n} = 2$ initial wave packets in $M = 3$ registers, starting from a state $|\Omega, \Psi_1, \Psi_0\rangle$. The target state is

$$\frac{1}{\sqrt{6}}\Big[\,|\Omega,\Psi_1,\Psi_0\rangle + |\Omega,\Psi_0,\Psi_1\rangle + |\Psi_0,\Psi_1,\Omega\rangle + |\Psi_1,\Psi_0,\Omega\rangle + |\Psi_0,\Omega,\Psi_1\rangle + |\Psi_1,\Omega,\Psi_0\rangle\,\Big]\,. \tag{5.66}$$

Unlike the (next to) trivial example in the main text, in this case the number of possible Bose permutation for this M and $\mathfrak{n}$ is not a power of two. Thus, we consider an ancilla register with $s = 3$ ancilla qubits. Applying a Hadamard gate to each qubit we obtain a Bell superposition with $2^3 = 8$ states. Thus from the initial state $|\Omega, \Psi_1, \Psi_0\rangle\,|0,0,0\rangle$, we obtain the state

$$\begin{aligned}\frac{1}{\sqrt{8}}\Big[\,&|\Omega,\Psi_1,\Psi_0\rangle\,|0,0,0\rangle + |\Omega,\Psi_0,\Psi_1\rangle\,|0,0,1\rangle + |\Psi_0,\Psi_1,\Omega\rangle\,|1,0,0\rangle + |\Psi_1,\Psi_0,\Omega\rangle\,|1,0,1\rangle \\ &+ |\Psi_0,\Omega,\Psi_1\rangle\,(|0,1,1\rangle + |1,1,0\rangle) + |\Psi_1,\Omega,\Psi_0\rangle\,(|0,1,0\rangle + |1,1,1\rangle)\Big]\,.\end{aligned} \tag{5.67}$$

As we mentioned in the generic algorithmic description above, the code implemented has already generated all the possible permutation terms in the Bose-symmetric wave-function, but the states $|\Psi_0, \Omega, \Psi_1\rangle$ and $|\Psi_1, \Omega, \Psi_0\rangle$ are now twice as likely as any other state[12].

These extra states can be eliminated by adding an additional ancilla $|0\rangle$, and flipping it to $|1\rangle$ if the code word is either $|1,1,1\rangle$ or $|1,1,0\rangle$ (i.e. $|1,1,-\rangle$), which can be done using a CCNOT gate. Then if the ancilla is measured and one observes the state $|1\rangle$, the

[12]For a more interested reader the code used was to swap the nearest particle registers according to the following rule, for an ordered triplet $|abc\rangle$: if $|001\rangle$, swap b and c; if $|010\rangle$, swap a and b; if $|100\rangle$, swap a and c, else apply the same rules always following them from left to right.

algorithm has failed and one needs to restart. If instead one observes the state $|0\rangle$, then one has produced the state given in Eq. (5.66).

A natural question is how likely is the algorithm to be successful. In this case, it is easily realized that the probability of success is $p_{\text{success}} = 6/8$. In fact, it is easy to realize that although the number of basic gate operations depends on the number of measurements on needs to perform in order to eliminate the undesired states, p_{success} only depends on M and $\mathfrak{n}$. In the case of the previous example, one could instead of just performing a single measurement have performed two separate measurements, each eliminating a single state (but never more than two measurements). In that case, assuming that measurements are independent, one would obtain that $p_{\text{success}} = (7/8) \times (6/7) = 6/8$. In general, one obtains that

$$p_{\text{success}} = \frac{\mathcal{N}}{2^s} > \frac{1}{2}\,, \tag{5.68}$$

where $\mathcal{N} = M!/(M-\mathfrak{n})!$ is the number of Bose-permutations and s an integer such that 2^s is the closest power of two to $\mathcal{N}$ from above, $s = \lceil \log_2(M!/(M-\mathfrak{n})!) \rceil = O(\log(M^{\mathfrak{n}}))$. In other words, the probability of success is simply the ratio the number of desired states to the total possible number of states. In Fig. 5.14 we show the evolution of p_{success} for two values of $\mathfrak{n}$ with M. We observe that for $M \gg 1$ (which one must require in order for the single particle to be applicable) there is a quasi-periodic behavior where certain values of M maximize the probability of preparing the correct initial state. Thus, with only a small extra cost, it is always possible to increase M such that the probabilistic approach we detailed is highly reliable. We also note that the probability of success is always larger than one half.

As mentioned above, the final step of the algorithm consists in erasing the information from the ancilla register. For the case $\mathfrak{n} = 2$, this can be done by using the occupation number and sign qubit, since the initial state wave-packets are prepared in at $\pm L$ and with opposite sign momenta. For cases with more initial state wave-packets, one would need to use r qubits per register to distinguish the different wave-packets. However, since the initial states have to be widely separated r has to always be much smaller than $\log_2 N_s^d$, and the cost of un-computing the ancillas would change from $O(M^{\mathfrak{n}})$, to $\sim O(M^{\mathfrak{n}} r) \ll O(M^{\mathfrak{n}} \log(\mathcal{V}))$. After detecting which ancilla qubits are in the state $|1\rangle$, one resets them to the state $|0\rangle$. There will be $s' \leq s$ of such ancillas, and one can always choose them much smaller than s with the appropriate code. Thus their contribution to the algorithm cost is sub-leading.

Overall, the algorithm requires s Hadamard gates to prepare the ancilla register, and $O(2^s \log \mathcal{V}) \sim O(M^{\mathfrak{n}} \log \mathcal{V})$ controlled SWAP operations. The final un-computation step requires $O(M^{\mathfrak{n}})$ operations. This leads to a net $O(M^{\mathfrak{n}} \log \mathcal{V})$ gate complexity.

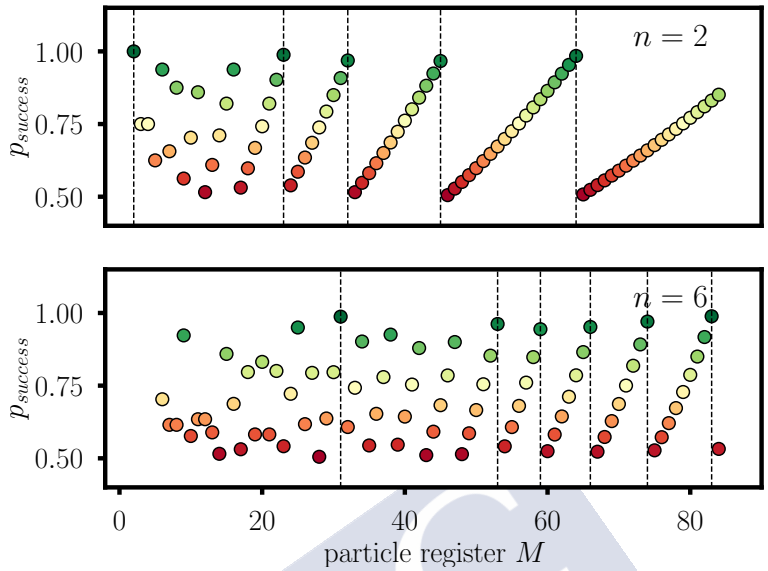

Figure 5.14: Probability of preparing the correct Bose symmetric state p_{success} as a function of the number for single particle registers M, for $n = 2$ (top) and $n = 6$ (bottom) initial single particle states. Dashed lines denote values for M which maximize p_{success}, and the color graduation tens towards green when the probability is maximized and to red when it approaches the lower bound of 1/2. Figure taken from [7].

5.B Details of the kinetic term

In this appendix we discuss some of the gates necessary to implement the time evolution operator U_0, particularly the energy gate $\boxed{\omega}$ and the phase gate $\boxed{S_\varphi^{1+\mathfrak{n}_\Omega}}$

The gate $\boxed{\omega}$ takes as an input two registers, one of which is a particle register $|\mathbf{q}\rangle$ and the other an ancilla register of l qubits in the state $|0\rangle^{\otimes l}$, implementing the transformation $|\mathbf{q}\rangle\otimes|0^{\otimes l}\rangle \to |\mathbf{q}\rangle\otimes|\omega_{\mathbf{q}}\rangle$. The function $\omega_{\mathbf{q}}$ (for any $\mathbf{q}$) is a simple arithmetic operation, thus provided classical and quantum algorithms exist to implement such an operation [218–222] and ensuring that $|\Omega\rangle$, $\omega_\Omega = 0$, $\boxed{\omega}$ can be treated as a quantum oracle[13].

The implementation of $\boxed{S_\varphi^{1+\mathfrak{n}_\Omega}}$, consists in the application of the (single control) gate $\boxed{S_\varphi}$ $1+\mathfrak{n}_\Omega$ times. In Fig. 5.15 we detail how one applies the single gate $\boxed{S_\varphi}$ the correct amount of times. The idea is that the 1 contribution is a global phase, while the remaining $\mathfrak{n}_\Omega$ applications can be done by looping over all M particle registers and activating the phase gate if the control is an empty state. We recall that this precise numerical factor comes from the fact that each occupied state gives rise to a phase, but off-diagonal states

[13]By quantum oracle, one can read a quantum black-box, whose inner workings are disregarded.

involving an empty and occupied state also give rise to a phase.

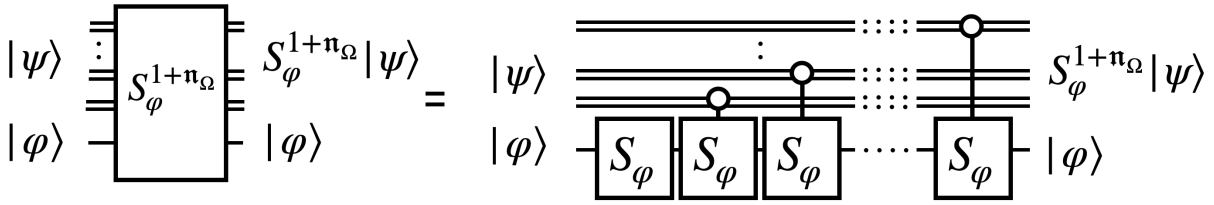

Figure 5.15: Circuit implementing $\boxed{S_\varphi^{1+\mathfrak{n}_\Omega}}$, necesary to implement U_0. Figure taken from [7].

Finally, the single phase gate $\boxed{S_\varphi}$ takes the state $|\psi\rangle \otimes |\varphi\rangle$ to $\exp\left(-i\frac{\delta}{M}\varphi\right)|\psi\rangle \otimes |\varphi\rangle$. It can be implemented using the conditional single qubit phase shift gate $\boxed{C_\phi}$ [74, 223], which is given in the computational basis by

$$C_\phi \equiv \begin{pmatrix} 1 & 0 \\ 0 & e^{i\phi} \end{pmatrix}, \tag{5.69}$$

where $\phi = -\frac{\delta}{M}2^d$ $(0 \leq d \leq l-1)$ chosen accordingly to the binary decomposition of φ. Putting together multiple $\boxed{C_\phi}$, with the correct phase, gives rise to $\boxed{S_\varphi}$.

5.C Details of the squeezing transformation

In this appendix we show that the squeezing operator S indeed satifies Eq. (5.37). First, note that

$$S a_{\mathbf{q}} S^\dagger = \prod_{\boldsymbol{p},\boldsymbol{p}'} e^{-z_{\boldsymbol{p}}(a^\dagger_{\boldsymbol{p}} a^\dagger_{-\boldsymbol{p}} - a_{-\boldsymbol{p}} A_{\boldsymbol{p}})} a_{\mathbf{q}} e^{z'_{\boldsymbol{p}}(a^\dagger_{\boldsymbol{p}'} a^\dagger_{-\boldsymbol{p}'} - a_{-\boldsymbol{p}'} a_{\boldsymbol{p}'})}. \tag{5.70}$$

Using the fact that $a_{\boldsymbol{p}}$ and $a^\dagger_{\boldsymbol{p}}$ obey the canonical commutation relations, Eq. (5.70) takes the form

$$e^X a_{\mathbf{q}} e^{-X} = \sum_{k=0}^{\infty} \frac{1}{k!} \underbrace{[X, [X, \ldots [X, a_{\mathbf{q}}]]}_{\text{k times}} \ldots], \tag{5.71}$$

where $X \equiv -z_{\mathbf{q}}(a^\dagger_{\mathbf{q}} a^\dagger_{-\mathbf{q}} - a_{-\mathbf{q}} a_{\mathbf{q}})$. Using the identities

$$[X, a_{\mathbf{q}}] = z_{\mathbf{q}} a^\dagger_{-\mathbf{q}}, \qquad [X, a^\dagger_{-\mathbf{q}}] = z_{\mathbf{q}} a_{\mathbf{q}}, \tag{5.72}$$

it follows directly that for $z_{\mathbf{q}} < 0$

$$e^X a_{\mathbf{q}} e^{-X} = \sum_{k=0}^{\infty} \frac{(z_{\mathbf{q}})^{2k}}{(2k)!} a_{\mathbf{q}} + \sum_{k=0}^{\infty} \frac{(z_{\mathbf{q}})^{2k+1}}{(2k+1)!} a^\dagger_{-\mathbf{q}} = \cosh(z_{\mathbf{q}}) a_{\mathbf{q}} + \frac{z_{\mathbf{q}}}{|z_{\mathbf{q}}|} \sinh(z_{\mathbf{q}}) a^\dagger_{-\mathbf{q}}. \tag{5.73}$$

In the main text, we introduced the bit increment operator $I_{\mathfrak{N}}$, in order to implement the squeezing operator in terms of single momentum mode and particle pairing operators. The bit increment operator performs the transformation $|j\rangle \to |j+1 \,(\mathrm{mod}\, 2^{\mathfrak{N}})\rangle$, where $|j\rangle = |j_0, j_1, \cdots, j_{\mathfrak{N}-2}, j_{\mathfrak{N}-1}\rangle$ and $j_i \in \{0,1\}$ for any i. We detail how this operator can be constructed using multiple controlled σ^x gates in Fig. 5.16, although more efficient constructions can be found in more recent work [224]. The idea of the implementation shown relies on the fact that unit increments in a binary basis consist in consecutively flipping all qubits, $|0\rangle \to |1\rangle$ and $|1\rangle \to |0\rangle$, while tracking the input qubit with an ancilla qubit prepared in the state $|1\rangle$. This is only flipped to $|0\rangle$ after one has preformed the transformation $|0\rangle \to |1\rangle$ on the main register. After this operation, all future flipping operations are prevented. This operation is implemented by the circuit to the left of the vertical red line in Fig. 5.16. In a last step (to the right of the red line), one uncomputes the ancilla back to the state $|1\rangle$ via a single σ^x gate, with the boundary case $|1,1,\cdots,1\rangle \otimes |1\rangle \to |0,0,\cdots,0\rangle \otimes |1\rangle$ taken into account by the last gate in the circuit depicted.

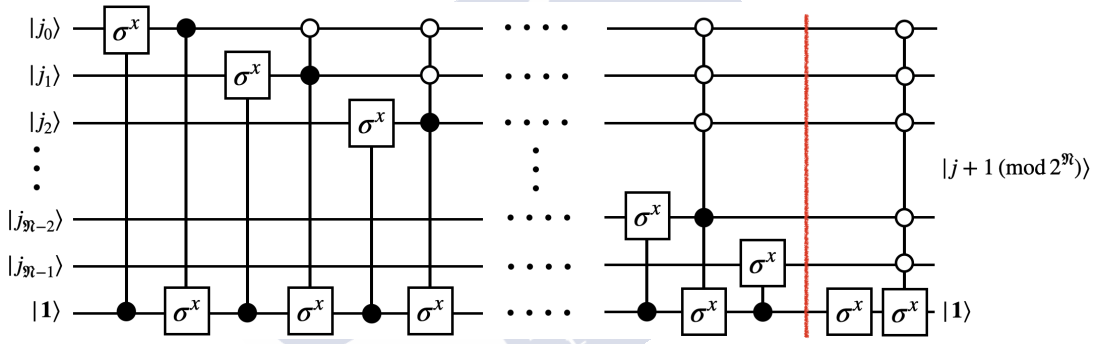

Figure 5.16: Circuit implementing the bit increment operator $I_{\mathfrak{N}}$, introduced by Kaye [11, 12]. The number of elementary quantum gate operations required scales as $O(\mathfrak{N}^2)$ for $\mathfrak{N} \geq 3$, leading to the polylogarithm scaling. Figure taken from [7].

5.D Details of the interaction term

In this appendix, we construct the operator $U^{\mathrm{diag}}_{I,\mathbf{n}}$, for the simplest case of $\mathbf{n} = -1/2$ and $M = 4$, and discuss how the generalize it to all $\mathfrak{n}$ and M.

In this simple case, $\phi^{(i)\,\mathrm{diag}}_{-1/2} = \sigma^z$ acting on the occupancy qubit of the register i (see Eq. (5.23)). Also, for $M = 4$, $U^{\mathrm{diag}}_{I,-1/2}$ acts only on the respective occupancy qubits of the four particle registers. Using the fact that $(\sigma^z)^2 = 1$, we obtain

$$U^{\mathrm{diag}}_{I,-1/2} \equiv \exp\left\{-i\Delta \sum_{s=0}^{2} c_{s,-1/2} O_{s,-1/2}\right\} . \tag{5.74}$$

Here we distinguish three types of operator: $O_{0,-1/2} = 1^{\otimes 4}$, $O_{1,-1/2} = (\sigma^z)^{\otimes 4}$ and $O_{2,-1/2} = \mathcal{P}_\Sigma(1\otimes 1\otimes\sigma^z\otimes\sigma^z)$. The coefficients can be computed after taking into account all possible combinations giving rise to each operator and read: $c_{0,-1/2} = 4!(4+12)$, $c_{1,-1/2} = 4!$ and $c_{2,-1/2} = 4!(2+1)$. The operator $\mathcal{P}_\Sigma(\hat{X})$, represents the sum over all possible permutations of $\hat{X}$, in the tensor product. By itself, each $O_{s,-1/2}$ is simply a product of Pauli matrices, and following the discussion in chapter 4, it can be easily implemented.

The generalization of Eq. (5.74) to arbitrary $\mathbf{n}$ (and M) requires replacing σ^z by its higher dimensional analogue, given in section 5.2.2. For $M > 4$ one has to repeat the algorithm for all $M(M-1)(M-2)(M-3)/4! \sim O(M^4)$ possible four-tuples formed out of M registers.

5.E Details of the renormalization procedure

In this appendix, we begin by discussing the RG construction at weak coupling. In this regime, Eq. (5.59) can be expanded in λ as

$$H^{\text{eff}} = H + [i\eta, H] + \frac{1}{2!}[i\eta[i\eta, H]] + \cdots = H_0 + H_I + [i\eta, H_0] + [i\eta, H_I] + \frac{1}{2}[i\eta, [i\eta, H_0]] + O(\lambda^3)\,, \tag{5.75}$$

where $H = H_0 + H_I$ and $H_I \sim O(\lambda)$, $\eta \sim O(\lambda)$. We label eigenstates $H_0|\alpha, i\rangle = E_{\alpha,i}|\alpha, i\rangle$, where $\alpha = l, h$ denote low and high energy sectors. To block-diagonalize H such that $\langle\alpha, i|H^{\text{eff}}|\beta, j\rangle = 0$ if $\alpha \neq \beta$, we require that the diagonal elements of $i\eta$ vanish, $\langle\alpha, i|i\eta|\alpha, j\rangle = 0$, and we set $\langle\alpha, i|i\eta|\beta, j\rangle = \langle\alpha, i|H_I|\beta, j\rangle/(E_{\alpha,i} - E_{\beta,j})$ for $\alpha \neq \beta$. With this, the off-diagonal elements of H^{eff} cancel to $O(\lambda^2)$. In this case, $H^{\text{eff}} = H_0 + H_I + \frac{1}{2}[i\eta, H_I] + O(\lambda^3)$, with the low energy matrix elements given by

$$\langle l, i|H_{\text{eff}}|l, j\rangle = \langle l, i|H|l, j\rangle + \frac{1}{2}\sum_k \langle l, i|H_I|h, k\rangle\langle h, k|H_I|l, j\rangle \left[\frac{1}{E_{l,i} - E_{h,k}} + \frac{1}{E_{l,j} - E_{h,k}}\right]. \tag{5.76}$$

The same transformation applies to any operator $O_{\text{eff}} = TOT^\dagger$, which can be expressed as $\langle l, i|O_{\text{eff}}|l, j\rangle = \langle l, i|O|l, j\rangle + \langle l, i|\Delta O|l, j\rangle$. For the matrix elements for an observable diagonal in the eigenbasis of H_0 (such as particle number), this reads

$$\langle l, i|\Delta O|l, j\rangle = \sum_k \left\{ \frac{\langle l, i|H_I|h, k\rangle}{E_{l,i} - E_{h,k}} \frac{\langle h, k|H_I|l, j\rangle}{E_{h,l} - E_{l,j}} \frac{1}{2}[O^l_j + O^l_i] - \frac{\langle l, i|H_I|h, k\rangle}{E_{h,k} - E_{l,j}} O^h_k \frac{\langle h, k|H_I|l, j\rangle}{E_{l,i} - E_{h,k}} \right\}, \tag{5.77}$$

where we abbreviated $\langle l, i|O|l, j\rangle \equiv O^l_i \delta_{ij}$. The procedure outlined can in principle be continued to arbitrary order $O(\lambda^n)$. See [7] for the case where the operator is not diagonal in the H_0 eigenbasis.

To generalize the renormalization procedure beyond weak coupling, one may use Wegner's formulation of an infinitesimal operator renormalization group [207] whereby states inside an energy shell of width δ around the cutoff Λ are integrated: $H(\Lambda - n\delta) = T(n)H(\Lambda)T^\dagger(n)$ with $T(n) = \exp(i\eta(n))$, $H(\Lambda - N\delta) = H^{\text{eff}}$ after a number of RG steps N, and $\eta(n) = [H_d(n), H(n)]$. Here $H_d(n)$ is the diagonal part of the Hamiltonian obtained after $n \leq N$ steps. The Hamiltonian $H(\Lambda \to \infty)$ is usually not known, and in practice one starts from an ansatz for H_{ll}^{eff} at finite Λ and takes the continuum limit.

USC
UNIVERSIDADE
DE SANTIAGO
DE COMPOSTELA

6

Towards the quantum simulation of jet quenching

In this chapter we take the first steps towards the quantum simulation of in-medium jet evolution. We focus on providing a strategy to quantum simulate the evolution of a parton (a quark) in the presence of a background field, allowing for modifications to its momentum to occur, but neglecting the possibility of it emitting radiation. In addition, we show that this strategy is capable of recovering the $\hat{q}$ parameter.

This chapter is based on [13].

6.1 Parton evolution in the Hamiltonian formulation

Our strating point is Eq. (2.81), which describes the effective in-medium scalar propagator of the quark up to next-to-eikonal accuracy. In particular, it is easily observed that this is the propagator for a single particle evolving under a potential $g\mathcal{A}^{-1}$ in two-dimensional Quantum Mechanics. Equivalently, the single particle evolution is determined by the non-relativistic Hamiltonian [81]

$$\mathcal{H}(t) = \frac{\boldsymbol{p}^2}{2\omega} + g\mathcal{A}^{-}(t, \boldsymbol{x}) \cdot T = \mathcal{H}_K + \mathcal{H}_{\mathcal{A}}(t)\,, \tag{6.1}$$

where ω is the quark energy, playing the role of a mass and $\boldsymbol{p}$ is (quark) momentum operator. In the strict eikonal limit, where $\frac{p^2}{\omega} \to 0$, the kinetic term drops out and the

[1] Here, we use $\mathcal{A}$ to denote the background field, unlike previous chapters. Also, we denote the color generators by T in order to avoid confusion with the time variable t.

evolution leads to the state acquiring a field dependent phase, as mentioned previously. The respective time evolution operator can be written as

$$\mathcal{U}(t,0) \equiv \mathcal{T} \exp\left[-i \int_0^t ds\, \mathcal{H}(s)\right] , \tag{6.2}$$

with $\mathcal{T}$ time time ordering operator. This operator acts on the Hilbert space of single free particle particle in two dimensions, such that an initial state $|\psi_0\rangle$ at time $t = 0$ is related to the state $|\psi_t\rangle$ via

$$|\psi_t\rangle = \mathcal{U}(t,0)|\psi_0\rangle\,. \tag{6.3}$$

The Hilbert spanned can be conveniently spanned by the position eigenvectors $|\boldsymbol{x}\rangle$ or by their Fourier pair $|\boldsymbol{p}\rangle$. It is natural to consider these two basis since $\hat{\boldsymbol{p}}\,|\boldsymbol{p}\rangle = \boldsymbol{p}\,|\boldsymbol{p}\rangle$ and $\hat{\mathcal{A}}^{-a}(t,\hat{\boldsymbol{x}})\,|\boldsymbol{x}\rangle = \mathcal{A}^{-a}(t,\boldsymbol{x})\,|\boldsymbol{x}\rangle$, where we used the hats to highlight the difference between operators and c-numbers; we also used the fact that the quark-medium interaction is localized in position space (and conversely highly delocalized in momentum space).

With this formulation of parton evolution in the medium, and using the results from chapter 4, we can provide a strategy to quantum simulate the quark evolution.

6.2 A quantum strategy to simulate in-medium evolution

Let us first summarize the several steps involved in the quantum simulation algorithm, which are summarized in Fig. 6.1.

1. **Input** – i) Template distribution to be loaded as an initial state $|\psi_0\rangle$ ii) A list of m field configurations $\mathcal{A}^-$ with the associated weights $p_{\mathcal{A}^-}$, storing the probability of generating each configuration;

2. **Encoding** – Map between the degrees of freedom of the quantum system and the qubits;

3. **Initial state preparation** – Preparation of $|\psi_0\rangle$;

4. **Time evolution** – Implementation of Eq. (6.3);

5. **Measurement** – Retrieving physical information by measuring the qubits, according to a sensible protocol.

6. **Output** – For each field configuration the algorithm will output the expected value of a random variable χ, which should be then medium-averaged over all m configurations.

The implementation is very similar to the one provided in chapter 5.

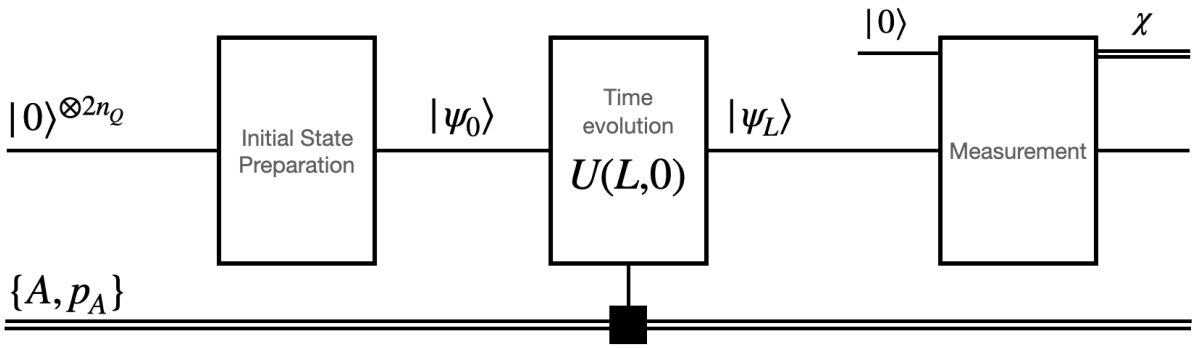

Figure 6.1: Overview of the circuit implementation of the quantum simulation algorithm detailed in the main text. Above each line we provide the state being store in the circuit; the ■ denotes that the time evolution gates parameters are to be determined from the field A. Figure taken from [13].

Encoding

We discretize the problem in a two-dimensional lattice, such that $|\boldsymbol{x}\rangle = |a_s \boldsymbol{n}\rangle$, with a_s the spatial lattice spacing and $\boldsymbol{n} = (n_1, n_2)$ a two component dimensionless transverse vector, where each component can take integer values between 0 and $N_s - 1$. The reciprocal momentum space lattice allows one to write the momentum vectors as $|\boldsymbol{p}\rangle = |a_d \boldsymbol{q}\rangle$ and $a_d = \frac{2\pi}{a_s N_s}$ the momentum space lattice spacing, with $\boldsymbol{q} = (q_1, q_2)$ a two dimensional vector with each component also taking integer values between 0 and $N_s - 1$. In the ensuing discussion we restrict ourselves to latices only spanning positive values of $\boldsymbol{x}$ and $\boldsymbol{p}$.

The Hamiltonian can be written in terms of a dimensionless Hamiltonian $H = \mathcal{H} a_s$ (see appendix 6.A for the details)

$$H = \frac{\boldsymbol{P}^2}{2E} + gA(t, \boldsymbol{X}) \cdot T = H_K + H_A(t)\,, \tag{6.4}$$

where $\hat{\boldsymbol{P}}\,|\boldsymbol{q}\rangle = \boldsymbol{q}\,|\boldsymbol{q}\rangle$ and $\hat{\boldsymbol{X}}\,|\boldsymbol{n}\rangle = \boldsymbol{n}\,|\boldsymbol{n}\rangle$ are the dimensionless position and momentum operators. In addition, $A(t, \boldsymbol{n}) \cdot T = a_s \mathcal{A}^-(t, a_s \boldsymbol{n}) \cdot T$ and $E = \frac{N_s^2 \omega a_s}{4\pi^2}$ is the dimensionless energy factor. In what follows, position and momentum vectors are assumed to be given in this dimensionless basis.

The mapping to the qubits is immediate: for each spatial dimension we employ a register with n_Q qubits, such that any component of the vector can be decomposed in a binary basis, using the convention introduced in chapter 4. Position and momentum space vectors are related by a standard qFT.

Initial state preparation

The preparation of an initial wave packet in position or momentum space can be done using the techniques detailed in chapter 5. In this chapter we are mainly interested in

the case where the initial state corresponds to a quark with transverse momentum $\boldsymbol{p} = \mathbf{0}$, which can always be achieved (theoretically) by rotating the reference frame.

We would like notice that, there are however many situations where exactly preparing $|\boldsymbol{p} = \mathbf{0}\rangle$ is not possible (for example the detailed encoding might not include this point as was the case in chapter 5) or one might be interested in studying initial state effects on the observe momentum distribution.

Time evolution

The time evolution operator in Eq. (6.2) can be written in terms of the dimensionless Hamiltonian H and $L' \equiv L/a_s$

$$U(L', 0) \equiv \mathcal{T} \exp\left[-i \int_0^{L'} dt\, H(t)\right] , \tag{6.5}$$

where we highlight that time has been made dimensionless by dividing by the spatial lattice spacing ${a_s}^2$.

Unlike the cases explored in chapters 4 and 5, in this case the Hamiltonian is time dependent due to the background field. As such, the Trotter-Suzuki formula is not valid. Nonetheless, time evolution controlled by time dependent Hamiltonians can still be quantum simulated easily. In this chapter we are not so concerned with providing an optimized implementation, but rather give an overall strategy. As such, we use the simplest product formula [225], decomposing U as

$$U(L', 0) \approx \prod_{k_t=1}^{N_t} \left\{ \exp\left[-iH_K \frac{L'}{N_t}\right] \exp\left[-iH_A\left(k_t \cdot \frac{L'}{N_t}\right)\frac{L'}{N_t}\right] \right\} \equiv \prod_{k_t=1}^{N_t} \left\{U_K(\varepsilon_t) U_A(k_t \cdot \varepsilon_t, \varepsilon_t)\right\} , \tag{6.6}$$

where we have sliced time into N_t steps, each with a length $\varepsilon_t \equiv L'/N_t$. In each time step, the evolution operator is split into a short evolution according to H_K, followed by an evolution in time with H_A. Notice that during the time interval $(k_t \cdot \varepsilon_t, (k_t + 1) \cdot \varepsilon_t)$ the field A is taken to be constant, leading to the constraint that $\varepsilon_t^{-1} \gg ||\partial_t H_A(t)||$; there exist algorithms [225] which circumvent this constraint, as well as other strategies (see for example [194,226–228]) to quantum simulate time dependent Hamiltonians with expected higher precision.

Similar to the previous chapter, we can now focus solely on the evolution during the k_t^{th} time slice, and similar to the previous chapter, we choose to time evolve according to H_K in the momentum basis, while the evolution according to H_A is done in position space, due to the locality of interactions. This is illustrated in Fig. 6.2.

The action of U_K is diagonal in the $|\boldsymbol{p}\rangle$ basis

$$U_K(\varepsilon_t) |\boldsymbol{p}\rangle = \exp\left(-i \frac{\varepsilon_t}{2E} \boldsymbol{p}^2\right) |\boldsymbol{p}\rangle , \tag{6.7}$$

[2] In general, one could choose another length scale to make time dimensionless, leading to the appearance of a ratio between a_s and said scale.

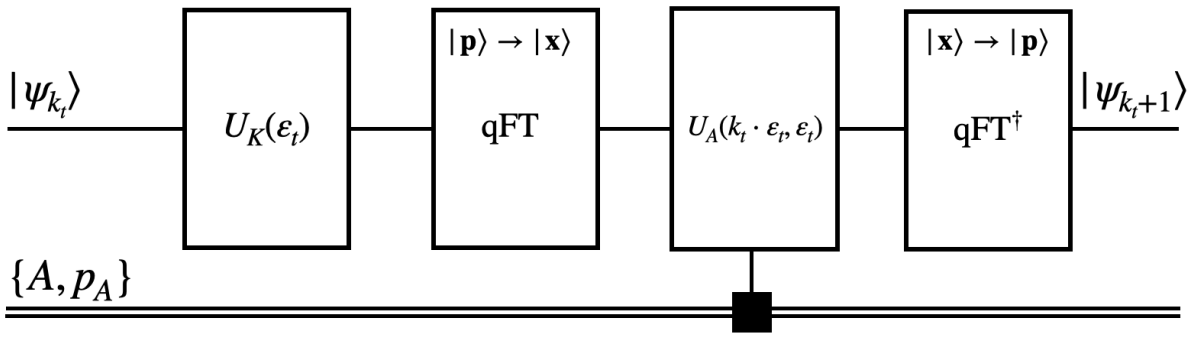

Figure 6.2: Outline of the implementation of the time evolution operator U in the k_t^{th} time step. Figure taken from [13].

thus one only needs to implement a circuit which generates a state dependent phase, similar to the case in the previous chapter and [178]; see appendix 6.B.

After performing the qFT, one has to compute the action of U_A in the $|\boldsymbol{x}\rangle$ basis

$$U_A(k_t \cdot \varepsilon_t, \varepsilon_t)\,|\boldsymbol{x}\rangle = \exp(-ig\varepsilon_t A(k_t \cdot \varepsilon_t, \boldsymbol{x}))\,|\boldsymbol{x}\rangle \ , \tag{6.8}$$

where, for now, we assume that the quark is a color singlet; see section 6.3 for details on how to deal with non-trivial color evolution.

In principle, one could again use a strategy similar to the one used to implement U_K. However, this assumes that one could construct N_t oracles which quantum compute $A(k_t \cdot \varepsilon_t, \boldsymbol{x})$ for every $\boldsymbol{x}$ in each time slice. Since in general one does not have a closed form expression or a simple numerical routine to compute the field values, such an approach might not be possible. A more realistic approach would consist in first computing the field values for spacetime points, which requires $O(N_t \times N_s^2)$ classical evaluations of the field, and thus it would defeat the purpose of the strategy outlined so far. Nonetheless, in practice a small number of qubits n_Q is needed to have a sufficiently good discretization (see section 6.4), and thus the actual number of field evaluations could in practice be performed by a classical computer.

Once one has evaluated all the relevant field values, they are stored in a classical memory and loaded onto the circuit as parameters to the basic gates implementing Eq. (6.8); see appendix 6.B. Clearly the implementation of the operator U_A would greatly benefit from native implementations of quantum diagonal gates, where each entry exponentiates a circuit input [229][3].

After performing this operation and transforming back to the momentum basis, this block is iterated until $k_t = N_t$.

[3]Quantum strategies to simulate the time evolution of the background field could also be coupled to our strategy. This could in principle simplify the implementation of U_A.

Measurement

Given the final state $|\psi_L\rangle = \sum_{\boldsymbol{q}} \psi_L^{\boldsymbol{q}} |\boldsymbol{q}\rangle$ one could measure all the $2n_Q$ qubits and obtain the probabilities $|\psi_L^{\boldsymbol{q}}|^2$ for every $\boldsymbol{q}$ and reconstruct the underlying probability distribution. However, such a strategy requires an exponentially large number of measurements. One can however, design more efficient protocols which give access to relevant physical information. In this section, we assume that the initial condition of the quark is $\boldsymbol{p} = \boldsymbol{0}$. In this case the coefficients $|\psi_L^{\boldsymbol{q}}|^2$ are directly related to the single particle broadening distribution; see appendix 6.C. To be more exact, this is only true after performing an average over all p_A field configurations, which can be done at the end of the algorithm. Thus, for each of the m field configurations one runs the algorithm the necessary number of times to extract the expectation value of some variable classical χ (to be detailed below) and then performs a medium average, reading

$$\langle \chi \rangle_{\mathrm{M}} = \frac{1}{\sum_{i=1}^{m} p_{A^{(i)}}} \sum_{i=1}^{m} p_{A^{(i)}} \langle \chi \rangle_{\mathrm{QM}}^{(i)} , \tag{6.9}$$

where i runs over all possible medium configurations and $\langle . \rangle_{\mathrm{M}}$ denotes the average over field configurations while $\langle . \rangle_{\mathrm{QM}}$ denotes the (quantum mechanical) expectation value. As mentioned above, this procedure can be replaced by a parallel circuit where the dynamics of the gauge field are simulated. The numerical value for m depends on field fluctuations, that are typically assumed to follow the MV model prescription [117–119, 230, 231]. We note however that in our approach, one is not constrained to assume the MV model, nor does one need to explicitly construct any field correlator. In addition, due to the formal similarities between jet quenching and saturation physics [133], the physical origin of $\mathcal{A}^-$, either generated from hot and dense Quark Gluon Plasma, the initial glasma [114] or from cold nuclear matter, is not constrained. Also, our approach should be able to explore the evolution of the jet quenching parameter $\hat{q}$, both in time and in orthogonal spatial directions [232]. The only practical constraint is that the larger the background field fluctuations become, the larger m must be, leading to a linear increase in cost for running the full algorithm.

Let us then consider the case for a single field configuration and how to extract $\hat{q}$ for that $\mathcal{A}^-$. First, we add an ancilla qubit to the circuit and perform the Hadamard test detailed in Fig. 6.3.

We first transform the ancilla by the Hadamard gate $H = H^\dagger$, and then apply a unitary transformation V on the physical state if the ancilla is in the state $|1\rangle$. We then reverse the transformation applied on the ancilla and measure the qubit. We associate the measured value to a random variable χ which takes the values -1 if we observe the state $|0\rangle$ and $+1$ if the state $|1\rangle$ is generated. The ancilla can be either prepared in the state $|0\rangle$ or in the superposition $1/\sqrt{2}(|0\rangle + i\,|1\rangle)$. This strategy is not unique, but it is particularly simple and inexpensive.

One can show that if the ancilla is in the initial state $|0\rangle$ (see 6.D), then

$$\langle \chi \rangle_{\mathrm{QM}} \equiv \langle \psi_L | \, V + V^\dagger \, | \psi_L \rangle = \Re \, \langle \psi_L | \, V \, | \psi_L \rangle \ . \tag{6.10}$$

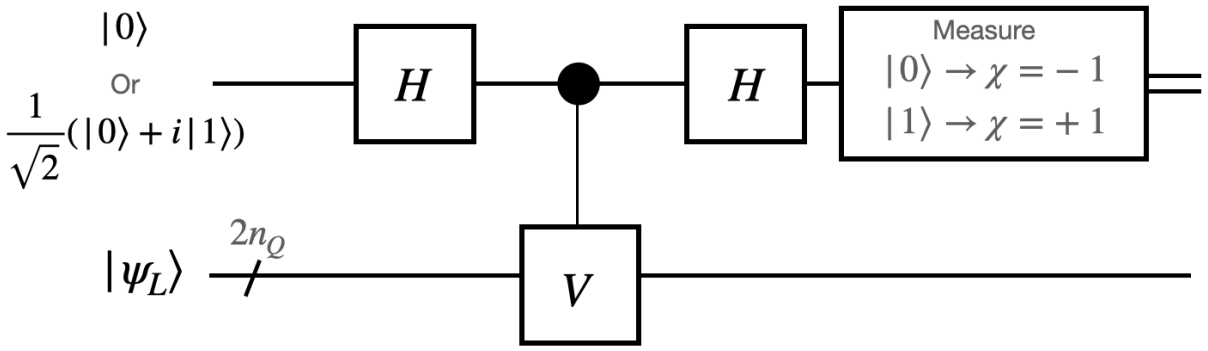

Figure 6.3: Detailed measurement strategy. Figure taken from [13].

On the other hand, if the ancilla is prepared in the state $1/\sqrt{2}(|0\rangle + i\,|1\rangle)$, we have that

$$\langle \chi \rangle_{\rm QM} = \Im \langle \psi_L | \, V \, | \psi_L \rangle \ , \tag{6.11}$$

which when combined give access to both the real and imaginary parts of the expectation value of the unitary operator V.

Let us consider first the case where $V = V_\alpha = \exp(i\alpha \boldsymbol{P}^2)$. Then

$$\Re \langle \psi_L | \, V_\alpha \, | \psi_L \rangle = \langle \cos(\alpha \boldsymbol{P}^2) \rangle_{\rm QM} \, , \tag{6.12}$$

and

$$\Im \langle \psi_L | \, V_\alpha \, | \psi_L \rangle = \langle \sin(\alpha \boldsymbol{P}^2) \rangle_{\rm QM} \, , \tag{6.13}$$

from which one extracts $\langle e^{i\alpha \boldsymbol{P}^2} \rangle_{\rm QM}$, by definition. We also have that

$$\langle e^{i\alpha \boldsymbol{P}^2} \rangle_{\rm QM} = 1 + \sum_{k=1}^{\infty} \frac{i\alpha^k}{k!} \langle \langle 2k \rangle \rangle \, , \tag{6.14}$$

where $\langle \langle 2k \rangle \rangle \equiv \langle \boldsymbol{P}^{2k} \rangle_{\rm QM}$ corresponds to the expectation value of the $2k$ power of the momentum operator. When initial state effects are absent, $a_d^2 \langle \langle 2 \rangle \rangle = \hat{q} L$, where we inserted a_d^2 to get the correct dimensions. Furthermore, one can choose α such that, for small enough α, only linear variations are relevant

$$\langle e^{i\alpha \boldsymbol{P}^2} \rangle_{\rm QM} \approx 1 + i \frac{\alpha}{a_d^2} \hat{q} L \rightarrow \langle \sin(\alpha \boldsymbol{P}^2) \rangle_{\rm QM} \approx \frac{\alpha}{a_d^2} \hat{q} L \, . \tag{6.15}$$

Notice that the left hand side corresponds to a quantity extracted from the quantum computer, while the right hand side is written in terms of the jet quenching parameter.

If one goes to higher orders in α, then one is sensitive to the even moments of the momentum distribution. One can imagine varying α and from the observed evolution retrieving the $\langle \langle 2k \rangle \rangle$ moments via a numerical fit. Of course, such a strategy, on top of

the additional polynomial cost in m, would increase the cost of running the algorithm by the number of α values to be explored.

If one is only interested in extracting $\hat{q}$, one could consider the unitary $V = \exp(iF(\boldsymbol{P}^2))$, with $F(\boldsymbol{P}^2) = \arccos(\boldsymbol{P}^2)$. Then, for the case where the ancilla is initially set to $|0\rangle$, we obtain

$$\langle X \rangle_{\mathrm{QM}} = \langle \psi_L | \cos(\arccos(\boldsymbol{P}^2)) | \psi_L \rangle = \langle \langle 2 \rangle \rangle \,. \tag{6.16}$$

Such a arithmetic oracle should be available, see references and discussion in chapter 5.

6.3 Treating color evolution

Let us now consider the case where the quark is in the fundamental representation of the color group. An immediate consequence is that H_A now has a non-trivial color structure, i.e. $A \cdot T = A^a T^a = \frac{1}{2} A^a \lambda^a$, where λ^a denotes the eight Gell-Mann matrices. To deal with this modification, we further split the time evolution operator to take the form $U = U_K \cdot U_{A^1} \cdot U_{A^2} \cdots U_{A^8}$ and we track the color of the quark by adding a new register with two qubits, which stores the color state of the quark. In particular we use the following map between the logical and physical states: $|0,0\rangle \equiv |\mathrm{red}\rangle = |R\rangle$, $|0,1\rangle \equiv |\mathrm{green}\rangle = |G\rangle$, $|1,0\rangle \equiv |\mathrm{blue}\rangle = |B\rangle$ and $|1,1\rangle \equiv |W\rangle$, with the latter state not being physical and therefore absent from any calculation.

We now detail how to implement H_{A^1}, with the other values of a following analogous implementations. The first Gell-Mann matrix is given by

$$\lambda_1 = \begin{pmatrix} 0 & 1 & 0 \\ 1 & 0 & 0 \\ 0 & 0 & 0 \end{pmatrix} \to \begin{pmatrix} 0 & 1 & 0 & 0 \\ 1 & 0 & 0 & 0 \\ 0 & 0 & 0 & 0 \\ 0 & 0 & 0 & 0 \end{pmatrix} \equiv \tilde{\lambda}_1 \,, \tag{6.17}$$

where in the second step we have embedded λ_1 into the two qubit Hilbert space. The action of $\tilde{\lambda}_1$ is to color rotate the quark state between the $|R\rangle$ and $|G\rangle$ states. One can diagonalize the above matrix using a control Hadamard gate CH

$$CH = \begin{pmatrix} 1/\sqrt{2} & 1/\sqrt{2} & 0 & 0 \\ 1/\sqrt{2} & -1/\sqrt{2} & 0 & 0 \\ 0 & 0 & 1 & 0 \\ 0 & 0 & 0 & 1 \end{pmatrix} \,, \tag{6.18}$$

such that we can write H_{A^1}, in k_t^{th} time interval, in terms of a diagonal operator (here we drop all spacetime dependence for clarity)

$$e^{-\frac{ig\varepsilon_t}{2} A^1 \otimes \tilde{\lambda}_1} = (1 \otimes CH) e^{-\frac{ig\varepsilon_t}{2} A^1 \otimes \tilde{\sigma}^Z} (1 \otimes CH) \,. \tag{6.19}$$

and we used the extended Pauli operator $\tilde{\sigma}^Z = \mathrm{diag}(1,-1,0,0)$[4]. Finally, to compute the exponential of the tensor product we notice that

$$e^{-i\frac{g\varepsilon_t}{2}A^1\otimes\tilde{\sigma}^Z}\,|\boldsymbol{x}\rangle\otimes|c\rangle = \sum_n \frac{(-ig\varepsilon_t)^n}{2^n n!}(A^1(\boldsymbol{X})\tilde{\sigma}^Z)^n\,|\boldsymbol{x}\rangle\,|c\rangle = |\boldsymbol{x}\rangle\sum_n \frac{(-ig\varepsilon_t A^1(\boldsymbol{x}))^n}{2^n n!}(\tilde{\sigma}^Z)^n\,|c\rangle\ , \tag{6.20}$$

where $|c\rangle$ denotes the two qubits register storing the state of the quark in color space. From the previous equation it is easy to observe that only $|0,0\rangle$ and $|0,1\rangle$ states result in a phase, the former with a $-i$ pre-factor and the latter with a $+i$; the circuit implementation of Eq. (6.19) is given in Fig. 6.4.

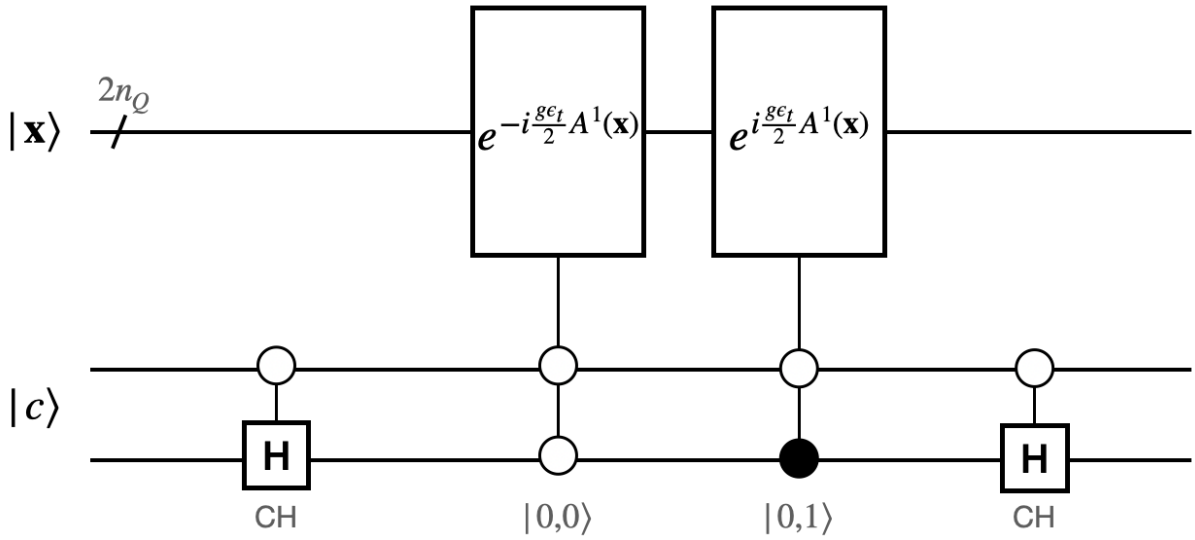

Figure 6.4: Implementation of the (infinitesimal) time evolution operator generated by H_{A^1}.

An important consequence of including non-trivial color evolution is the fact that the final and initial state are differential in color. Therefore, when preparing the state one has to set colors either according to some initial state prescription or in an equitative way. Conversely, in the measurement protocol the output must be color averaged, which can be performed classically[5].

6.4 Numerical estimates for the circuit parameters

Finally, let us estimate the necessary resources needed in order to implement this algorithm, based on the discussion in chapters 2 and 3.

[4]To be more precise, this definition takes $\tilde{\sigma}^Z$ to be non-unitary, unlike σ^Z. This is done, in order to ensure that only the $|R\rangle$ and $|G\rangle$ states transform non-trivially.

[5]This is not necessary if the qubits storing the color information are not measured.

When traversing a dense medium of length L, the quark will acquire an average transverse momentum of the order of the saturation scale, $\langle \boldsymbol{p}^2 \rangle \sim \hat{q}L \equiv Q_s^2$. L is roughly of the order of the nuclear radius of heavy elements, like Pb or Au, which we take to be $L \sim O(10\,\mathrm{fm}) = O(50\,\mathrm{GeV}^{-1})$, for experimental set-ups such as the LHC, RHIC or the EIC. In addition, to bridge these experimental conditions, we assume that $O(0.1\,\mathrm{GeV}^2\mathrm{fm}^{-1}) \leq \hat{q} \leq O(10\,\mathrm{GeV}^2\mathrm{fm}^{-1})$ [6,153,155]. The saturation scale Q_s^2 is then approximately bounded by $Q_s^2 \sim O(1 - 100\,\mathrm{GeV}^2)$.

Setting the ultraviolet momentum cutoff induced by the digitization $\boldsymbol{p}_{\mathrm{max.}}$ to be much larger than the saturation scale Q_s, we obtain

$$|\boldsymbol{p}_{\mathrm{max.}}| \approx \frac{2\pi}{a_s} \gg O(1 - 10\,\mathrm{GeV})\,, \tag{6.21}$$

thus

$$a_s \ll O(1 - 10\,\mathrm{GeV}^{-1}) = O(0.1 - 1\,\mathrm{fm})\,. \tag{6.22}$$

Conversely, we require that the momentum space discretization is neither to coarse nor to fine. A simple way to ensure this is to impose

$$\mu < a_d < Q_s \sim \frac{\mu}{Q_s} < \frac{1}{N_s} < 1\,, \tag{6.23}$$

where typically $\mu \sim O(0.1 - 1\,\mathrm{GeV})$ [6, 113, 125]. Recalling that $N_s = 2^{n_Q}$, we obtain

$$1 < N_s < 100 \iff 0 < n_Q < 7\,. \tag{6.24}$$

Thus, one roughly needs $O(2^7 = 128)$ states per dimension to adequately discretize the theory. In practice this number will have to be larger since the correct energy ratio should be $\mu/|\boldsymbol{p}_{\mathrm{max.}}|$, which here we took $|\boldsymbol{p}_{\mathrm{max.}}| = Q_s$, such that the peak of the broadening distribution is well captured. Even so, one would expect that (roughly) $n_Q < 20$ or $N_s < O(10^6)$.

The longitudinal scales also impose a constraint on the circuit parameters. We recall that in the multiple soft scattering approximation, one requires that λ is much larger than the typical correlation length in the medium $1/\mu$, ensuring that there are no color correlations between different scatterings centers. This condition can be written as

$$1 \geq \frac{\lambda}{L} \gg \frac{1}{\mu L}\,. \tag{6.25}$$

The opacity of the medium, $\chi_{\mathrm{med.}} \equiv L/\lambda$ [101, 102], can be identified with $\chi_{\mathrm{med.}} \sim N_t = L'/\varepsilon_t$, leading to

$$1 \leq N_t \ll \mu L \implies 1 \leq N_t \ll O(100)\,. \tag{6.26}$$

The remaining circuit parameter that directly depends on the physics one wants to explore is m, the number of field configurations to be generated. As alluded above, the numerical value for m intrinsically depends on the model/prescription for the gauge field and its fluctuations, and therefore it is tied to the underlying physical origin of this field. As such, we are not able to give an estimate for it, without assuming some model.

6.5 A brief summary

In this chapter we have introduced a simple algorithm to quantum simulate parton propagation inside the medium. This allowed us to extract the jet quenching parameter $\hat{q}$. The algorithm requires $2n_Q+l$ qubits (assuming one can re-use ancillas) and $O(N_t \times \text{polylog} N_s)$ basic gate operations. However, there is an underlying classical cost coming from the $m \times N_t \times N_s^2$ evaluations of the gauge field. This is the major drawback of our strategy, since it is not guaranteed that the classical evaluations of $\mathcal{A}$ can be performed efficiently. Additionally, there is an overall additional polynomial cost in the measurement section, if one decides to scan several values of α.

The strategy used is a classical-quantum hybrid one, already explored in other studies [233–235] and being a promising avenue for near term applications. Nonetheless, simulating momentum broadening, which is a (classical) α_s^0 effect, is by itself not interesting since it is easily calculable using standard techniques. Nonetheless, the formulation of a full medium induced cascade is of great interest and simulating single particle broadening constitutes a first step in this direction. Also, recent interest has sparked the design of quantum circuits to simulate hard probe's evolution in the medium [235], using an open quantum system formulation. This is set-up is however not fully developed in the context of jet quenching (see however [236, 237]). This is unlike our approach, formulated well within the BDMPS-Z/ASW framework.

Going beyond α_s^0 effects amounts to include Eqs. (2.71) and (2.74) in the Hamiltonian $\mathcal{H}$ [81]. Nonetheless, this entails having an efficient way of simulating branching processes using a quantum computer which, as far as we are aware, is not currently known, at least in the way we formulate the problem. If this is possible and one can simulate both broadening and in-medium branching effects, then such an approach could physically outperform classical Monte Carlo simulations, which can not treat multi-particle interference effects exactly. Further work is necessary to determine if this is feasible or not in the near future.

6.A Discretization and encoding details

In this appendix we give the details on the discretization of the quantum mechanical system considered in the main text and the map to the qubits available in the quantum computer.

Taking a two dimensional lattice, with lattice spacing a_s and N_s sites per dimension, we can write $|\boldsymbol{x}\rangle = |a_s \boldsymbol{n}\rangle$ and $|\boldsymbol{p}\rangle = |a_d \boldsymbol{n}\rangle$, with $a_d = \frac{2\pi}{N_s a_s}$. These two basis are related by

$$|\boldsymbol{p}\rangle = \int_{\boldsymbol{x}} e^{-i\boldsymbol{p}\cdot\boldsymbol{x}} |\boldsymbol{x}\rangle \to a_s^2 \sum_{\boldsymbol{n}} e^{-2\pi i \frac{\boldsymbol{q}\cdot\boldsymbol{n}}{N_s}} |\boldsymbol{n} a_s\rangle \,, \tag{6.27}$$

$$|\boldsymbol{x}\rangle = \int_{\boldsymbol{p}} e^{i\boldsymbol{p}\cdot\boldsymbol{x}}|\boldsymbol{p}\rangle \to \frac{a_d^2}{(2\pi)^2}\sum_{\boldsymbol{q}} e^{2\pi i\frac{\boldsymbol{q}\cdot\boldsymbol{n}}{N_s}}|\boldsymbol{q}a_d\rangle\,, \tag{6.28}$$

where $\int_{\boldsymbol{x}} = \int d^2\boldsymbol{x}$ and $\int_{\boldsymbol{p}} = \int (2\pi)^{-2} d^2\boldsymbol{p}$ and we provide the discretized version of the Fourier integrals. Using that

$$\langle \boldsymbol{x}|\boldsymbol{p}\rangle = e^{-i\boldsymbol{p}\cdot\boldsymbol{x}} \to e^{-2\pi i\frac{\boldsymbol{n}\cdot\boldsymbol{q}}{N_s}}\,, \tag{6.29}$$

one can show that

$$\langle \boldsymbol{x}|\boldsymbol{y}\rangle = \delta^{(2)}(\boldsymbol{x}-\boldsymbol{y}) = \frac{\delta_{\boldsymbol{n},\boldsymbol{m}}}{a_s^2}\,, \tag{6.30}$$

$$\langle \boldsymbol{p}|\boldsymbol{k}\rangle = (2\pi)^2\delta^{(2)}(\boldsymbol{k}-\boldsymbol{p}) = (2\pi)^2\frac{\delta_{\boldsymbol{q_k},\boldsymbol{q_p}}}{a_d^2}\,, \tag{6.31}$$

where we used the closure identity

$$\sum_{\boldsymbol{n}} e^{2\pi i\frac{\boldsymbol{n}\cdot\boldsymbol{q}}{N_s}} = N_s^2\delta_{\boldsymbol{q},0}\,. \tag{6.32}$$

We define the dimensionless basis states

$$|\boldsymbol{n}\rangle = a_s\,|\boldsymbol{x}\rangle\,, \quad |\boldsymbol{q}\rangle = \frac{a_d}{2\pi}\,|\boldsymbol{p}\rangle\,, \tag{6.33}$$

which satisfy $\langle \boldsymbol{n}|\boldsymbol{m}\rangle = \delta_{\boldsymbol{n},\boldsymbol{m}}$, $\langle \boldsymbol{q_p}|\boldsymbol{q_k}\rangle = \delta_{\boldsymbol{q_p},\boldsymbol{q_k}}$ and $\langle \boldsymbol{n}|\boldsymbol{q}\rangle = N_s^{-1}\exp(-2\pi i N_s^{-1}\boldsymbol{n}\cdot\boldsymbol{q})$. The Fourier transforms now read

$$|\boldsymbol{n}\rangle = \frac{1}{\sqrt{N_s^2}}\sum_{\boldsymbol{q}} e^{2\pi i\frac{\boldsymbol{q}\cdot\boldsymbol{n}}{N_s}}\,|\boldsymbol{q}\rangle\,, \tag{6.34}$$

$$|\boldsymbol{q}\rangle = \frac{1}{\sqrt{N_s^2}}\sum_{\boldsymbol{n}} e^{-2\pi i\frac{\boldsymbol{q}\cdot\boldsymbol{n}}{N_s}}\,|\boldsymbol{n}\rangle\,. \tag{6.35}$$

It is natural to introduce the operators $\boldsymbol{P} = \boldsymbol{p}/a_d$ and $\boldsymbol{X} = \boldsymbol{x}/a_s$, satisfying $\hat{\boldsymbol{X}}\,|\boldsymbol{n}\rangle = \boldsymbol{n}\,|\boldsymbol{n}\rangle$ and $\hat{\boldsymbol{P}}\,|\boldsymbol{q}\rangle = \boldsymbol{q}\,|\boldsymbol{q}\rangle$. Inserting this operator definitions into Eq. (6.1), one can extract the dimensionless Hamiltonian $H = a_s\mathcal{H}$, given in Eq. (6.4).

The map to the 1/2-spin registers in the quantum computer is achieved by decomposing each component of the vector $\boldsymbol{n} = (n_1, n_2)$ in the binary basis, e.g.

$$n_1 = \sum_{i=0}^{2^{n_Q}-1} n_1^{(i)}2^i\,, \tag{6.36}$$

where $n_1^{(i)} \in \{0,1\}$ and we assume that there are n_Q qubits available, such that $2^{n_Q} = N_s$ is total number of possible states. If $n_1^{(i)} = 0$ then we associate a qubit in the state $|\uparrow\rangle = |0\rangle$ to it; conversely if $n_1^{(i)} = 1$ we assign $|\downarrow\rangle = |1\rangle$. Eqs. (6.34) and (6.35), correspond to standard qFTs. The extension to include signed values of $\boldsymbol{x}$ and $\boldsymbol{p}$ can be done following chapter 5.

6.B Time evolution details

In this appendix we detail the circuit implementation of U_K and U_A in one spatial dimension, without loss of generality.

The strategy considered to implement U_K was first discussed in [178]. Starting from a state $|\boldsymbol{p}\rangle$ one generates $\exp(-is_K\boldsymbol{p}^2)\,|\boldsymbol{p}\rangle$, with $s_K = \varepsilon_t/(2E)$ a pure real number. This operation can be implemented by i) adding an ancilla register with l qubits all in state $|0\rangle$ ii) assuming that a quantum black-box (quantum oracle) can be constructed that given $|\boldsymbol{p}\rangle$ outputs $|F(\boldsymbol{p})\rangle = |\boldsymbol{p}^2\rangle$. Regarding the first point, the value of l solely depends on the numerical accuracy one wants to represent $\boldsymbol{p}^2$ in a binary basis, roughly $l \geq n_Q$, see chapter 5.

We perform the following set of operations

$$|\boldsymbol{p}\rangle\otimes|0\rangle^{\otimes l} \xrightarrow{\mathrm{a}_1} |\boldsymbol{p}\rangle\otimes|F(\boldsymbol{p})\rangle \xrightarrow{\mathrm{a}_2} \exp(-is_K F(\boldsymbol{p}))\,|\boldsymbol{p}\rangle\otimes|F(\boldsymbol{p})\rangle \xrightarrow{\mathrm{a}_3} \exp(-is_K F(\boldsymbol{p}))\,|\boldsymbol{p}\rangle\otimes|0\rangle^{\otimes l}\,. \tag{6.37}$$

In a first step –a_1– one applies the quantum oracle, with input $|\boldsymbol{p}\rangle$ and stores the output $F(\boldsymbol{p})$ in the ancilla register. In step a_2 one performs a transformation of the form

$$|x\rangle \to \exp(-is_K x)\,|x\rangle\,, \tag{6.38}$$

with s_K a real number and $|x\rangle$ denotes the binary decomposition, with l qubits, of an integer number. This exponentiation operation can always be performed by applying l single qubit gates $R_j(\varepsilon) = \mathrm{diag}(1, e^{-is_K 2^j})$, taking into account that x can be decomposed as

$$x = \sum_{j=0}^{l} x_j 2^j\,, \tag{6.39}$$

where $x_j \in \{0,1\}$. Acting on a single qubit the above operator has non-zero matrix elements $\langle 0|\,R_j(s_K)\,|0\rangle = 1$ and $\langle 1|\,R_j(s_K)\,|1\rangle = \exp(-is_K 2^j)$. Coupling l of such operators with increasing values of j

$$R(s_K) \equiv R_0(s_K)\otimes R_1(s_K)\otimes\cdots\otimes R_l(s_K)\,, \tag{6.40}$$

results in a multi-qubit operator implementing the desired transformation, i.e. $R(s_K)\,|x\rangle = \exp(-is_K x)\,|x\rangle$.

The final step – a_3 – consists in erasing the ancilla register back to the state $|0\rangle^{\otimes l}$, which can be achieved by applying the Hermitian conjugate circuit used in step a_1.

In the implementation of U_A, one is handed a list of $N_t \times N_s^2$ values, describing the field values at all the relevant spacetime points. Stringing together $2n_Q$ single qubit gates $R_{\alpha,\beta} \equiv \mathrm{diag}(\exp(i\alpha), \exp(i\beta))$, which can be written as the product of the exponential of the σ^x Pauli gate and the R_j gates, U_A can be implemented. In one spatial dimension and for $n_Q = 1$ and for the k_t^{th} time slice, one would obtain $\alpha_{k_t} = -g\epsilon_t A(k_t\cdot\varepsilon_t, \mathbf{0})$ and $\beta_{k_t} = -g\varepsilon A(k_t\cdot\varepsilon_t, \mathbf{1})$, where the sub-index denotes the time slice and there are only

two spatial lattice points ($|\mathbf{0}\rangle$ and $|\mathbf{1}\rangle$). If we now consider $n_Q = 2$, the respective time evolution operator would be obtained by

$$R_{\alpha,\beta} \otimes R_{\sigma,\gamma} = \begin{pmatrix} \mathrm{e}^{i(\alpha+\sigma)} & 0 & 0 & 0 \\ 0 & \mathrm{e}^{i(\alpha+\gamma)} & 0 & 0 \\ 0 & 0 & \mathrm{e}^{i(\beta+\sigma)} & 0 \\ 0 & 0 & 0 & \mathrm{e}^{i(\beta+\gamma)} \end{pmatrix}, \tag{6.41}$$

for each time slice. By solving the associated system of linear equations, one can map $\{\alpha, \beta, \sigma, \gamma\}$ to $\{A(\mathbf{x})\}$, which can be done offline for any t in a classical computer.

6.C Relation between $|\psi_L\rangle$ and the single particle momentum distribution

The single particle broadening distribution, introduced in section 2.3, gives the probability of observing a quark with momentum $\boldsymbol{k}$ due to interactions with the medium for a time L

$$\mathcal{P}(\boldsymbol{k}, L) = \frac{1}{N_c} \int_{\boldsymbol{x},\boldsymbol{y}} \mathrm{e}^{-i\boldsymbol{k}\cdot(\boldsymbol{x}-\boldsymbol{y})} \mathrm{Tr} \langle \mathcal{W}(\boldsymbol{x}, L) \mathcal{W}^\dagger(\boldsymbol{y}, L) \rangle_{\mathrm{M}} \,, \tag{6.42}$$

where $\mathcal{W}(\boldsymbol{x})$ is a Wilson line operator along the future pointing light-cone at a transverse position $\boldsymbol{x}$, which can be written in the gauge choice employed in the main text as

$$\mathcal{W}(\boldsymbol{x}) = \mathcal{T} \exp\left(ig \int_0^L dt \, \mathcal{A}^-(t, \boldsymbol{x}) \cdot T \right). \tag{6.43}$$

Notice that here we have not assumed that the transverse profile of the medium is isotropic and thus the dependence on $\boldsymbol{x}$ and $\boldsymbol{y}$.

It is not difficult to check that, in the strict eikonal limit, where $H = H_A$, the circuit detailed in the main text mirrors the $\mathcal{P}$ distribution. For clarity, we ignore the details in the implementation of the time evolution operator and we assume that the initial state is that of a quark with zero transverse momentum $|\psi_0\rangle = |\boldsymbol{p} = \mathbf{0}\rangle$.

In this scenario the circuit simplifies significantly since all but an initial and a final qFT cancel out and the system state transforms as

$$|\mathbf{0}\rangle \xrightarrow{\mathrm{qFT}} \frac{1}{\sqrt{N_s^2}} \sum_{\boldsymbol{x}} |\boldsymbol{x}\rangle \xrightarrow{U_A} \frac{1}{\sqrt{N_s^2}} \sum_{\boldsymbol{x}} U_A(L, \boldsymbol{x}) |\boldsymbol{x}\rangle \xrightarrow{\mathrm{qFT}^\dagger} \frac{1}{N_s^2} \sum_{\boldsymbol{q}} \left[\sum_{\boldsymbol{x}} U_A(L, \boldsymbol{x}) \mathrm{e}^{2\pi i \frac{\boldsymbol{x}\cdot\boldsymbol{q}}{N_s}} \right] |\boldsymbol{q}\rangle \,. \tag{6.44}$$

The probability of measuring the state $|\boldsymbol{k}\rangle$, $\mathcal{P}_{\boldsymbol{k}}$, is simply given by

$$\mathcal{P}_{\boldsymbol{k}} = \frac{1}{(N_s^2)^2} \sum_{\boldsymbol{x},\boldsymbol{y}} \mathrm{e}^{2\pi i \frac{\boldsymbol{k}(\boldsymbol{x}-\boldsymbol{y})}{N_s}} U_A^\dagger(L, \boldsymbol{y}) U_A(L, \boldsymbol{x}) \,. \tag{6.45}$$

Averaging over all field configurations and noting that $\mathcal{W}(\boldsymbol{x}) = U_A^\dagger(\boldsymbol{x})$ we obtain

$$\mathcal{P}_{\boldsymbol{k}} = \frac{1}{(N_s^2)^2} \sum_{\boldsymbol{x},\boldsymbol{y}} \mathrm{e}^{2\pi i \frac{\boldsymbol{k}(\boldsymbol{x}-\boldsymbol{y})}{N_s}} \langle \mathcal{W}(\boldsymbol{y}, L)\mathcal{W}^\dagger(\boldsymbol{x}, L)\rangle_{\mathrm{M}} \,, \tag{6.46}$$

which is just the discretized version of the single particle broadening distribution $\mathcal{P}(\boldsymbol{k}, L)$, as expected (ignoring the color average, which can be performed as detailed in section 6.3). Also, since $\mathcal{P}$ is a probability $\int_{\boldsymbol{k}} \mathcal{P}(\boldsymbol{k}, L) = 1$, which is trivially true in the discrete version.

6.D Measurement details

In this appendix we provide some details on the measurement protocol outlined in the main text. Taking the initial ancilla state to be $|0\rangle$

$$\begin{aligned} |0\rangle\,|\psi_L\rangle &\xrightarrow{H} \frac{1}{\sqrt{2}}(|0\rangle + |1\rangle)\,|\psi_L\rangle \xrightarrow{V} \frac{1}{\sqrt{2}}(|0\rangle\,|\psi_L\rangle + |1\rangle\,V\,|\psi_L\rangle) \\ &\xrightarrow{H} \frac{1}{2}\left[(1+V)\,|0\rangle\,|\psi_L\rangle + (1-V)\,|1\rangle\,|\psi_L\rangle\right] . \end{aligned} \tag{6.47}$$

Then the expectation value for the random variable χ reads

$$\langle\chi\rangle_{\mathrm{QM}} = \frac{+1}{4}|\,|\psi_L\rangle + V\,|\psi_L\rangle\,|^2 + \frac{(-1)}{4}|\,|\psi_L\rangle - V\,|\psi_L\rangle\,|^2 = \frac{1}{2}\langle V + V^\dagger\rangle_{\mathrm{QM}} \,, \tag{6.48}$$

which is equivalent to the expression in the main text.

The case where the initial ancilla state is $1/\sqrt{2}(|0\rangle + i\,|1\rangle)$, which can be easily generated from the pure state $|0\rangle$, reads

$$\begin{aligned} &\frac{1}{\sqrt{2}}(|0\rangle + i\,|1\rangle)\,|\psi_L\rangle \xrightarrow{HV} \frac{1}{2}((1+i)\,|0\rangle\,|\psi_L\rangle + (1-i)\,|1\rangle\,V\,|\psi_L\rangle) \\ &\xrightarrow{H} \frac{1}{\sqrt{8}}[((1+i)+(1-i)V)\,|0\rangle\,|\psi_L\rangle + ((1+i)-(1-i)V)\,|1\rangle\,|\psi_L\rangle] \,. \end{aligned} \tag{6.49}$$

Then the expectation value for χ reads

$$\langle\chi\rangle_{\mathrm{QM}} = \frac{i}{2}\langle V^\dagger - V\rangle_{\mathrm{QM}} \,, \tag{6.50}$$

as indicated in the main text.

USC
UNIVERSIDADE
DE SANTIAGO
DE COMPOSTELA

Summary and Conclusions

The main focus of this thesis was on i) establishing the IOE/M framework as a suitable scheme for jet quenching analytic studies beyond the MS *vs* SH divide, commonly found in the literature ii) proposing a novel strategy to quantum simulate high energy scattering in digital quantum computers iii) taking the first steps towards the quantum simulation of full medium induced parton showers.

In chapter 3, we first studied the IOE/M scheme applied to the medium induced gluon energy spectrum beyond NLO accuracy, focusing on the asymptotic regions where the correct/expected physical picture becomes clear. This study was done by tracking all the leading logarithmic dependencies, which are important to fully control the behavior of the spectrum. A particularly relevant side result was the construction of the LT map given in Eq. (2.48), which allows for meaningful comparison between different medium models.

At high energies, we confirmed the NLO term recovers the results from GLV/W, while higher order terms are power suppressed in energy. In fact, we explicitly checked that the LO and NNLO terms contributed at the same order in the high energy expansion, and when combined with sub-leading NLO terms, the dependence on the matching scale disappeared. This provided i) a check that indeed the matching scale vanishes once all orders are taken into account ii) the NLO leading energy term, which is independent of the matching scale, is always the dominant contribution. In conclusion, the goal of recovering the GLV/W solution, using the IOE/M approach, at high energies is never spoiled.

On the other hand, at small frequencies we observed that the spectrum has a much richer structure. The most important message one should take is that the spectrum in this region reduces to the BDMPS-Z/ASW result with a renormalized jet quenching parameter

$$\hat{q}_{\text{eff}}(Q_c) = \hat{q}_0 \log\left(\frac{Q_c^2}{\mu_\star^2}\right)\left[1 + \frac{1.016}{\log\left(\frac{Q_c^2}{\mu_\star^2}\right)} + \frac{0.316}{\log^2\left(\frac{Q_c^2}{\mu_\star^2}\right)} + \mathcal{O}\left(\log^{-3}\left(\frac{Q_c^2}{\mu_\star^2}\right)\right)\right],$$

and unlike the BDMPS-Z/ASW result, the matching scale must obey

$$Q_c^2 = \sqrt{\hat{q}_0\,\omega \log\left(\frac{Q_c^2}{\mu_\star^2}\right)},$$

which prevents the appearance of *fake* diverges and provides a prescription to glue the MS and SH regimes. Very broadly, these results are a consequence of requiring that the spectrum is invariant under variations of the matching scale Q^2.

In a second study, we applied the IOE/M approach to momentum broadening. We observed that, as expected, this framework is able to capture the full broadening distribution, although the scheme only seems numerically reasonable at LHC or RHIC energies. Nonetheless, for many studies having a simple formula including both the SH and MS regimes will certainly be important.

In the future, we plan to study the fully differential gluon spectrum [5,238], thus concluding the application of the IOE/M framework to the standard quantities which form the basis of jet quenching phenomenology. In fact, recently the broadening and energy spectrum results discussed in this thesis have already been applied in a full phenomenological jet quenching study [152], thus showing that the results presented in this thesis are already relevant for direct applications. Another avenue in which the application of IOE/M seems promising is in finding signals for the presence of quasi-particle scattering centers in the QGP [239,240]. This could be applied either in studies of dijet asymmetry or using novel sub-structure observables [241,242]. Although the former has been explored for a longer period of time, the signal for the presence of hard scattering centers directly competes with underlying event and other contributions uncorrelated with the dijet pair, and thus one expects it to be experimentally hard to pin down. On the other hand, the latter approach seems more promising since jet substructure observables sensitive to hard scattering should be less contaminated by other contributions.

In a second section of this thesis, we have introduced a novel strategy to quantum simulate high energy scattering in ϕ^4 theory. Although this is a toy theory, many of the problems faced in more complicated theories already emerge in this case, and thus it provides a good starting point. The major advantage of our approach, which is partially motivated by the emergent partonic picture of QCD at high energies, compared to the seminal work of Jordan, Lee and Preskill [10,64,65], lies on the fact that the number of qubits only scales logarithmically with the lattice volume (and linearly with the number of particles). Thus, for scattering problems, where typically the number of particle is small but the phase space is large, it is natural to consider this approach. In addition, the basis used matches the perturbative Feynman diagrammatic calculus picture, so familiar to high energy physicists. Thus, the interpretation and implementation of our approach seems more straightforward and natural, especially if compared to perturbative QFT approaches. In addition, we have shown that our algorithm directly mirrors scattering events at the LHC or RHIC, and the act of measuring the qubits is analogous to the experimental measurement protocols. On top of this, we showed that, in principle, a quantum computer can in fact outperform the experimental set-up, since one has full control over the final state of the system.

In a next step, we plan to perform a numerical study focusing on the simplest case of $d = 1$ spatial dimensions. Using exact diagonalization numerical packages, we will study how well the spectrum of the theory can be reproduced in the interacting theory at finite λ for given lattice discretization and M, similar to the JLP associated study [10]. Our strategy can also be classically computed for the case of $M = 2$ in $d = 1$ dimensions with $N_s = 8$ (16) lattice sites, which could serve to test the resilience of the algorithm against quantum errors. In a final step, one could implement the resulting circuit in a quantum hardware, although even correctly preparing the initial state of the system would be a notable achievement. Perhaps more interestingly, one could look for simpler problems where the single particle strategy might be already applied in quantum hardware. An example of this could be the extension of our strategy to quantum simulate jet quenching,

where the single particle picture is natural to consider.

In the last topic treated in this thesis, we have presented a simple algorithm to simulate single particle momentum broadening in a digital quantum computer, with the intention of extending this program in the future to a full in-medium parton shower. This effort is inline with recent interest in applying quantum computers to study high energy and nuclear physics phenomenology [62, 63, 235, 243–246]. **If** in the future one is able to efficiently implement a circuit simulating a full medium induced shower, then it is expected that, physics wise, the resulting algorithm outperforms current classical approaches [51, 52]. This is nonetheless still a wide open question and it is not even clear if it can be done in near to mid term hardware, if ever. In addition, one must always keep in mind that due to the special character of the act of measurement in quantum mechanics, even if such a quantum algorithm exists, it will certainly not be able to outperform its classical counterparts in all tasks. Rather, depending on what the precise question of interest is, a quantum strategy might make sense or not.

USC
UNIVERSIDADE
DE SANTIAGO
DE COMPOSTELA

Resumo

QCD é a teoría que describe a forza forte, unha das interaccións fundamentais e un dos piares do modelo estándar de física de partículas. Esta teoría detalla as interaccións entre quarks e gluóns, que son as partículas fundamentais que constitúen os hadróns que forman a maioría da materia ordinaria.

As propiedades máis importantes da QCD poden entenderse do comportamento da súa constante de acoplo α_s. A baixas enerxías ou grandes separacións o acoplamento é grande e, polo tanto, quarks e gluóns non poden existir libremente. Pola contra, estes están fortemente soldados entre si e, como consecuencia, nas escalas macro nas que experimentamos a natureza, forman obxectos neutros en cor que compoñen a maior parte da masa observable no Universo: os hadróns. Non obstante, a medida que aumentamos a enerxía ou miramos máis profundamente dentro dos hadróns, o acoplamento efectivo diminúe e hai unha transición de fases entre as fases confinante e desconfinada da teoría. De feito, a enerxías asintóticamente grandes o acoplamiento desaparece garantindo que os quarks e os gluóns se comporten libremente. Neste réxime de liberdade asintótica as técnicas de teoría da perturbación son aplicables e axeitadas para a caracterización dos correspondentes fenómenos físicos, dado que o acoplamento é pequeno. Por outra banda, a baixas enerxías, as contribucións non perturbativas tórnanse importantes e son necesarios outros enfoques, como os cálculos de lattice.

Ao estudar a dispersión de alta enerxía dos hadróns, a separación anterior entre unha física branda (*soft*) e dura (*hard*) é extremadamente útil. Permite descompor o proceso de dispersión en dúas compoñentes factorizadas, por unha banda a estrutura non perturbativa dos hadróns está codificada en funcións de distribución universais, como as funcións de distribución partónica e, por outra banda, os procesos *hard*, que teñen lugar entre entre os quarks e gluons e que poden ser calculados perturbativamente. Aínda que a estrutura de hadróns non é perturbativa, pódense aplicar métodos de grupo de renormalización para que se poida predicir a estrutura destes obxectos á escala de enerxía relevante. Isto proporciona un xeito de determinar o contido de quark e gluón dos hadróns, dada unha mostra de datos inicial. Por outra banda, os procesos de dispersión dura pódense calcular empregando métodos tradicionais de teoría da perturbación.

Ademais das colisións de hadróns individuais (normalemente protóns) a alta enerxía, que normalmente se consideran eventos moi limpos, pódese explorar o diagrama de fase da QCD facendo colisionar obxectos máis grandes como os núcleos de ouro ou chumbo. Nestes casos, a densidade e a presión da enerxía son tales que se forma un novo estado da materia, o Quark Gluon Plasma. Isto corresponde a un estado desconfinado da materia, que se comporta como un líquido perfecto ás enerxías dos colisionadores actuais, e onde os graos fundamentais de liberdade son os quarks e gluóns libres ás enerxías asintóticas. O estudo do QGP é de extrema importancia para o desenvolvemento da física fundamental, desde aspectos relacionados coas propiedades do QCD como a súa ecuación de estado ou a natureza do Universo inicial. Para describir as colisións de núcleos onde se forma o QGP, asúmese que a factorización citada anteriormente entre procesos físicos *soft* e

hard é aínda válida. As principais diferenzas, con respecto ao caso hadrónico, son que as compoñentes *soft* describen agora a estrutura non perturbativa de obxectos compostos por moitos hadróns, que en xeral non é a suma incoherente das súas compoñentes, e o feito de que os estados finais dos procesos duros se modifican debido á interacción co QGP subxacente producido durante o evento.

Nesta tese, estudamos a modificación que se produce nos estados finais debido á interacción co medio. En particular, consideramos a modificación que a presenza dun mediu induce no chuveiro de partículas procedentes de partóns *hard*. Este efecto, coñecido como *jet quenching*, leva á desviación das partículas dentro do jet e á produción de radiación *bremsstrahlung* debido ás interaccións co medio. Normalmente, isto leva ao alargamento da estrutura do jet, mentres que os modos de radiación máis suaves desvíanse a ángulos máis grandes, termalizándose finalmente unha vez que alcanzan a escala típica de temperatura do medio. Como consecuencia, o núcleo interno do jet amplíase lixeiramente pero leva unha porcentaxe maior da enerxía global do cono.

Dende o punto de vista teórico, a descrición do chuveiro de partóns inducidos polo medio baséase na descrición da evolución no medio dun partón individual. Na orde α_s^0, a interacción entre o partón e o medio leva á modificación do impulso do partón, mentres que na orde α_s, a interacción do medio partón leva á produción de radiación inducida. O estudo analítico destes observables realizouse tradicionalmente no réxime onde domina unha única dispersión dura co medio ou no réxime oposto onde as dispersións suaves múltiples, que poden actuar de forma coherente, son o efecto físico dominante. Non obstante, as condicións experimentais que se exploran actualmente non se atopan dentro de ningún destes réximes. Como consecuencia, ter un marco unificado que abrangue tanto o sector dominado por un scattering duro como aquel dominado por multiples scatterings soft é necesario para unha fenomenoloxía de jet quenching precisa.

Nunha primeira parte desta tese, exploramos tal enfoque denominado Expansión da Opacidade Mellorada (*Improved Opacity Expansion (IOE)*), demostrando que de feito describe adecuadamente o espectro de gluóns inducido polo medio a todas as ordes. Ademais, estendemos este marco para o cálculo do alargamento (*broadening*) da distribución de momentos de partículas individuais.

No capítulo 3, estudamos primeiro o esquema IOE/M aplicado ao espectro de enerxía do gluón inducido polo medio máis alá da precisión de NLO, centrándonos nas rexións asintóticas onde a imaxe física correcta/esperada queda clara. Este estudo fíxose seguindo todas as dependencias logarítmicas principais, que son importantes para controlar completamente o comportamento do espectro. Un resultado secundario especialmente relevante foi a construción do mapa LT indicado na Eq.(2.48), que permite unha comparación significativa entre diferentes modelos medios.

A altas enerxías, confirmamos que o termo NLO recupera os resultados de Giulassy-Levai-Vitev-Wiedemann (GLV/W), mentres que os termos de orde superior son suprimidos. De feito, comprobamos explicitamente que os termos LO e NNLO contribúen á mesma orde na expansión a alta enerxía e que, cando se combinaron con termos NLO sub-dominantes, a dependencia da escala de *matching* desapare. Isto proporciona i) unha

comprobación de que a escala de it matching desaparece unha vez que se teñen en conta todas as ordes; ii) o termo NLO dominante en enerxía, que é independente da escala de matching, é sempre a contribución dominante. En conclusión, o obxectivo de recuperar a solución GLV/W, utilizando o enfoque IOE/M, a altas enerxías nunca se estraga.

Por outra banda, a pequenas frecuencias observamos que o espectro ten unha estrutura moito máis rica. A mensaxe máis importante que debemos levar é que o espectro desta rexión redúcese ao resultado Baier-Dokshitzer-Mueller-Peigné-Schiff-Zakharov/Armesto-Salgado-Wiedemann (BDMPS-Z/ASW) cun parámetro de jet quenching renormalizado.

$$\hat{q}_{\text{eff}}(Q_c) = \hat{q}_0 \log\left(\frac{Q_c^2}{\mu_\star^2}\right)\left[1 + \frac{1.016}{\log\left(\frac{Q_c^2}{\mu_\star^2}\right)} + \frac{0.316}{\log^2\left(\frac{Q_c^2}{\mu_\star^2}\right)} + \mathcal{O}\left(\log^{-3}\left(\frac{Q_c^2}{\mu_\star^2}\right)\right)\right],$$

e a diferenza do resultado BDMPS-Z / ASW, a escala de *matching* debe obedecer

$$Q_c^2 = \sqrt{\hat{q}_0\,\omega \log\left(\frac{Q_c^2}{\mu_\star^2}\right)},$$

o que impide a aparición de falsas diverxencias e proporciona unha prescrición para colar os réximes MS e SH. En liñas xerais, estes resultados son consecuencia de requirir que o espectro sexa invariante baixo variacións da escala de *matching* Q^2. Un xeito explícito de comprobalo é esixir que o espectro de emisións teña unha derivada cero con respecto a Q^2, o que de feito leva á escala anterior Q_c.

Nun segundo estudo, aplicamos o enfoque IOE/M para *broadening* de momento. Observamos que, como era de esperar, este marco é capaz de captar a distribución de broadening completa, aínda que o esquema só parece numéricamente razoable nas enerxías de LHC ou RHIC. Non obstante, para moitos estudos ter unha fórmula sinxela que inclúa os réximes SH e MS certamente será importante. Un punto relevante que hai que destacar é que o IOE/M deixa claro por que o resultado SH non é capaz de captar o comportamento gaussiano de baixo momento. Como se detalla no texto principal, para obter a contribución hard hai que expandir a distribución de broadening completa en termos dunha serie asintótica. É ben sabido que tales series non son únicas, a diferenza das series de Taylor, senón que poden corresponder a moitas funcións diferentes. Isto implica indirectamente que, traballando cunha representación en serie, o resultado perde a conexión coa función orixinal que deu lugar a este comportamento asintótico e, por tanto, a solución gaussiana está ausente. No IOE/M, con todo, o comportamento gaussiano está sempre incluído polo termo LO, resolvendo así este problema co enfoque máis tradicional de expansión da opacidade.

No futuro, planeamos estudar o espectro do gluón completamente diferencial [5, 238], concluíndo así a aplicación do marco IOE/M ás cantidades estándar que forman a base da fenomenoloxía de jet quenching. De feito, recentemente os espectros de broadening e de enerxía discutidos nesta tese foron aplicados nun estudo fenomenolóxico completo

de jet quenching [152], mostrando así xa que os nosos resultados son relevantes para aplicacións prácticas. Outra vía na que a aplicación de IOE / M semella prometedora consiste en atopar sinais para a presenza de centros de dispersión de cuasi-partículas no QGP [239, 240]. Isto podería aplicarse en estudos de asimetría de dijets ou utilizando novos observables de subestructura de jets [241, 242]. Aínda que o primeiro leva sendo explorado durante algún tempo, o sinal da presenza de centros de dispersión dura compite directamente co evento subxacente e outras contribucións sen correlación co par de dijets sendo, polo tanto, unha detección difícil desde o punto de vista experimental. Por outra banda, o segundo enfoque parece máis prometedor xa que os observables de subestruturas de jets sensibles á dispersión dura deberían estar menos contaminadas por outras contribucións.

Aínda que a imaxe factorizada introducida anteriormente é útil para simular procesos de dispersión hadrónica e nuclear a altas enerxías empregando métodos estándar de Teoría Cuántica de Campos , os desenvolvementos recentes noutras áreas abriron a posibilidade de explorar novas formas de simular eses procesos, posiblemente de xeito máis eficiente e capaz para extraer nova información. Se na última década os avances se teñen centrado moito, por exemplo, na aplicación dos resultados da aprendizaxe automática, nos últimos anos xurdiu un grande interese polas técnicas de computación cuántica. A aparente vantaxe que podería traer a computación cuántica é que, para algúns problemas, os ordenadores cuánticos son exponencialmente máis rápidos que calquera contraparte clásica. Ademais, como o nome indica, a natureza cuántica destes dispositivos convérteos en candidatos naturais para simular a natureza no seu nivel máis fundamental.

A diferenza da imaxe factorizada comentada anteriormente, a simulación completa de procesos de dispersión de alta enerxía pode implementarse naturalmente nun dispositivo cuántico usando o algoritmo de simulación cuántica. Este algoritmo, aplicado a este tipo de procesos, consistiría esencialmente en preparar un estado inicial correspondente aos hadróns que colisionan e logo evolucionar o sistema completo baixo o QCD hamiltoniano. Como tal, ten en conta (non perturbativamente) procesos tanto duros como suaves, a costa de perder algún control analítico. Aínda que o mesmo algoritmo podería, en principio, implementarse nunha computadora clásica, o gran tamaño do espazo de Hilbert necesario para capturar a dinámica, requiriría unha cantidade exponencial de recursos e tempo de execución para poder calcular calquera proceso. Por outra banda, a implementación de algoritmos cuánticos adoita ser complicada xa que difire significativamente do caso clásico, debido á unitaridade da mecánica cuántica e o rol especial que a medida posúe no mundo cuántico. Como tal, é necesario moito enxeño para deseñar estes algoritmos.

Nunha segunda sección desta tese, introducimos unha nova estratexia para simular cuánticamente a dispersión de alta enerxía na teoría ϕ^4. Aínda que se trata dun *toy-model*, moitos dos problemas enfrontados en teorías máis complicadas xa xorden neste caso e, polo tanto, proporciona un bo punto de partida. Ademais, isto representa un primeiro paso para realizar, algún día unha simulación dunha teoría como QCD, que sería extremadamente interesante. A maior vantaxe do noso enfoque, que está parcialmente motivado pola imaxe partónica emerxente de QCD a altas enerxías, en comparación co

traballo fundamental de Jordan, Lee e Preskill [10, 64, 65], reside no feito que o número de qubits só se escala logaritmicamente co volume da lattice (e linealmente co número de partículas). Así, para problemas de dispersión, onde normalmente o número de partículas é pequeno pero o espazo de fase é grande, é natural considerar este enfoque. Ademais, a base empregada coincide coa imaxe perturbativa do cálculo diagramático de Feynman, tan familiar para os físicos de altas enerxías. Así, a interpretación e implementación do noso enfoque parece máis directa e natural, especialmente se se compara con enfoques de TCC perturbativa. Ademáis, demostramos que o noso algoritmo reflicte directamente os eventos de dispersión no LHC ou RHIC, e que a acción de medir os qubits é análoga aos protocolos de medida experimentais. Ademais diso, demostramos que, en principio, unha computadora cuántica pode superar de feito á configuración experimental, xa que se ten un control total sobre o estado final do sistema.

Nun seguinte paso, planeamos realizar un estudo numérico enfocando no caso máis sinxelo de $d = 1$ dimensións espaciais. Usando paquetes numéricos de diagonalización exacta, estudaremos a calidade coa que se pode reproducir o espectro da teoría a λ finita para unha discretización de lattice dada e M similar ao estudo JLP [10]. A nosa estratexia tamén se pode calcular de xeito clásico para o caso de $M = 2$ en $d = 1$ dimensións con $N_s = 8$ (16) nodos de lattice, o que podería servir para comprobar a resistencia do algoritmo fronte a erros cuánticos. Nun último paso, podería implementarse o circuíto resultante nun hardware cuántico, aínda que incluso preparar correctamente o estado inicial do sistema sería un logro notable. Quizais máis interesante podería ser buscar problemas máis sinxelos onde unha estratexia para unha única partícula podería xa aplicarse en hardware cuántico. Un exemplo disto podería ser a extensión da nosa estratexia para simular cuánticamente o jet quenching, onde é natural ter en conta a imaxe dunha única partícula.

Finalmente, aínda que o algoritmo de simulación cuántica pódese aplicar para simular a dinámica completa da dispersión de alta enerxía e a correspondente teoría cuántica de campos, como se comentou anteriormente, a implementación destas estratexias en dispositivos cuánticos aínda está demasiado lonxe para levar a novos resultados significativos nun futuro próximo. Non obstante, os algoritmos cuánticos xa poden proporcionar información sobre QCD (e outras teorías) aplicándoos a problemas máis específicos, que son menos esixentes en termos de recursos. Volvendo á discusión sobre o chuveiro de partóns inducidos polo medio, os resultados da presente tese téñense centrado na evolución dun único partón no medio. Non obstante, está claro que tal enfoque non inclúe os efectos de interferencia entre múltiples partículas, xa que se trata de correccións puramente cuánticas que non están presentes na imaxe do partón único a calquera orde. Como consecuencia, as estratexias cuánticas aplicadas a estes procesos máis sinxelos xa introducen unha clara vantaxe física e permitirían calibrar os efectos moito máis alá do rango dos métodos clásicos.

No último tema tratado nesta tese, presentamos un algoritmo sinxelo para simular o broadening de momento dunha única partícula nun ordenador cuántico dixital, coa intención de estender este programa no futuro a un chuveiro de partóns completo. Este

esforzo está en liña co recente interese en aplicar computadores cuánticos para estudar a fenomenoloxía da física de alta enerxía e nuclear [62, 63, 235, 243–246]. **Se** nun futuro fosemos quen de implementar de forma eficiente un circuíto simulando de maneira completa un chuveiro inducido polo medio, entón agárdase que, desde o punto de vista físico, o algoritmo resultante supere os enfoques clásicos actuais [51, 52]. Non obstante, aínda é unha pregunta aberta e nin sequera está claro se se pode facer nun hardware a curto ou medio prazo, ou se se chegará a facer algunha vez. Ademais, sempre hai que ter en conta que, debido ao carácter especial do acto de medición na mecánica cuántica, aínda que exista un algoritmo cuántico seguro, non será capaz de superar aos seus homólogos clásicos en todas as tarefas. Pola contra, dependendo de cal é a cuestión de interese, unha estratexia cuántica pode ter sentido ou non.

USC
UNIVERSIDADE
DE SANTIAGO
DE COMPOSTELA

Bibliography

[1] P. Zyla, et al., Review of Particle Physics, PTEP 2020 (8) (2020) 083C01. doi:10.1093/ptep/ptaa104.

[2] J. Barata, Y. Mehtar-Tani, Improved opacity expansion at NNLO for medium induced gluon radiation, JHEP 10 (2020) 176. arXiv:2004.02323, doi:10.1007/JHEP10(2020)176.

[3] C. Andres, L. Apolinário, F. Dominguez, Medium-induced gluon radiation with full resummation of multiple scatterings for realistic parton-medium interactions, JHEP 07 (2020) 114. arXiv:2002.01517, doi:10.1007/JHEP07(2020)114.

[4] C. Andres, F. Dominguez, M. G. Martinez, From soft to hard radiation: the role of multiple scatterings in medium-induced gluon emissions (11 2020). arXiv:2011.06522.

[5] J. a. Barata, Y. Mehtar-Tani, A. Soto-Ontoso, K. Tywoniuk, Medium-induced radiative kernel with the Improved Opacity Expansion (6 2021). arXiv:2106.07402.

[6] J. Barata, Y. Mehtar-Tani, A. Soto-Ontoso, K. Tywoniuk, Revisiting transverse momentum broadening in dense QCD media (9 2020). arXiv:2009.13667.

[7] J. Barata, N. Mueller, A. Tarasov, R. Venugopalan, Single-particle digitization strategy for quantum computation of a ϕ^4 scalar field theory (11 2020). arXiv:2012.00020.

[8] V. Vedral, A. Barenco, A. Ekert, Quantum networks for elementary arithmetic operations, Physical Review A 54 (1) (1996) 147.

[9] T. G. Draper, Addition on a quantum computer, arXiv preprint quant-ph/0008033 (2000).

[10] N. Klco, M. J. Savage, Digitization of scalar fields for quantum computing, Phys. Rev. A 99 (5) (2019) 052335. arXiv:1808.10378, doi:10.1103/PhysRevA.99.052335.

[11] P. Kaye, Optimized quantum implementation of elliptic curve arithmetic over binary fields, Quantum Inf. Comput. 5 (2005) 474–491. arXiv:quant-ph/0407095.

[12] P. Kaye, Reversible addition circuit using one ancillary bit with application to quantum computing (2004). arXiv:quant-ph/0408173.

[13] J. Barata, C. A. Salgado, A quantum strategy to compute the jet quenching parameter $\hat{q}$ (4 2021). arXiv:2104.04661.

[14] F. Wilczek, What QCD tells us about nature - and why we should listen, Nucl. Phys. A 663 (2000) 3–20. arXiv:hep-ph/9907340, doi:10.1016/S0375-9474(99)00567-9.

[15] H. Fritzsch, History of QCD, Subnucl. Ser. 50 (2014) 23–27. doi:10.1142/9789814603904_0004.

[16] G. Zweig, An SU(3) model for strong interaction symmetry and its breaking. Version 1 (1 1964).

[17] M. Gell-Mann, The Eightfold Way: A Theory of strong interaction symmetry (3 1961). doi:10.2172/4008239.

[18] M. Gell-Mann, A Schematic Model of Baryons and Mesons, Phys. Lett. 8 (1964) 214–215. doi:10.1016/S0031-9163(64)92001-3.

[19] V. E. Barnes, et al., Observation of a Hyperon with Strangeness Minus Three, Phys. Rev. Lett. 12 (1964) 204–206. doi:10.1103/PhysRevLett.12.204.

[20] R. A. Arndt, W. J. Briscoe, I. I. Strakovsky, R. L. Workman, Extended partial-wave analysis of piN scattering data, Phys. Rev. C 74 (2006) 045205. arXiv:nucl-th/0605082, doi:10.1103/PhysRevC.74.045205.

[21] O. W. Greenberg, Spin and Unitary Spin Independence in a Paraquark Model of Baryons and Mesons, Phys. Rev. Lett. 13 (1964) 598–602. doi:10.1103/PhysRevLett.13.598.

[22] C. N. Yang, R. L. Mills, Conservation of isotopic spin and isotopic gauge invariance, Phys. Rev. 96 (1954) 191–195. doi:10.1103/PhysRev.96.191.
URL https://link.aps.org/doi/10.1103/PhysRev.96.191

[23] M. D. Schwartz, Quantum Field Theory and the Standard Model, Cambridge University Press, 2014.

[24] M. E. Peskin, D. V. Schroeder, An Introduction to quantum field theory, Addison-Wesley, Reading, USA, 1995.

[25] S. Weinberg, Nonabelian Gauge Theories of the Strong Interactions, Phys. Rev. Lett. 31 (1973) 494–497. doi:10.1103/PhysRevLett.31.494.

[26] H. Fritzsch, M. Gell-Mann, H. Leutwyler, Advantages of the Color Octet Gluon Picture, Phys. Lett. B 47 (1973) 365–368. doi:10.1016/0370-2693(73)90625-4.

[27] D. J. Gross, F. Wilczek, ASYMPTOTICALLY FREE GAUGE THEORIES. 2., Phys. Rev. D 9 (1974) 980–993. doi:10.1103/PhysRevD.9.980.

[28] L. D. Faddeev, V. N. Popov, Feynman Diagrams for the Yang-Mills Field, Phys. Lett. B 25 (1967) 29–30. doi:10.1016/0370-2693(67)90067-6.

[29] D. J. Gross, F. Wilczek, Asymptotically Free Gauge Theories - I, Phys. Rev. D 8 (1973) 3633–3652. doi:10.1103/PhysRevD.8.3633.

[30] H. D. Politzer, Reliable Perturbative Results for Strong Interactions?, Phys. Rev. Lett. 30 (1973) 1346–1349. doi:10.1103/PhysRevLett.30.1346.

[31] J. C. Collins, D. E. Soper, G. F. Sterman, Factorization of Hard Processes in QCD, Adv. Ser. Direct. High Energy Phys. 5 (1989) 1–91. arXiv:hep-ph/0409313, doi:10.1142/9789814503266_0001.

[32] R. K. Ellis, H. Georgi, M. Machacek, H. D. Politzer, G. G. Ross, Perturbation Theory and the Parton Model in QCD, Nucl. Phys. B 152 (1979) 285–329. doi:10.1016/0550-3213(79)90105-6.

[33] G. Altarelli, G. Parisi, Asymptotic Freedom in Parton Language, Nucl. Phys. B 126 (1977) 298–318. doi:10.1016/0550-3213(77)90384-4.

[34] Y. L. Dokshitzer, D. Diakonov, S. I. Troian, Hard Processes in Quantum Chromodynamics, Phys. Rept. 58 (1980) 269–395. doi:10.1016/0370-1573(80)90043-5.

[35] V. N. Gribov, L. N. Lipatov, e+ e- pair annihilation and deep inelastic e p scattering in perturbation theory, Sov. J. Nucl. Phys. 15 (1972) 675–684.

[36] J. D. Bjorken, Asymptotic Sum Rules at Infinite Momentum, Phys. Rev. 179 (1969) 1547–1553. doi:10.1103/PhysRev.179.1547.

[37] R. P. Feynman, Photon-hadron interactions, CRC Press, 2018.

[38] Y. V. Kovchegov, E. Levin, Quantum chromodynamics at high energy, Vol. 33, Cambridge University Press, 2012. doi:10.1017/CBO9781139022187.

[39] B. Ioffe, Space-time picture of photon and neutrino scattering and electroproduction cross-section asymptotics, Phys. Lett. B 30 (1969) 123–125. doi:10.1016/0370-2693(69)90415-8.

[40] V. N. Gribov, B. L. Ioffe, I. Y. Pomeranchuk, What is the range of interactions at high-energies, Yad. Fiz. 2 (1965) 768–776.

[41] T. D. Lee, G. C. Wick, Vacuum Stability and Vacuum Excitation in a Spin 0 Field Theory, Phys. Rev. D 9 (1974) 2291–2316. doi:10.1103/PhysRevD.9.2291.

[42] J. C. Collins, M. J. Perry, Superdense Matter: Neutrons Or Asymptotically Free Quarks?, Phys. Rev. Lett. 34 (1975) 1353. doi:10.1103/PhysRevLett.34.1353.

[43] L. Apolinário, J. G. Milhano, G. P. Salam, C. A. Salgado, Probing the time structure of the quark-gluon plasma with top quarks, Phys. Rev. Lett. 120 (23) (2018) 232301. arXiv:1711.03105, doi:10.1103/PhysRevLett.120.232301.

[44] P. Dorau, J.-B. Rose, D. Pablos, H. Elfner, Jet Quenching in the Hadron Gas: An Exploratory Study, Phys. Rev. C 101 (3) (2020) 035208. arXiv:1910.07027, doi:10.1103/PhysRevC.101.035208.

[45] G. P. Salam, Towards Jetography, Eur. Phys. J. C 67 (2010) 637–686. arXiv:0906.1833, doi:10.1140/epjc/s10052-010-1314-6.

[46] S. Marzani, G. Soyez, M. Spannowsky, Looking inside jets: an introduction to jet substructure and boosted-object phenomenology, Vol. 958, Springer, 2019. arXiv:1901.10342, doi:10.1007/978-3-030-15709-8.

[47] F. Gelis, T. Lappi, R. Venugopalan, High energy factorization in nucleus-nucleus collisions, Phys. Rev. D 78 (2008) 054019. arXiv:0804.2630, doi:10.1103/PhysRevD.78.054019.

[48] R. Sassot, M. Stratmann, P. Zurita, Fragmentations Functions in Nuclear Media, Phys. Rev. D 81 (2010) 054001. arXiv:0912.1311, doi:10.1103/PhysRevD.81.054001.

[49] J. D. Bjorken, Energy Loss of Energetic Partons in Quark - Gluon Plasma: Possible Extinction of High p(t) Jets in Hadron - Hadron Collisions (8 1982).

[50] K. Adcox, et al., Suppression of hadrons with large transverse momentum in central Au+Au collisions at $\sqrt{s_{NN}}$ = 130-GeV, Phys. Rev. Lett. 88 (2002) 022301. arXiv:nucl-ex/0109003, doi:10.1103/PhysRevLett.88.022301.

[51] P. Caucal, E. Iancu, A. H. Mueller, G. Soyez, Vacuum-like jet fragmentation in a dense QCD medium, Phys. Rev. Lett. 120 (2018) 232001. arXiv:1801.09703, doi:10.1103/PhysRevLett.120.232001.

[52] J. Casalderrey-Solana, D. C. Gulhan, J. G. Milhano, D. Pablos, K. Rajagopal, A Hybrid Strong/Weak Coupling Approach to Jet Quenching, JHEP 10 (2014) 019, [Erratum: JHEP 09, 175 (2015)]. arXiv:1405.3864, doi:10.1007/JHEP09(2015)175.

[53] B. Schenke, C. Gale, S. Jeon, MARTINI: An Event generator for relativistic heavy-ion collisions, Phys. Rev. C 80 (2009) 054913. arXiv:0909.2037, doi:10.1103/PhysRevC.80.054913.

[54] Y. He, T. Luo, X.-N. Wang, Y. Zhu, Linear Boltzmann Transport for Jet Propagation in the Quark-Gluon Plasma: Elastic Processes and Medium Recoil, Phys. Rev. C 91 (2015) 054908, [Erratum: Phys.Rev.C 97, 019902 (2018)]. arXiv:1503.03313, doi:10.1103/PhysRevC.91.054908.

[55] S. Cao, T. Luo, G.-Y. Qin, X.-N. Wang, Linearized Boltzmann transport model for jet propagation in the quark-gluon plasma: Heavy quark evolution, Phys. Rev. C 94 (1) (2016) 014909. arXiv:1605.06447, doi:10.1103/PhysRevC.94.014909.

[56] K. C. Zapp, F. Krauss, U. A. Wiedemann, A perturbative framework for jet quenching, JHEP 03 (2013) 080. arXiv:1212.1599, doi:10.1007/JHEP03(2013)080.

[57] K. Zapp, G. Ingelman, J. Rathsman, J. Stachel, U. A. Wiedemann, A Monte Carlo Model for 'Jet Quenching', Eur. Phys. J. C 60 (2009) 617–632. arXiv:0804.3568, doi:10.1140/epjc/s10052-009-0941-2.

[58] R. P. Feynman, Simulating physics with computers, Int. J. Theor. Phys. 21 (1982) 467–488. doi:10.1007/BF02650179.

[59] J. D. Whitfield, J. Biamonte, A. Aspuru-Guzik, Simulation of electronic structure hamiltonians using quantum computers, Molecular Physics 109 (5) (2011) 735–750.

[60] M. Schuld, I. Sinayskiy, F. Petruccione, An introduction to quantum machine learning, Contemporary Physics 56 (2) (2014) 172–185. doi:10.1080/00107514.2014.964942.
URL http://dx.doi.org/10.1080/00107514.2014.964942

[61] R. Orús, S. Mugel, E. Lizaso, Quantum computing for finance: Overview and prospects, Reviews in Physics 4 (2019) 100028. doi:10.1016/j.revip.2019.100028.
URL http://dx.doi.org/10.1016/j.revip.2019.100028

[62] I. C. Cloët, M. R. Dietrich, J. Arrington, A. Bazavov, M. Bishof, A. Freese, A. V. Gorshkov, A. Grassellino, K. Hafidi, Z. Jacob, et al., Opportunities for nuclear physics & quantum information science, arXiv preprint arXiv:1903.05453 (2019).

[63] K. Matchev, S. Mrenna, P. Shyamsundar, J. Smolinsky, Quantum computing for hep theory and phenomenology, Quantum (2020).

[64] S. P. Jordan, K. S. Lee, J. Preskill, Quantum computation of scattering in scalar quantum field theories, arXiv preprint arXiv:1112.4833 (2011).

[65] S. P. Jordan, K. S. Lee, J. Preskill, Quantum algorithms for quantum field theories, Science 336 (6085) (2012) 1130–1133.

[66] P. W. Shor, Polynomial-Time Algorithms for Prime Factorization and Discrete Logarithms on a Quantum Computer, arXiv e-prints (1995) quant–ph/9508027arXiv:quant-ph/9508027.

[67] R. Cleve, A. Ekert, C. Macchiavello, M. Mosca, Quantum algorithms revisited, Proceedings of the Royal Society of London Series A 454 (1969) (1998) 339. arXiv:quant-ph/9708016, doi:10.1098/rspa.1998.0164.

[68] L. K. Grover, A fast quantum mechanical algorithm for database search, arXiv e-prints (1996) quant–ph/9605043arXiv:quant-ph/9605043.

[69] G. Brassard, P. Hoyer, An Exact Quantum Polynomial-Time Algorithm for Simon's Problem, arXiv e-prints (1997) quant–ph/9704027arXiv:quant-ph/9704027.

[70] Y. Manin, Computable and uncomputable (in russian) (1980).

[71] S. Lloyd, Universal quantum simulators, Science 273 (5278) (1996) 1073–1078.
URL http://www.jstor.org/stable/2899535

[72] A. Gilyén, Y. Su, G. Hao Low, N. Wiebe, Quantum singular value transformation and beyond: exponential improvements for quantum matrix arithmetics, arXiv e-prints (2018) arXiv:1806.01838arXiv:1806.01838.

[73] D. P. DiVincenzo, The physical implementation of quantum computation, Fortschritte der Physik 48 (9-11) (2000) 771–783. doi:10.1002/1521-3978(200009)48:9/11<771::aid-prop771>3.0.co;2-e.
URL http://dx.doi.org/10.1002/1521-3978(200009)48:9/11<771::AID-PROP771>3.0.CO;2-E

[74] M. A. Nielsen, I. L. Chuang, Quantum Computation and Quantum Information, Cambridge University Press, 2010.

[75] C. J. Hood, T. W. Lynn, A. C. Doherty, A. S. Parkins, H. J. Kimble, The atom-cavity microscope: Single atoms bound in orbit by single photons, Science 287 (5457) (2000) 1447–1453. arXiv:https://science.sciencemag.org/content/287/5457/1447.full.pdf, doi:10.1126/science.287.5457.1447.
URL https://science.sciencemag.org/content/287/5457/1447

[76] M. Devoret, R. Schoelkopf, Superconducting circuits for quantum information: An outlook, Science (New York, N.Y.) 339 (2013) 1169–74. doi:10.1126/science.1231930.

[77] A. Blais, R.-S. Huang, A. Wallraff, S. M. Girvin, R. J. Schoelkopf, Cavity quantum electrodynamics for superconducting electrical circuits: An architecture for quantum computation, pra 69 (6) (2004) 062320. arXiv:cond-mat/0402216, doi:10.1103/PhysRevA.69.062320.

[78] E. T. Jaynes, F. W. Cummings, Comparison of quantum and semiclassical radiation theories with application to the beam maser, Proceedings of the IEEE 51 (1) (1963) 89–109. doi:10.1109/PROC.1963.1664.

[79] F. W. Cummings, Stimulated emission of radiation in a single mode, Phys. Rev. 140 (1965) A1051–A1056. doi:10.1103/PhysRev.140.A1051.
URL https://link.aps.org/doi/10.1103/PhysRev.140.A1051

[80] M. H. Michael, M. Silveri, R. T. Brierley, V. V. Albert, J. Salmilehto, L. Jiang, S. M. Girvin, New Class of Quantum Error-Correcting Codes for a Bosonic Mode, Physical Review X 6 (3) (2016) 031006. arXiv:1602.00008, doi:10.1103/PhysRevX.6.031006.

[81] J.-P. Blaizot, Y. Mehtar-Tani, Jet Structure in Heavy Ion Collisions, Int. J. Mod. Phys. E 24 (11) (2015) 1530012. arXiv:1503.05958, doi:10.1142/S021830131530012X.

[82] J. Casalderrey-Solana, C. A. Salgado, Introductory lectures on jet quenching in heavy ion collisions, Acta Phys. Polon. B 38 (2007) 3731–3794. arXiv:0712.3443.

[83] Y. Mehtar-Tani, J. G. Milhano, K. Tywoniuk, Jet physics in heavy-ion collisions, Int. J. Mod. Phys. A 28 (2013) 1340013. arXiv:1302.2579, doi:10.1142/S0217751X13400137.

[84] A. Kurkela, U. A. Wiedemann, Picturing perturbative parton cascades in QCD matter, Phys. Lett. B 740 (2015) 172–178. arXiv:1407.0293, doi:10.1016/j.physletb.2014.11.054.

[85] J.-P. Blaizot, F. Dominguez, E. Iancu, Y. Mehtar-Tani, Probabilistic picture for medium-induced jet evolution, JHEP 06 (2014) 075. arXiv:1311.5823, doi:10.1007/JHEP06(2014)075.

[86] R. Baier, A. H. Mueller, D. Schiff, D. T. Son, 'Bottom up' thermalization in heavy ion collisions, Phys. Lett. B 502 (2001) 51–58. arXiv:hep-ph/0009237, doi:10.1016/S0370-2693(01)00191-5.

[87] S. Jeon, G. D. Moore, Energy loss of leading partons in a thermal QCD medium, Phys. Rev. C 71 (2005) 034901. arXiv:hep-ph/0309332, doi:10.1103/PhysRevC.71.034901.

[88] J.-P. Blaizot, E. Iancu, Y. Mehtar-Tani, Medium-induced QCD cascade: democratic branching and wave turbulence, Phys. Rev. Lett. 111 (2013) 052001. arXiv:1301.6102, doi:10.1103/PhysRevLett.111.052001.

[89] E. Braaten, M. H. Thoma, Energy loss of a heavy quark in the quark - gluon plasma, Phys. Rev. D 44 (9) (1991) 2625. doi:10.1103/PhysRevD.44.R2625.

[90] N. Armesto, et al., Comparison of Jet Quenching Formalisms for a Quark-Gluon Plasma 'Brick', Phys. Rev. C 86 (2012) 064904. arXiv:1106.1106, doi:10.1103/PhysRevC.86.064904.

[91] R. Baier, Y. L. Dokshitzer, A. H. Mueller, S. Peigne, D. Schiff, Radiative energy loss and p(T) broadening of high-energy partons in nuclei, Nucl. Phys. B484 (1997) 265–282. arXiv:hep-ph/9608322, doi:10.1016/S0550-3213(96)00581-0.

[92] R. Baier, Y. L. Dokshitzer, A. H. Mueller, S. Peigne, D. Schiff, Radiative energy loss of high-energy quarks and gluons in a finite volume quark - gluon plasma, Nucl. Phys. B483 (1997) 291–320. arXiv:hep-ph/9607355, doi:10.1016/S0550-3213(96)00553-6.

[93] B. G. Zakharov, Fully quantum treatment of the Landau-Pomeranchuk-Migdal effect in QED and QCD, JETP Lett. 63 (1996) 952–957. arXiv:hep-ph/9607440, doi:10.1134/1.567126.

[94] B. G. Zakharov, Radiative energy loss of high-energy quarks in finite size nuclear matter and quark - gluon plasma, JETP Lett. 65 (1997) 615–620. arXiv:hep-ph/9704255, doi:10.1134/1.567389.

[95] R. Baier, Y. L. Dokshitzer, S. Peigne, D. Schiff, Induced gluon radiation in a QCD medium, Phys. Lett. B 345 (1995) 277–286. arXiv:hep-ph/9411409, doi:10.1016/0370-2693(94)01617-L.

[96] R. Baier, Y. L. Dokshitzer, A. H. Mueller, S. Peigne, D. Schiff, The Landau-Pomeranchuk-Migdal effect in QED, Nucl. Phys. B 478 (1996) 577–597. arXiv:hep-ph/9604327, doi:10.1016/0550-3213(96)00426-9.

[97] B. G. Zakharov, Light cone path integral approach to the Landau-Pomeranchuk-Migdal effect, Phys. Atom. Nucl. 61 (1998) 838–854. arXiv:hep-ph/9807540.

[98] R. Baier, Y. L. Dokshitzer, A. H. Mueller, D. Schiff, Medium induced radiative energy loss: Equivalence between the BDMPS and Zakharov formalisms, Nucl. Phys. B 531 (1998) 403–425. arXiv:hep-ph/9804212, doi:10.1016/S0550-3213(98)00546-X.

[99] N. Armesto, C. A. Salgado, U. A. Wiedemann, Medium induced gluon radiation off massive quarks fills the dead cone, Phys. Rev. D 69 (2004) 114003. arXiv:hep-ph/0312106, doi:10.1103/PhysRevD.69.114003.

[100] C. A. Salgado, U. A. Wiedemann, Calculating quenching weights, Phys. Rev. D 68 (2003) 014008. arXiv:hep-ph/0302184, doi:10.1103/PhysRevD.68.014008.

[101] M. Gyulassy, P. Levai, I. Vitev, Reaction operator approach to nonAbelian energy loss, Nucl. Phys. B594 (2001) 371–419. arXiv:nucl-th/0006010, doi:10.1016/S0550-3213(00)00652-0.

[102] U. A. Wiedemann, Gluon radiation off hard quarks in a nuclear environment: Opacity expansion, Nucl. Phys. B588 (2000) 303–344. arXiv:hep-ph/0005129, doi:10.1016/S0550-3213(00)00457-0.

[103] L. Apolinário, N. Armesto, J. G. Milhano, C. A. Salgado, Medium-induced gluon radiation and colour decoherence beyond the soft approximation, JHEP 02 (2015) 119. arXiv:1407.0599, doi:10.1007/JHEP02(2015)119.

[104] L. Apolinario, N. Armesto, C. A. Salgado, Medium-induced emissions of hard gluons, Phys. Lett. B 718 (2012) 160–168. arXiv:1204.2929, doi:10.1016/j.physletb.2012.10.040.

[105] J.-P. Blaizot, F. Dominguez, E. Iancu, Y. Mehtar-Tani, Medium-induced gluon branching, JHEP 01 (2013) 143. arXiv:1209.4585, doi:10.1007/JHEP01(2013)143.

[106] F. Domínguez, J. G. Milhano, C. A. Salgado, K. Tywoniuk, V. Vila, Mapping collinear in-medium parton splittings, Eur. Phys. J. C 80 (1) (2020) 11. arXiv:1907.03653, doi:10.1140/epjc/s10052-019-7563-0.

[107] Y. Mehtar-Tani, Relating the description of gluon production in pA collisions and parton energy loss in AA collisions, Phys. Rev. C 75 (2007) 034908. arXiv:hep-ph/0606236, doi:10.1103/PhysRevC.75.034908.

[108] F. Gelis, Y. Mehtar-Tani, Gluon propagation inside a high-energy nucleus, Phys. Rev. D 73 (2006) 034019. arXiv:hep-ph/0512079, doi:10.1103/PhysRevD.73.034019.

[109] S. J. Brodsky, G. P. Lepage, Exclusive Processes in Quantum Chromodynamics, Adv. Ser. Direct. High Energy Phys. 5 (1989) 93–240. doi:10.1142/9789814503266_0002.

[110] S. J. Brodsky, H.-C. Pauli, S. S. Pinsky, Quantum chromodynamics and other field theories on the light cone, Phys. Rept. 301 (1998) 299–486. arXiv:hep-ph/9705477, doi:10.1016/S0370-1573(97)00089-6.

[111] Y. L. Dokshitzer, V. A. Khoze, A. H. Mueller, S. I. Troian, Basics of perturbative QCD, 1991.

[112] X. G. Feal, High energy scattering and emission in QED&QCD media, Ph.D. thesis, Santiago de Compostela U., IGFAE (2018). arXiv:1812.06903.

[113] X.-N. Wang, M. Gyulassy, Gluon shadowing and jet quenching in A + A collisions at s**(1/2) = 200-GeV, Phys. Rev. Lett. 68 (1992) 1480–1483. doi:10.1103/PhysRevLett.68.1480.

[114] F. Gelis, E. Iancu, J. Jalilian-Marian, R. Venugopalan, The Color Glass Condensate, Ann. Rev. Nucl. Part. Sci. 60 (2010) 463–489. arXiv:1002.0333, doi:10.1146/annurev.nucl.010909.083629.

[115] J. P. Blaizot, F. Gelis, R. Venugopalan, High-energy pA collisions in the color glass condensate approach. 1. Gluon production and the Cronin effect, Nucl. Phys. A 743 (2004) 13–56. arXiv:hep-ph/0402256, doi:10.1016/j.nuclphysa.2004.07.005.

[116] J.-P. Blaizot, Y. Mehtar-Tani, The Classical field created in early stages of high energy nucleus-nucleus collisions, Nucl. Phys. A 818 (2009) 97–119. arXiv:0806.1422, doi:10.1016/j.nuclphysa.2008.11.010.

[117] L. D. McLerran, R. Venugopalan, Computing quark and gluon distribution functions for very large nuclei, Phys. Rev. D 49 (1994) 2233–2241. arXiv:hep-ph/9309289, doi:10.1103/PhysRevD.49.2233.

[118] L. D. McLerran, R. Venugopalan, Gluon distribution functions for very large nuclei at small transverse momentum, Phys. Rev. D 49 (1994) 3352–3355. arXiv:hep-ph/9311205, doi:10.1103/PhysRevD.49.3352.

[119] L. D. McLerran, R. Venugopalan, Green's functions in the color field of a large nucleus, Phys. Rev. D 50 (1994) 2225–2233. arXiv:hep-ph/9402335, doi:10.1103/PhysRevD.50.2225.

[120] N. Van Kampen, Stochastic Processes in Physics and Chemistry, North-Holland Personal Library, Elsevier Science, 1992.
URL https://books.google.es/books?id=3e7XbMoJzmoC

[121] Y. V. Kovchegov, NonAbelian Weizsacker-Williams field and a two-dimensional effective color charge density for a very large nucleus, Phys. Rev. D 54 (1996) 5463–5469. arXiv:hep-ph/9605446, doi:10.1103/PhysRevD.54.5463.

[122] Y. V. Kovchegov, Quantum structure of the nonAbelian Weizsacker-Williams field for a very large nucleus, Phys. Rev. D 55 (1997) 5445–5455. arXiv:hep-ph/9701229, doi:10.1103/PhysRevD.55.5445.

[123] M. Gyulassy, P. Levai, I. Vitev, Reaction operator approach to multiple elastic scatterings, Phys. Rev. D 66 (2002) 014005. arXiv:nucl-th/0201078, doi:10.1103/PhysRevD.66.014005.

[124] I. Kolbé, M. Lushozi, L. D. McLerran, G. Yu, Distribution of Nuclear Matter and Radiation in the Fragmentation Region (9 2020). arXiv:2009.05680.

[125] P. Aurenche, F. Gelis, H. Zaraket, A Simple sum rule for the thermal gluon spectral function and applications, JHEP 05 (2002) 043. arXiv:hep-ph/0204146, doi:10.1088/1126-6708/2002/05/043.

[126] E. Iancu, K. Itakura, D. Triantafyllopoulos, Cronin effect and high p-perpendicular suppression in the nuclear gluon distribution at small x, Nucl. Phys. A 742 (2004) 182–252. arXiv:hep-ph/0403103, doi:10.1016/j.nuclphysa.2004.06.033.

[127] M. Djordjevic, U. Heinz, Radiative heavy quark energy loss in a dynamical QCD medium, Phys. Rev. C 77 (2008) 024905. arXiv:0705.3439, doi:10.1103/PhysRevC.77.024905.

[128] T. Altinoluk, N. Armesto, G. Beuf, A. Moscoso, Next-to-next-to-eikonal corrections in the CGC, JHEP 01 (2016) 114. arXiv:1505.01400, doi:10.1007/JHEP01(2016)114.

[129] T. Altinoluk, N. Armesto, G. Beuf, M. Martínez, C. A. Salgado, Next-to-eikonal corrections in the CGC: gluon production and spin asymmetries in pA collisions, JHEP 07 (2014) 068. arXiv:1404.2219, doi:10.1007/JHEP07(2014)068.

[130] T. Altinoluk, G. Beuf, A. Czajka, A. Tymowska, Quarks at next-to-eikonal accuracy in the CGC I: Forward quark-nucleus scattering (12 2020). arXiv:2012.03886.

[131] H. Kleinert, Path Integrals in Quantum Mechanics, Statistics, Polymer Physics, and Financial Markets (2004).

[132] M. D. Sievert, I. Vitev, Quark branching in QCD matter to any order in opacity beyond the soft gluon emission limit, Phys. Rev. D 98 (9) (2018) 094010. arXiv:1807.03799, doi:10.1103/PhysRevD.98.094010.

[133] Y. Mehtar-Tani, Relating the description of gluon production in pA collisions and parton energy loss in AA collisions, Phys. Rev. C 75 (2007) 034908. arXiv:hep-ph/0606236, doi:10.1103/PhysRevC.75.034908.

[134] Y. Mehtar-Tani, K. Tywoniuk, Jet coherence in QCD media: the antenna radiation spectrum, JHEP 01 (2013) 031. arXiv:1105.1346, doi:10.1007/JHEP01(2013)031.

[135] A. Kovner, U. A. Wiedemann, Gluon radiation and parton energy loss (2003) 192–248arXiv:hep-ph/0304151, doi:10.1142/9789812795533_0004.

[136] P. B. Arnold, G. D. Moore, L. G. Yaffe, Photon and gluon emission in relativistic plasmas, JHEP 06 (2002) 030. arXiv:hep-ph/0204343, doi:10.1088/1126-6708/2002/06/030.

[137] S. Caron-Huot, C. Gale, Finite-size effects on the radiative energy loss of a fast parton in hot and dense strongly interacting matter, Phys. Rev. C82 (2010) 064902. arXiv:1006.2379, doi:10.1103/PhysRevC.82.064902.

[138] X. Feal, R. Vazquez, Intensity of gluon bremsstrahlung in a finite plasma, Phys. Rev. D98 (7) (2018) 074029. arXiv:1811.01591, doi:10.1103/PhysRevD.98.074029.

[139] W. Ke, Y. Xu, S. A. Bass, A modified-Boltzmann approach for modeling the hot QCD medium-induce splitting vertices in the deep LPM region, Phys. Rev. C100 (6) (2019) 064911. arXiv:1810.08177, doi:10.1103/PhysRevC.100.064911.

[140] P. B. Arnold, Simple Formula for High-Energy Gluon Bremsstrahlung in a Finite, Expanding Medium, Phys. Rev. D 79 (2009) 065025. arXiv:0808.2767, doi:10.1103/PhysRevD.79.065025.

[141] Y. Mehtar-Tani, Gluon bremsstrahlung in finite media beyond multiple soft scattering approximation, JHEP 07 (2019) 057. arXiv:1903.00506, doi:10.1007/JHEP07(2019)057.

[142] L. D. Landau, I. Pomeranchuk, Electron cascade process at very high-energies, Dokl. Akad. Nauk Ser. Fiz. 92 (1953) 735–738.

[143] A. B. Migdal, Bremsstrahlung and pair production in condensed media at high-energies, Phys. Rev. 103 (1956) 1811–1820. doi:10.1103/PhysRev.103.1811.

[144] P. L. Anthony, et al., An Accurate measurement of the Landau-Pomeranchuk-Migdal effect, Phys. Rev. Lett. 75 (1995) 1949–1952. doi:10.1103/PhysRevLett.75.1949.

[145] P. B. Arnold, C. Dogan, QCD Splitting/Joining Functions at Finite Temperature in the Deep LPM Regime, Phys. Rev. D 78 (2008) 065008. arXiv:0804.3359, doi:10.1103/PhysRevD.78.065008.

[146] H. Bethe, W. Heitler, On the Stopping of fast particles and on the creation of positive electrons, Proc. Roy. Soc. Lond. A 146 (1934) 83–112. doi:10.1098/rspa.1934.0140.

[147] S. Wicks, Up to and beyond ninth order in opacity: Radiative energy loss with GLV (4 2008). arXiv:0804.4704.

[148] Y. Mehtar-Tani, K. Tywoniuk, Improved opacity expansion for medium-induced parton splitting, JHEP 06 (2020) 187. arXiv:1910.02032, doi:10.1007/JHEP06(2020)187.

[149] G. Molière, Theorie der Streuung schneller geladener Teilchen II. Mehrfach- und Vielfachstreuung, Zeitschrift Naturforschung Teil A 3 (2) (1948) 78–97. doi:10.1515/zna-1948-0203.

[150] H. Bethe, Moliere's theory of multiple scattering, Phys. Rev. 89 (1953) 1256–1266. doi:10.1103/PhysRev.89.1256.

[151] Y. Mehtar-Tani, D. Pablos, K. Tywoniuk, Cone-size dependent jet spectrum in heavy-ion collisions, in: 10th International Conference on Hard and Electromagnetic Probes of High-Energy Nuclear Collisions: Hard Probes 2020 , 2020. arXiv:2009.14054.

[152] Y. Mehtar-Tani, D. Pablos, K. Tywoniuk, Cone size dependence of jet suppression in heavy-ion collisions (1 2021). arXiv:2101.01742.

[153] X. Feal, C. A. Salgado, R. A. Vazquez, Jet quenching tests of the QCD Equation of State (11 2019). arXiv:1911.01309.

[154] I. Kolbé, K. Roy, F. Salazar, B. Schenke, R. Venugopalan, Inclusive prompt photon-jet correlations as a probe of gluon saturation in electron-nucleus scattering at small x, JHEP 21 (2020) 052. arXiv:2008.04372, doi:10.1007/JHEP01(2021)052.

[155] X. Liu, F. Ringer, W. Vogelsang, F. Yuan, Lepton-jet Correlations in Deep Inelastic Scattering at the Electron-Ion Collider, Phys. Rev. Lett. 122 (19) (2019) 192003. arXiv:1812.08077, doi:10.1103/PhysRevLett.122.192003.

[156] A. Chi-Chih Yao, Quantum circuit complexity, in: Proceedings of 1993 IEEE 34th Annual Foundations of Computer Science, 1993, pp. 352–361. doi:10.1109/SFCS.1993.366852.

[157] I. M. Georgescu, S. Ashhab, F. Nori, Quantum Simulation, Rev. Mod. Phys. 86 (2014) 153. arXiv:1308.6253, doi:10.1103/RevModPhys.86.153.

[158] J. J. Sakurai, J. Napolitano, Modern Quantum Mechanics, Quantum physics, quantum information and quantum computation, Cambridge University Press, 2020. doi:10.1017/9781108587280.

[159] M. M. Mano, C. Kime, Logic and Computer Design Fundamentals, 4th Edition, Prentice Hall Press, USA, 2007.

[160] B. M. Terhal, Quantum error correction for quantum memories, Reviews of Modern Physics 87 (2) (2015) 307–346. doi:10.1103/revmodphys.87.307.
URL http://dx.doi.org/10.1103/RevModPhys.87.307

[161] C. M. Dawson, M. A. Nielsen, The solovay-kitaev algorithm, Quantum Info. Comput. 6 (1) (2006) 81–95.

[162] H. F. Trotter, On the product of semi-groups of operators, Proc. Am. Math. Soc. 10 (1959) 545.

[163] M. Suzuki, Generalized Trotter's Formula and Systematic Approximants of Exponential Operators and Inner Derivations with Applications to Many Body Problems, Commun. Math. Phys. 51 (1976) 183–190. doi:10.1007/BF01609348.

[164] M. Suzuki, Decomposition formulas of exponential operators and Lie exponentials with some applications to quantum mechanics and statistical physics, Journal of Mathematical Physics 26 (4) (1985) 601–612. doi:10.1063/1.526596.

[165] A. M. Childs, Y. Su, M. C. Tran, N. Wiebe, S. Zhu, Theory of trotter error with commutator scaling, Physical Review X 11 (1) (Feb 2021). doi:10.1103/physrevx.11.011020.
URL http://dx.doi.org/10.1103/PhysRevX.11.011020

[166] J. Preskill, Quantum computing in the nisq era and beyond, Quantum 2 (2018) 79.

[167] G. Hao Low, I. L. Chuang, Hamiltonian Simulation by Qubitization, arXiv e-prints (2016) arXiv:1610.06546arXiv:1610.06546.

[168] A. M. Childs, N. Wiebe, Hamiltonian Simulation Using Linear Combinations of Unitary Operations, arXiv e-prints (2012) arXiv:1202.5822arXiv:1202.5822.

[169] B. A. Lippmann, J. Schwinger, Variational principles for scattering processes. i, Physical Review 79 (3) (1950) 469.

[170] R. G. Newton, Scattering theory of waves and particles, Springer Science & Business Media, 2013.

[171] H.-D. Meyer, J. Horáek, L. Cederbaum, Schwinger and anomaly-free kohn variational principles and a generalized lanczos algorithm for nonsymmetric operators, Physical Review A 43 (7) (1991) 3587.

[172] E. P. Wigner, L. Eisenbud, Higher angular momenta and long range interaction in resonance reactions, Physical Review 72 (1) (1947) 29.

[173] K. Yeter-Aydeniz, G. Siopsis, R. C. Pooser, Scattering in the Ising Model Using Quantum Lanczos Algorithm (8 2020). arXiv:2008.08763.

[174] N. Mueller, A. Tarasov, R. Venugopalan, Deeply inelastic scattering structure functions on a hybrid quantum computer, Phys. Rev. D 102 (1) (2020) 016007. arXiv:1908.07051, doi:10.1103/PhysRevD.102.016007.

[175] L. Grover, T. Rudolph, Creating superpositions that correspond to efficiently integrable probability distributions, arXiv preprint quant-ph/0208112 (2002).

[176] P. Kaye, M. Mosca, Quantum networks for generating arbitrary quantum states, arXiv preprint quant-ph/0407102 (2004).

[177] A. Kitaev, W. A. Webb, Wavefunction preparation and resampling using a quantum computer, arXiv e-prints (2008) arXiv:0801.0342arXiv:0801.0342.

[178] C. Zalka, Efficient simulation of quantum systems by quantum computers, Proc. Roy. Soc. Lond. A 454 (1998) 313–322. arXiv:quant-ph/9603026, doi:10.1098/rspa.1998.0162.

[179] K. Yeter-Aydeniz, G. Siopsis, Quantum computation of scattering amplitudes in scalar quantum electrodynamics, Physical Review D 97 (3) (2018) 036004.

[180] M. M. Nieto, D. R. Truax, Holstein-primakoff/bogoliubov transformations and the multiboson system, Fortschritte der Physik/Progress of Physics 45 (2) (1997) 145–156.

[181] C. Gerry, P. Knight, Quantum optics (2000).

[182] K. Marshall, R. Pooser, G. Siopsis, C. Weedbrook, Quantum simulation of quantum field theory using continuous variables, Physical Review A 92 (6) (2015) 063825.

[183] T. A. Brun, Quantum error correction (2019). arXiv:1910.03672.

[184] J. R. Stryker, Oracles for gauss's law on digital quantum computers, Physical Review A 99 (4) (2019) 042301.

[185] M. C. Tran, Y. Su, D. Carney, J. M. Taylor, Faster digital quantum simulation by symmetry protection, arXiv preprint arXiv:2006.16248 (2020).

[186] H. Lamm, S. Lawrence, Y. Yamauchi, Suppressing coherent gauge drift in quantum simulations, arXiv preprint arXiv:2005.12688 (2020).

[187] J. C. Halimeh, H. Lang, J. Mildenberger, Z. Jiang, P. Hauke, Gauge-symmetry protection using single-body terms, arXiv preprint arXiv:2007.00668 (2020).

[188] M. C. Tran, S.-K. Chu, Y. Su, A. Childs, A. V. Gorshkov, Destructive error interference in lattice simulation with product formula (2020).

[189] S. A. Cuccaro, T. G. Draper, S. A. Kutin, D. P. Moulton, A new quantum ripple-carry addition circuit, arXiv preprint quant-ph/0410184 (2004).

[190] D. S. Oliveira, R. V. Ramos, Quantum bit string comparator: circuits and applications, Quantum Comput. Comput 7 (1) (2007) 17–26.

[191] H. Xia, H. Li, H. Zhang, Y. Liang, J. Xin, An efficient design of reversible multi-bit quantum comparator via only a single ancillary bit, International Journal of Theoretical Physics 57 (12) (2018) 3727–3744.

[192] G. Brassard, P. Hoyer, M. Mosca, A. Tapp, Quantum amplitude amplification and estimation, Contemporary Mathematics 305 (2002) 53–74.

[193] G. G. Guerreschi, Repeat-until-success circuits with fixed-point oblivious amplitude amplification, Physical Review A 99 (2) (Feb 2019). doi:10.1103/physreva.99.022306.
URL http://dx.doi.org/10.1103/PhysRevA.99.022306

[194] D. W. Berry, A. M. Childs, R. Cleve, R. Kothari, R. D. Somma, Exponential improvement in precision for simulating sparse hamiltonians, Proceedings of the 46th Annual ACM Symposium on Theory of Computing - STOC '14 (2014). doi:10.1145/2591796.2591854.
URL http://dx.doi.org/10.1145/2591796.2591854

[195] A. Paetznick, K. M. Svore, Repeat-until-success: Non-deterministic decomposition of single-qubit unitaries (2014). arXiv:1311.1074.

[196] A. H. Mueller, On the multiplicity of hadrons in qcd jets, Physics Letters B 104 (2) (1981) 161–164.

[197] Y. Dokshitzer, Basics of perturbative QCD, Atlantica Séguier Frontières, 1991.

[198] B. Webber, Fragmentation and hadronization, eConf C990809 (2000) 577–606. arXiv:hep-ph/9912292, doi:10.1142/S0217751X00005334.

[199] B. Andersson, The lund model, Vol. 7, Cambridge University Press, 2005.

[200] O. A. McBryan, J. Rosen, Existence of the Critical Point in phi**4 Field Theory, Commun. Math. Phys. 51 (1976) 97–105. doi:10.1007/BF01609341.

[201] J. Glimm, A. M. Jaffe, The phi**4 in Two Dimensions Quantum Field Model in the Single Phase Region: Differentiability of the Mass and Bounds on Critical Exponents, Phys. Rev. D 10 (1974) 536. doi:10.1103/PhysRevD.10.536.

[202] F. Guerra, L. Rosen, B. Simon, Correlation Inequalities and the Mass Gap in p (phi) in Two-Dimensions. 1. Mass Gap for a Class of Strongly Coupled Theories with Nonzero External Field, Commun. Math. Phys. 41 (1975) 19–32. doi:10.1007/BF01608544.

[203] R. Cleve, A. Ekert, C. Macchiavello, M. Mosca, Quantum algorithms revisited, Proceedings of the Royal Society of London. Series A: Mathematical, Physical and Engineering Sciences 454 (1969) (1998) 339–354.

[204] D. S. Abrams, S. Lloyd, Quantum algorithm providing exponential speed increase for finding eigenvalues and eigenvectors, Physical Review Letters 83 (24) (1999) 5162.

[205] E. Knill, G. Ortiz, R. D. Somma, Optimal quantum measurements of expectation values of observables, Physical Review A 75 (1) (2007) 012328.

[206] A. Roggero, A. Baroni, Short-depth circuits for efficient expectation-value estimation, Physical Review A 101 (2) (2020) 022328.

[207] F. Wegner, Flow-equations for hamiltonians, Annalen der physik 506 (2) (1994) 77–91.

[208] R. J. Perry, K. G. Wilson, Perturbative renormalizability with an infinite number of relevant and marginal operators, Nucl. Phys. B 403 (1993) 587–604. doi:10.1016/0550-3213(93)90363-T.

[209] S. D. Glazek, K. G. Wilson, Renormalization of hamiltonians, Physical Review D 48 (12) (1993) 5863.

[210] R. J. Perry, A renormalization group approach to hamiltonian light-front field theory, Annals of Physics 232 (1) (1994) 116–222.

[211] S. Bravyi, D. P. DiVincenzo, D. Loss, Schrieffer–wolff transformation for quantum many-body systems, Annals of physics 326 (10) (2011) 2793–2826.

[212] J. Otterbach, R. Manenti, N. Alidoust, A. Bestwick, M. Block, B. Bloom, S. Caldwell, N. Didier, E. S. Fried, S. Hong, et al., Unsupervised machine learning on a hybrid quantum computer, arXiv preprint arXiv:1712.05771 (2017).

[213] A. Peruzzo, J. McClean, P. Shadbolt, M.-H. Yung, X.-Q. Zhou, P. J. Love, A. Aspuru-Guzik, J. L. O'brien, A variational eigenvalue solver on a photonic quantum processor, Nature communications 5 (2014) 4213.

[214] A. Y. Kitaev, Quantum measurements and the abelian stabilizer problem, arXiv preprint quant-ph/9511026 (1995).

[215] E. Farhi, J. Goldstone, S. Gutmann, M. Sipser, Quantum computation by adiabatic evolution, arXiv preprint quant-ph/0001106 (2000).

[216] E. Farhi, J. Goldstone, S. Gutmann, A quantum approximate optimization algorithm, arXiv preprint arXiv:1411.4028 (2014).

[217] M. Motta, C. Sun, A. T. Tan, M. J. O'Rourke, E. Ye, A. J. Minnich, F. G. Brandão, G. K.-L. Chan, Determining eigenstates and thermal states on a quantum computer using quantum imaginary time evolution, Nature Physics 16 (2) (2020) 205–210.

[218] H. M. H. Babu, Quantum Computing, 2053-2563, IOP Publishing, 2020. doi:10.1088/978-0-7503-2747-3.
URL http://dx.doi.org/10.1088/978-0-7503-2747-3

[219] Y. Cao, A. Papageorgiou, I. Petras, J. Traub, S. Kais, Quantum algorithm and circuit design solving the poisson equation, New Journal of Physics 15 (1) (2013) 013021. doi:10.1088/1367-2630/15/1/013021.
URL http://dx.doi.org/10.1088/1367-2630/15/1/013021

[220] E. Muñoz-Coreas, H. Thapliyal, T-count and qubit optimized quantum circuit design of the non-restoring square root algorithm (2018). arXiv:1712.08254.

[221] M. K. Bhaskar, S. Hadfield, A. Papageorgiou, I. Petras, Quantum algorithms and circuits for scientific computing (2015). arXiv:1511.08253.

[222] T. Häner, M. Roetteler, K. Svore, Optimizing quantum circuits for arithmetic, ArXiv abs/1805.12445 (2018).

[223] Q. Turchette, C. Hood, W. Lange, H. Mabuchi, H. Kimble, Measurement of conditional phase shifts for quantum logic, Phys. Rev. Lett. 75 (1995) 4710–4713. arXiv:quant-ph/9511008, doi:10.1103/PhysRevLett.75.4710.

[224] A. F. Shaw, P. Lougovski, J. R. Stryker, N. Wiebe, Quantum algorithms for simulating the lattice schwinger model, arXiv preprint arXiv:2002.11146 (2020).

[225] D. Poulin, A. Qarry, R. Somma, F. Verstraete, Quantum simulation of time-dependent hamiltonians and the convenient illusion of hilbert space, Physical Review Letters 106 (17) (Apr 2011). doi:10.1103/physrevlett.106.170501.
URL http://dx.doi.org/10.1103/PhysRevLett.106.170501

[226] D. W. Berry, A. M. Childs, R. Cleve, R. Kothari, R. D. Somma, Simulating hamiltonian dynamics with a truncated taylor series, Physical Review Letters 114 (9) (Mar 2015). doi:10.1103/physrevlett.114.090502.
URL http://dx.doi.org/10.1103/PhysRevLett.114.090502

[227] D. W. Berry, A. M. Childs, Y. Su, X. Wang, N. Wiebe, Time-dependent hamiltonian simulation with l1-norm scaling, Quantum 4 (2020) 254. doi:10.22331/q-2020-04-20-254.
URL http://dx.doi.org/10.22331/q-2020-04-20-254

[228] N. Wiebe, D. Berry, P. Høyer, B. C. Sanders, Higher order decompositions of ordered operator exponentials, Journal of Physics A: Mathematical and Theoretical 43 (6) (2010) 065203. doi:10.1088/1751-8113/43/6/065203.
URL http://dx.doi.org/10.1088/1751-8113/43/6/065203

[229] R. W. Heeres, B. Vlastakis, E. Holland, S. Krastanov, V. V. Albert, L. Frunzio, L. Jiang, R. J. Schoelkopf, Cavity state manipulation using photon-number selective phase gates, Physical Review Letters 115 (13) (Sep 2015). doi:10.1103/physrevlett.115.137002.
URL http://dx.doi.org/10.1103/PhysRevLett.115.137002

[230] Y. V. Kovchegov, NonAbelian Weizsacker-Williams field and a two-dimensional effective color charge density for a very large nucleus, Phys. Rev. D 54 (1996) 5463–5469. arXiv:hep-ph/9605446, doi:10.1103/PhysRevD.54.5463.

[231] Y. V. Kovchegov, Quantum structure of the nonAbelian Weizsacker-Williams field for a very large nucleus, Phys. Rev. D 55 (1997) 5445–5455. arXiv:hep-ph/9701229, doi:10.1103/PhysRevD.55.5445.

[232] A. Ipp, D. I. Müller, D. Schuh, Jet momentum broadening in the pre-equilibrium Glasma, Phys. Lett. B 810 (2020) 135810. arXiv:2009.14206, doi:10.1016/j.physletb.2020.135810.

[233] N. Mueller, A. Tarasov, R. Venugopalan, Deeply inelastic scattering structure functions on a hybrid quantum computer, Physical Review D 102 (1) (2020) 016007.

[234] B. Bauer, D. Wecker, A. J. Millis, M. B. Hastings, M. Troyer, Hybrid quantum-classical approach to correlated materials, Phys. Rev. X 6 (2016) 031045. doi:10.1103/PhysRevX.6.031045.
URL https://link.aps.org/doi/10.1103/PhysRevX.6.031045

[235] W. A. De Jong, M. Metcalf, J. Mulligan, M. Ploskoń, F. Ringer, X. Yao, Quantum simulation of open quantum systems in heavy-ion collisions (10 2020). arXiv:2010.03571.

[236] V. Vaidya, X. Yao, Transverse momentum broadening of a jet in quark-gluon plasma: an open quantum system EFT, JHEP 10 (2020) 024. arXiv:2004.11403, doi:10.1007/JHEP10(2020)024.

[237] V. Vaidya, Forward scattering in a thermal Plasma (1 2021). arXiv:2101.02225.

[238] B. Blok, Heavy Quark Radiation in the Quark-Gluon Plasma in the Moller Theory: Angular Distribution of the Radiation (8 2020). arXiv:2009.00465.

[239] F. D'Eramo, M. Lekaveckas, H. Liu, K. Rajagopal, Momentum Broadening in Weakly Coupled Quark-Gluon Plasma (with a view to finding the quasiparticles within liquid quark-gluon plasma), JHEP 05 (2013) 031. arXiv:1211.1922, doi:10.1007/JHEP05(2013)031.

[240] F. D'Eramo, K. Rajagopal, Y. Yin, Molière scattering in quark-gluon plasma: finding point-like scatterers in a liquid, JHEP 01 (2019) 172. arXiv:1808.03250, doi:10.1007/JHEP01(2019)172.

[241] Y. Mehtar-Tani, A. Soto-Ontoso, K. Tywoniuk, Dynamical grooming of QCD jets, Phys. Rev. D 101 (3) (2020) 034004. arXiv:1911.00375, doi:10.1103/PhysRevD.101.034004.

[242] A. J. Larkoski, S. Marzani, G. Soyez, J. Thaler, Soft Drop, JHEP 05 (2014) 146. arXiv:1402.2657, doi:10.1007/JHEP05(2014)146.

[243] J. Carlson, D. J. Dean, M. Hjorth-Jensen, D. Kaplan, J. Preskill, K. Roche, M. J. Savage, M. Troyer, Quantum computing for theoretical nuclear physics, a white paper prepared for the us department of energy, office of science, office of nuclear physics, Tech. rep., USDOE Office of Science (SC)(United States) (2018).

[244] K. Bepari, S. Malik, M. Spannowsky, S. Williams, Towards a Quantum Computing Algorithm for Helicity Amplitudes and Parton Showers (10 2020). arXiv:2010.00046.

[245] C. W. Bauer, W. A. de Jong, B. Nachman, D. Provasoli, Quantum Algorithm for High Energy Physics Simulations, Phys. Rev. Lett. 126 (6) (2021) 062001. arXiv:1904.03196, doi:10.1103/PhysRevLett.126.062001.

[246] C. W. Bauer, M. Freytsis, B. Nachman, Simulating collider physics on quantum computers using effective field theories (2 2021). arXiv:2102.05044.

USC
UNIVERSIDADE
DE SANTIAGO
DE COMPOSTELA